Application of Artificial Neural Networks to the study of hydraulic turbine draft tubes

Pedro Henrique Dias de Véras Sousa

THÈSE

Pour obtenir le grade de

DOCTEUR DE L'UNIVERSITE GRENOBLE ALPES

Spécialité : MEP : **Mécanique des fluides, Energétique, Procédés**

Arrêté ministériel : 25 mai 2016

Présentée par

Pedro Henrique DIAS DE VÉRAS SOUSA

Thèse dirigée par **Oliver METAIS**, Professeur des Universités,
et co-encadrée par **Guillaume BALARAC**, Professeur des Universités, Grenoble INP

préparée au sein du **Laboratoire des Ecoulements Géophysiques et Industriels**
dans **l'École Doctorale I-MEP2 – Ingénierie – Matériaux, Mécanique, Energétique, Environnement, Procédés, Production**

Application des réseaux de neurones pour l'étude des aspirateurs des turbines hydrauliques

Application of Artificial Neural Networks to the study of hydraulic turbine draft tubes

Thèse soutenue publiquement le **28 septembre 2021**,
devant le jury composé de :

Monsieur Yves DELANNOY
PROFESSEUR DES UNIVERSITES, Grenoble INP, Président
Monsieur Michel CERVANTES
PROFESSEUR, Lulea Tekniska Universitet, Rapporteur
Monsieur Christophe CORRE
PROFESSEUR, Ecole Centrale de Lyon, Rapporteur
Monsieur Olivier MÉTAIS
PROFESSEUR DES UNIVERSITES, Grenoble INP, Directeur de thèse
Monsieur Guillaume BALARAC
PROFESSEUR DES UNIVERSITES, Grenoble INP, Codirecteur de thèse
Monsieur Antoine BOMBENGER
INGENIEUR, GE Renewable Energy (Grenoble), Invité
Madame Claire SÉGOUFIN
INGENIEUR-DOCTEUR, GE Renewable Energy (Grenoble), Invitée
Monsieur Didier GEORGES
PROFESSEUR DES UNIVERSITES, Grenoble INP, Invité

Résumé

L'aspirateur d'une turbine hydraulique est un élément hydraulique divergent situé en aval de la roue et dont le rôle est de convertir de façon efficace l'énergie cinétique résiduelle en sortie de roue en pression, en augmentant ainsi la charge utile et la performance de la machine. Puisque les pertes de charge dans les aspirateurs peuvent représenter une partie significative des pertes totales, notamment dans le cas des turbines de basse chute de type bulbe, prédire avec précision le comportement de l'écoulement dans ces éléments est important pour concevoir des machines plus efficaces et compétitives. Dans ce contexte, les simulations numériques sont moins chères que les campagnes expérimentales et donnent accès à une description plus détaillée de l'écoulement dans l'aspirateur. Comparées aux simulations conventionnelles du type RANS, les simulations de type LES permettent de reproduire plus fidèlement la dynamique complexe de l'écoulement dans l'aspirateur (i.e. fortement turbulent, avec une haute gamme d'échelles de mouvement, rotationnel et soumis à des gradients de pression adverses). Cependant, vu que le comportement de l'écoulement dans l'aspirateur est très sensible aux conditions d'entrée imposées et que les mesures expérimentales détaillées y sont difficiles à obtenir, l'enjeu principal pour ces simulations reste la détermination économique et adéquate des champs moyens et fluctuants en entrée du domaine de calcul. Ainsi, une approche innovante basée sur les techniques dites "data-driven", telles que l'apprentissage automatique, est proposée. Son objectif est d'utiliser toutes les informations disponibles sur l'écoulement en aval, ainsi qu'une base de données créée a priori, afin de déterminer les conditions d'entrée partiellement ou totalement inconnues pour une simulation numérique. Grâce à une extension artificielle positionnée en amont du domaine de calcul, l'approche proposée permet de plus aux fluctuations turbulentes synthétiques injectées en LES de se développer avant de pénétrer dans l'aspirateur. Dans un premier temps, l'approche est appliquée au cas géométriquement simple mais dynamiquement complexe du diffuseur conique d'ERCOFTAC. Comparés aux expériences et aux précédents travaux numériques, les résultats obtenus avec l'approche proposée sont de très bonne qualité. L'approche est ensuite appliquée au cas plus complexe de l'écoulement dans l'aspirateur d'une turbine bulbe. Les résultats numériques sont considérablement améliorés par rapport aux résultats basés sur des méthodes classiques. Finalement, une analyse détaillée des pertes de charge et des structures tourbillonnaires dans l'aspirateur permettent de montrer l'impact majeur des conditions d'entrée pour la conception d'aspirateurs plus efficaces.

Mots clefs : aspirateur de turbine bulbe, conditions d'entrée, turbulence synthétique, apprentissage automatique, simulation des grandes échelles, énergie hydroélectrique

Application of Artificial Neural Networks to the study of hydraulic turbine draft tubes

Abstract

The draft tube of a hydraulic turbine are divergent shaped equipment located downstream the runner and responsible for efficiently converting the residual kinetic energy leaving the runner into pressure, thus increasing the effective head and performance of the machine. As the head losses inside a draft tube can represent an important portion of the total energy losses, especially in the case of low head bulb turbines, it is essential to accurately predict the flow behaviour inside the draft tube if more efficient and competitive hydraulic machines are to be designed. In this context, numerical simulations are less expensive than experiments and give access to a more detailed description of the flow inside the draft tube. Compared to conventional RANS simulations using two-equation linear eddy-viscosity models, LES is more capable of capturing the complicated flow dynamics inside the draft tube (i.e. highly turbulent flow, with a wide range of vortical motions, swirling and subjected to an adverse pressure gradient). However, as the downstream flow behaviour is highly influenced by the inlet conditions and since comprehensive experimental measurements at the inlet of the draft tube are expensive, rarely available and often limited to mean flow quantities measured at a single radial traverse, the real challenge for performing these simulations consists in determining proper mean and fluctuating inlet boundary conditions. Thus, a new approach based on data-driven techniques, such as machine learning, is proposed. Its goal is to use any known information about the downstream flow along with a previously generated database to reconstruct the unknown or incomplete inlet boundary conditions for a numerical simulation. Thanks to an artificial upstream extension added to the original domain, the proposed approach gives more space and time for the simple synthetic fluctuations being injected in LES to develop before reaching the important portion of the computational domain. First, the simple yet challenging case of the swirling flow inside the ERCOFTAC conical diffuser is investigated. Compared to the experimental data and previous numerical works that used *ad hoc* inlet boundary conditions, the obtained results are very good. Then, in the case of the more complex flow inside a bulb turbine draft tube, the proposed approach yields better results in both RANS and LES in comparison to the initial simulations using basic inlet boundary conditions. Finally, a detailed analysis of the flow topology and head losses inside the draft tube demonstrates the impact of proper inlet boundary conditions for the design of more efficient draft tubes.

Keywords: bulb turbine draft tube, inlet boundary conditions, synthetic turbulence, machine learning, large eddy simulation, hydroelectric power

Acknowledgements

I would like to start by expressing my sincere gratitude to my thesis advisor, Prof. Olivier Métais, for guiding me with all his invaluable advice and support during all these years. In the context of my thesis, he gave me all the freedom and trust I needed to explore different solutions for our problems, and our many discussions (in-person or online) encouraged me to always go further in my research. Beyond my thesis, he has been a very thoughtful person, and I will be forever grateful for all his assistance since the beginning of my journey in France.

In addition to that, I am also very grateful to my thesis co-advisor, Prof. Guillaume Balarac, for his constant support and numerous discussions that allowed me to quickly learn the numerical tools used in this work. Guillaume is an inspiring person and his incredible commitment to his research will shape the way I see myself as a researcher.

This research was only possible thanks to the collaboration of General Electric Renewable Energy. Therefore, I would like to thank Antoine Bombenger, who I had the pleasure of working with since before my thesis and who taught me so much about hydraulic machines, and Claire Ségoufin, whose meticulous view and extensive knowledge undoubtedly contributed to this work.

I would also like to express my gratitude to Prof. Didier Georges, who kindly accepted to share his knowledge with me and whose contribution to this work, particularly in machine learning, was crucial to its accomplishment.

I also wish to thank my thesis committee members, in particular the president of the jury, Prof. Yves Delannoy, and the reviewers, Prof. Michel Cervantes and Prof. Christophe Corre, for their interest in my thesis and for their comments, discussions and suggestions that made this work more valuable.

I had the pleasure of preparing this thesis at LEGI, where I was surrounded by great people who made my days in the lab much more pleasant. In this regerd, I would like to thank Patrick Bégou for his patience and willingness to assist me whenever I needed it, Giovanni Ghigliotti for the many interesting discussions and for giving me the opportunity to teach at the university, my colleagues Guillaume Sahut and Himani Garg, with whom I had the pleasure to share the office during these years, Hugo Frezat for his helpful insights on different aspects of machine learning, and all the other members of the MoST team: Manuel, François, Mathieu, Matei, Anastasia, Cyril, Jérémie, Alexis, Savinien, Thomas. I also wish to thank Helder Guta and his wife, Pauline, for their friendship and for making life away from my family easier.

A special thanks to my parents, Mauricio and Miriam, for their unconditional support and encouragement during the years since childhood. Moreover, I would also like to thank my sister, Ana Cláudia, whose dedication has always been an inspiration to me.

Finally, I would like to express my deepest gratitude to my dear wife, Mariana. She kindly accompanied me on this journey, always encouraging me and believing in me, despite the many difficulties that we have faced on the way. Undoubtedly, this work would not be possible without her endless care, support, understanding, and love. *Eu te amo, Mari.*

Contents

List of Figures

List of Tables

List of Symbols

Symbol	Units (SI)	Definition
Latin symbols		
D	m	Diameter
E_n	J/kg	Net specific energy
g	m/s^2	Acceleration of gravity
h	m	Height
H	m	Head
H_g	m	Gross head
H_i	m	Internal head
H_n	m	Net head
I_t	-	Turbulence intensity
k	m^2/s^2	Turbulent kinetic energy
K	m^2/s^2	Mean kinetic energy
l_i	m	Integral scale
l_K	m	Kolmogorov's length scale
l_m	m	Mixing length
L	m	Length of the draft tube
L_s	m	Characteristic scale of the mean flow
n	rpm	Rotation speed
n_{11}	-	Unit speed
P	m^2/s^3	Turbulent kinetic energy production
P_i	W	Internal power
P_n	W	Net power
P_s, p	Pa	Static pressure
P_t	Pa	Total pressure
r	m	Radius
R	m	Maximum radius
Re	-	Reynolds number
S	s^{-1}	Strain rate tensor
S_w	-	Swirl number
q	Pa	Dynamic Pressure
Q	m^3/s	Flow rate
Q_{11}	-	Unit flow rate
t	s	Time
T	N.m	Torque
U_r	m/s	Radial velocity
U_x	m/s	Streamwise velocity
U_z	m/s	Axial velocity
U_θ	m/s	Circumferential velocity

U_{inj}	m/s	Injection velocity
$\vec{u}$	m/s	Velocity vector
u^+	-	Dimensionless velocity
u_τ	-	Friction velocity
U_b	m/s	Bulk velocity
V	m/s	Velocity
V_b	m/s	Bulk velocity
V_r	m/s	Radial velocity
V_u,V_θ	m/s	Tangential velocity
V_z	m/s	Axial velocity
$\vec{x}$	m	Position vector
y	m	Normal distance to the wall
y^+	-	Dimensionless wall distance
z	m	Axial position
Z	m	Altitude

Greek symbols

α	$^\circ$	Runner blade angle
γ	$^\circ$	Guide vane angle
δ_{ij}	-	Kronecker delta
ϵ	m^2/s^3	Turbulence dissipation
η	-	Hydraulic efficiency
η_l	-	Learning rate
ν	m^2/s	Kinematic viscosity
ν_t	m^2/s	Turbulent viscosity
ν_{sgs}	m^2/s	Subgrid scale viscosity
ρ	kg/m^3	Fluid density
τ_w	N/m^2	Wall shear stress
χ	-	Pressure recovery coefficient
ω	s^{-1}	Turbulence characteristic frequency
Ω	rad/s	Rotation speed

Abbreviation	**Definition**

Subscripts/Superscripts

atm	Atmosphere
dyn	Dynamic
in	Inlet
ip	Integration point
opt	Optimal
re	Reservoir
sec	Section
sta	Static
tot	Total
tw	Tail water

List of abbreviations

ANN	Artificial Neural Network
ASM	Algebraic Reynolds Stress
CFD	Computational Fluid Dynamics
CFL	Courant–Friedrichs–Lewy
DDES	Delayed Detached Eddy Simulations
DES	Detached Eddy Simulations
DF	Digital Filters
DNS	Direct Numerical Simulation
DPCG	Deflated Preconditioned Conjugate Gradient
ELU	Exponential Linear Unit
ERCOFTAC	European Research Community On Flow Turbulence And Combustion
EPFL	École Polytechnique Fédérale de Lausanne
FC	Fully Connected
FLINDT	Flow Investigation in Draft Tube
FVM	Finite Volume Method
GE	General Electric
GRC	Global Research Center
HIT	Homogeneous Isotropic Turbulence
HPC	High-Performance Computing
IEC	International Electrotechnical Commission
MLP	Multilayer Perceptron
MoST	Modélisation et Simulation de la Turbulence
MSE	Mean Squared Error
NAG	Nesterov Accelerated Gradient
PDE	Partial Differential Equations
RANS	Reynolds Average Navier-Stokes
ReLU	Rectified Linear Unit
RFG	Random Flow Generation
RSM	Reynolds Stresses Model
LDV	Laser-Doppler Velocimetry
LEGI	Laboratoire des Écoulements Géophysiques et Industriels
LES	Large Eddy Simulation
SAS	Scale-Adaptive Simulations
SEM	Synthetic-Eddy Method
SGD	Stochastic Gradient Descent
SGS	Subgrid Scale
SST	Shear Stress Transport
URANS	Unsteady Reynolds Average Navier-Stokes
VLES	Very Large-Eddy Simulations
WMLES	Wall Model Large Eddy Simulation

Chapter 1

Introduction

Contents

Hydropower is a well established technology and one of the most important renewable energy sources. In this type of technology, the potential energy of the water coming from the water cycle is used to rotate the runner of a hydraulic turbine and to generate electrical power for the grid. In spite of the increasing participation of other energy sources such as wind and solar, hydropower generation is growing and still represents almost 60% of the total renewable energy generation and 17% of the total electrical energy production in the world [1]. China is by far the world's largest hydropower producer, with over 1.35 TWh produced in 2020, almost 3.5 times that from the second place, Brazil. Nowadays, as viable large hydro sites are almost accomplished in developed countries, the exploitation of low head sites has become more attractive. The problem is that turbines which are better suited for operating at these conditions, notably bulb turbines, are highly affected by the head losses inside their draft tube, a divergent shaped equipment responsible for efficiently converting the residual kinetic energy leaving the runner into pressure and increasing the turbine's performance [61]. Therefore, being able to accurately predicting the flow behaviour and head losses inside draft tubes is essential for the design of more efficient and competitive low head turbines.

In their search for more competitive machines and improved efficiency, manufacturers have adopted Computational Fluid Dynamics (CFD) in their design process due to its lower cost, flexibility, and access to larger database than traditional experimental measurements. In this context, this thesis is part of a collaboration between the hydraulic turbines manufacturer General

Electric (GE) Renewable Energy and the *Modélisation et Simulation de la Turbulence* (MoST) team at the *Laboratoire des Écoulements Géophysiques et Industriels* (LEGI). The goal being to improve the numerical prediction of draft tube performances, this work is a continuation of the multiple thesis presented in the past, but is particularly based on that from Wilhelm [160]. To understand the main motivations and objectives of this thesis, as well as the discussions in the following chapters, the basic aspects about hydropower generation are explained next.

1.1 General aspects of hydroelectric power plants

1.1.1 Arrangement of a hydroelectric power plant

Figure 1.1 shows the scheme of a hydroelectric power plant used to convert the energy of a water flow into electricity. An accumulation dam is used to store the water in an upstream reservoir, which then enters the hydropower plant through an intake and is directed to the turbine through a conduit system (penstock). Inside these conduits, the water flow increases its velocity and the potential energy of the water is converted into kinetic energy. Depending on the turbine, a spiral case and a distributor directs the flow to the guide vanes, which varies the opening angle of its blades to control the flow rate and direction of the water flow upstream the runner. The runner recovers this hydraulic energy on the flow and converts it into mechanical energy in the form of a rotating shaft, which is linked to an electric generator that will then convert this mechanical energy into electrical energy. After the runner, the water flow passes through a draft tube, where part of the residual kinetic energy of the flow is recovered, and then it discharges into the tail race canal.

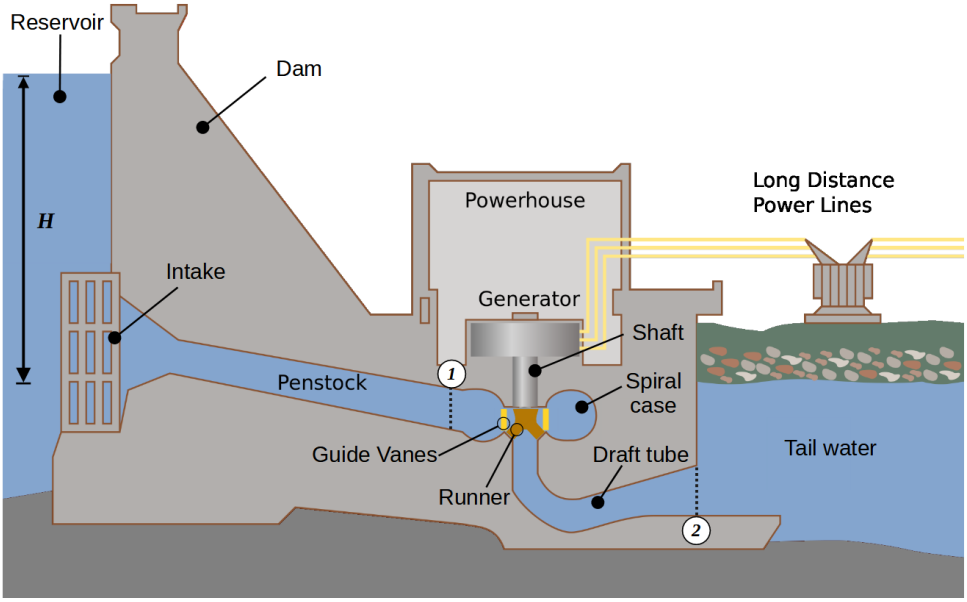

Figure 1.1: Diagram of a typical hydroelectric power plant. Source: adapted from *https://populationeducation.org/what-are-pros-and-cons-hydropower-and-tidal-energy/*

1.1.2 Energy conversion

The water flow from the upper to the lower level in a hydroelectric power plant represents a hydraulic power potential that can be exploited to generate mechanical power on the shafts of turbines. The amount of power produced by the power plant is a function of the difference between the water levels and the resulting water flow passing through its multiple elements (e.g., intake conduits, guide vanes, runner, draft tube etc.). This power is evaluated by the application

of Bernoulli's principle and the assessment of the head at multiple locations inside the power plant. For instance, the *head*, given in meters (m), at location 0 is defined as:

$$H_0 = \frac{p_0}{\rho g} + \frac{V_0^2}{2g} + Z_0 \tag{1.1}$$

where ρ is the density of the water, g is the acceleration of gravity and p_0, V_0 and Z_0 are, respectively, the static pressure, mean velocity and altitude at station 0. The *gross head* is defined as the difference between the head at the upstream reservoir (re) and downstream tail water (tw) in a hydropower plant, i.e.,

$$H_g = H_{re} - H_{tw} = \left(\frac{p_{re}}{\rho g} + \frac{V_{re}^2}{2g} + Z_{re}\right) - \left(\frac{p_{tw}}{\rho g} + \frac{V_{tw}^2}{2g} + Z_{tw}\right) \tag{1.2}$$

However, considering that the static pressure upstream and downstream the hydropower plant are equal to the atmospheric pressure, $p_{re} = p_{tw} = p_{atm}$, and that the free surface velocities at these two locations are negligible compared to the velocities found inside the different elements of the plant, i.e., $V_{re} \approx V_{tw} \approx 0$, the gross head, H_g, is given by the difference between the upstream and downstream water level. Since the water flowing through the conduits from the intake side of the turbine (i.e., upstream section 1 in Fig. 1.1) and from the draft tube outlet to the tailwater (downstream section 2 in Fig. 1.1) generate some head losses, ΔH_{loss}, the effective head, or *net head*, available for the turbine is given by:

$$H_n = H_g - \Delta H_{loss} \tag{1.3}$$

which, assuming a steady and uniform flow at stations 1 and 2, can be rewritten as the difference in head between these two stations, i.e.,

$$H_n = H_1 - H_2 = \left(\frac{p_1}{\rho g} + \frac{V_1^2}{2g} + Z_1\right) - \left(\frac{p_2}{\rho g} + \frac{V_2^2}{2g} + Z_2\right) \tag{1.4}$$

Considering the available specific energy, or the *net specific energy*, in J/kg,

$$E_n = gH_n = gH_1 - gH_2 \tag{1.5}$$

the *net power* for the turbines in the power plant in Watt, P_n, is equal to the product between this net specific energy and the mass flow passing through the turbine, that is:

$$P_n = \rho Q E_n = \rho g Q H_n \tag{1.6}$$

where Q is the flow rate. However, part of this net power is lost due to multiple factors (e.g., head losses in the machine, friction, labyrinth leakage etc.) and the mechanical power available at the shaft of the runner, also called *internal power*, P_i, is smaller than P_n. It can be evaluated though from the torque, T, and the rotation speed, Ω, on the shaft:

$$P_i = \Omega T \tag{1.7}$$

The *hydraulic efficiency*, η, of the turbine is calculated as the ration between the mechanical power and the net power, i.e.,

$$\eta = \frac{P_i}{P_n} \tag{1.8}$$

1.2 Overview of the draft tube

The water flow leaving the runner still has some residual velocity, and therefore kinetic energy, associated with it, which represents a portion of the total energy available for the turbine that was not converted into mechanical energy and electricity. The draft tube is a divergent shaped equipment, positioned downstream the runner, that directs the water flow to the downstream tail race canal and reduces the velocity of the flow leaving the runner in order to maximize the internal power of the turbine. To understand how exactly this is accomplished, Wilhelm [160] performed a very detailed analysis of the role of the draft tube in a hydraulic turbine. For instance, starting from the equation for the internal power of the turbine, Eq. (1.7), even though this is a mechanical power according to its definition, it can be written in terms of an *internal head*, H_i, such that:

$$P_i = \rho g Q H_i \tag{1.9}$$

If $\Delta H_{A,B}$ is the head loss between the inlet and outlet of the runner (respectively, sections A and B in Fig. 1.2) and ΔH_{runner} the losses within this region of the flow, the internal head, H_i, can be written as:

$$H_i = \Delta H_{A,B} - \Delta H_{runner} = (Z_A - Z_B) + \frac{1}{\rho g}(p_A - p_B) + \frac{1}{2g}(V_A^2 - V_B^2) - \Delta H_{runner} \tag{1.10}$$

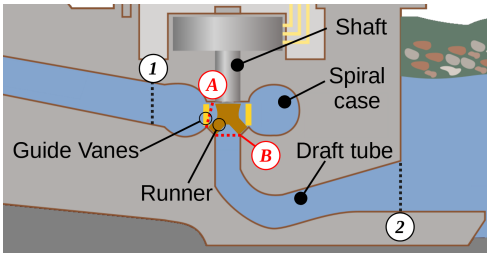

Figure 1.2: Definitions of sections used to analyse the head losses inside the draft tube. Source: adapted from *https://populationeducation.org/what-are-pros-and-cons-hydropower-and-tidal-energy/*

In this equation, Z_A and Z_B are fixed by the setup of the turbine, while V_A, V_B and the losses Δ_{runner} are fixed by its operating condition and geometry. Moreover, as the static pressure at the runner inlet, p_A, is fixed by the head losses upstream the turbine, then the internal head is only a function of the static pressure at the runner outlet, p_B, and it can be increased by reducing this pressure. However, p_B, is a function of the head loss between the runner outlet, H_B and the surface of the tail water (H_{tw}), where the static pressure is equal to the atmospheric pressure, p_{atm}, and the velocity is negligible:

$$\Delta H_{B,tw} = (Z_B - Z_{tw}) - \frac{1}{\rho g}(p_B - p_{atm}) + \frac{1}{2g}(V_b^2) = \Delta H_{B,2} + \Delta H_{2,tw} \tag{1.11}$$

where $\Delta H_{B,2}$ is the head losses inside the draft tube and $\Delta H_{2,tw}$ the head losses between the outlet of the draft tube and the tail water. This latter can be considered as being equal to the head losses in a sudden expansion with loss coefficient 1, i.e., $\Delta H_{2,tw} = V_2^2/2g$. Thus, isolating p_B in Eq. (1.11) and replacing the obtained result in Eq. (1.10), given the following expression for the internal head:

$$H_i = (Z_A - Z_{tw}) + \frac{1}{\rho g}(p_A - p_{atm}) + \frac{1}{2g}(V_A^2 - V_2^2) - \Delta H_{runner} - \Delta H_{B,2} \tag{1.12}$$

Given that Z_A, Z_{tw}, p_A, V_A and ΔH_{runner} are all fixed, it is clear that the internal head, H_i, depends only on the velocity at the exit of the draft tube, V_2, as well as its head losses, $\Delta H_{B,2}$. Conversely, if there was no draft tube downstream the runner's outlet, then the head losses $\Delta H_{B,tw}$ could be considered as being equal to the head losses due to a sudden expansion with a loss coefficient equal to 1, such that $\Delta H_{B,tw} = V_B^2/2g$, and the internal head, H_i^*, would be given by:

$$H_i^* = (Z_A - Z_{tw}) + \frac{1}{\rho g}(p_A - p_{atm}) + \frac{1}{2g}(V_A^2 - V_B^2) - \Delta H_{B,2} \tag{1.13}$$

Therefore, the benefits of having a draft tube downstream the runner can be quantified by the difference in internal heads:

$$H_i - H_i^* = \frac{1}{2g}(V_B^2 - V_2^2) - \Delta H_{B,2} \tag{1.14}$$

From this equation, it is clear that as long as its right-hand side is positive, the draft tube actually increases the internal head of the hydraulic turbine. Assuming that the velocity of the flow leaving the runner, V_B, is fixed, than the velocity of the flow leaving the draft tube, V_2, should be reduced while limiting the head losses $\Delta H_{B,2}$. In addition to that, the maximum value of the velocity V_2 is limited by environmental constraints and fixed by the client of the turbine manufacturer (GE). Therefore, the reason behind the divergent shape of the draft tube is to increase the cross-section area and to reduce the velocity at its outlet for a given flow rate. After applying Bernoulli's principle to the flow inside the draft tube and assuming a constant $\Delta H_{B,2}$, a direct consequence of this velocity reduction is an increase in static pressure, meaning that the draft tube acts like a diffuser and recovers part of the residual kinetic energy leaving the runner in the form of static pressure. Indeed, one way to evaluate the draft tube's performance is to calculate the pressure recovery coefficient, χ, which measures the amount kinetic energy that has been converted into static pressure and given by:

$$\chi = \frac{\overline{p}_2 - \overline{p}_B}{\frac{1}{2}\rho\left(\frac{Q}{A_B}\right)^2} \tag{1.15}$$

where $\overline{p}_2$ and $\overline{p}_B$ are, respectively, the average *static* pressure at the inlet and outlet of the draft tube and A_B is the area of the section B.

The velocity of the flow leaving the draft tube can be further reduced by increasing the area ratio between its inlet and outlet cross-sections. This can be easily achieved either by increasing its length or its divergence angle. However, while the former results in higher civil construction costs, the latter could lead to the separation of the boundary layer. Similarly, if V_2 is too much reduced and the static pressure recovery is too important, the flow inside the draft tube can be subjected to adverse pressure gradients which again can cause the boundary layer to detach from the walls and increase the head losses, $H_{B,2}$. Indeed, these losses are one of the most important aspects in a draft tube and are given by the difference in *total* pressure between the draft tube's inlet and outlet, i.e.,

$$\Delta H_{B,2} = \frac{1}{\rho g}(\overline{P}_{t,B} - \overline{P}_{t,2}) \tag{1.16}$$

where $\overline{P}_t$ is the average total pressure at a given section.

Accurately predicting these losses is crucial when designing a draft tube to optimize its geometry and to evaluate the overall performance of the hydropower plant. However, the flow dynamics inside a draft tube is very complex and determining these losses is a challenging task.

For instance, the flow leaving the runner and entering the draft tube is particularly unsteady, with important variations in the azimuthal direction (especially in the case of turbines with small number of runner blades) and with multiple vortices forming downstream the runner and guide vanes [5, 157, 84]. The flow inside the draft tube is highly turbulent, with a wide range of vortical motions, including the formation of a large vortical structure in the centre of the draft tube, called *central vortex* due to the interaction between the swirling flow and the central hub and whose characteristics vary depending on the operating point of the draft tube, and that can have negative effects on the overall performance of the hydraulic turbine [112, 72, 43]. Finally, the divergent shape of the draft tube lead to important adverse pressure gradients which can lead to the boundary layer separation from the walls and consequent increase of the head losses and reduction of its hydraulic performance [65, 38].

1.3 Bulb turbines

1.3.1 Classification of hydraulic turbines

Depending on the application, different types of turbines can be utilized to generate electricity from the variation of hydraulic head. In Fig. 1.3, the four main types of hydraulic turbines are separated according to the head and the flow rate available at the hydropower plant. In addition to that, the turbines are also separated into two main groups, according to the way the hydraulic energy is converted into mechanical energy: *impulse* turbines and *reaction* turbines.

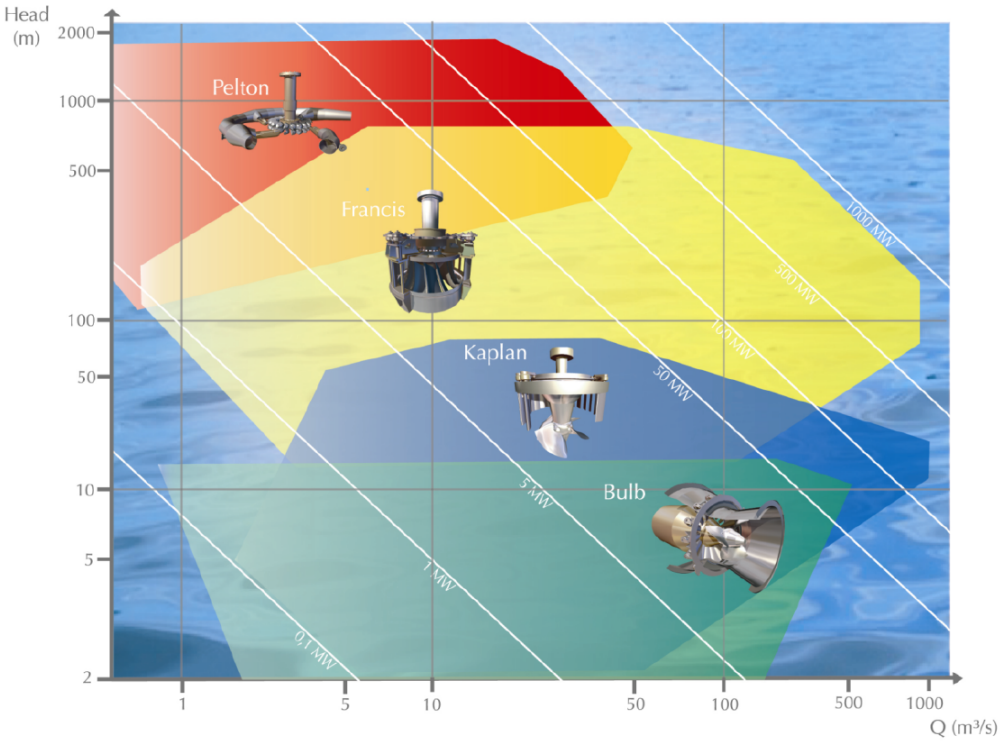

Figure 1.3: Types of hydraulic turbines separated the head and flow rate. Source: GE Renewable Energy

Impulse turbines, such as Pelton turbines, are employed at locations with a *very* significant head but low flow rate. In this type of turbine, the potential energy of the water stored at the upstream reservoir is completely converted into kinetic energy thanks to a series of nozzles, and the resulting water jets are deflected after hitting the runner buckets. This variation in flow direction is what allows the runner to convert the kinetic energy of the water jet into rotational mechanical energy in the runner's shaft.

Reaction turbines can be applied in a wide range of head and flow rates, and comprise, normally, Francis, Kaplan and Bulb turbines. Contrarily to impulse turbines, the runner is completely submerged in a reaction turbine. As a result, there are two mechanisms responsible for the conversion of the water flow energy into mechanical energy: (i) the pressure drop between the inlet and outlet of the runner and (ii) the changes in direction of the flow caused by the blades in the runner. Despite being based on the same energy conversion mechanisms, Francis turbines are distinct from Kaplan and Bulb turbines as the flow enters the runner radially (perpendicular to the axis of rotation) and leaves it axially (parallel to the axis of rotation), whereas in the other two cases it enters and leaves axially. Moreover, their runner is composed by several blades and are particularly suited. Kaplan turbines also have a vertical axis of rotation, but their runner is composed by a limited number of blades, which are especially designed for low head operations and high flow rates. In the case of very low heads (e.g., below 20 m), Bulb turbines are the most adapted due to their horizontal axis and, similarly to Kaplan turbines, possibility of adjusting the angle of the blades in both guide vanes and runner.

1.3.2 Description of a bulb turbine

In this thesis, we will investigate the turbulent flow inside a bulb turbine draft tube. These turbines do not need large upstream reservoirs and, as previously mentioned, allow the exploitation of low head high flow rates sites like rivers, hence their characterization as a *run-of-the-river* turbine. Figure 1.4 shows the scheme of a bulb turbine. Compared to the scheme shown in Fig. 1.1, these turbines are horizontally arranged and the draft tube downstream the runner is straight, so no *elbow* is required to change the direction of the flow. Moreover, there is no spiral case and distributor upstream the runner and the guide vanes. Its runner is characterized by having only a few blades, between 3 and 5, whereas more common Francis turbines runners have between 10 and 20. In general, a bulb turbine is very similar to a Kaplan turbine, except for the horizontal disposition of its elements. This has a positive effect on the overall hydraulic performance of the turbine, especially because of the absence of an elbow on the draft tube and can reduce the construction costs for a given power output.

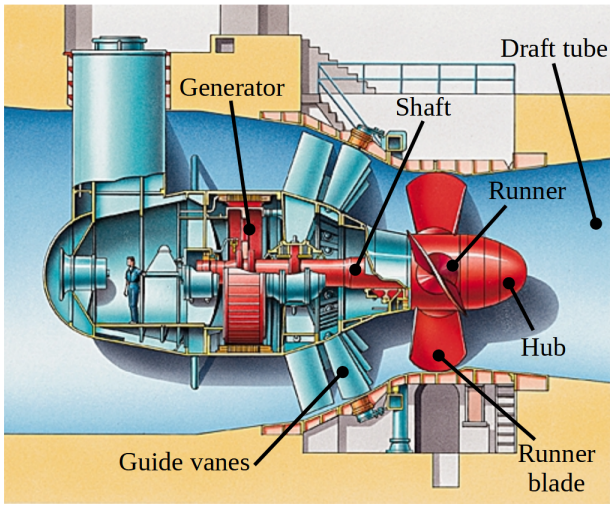

Figure 1.4: Scheme of a bulb turbine. Source: adapted from Brugière [14].

1.3.3 Characteristic curves

One of the main advantages of Kaplan and bulb turbines is the fact they are double regulated, that is, it is possible to adjust the pitch of guide vanes and runner's blades. This allows the turbine to adapt to the water flow and therefore improve its performance over a wide range of

operating conditions. For instance, an operating point of the turbine is characterized by the opening angle of the guide vanes, γ (which controls the flow rate), a runner blade angle, α, and a net head, H_n. A turbine is said to be operating *on-cam* when the combination of γ, α and H_n is such that its power output is maximized. Conversely, a turbine is said to operating *off-cam* when the combination of γ, α and H_n is not ideal.

To simplify the study of hydraulic turbines, it is common practice to use dimensionless quantities to characterize their operating condition. For instance, the unit flow rate Q_{11} and unit speed n_{11} can be defined as:

$$Q_{11} = \frac{Q}{D^2\sqrt{H_n}} \tag{1.17}$$

$$n_{11} = \frac{nD}{\sqrt{H_n}} \tag{1.18}$$

where Q is the flow rate, D is the turbine diameter and n its rotational speed in *rotations per minute*, rpm, and H_n the net head.

Figure 1.5 shows an example of the characteristic curves for the case of a double regulated turbine. To generate the propeller curves of the turbine, Fig. 1.5a, the net head H_n and runner blade angle α are fixed while the opening angle of the guide vanes γ is gradually increased, which in turn modifies the flow rate and turbine efficiency. The best efficiency point in this curve correspond to the on-cam point of the turbine at a given H_n and α. The combination of the on-cam points at several flow configurations generate the performance hill chart shown in Fig. 1.5b. In this chart, the iso-curves of efficiency η and runner blade angle α are plotted as a function of the dimensionless quantities Q_{11} and n_{11}. The best efficiency on-cam point in this chart is called the best (or optimal) operating point.

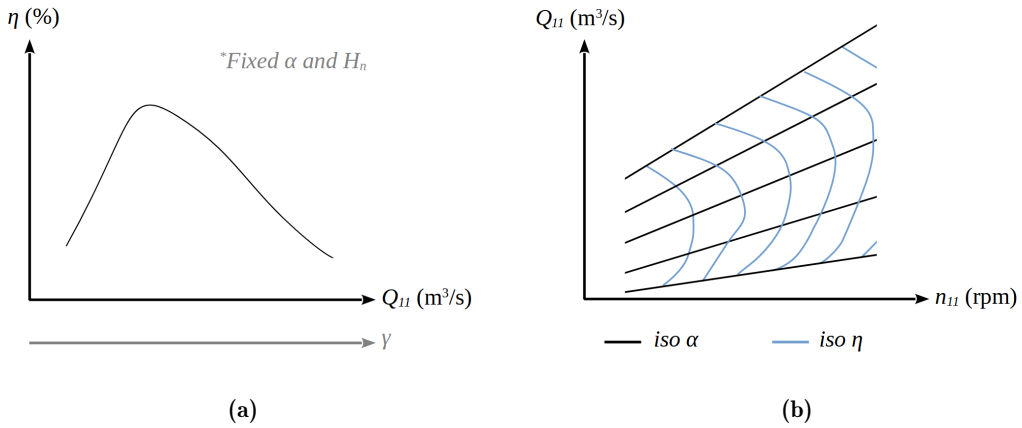

Figure 1.5: Characteristic curves of a bulb turbine. (a) propeller curve; (b) hill chart.

1.3.4 Velocity triangles

Indeed, to understand how the hydraulic energy of the flow is converted into mechanical energy in a bulb turbine, we can analyse the velocity field upstream and downstream the runner. From the application of Euler's turbine equation, it is possible to associate the torque at the runner shaft to a change in flow direction and, therefore, in the velocity triangles at these two regions of the flow. For instance, considering a fluid particle moving at a velocity $\vec{V}$ with respect to a fixed coordinate system and relative velocity $\vec{W}$ with respect to a coordinate system rotating at the same angular speed Ω of the runner, then the blade rotational velocity, $\vec{U}$, which is fixed,

is given by the cross product $\vec{U} = \vec{\Omega} \times \vec{r}$, where $\vec{r}$ is the position vector of the fluid particle, and we can write then:

$$\vec{V} = \vec{W} + \vec{U} \tag{1.19}$$

Using the equation above and analysing the flow passing through the runner at a constant radius (i.e., function only of the axial position z and angular position θ), the velocity triangles upstream and downstream the runner can be traced according to the operating condition of the hydraulic turbine (on-cam and off-cam), as shown in Fig. 1.6.

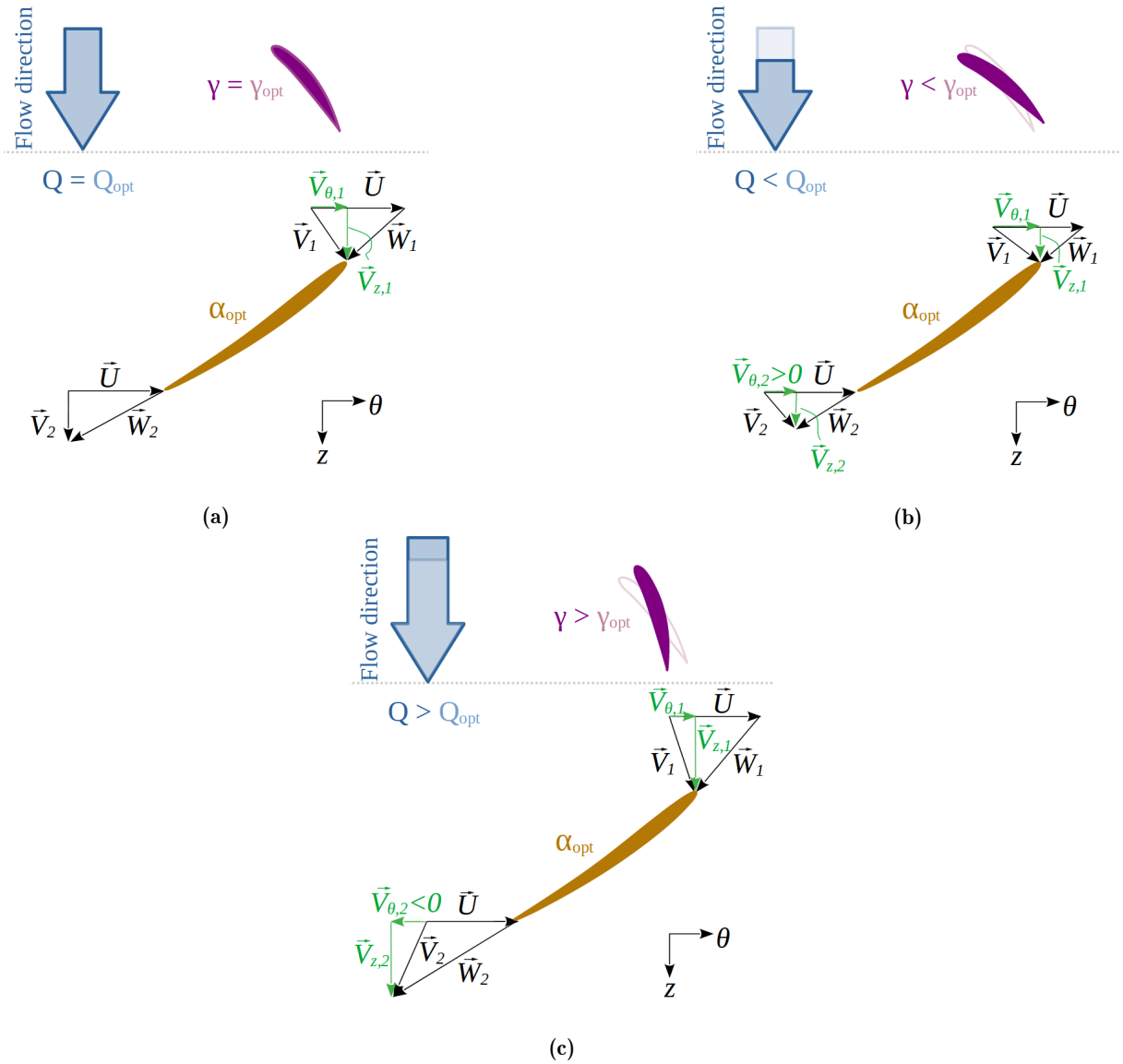

Figure 1.6: Velocity triangles for a bulb turbine operating at (a) the best efficiency point, (b) at partial load and (c) at high load. In orange the runner, in purple the guide vanes. γ is the opening angle of the guide vanes and α the runner blade angle. Source: adapted from Wilhelm [160].

In the velocity triangles shown in Fig. 1.6, V_θ is defined as the tangential velocity and V_z is the axial velocity. At the best operating point, the tangential velocity of the flow leaving the runner $V_{\theta,2}$ is equal to zero and the flow entering the draft tube is mostly axial (except for a small radial velocity component). At partial load, however, the opening angle of the guide vanes γ is reduced compared to the best operating point and the tangential velocity of the flow entering the runner, $V_{\theta,1}$ is increased. As a result, the flow leaving the runner still conserves

part of this tangential velocity and $V_{\theta,2}$ ends up being greater than zero (the flow is rotating at the same direction of the runner). Conversely, when the turbine is operating at a high load, the opening angle γ is increased compared to the best operating point and $V_{\theta,1}$ is reduced. As a consequence, $V_{\theta,2}$ is lower than zero and the flow entering the draft tube is counter-rotating with respect to the runner. Notice, however, that in practice, the runners are designed to preserve a small flow tangential velocity at its exit. This is important to improve the performance of the draft tube as it prevents the boundary layer from separating from the walls due to the resulting centrifugal force caused by the flow rotation [99].

1.3.5 Draft tube of a bulb turbine

As previously mentioned at the beginning of this section, one of the characteristics of a bulb turbine is its straight draft tube, as it is shown in Fig. 1.7. Its cross-section area is constantly increasing precisely to reduce the velocity of the water flow and thus recover part of the residual kinetic energy leaving the runner. The initial portion of the draft tube has a conical shape (therefore called the *cone* of the draft tube), which is followed by a transition region where this circular shape gradually transitions into a rectangle (at the draft tube's exit). The flow leaving the bulb turbine runner is very complex and creates complicated flow dynamics inside the draft tube. However, for the particular case of a bulb turbine, the head losses inside this element (as discussed in Section 1.2) can represent an important portion of the total energy losses inside the turbine. Therefore, it is crucial to accurately reproduce the flow inside a bulb turbine draft tube (and any draft tube indeed), not only to correctly estimate the efficiency of the machine, but especially to understand the phenomena responsible for these losses.

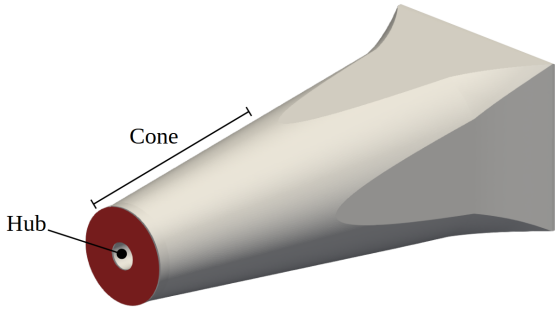

Figure 1.7: Scheme of a bulb turbine draft tube.

1.4 Motivation

1.4.1 Industrial perspective

In the early stages of designing a hydraulic turbine, the numerical simulations of its different elements are very important. Indeed, they are faster to conduct and less expensive than experimental campaigns, and allow for the comparison of multiple designs and operating conditions of the turbine. Moreover, they give access to a more complete description of the flow inside the turbine and allow a better understanding of the multiple physical phenomena taking place. Preferably, these numerical simulations should not take a long time to perform, however, it is imperative that the obtained results are very accurate, in particular the turbine efficiency. Since the head losses inside the draft tube can have an important impact on the overall performance of the hydraulic turbine, especially on those operating at low heads, it is crucial to numerically predict the flow behaviour inside these equipments. However, given the complexity of this flow (e.g., unsteady, turbulent, swirling and subjected to adverse pressure gradients), accurate simulations are challenging and therefore advanced numerical methods are needed.

1.4.2 Academic perspective

The complexity of the flow considered in this thesis and the advanced numerical methods used to simulate it represent an interesting study case in the academic point of view. For instance, most of the discussions in this work are based on the results obtained with Large-Eddy Simulations of the flow inside the draft tube performed in the flow solver YALES2 (more details in Chapter 2). Despite the high computational cost associated with these approaches, this thesis shows some of their benefits in comparison to simpler and less computationally expensive statistical approaches, such as Reynolds Averaged Navier-Stokes (RANS) approaches. In addition to that, another very important aspect of this thesis is the application of data-driven techniques, such as Machine Learning, to determine proper inlet boundary conditions for a numerical simulation. Indeed, not only this is a major challenge in the field of draft tube simulations due to the complexity of the flow (see Section 3.1.2), but it is also a challenge for numerical simulations of spatially developing flows in general (e.g., jets, mixing layers, wall-bounded flows etc.). Although we concentrate on the flow inside a bulb turbine draft tube, the proposed approach to determine proper inlet conditions is also applied to the canonical case of the swirling flow inside a conical diffuser. In any case, this problem extends to many other academic and industrial applications.

1.4.3 Collaboration with General Electric Renewable Energy

The present thesis is inserted in the context of a long term collaboration between the hydraulic branch of General Electric in Grenoble and the MoST team at LEGI. This collaboration started back in 2006 with the thesis of Duprat [36], who performed a numerical study of the draft tube of a Francis turbine using Large-Eddy Simulations. The goal was primarily to reproduce the complex flow inside the draft tube, but also to analyse a sudden drop in performance of a rehabilitated hydraulic turbine close to its best efficiency point. While the comparison with experimental results of Tridon [150] did not yield totally satisfactory results, one of the great contributions of Duprat was the development of a wall model more adapted for the type of flows observed inside draft tubes [37]. In 2015, Brugière [14] investigated the flow passing through the distributor of a Francis turbine and inside a bulb turbine draft tube using numerical simulations. In addition to LES, Brugière also utilized RANS simulations to study these flows. The goal was to analyse the uncertainties associated with these simulations and therefore improve the reliability of the obtained results. However, while the numerical results have shown a strong influence of the imposed inlet boundary conditions, the uncertainties associated with these conditions could not explain the differences with respect to the experimental measurements. In 2016, Wilhelm [160] studied once again the problem of the flow inside a bulb turbine draft tube. Having access to more experimental data, including Laser-Doppler Velocimetry (LDV) measurements, the goal was to improve the prediction of numerical simulations and to investigate the head losses inside the draft tube using unsteady RANS (URANS) simulations and LES. An equation was developed to identify the different mechanisms responsible for these head losses [159] and, conversely to Brugière [14], the axisymmetric inlet boundary conditions were replaced by a two-dimensional boundary condition issued from a guide vane/runner RANS simulations. While the proposed equation allowed to precisely locate the regions and mechanisms responsible for most of the losses inside the draft tube, especially with LES, the comparisons with experimental data was still not fully satisfactory. Indeed, in spite of the good agreement between numerical and experimental velocity profiles, the boundary layer was still not well predicted. The results were improved by modifying the wall roughness in the simulations, but Wilhelm [160] argued that the boundary conditions should be better characterized to obtain better numerical predictions. Recently, Doussot [33] investigated the dynamics of the inter-blade vortices using RANS, LES and Scale-Adaptive Simulations (SAS) based on the thesis of Bouajila [11], who studied the pressure frequency of different Francis runners operating at partial load.

1.5 Objectives

The previous collaborations between GE and LEGI have shown the interest for improving the numerical predictions of the flow inside hydraulic machines, in particular their draft tubes. Indeed, as the head losses inside these elements can have a major impact on the overall performance of the turbine, especially on those operating at low heads, it is crucial to accurately determine the behaviour of the flow inside draft tubes. Based on Brugière's [14] and Wilhelm's [160] theses, it is clear that one of the greatest challenges to simulate these type of flows consist in imposing proper mean and fluctuating inlet boundary conditions for the simulations, particularly due to the complexity of the flow leaving the runner and entering the draft tube. Thus, the objective of this thesis are twofold:

- **To develop a method capable of determining the proper mean and fluctuating inlet boundary conditions for draft tube numerical simulations.** Indeed, starting from the results of an experimental campaign conducted by GE, we show the influence of the inlet conditions, particularly the turbulent field, on the evolution of the flow inside a draft tube. Given the difficulty to gather this information experimentally, an innovative method to generate proper mean and fluctuating inlet boundary conditions and based on data-driven techniques, such as Machine Learning, is proposed. The performance of these methods is investigated both in the simple case of a conical diffuser and in the complex bulb turbine draft tube.

- **To improve the numerical prediction of the flow inside the draft tube, particularly its head losses.** Given the importance of accurately predicting the head losses inside the draft tube, especially in the case of low head turbines, a detailed analysis of these losses is performed to ensure a good representation of the physics behind the mechanisms responsible for them. In this regard, the head losses equation developed in Wilhelm *et al.* [159] is used and applied to the numerical simulations of the draft tube.

1.6 Thesis outline

In this first chapter, the general concepts about hydraulic machines required for the good understanding of this thesis were presented. The basic aspects allowing hydroelectric power plants to generate electricity from a water flow were discussed, as well as the importance of the draft tube to improve its overall performance. The main characteristics of a bulb turbine, including its draft tube, were explained and the motivation for this work was determined. Finally, after contextualizing the present thesis as part of a continuous collaboration between GE Renewable Energy and the MoST team at LEGI, its objectives were defined.

In the second chapter, the numerical methods used to model the turbulent flows investigated in this thesis are presented. Starting with the governing equations of the flow, the physics behind the turbulence and, in particular, its energetic characteristics are discussed. Then, the main aspects of the two approaches utilized to model the turbulence effects on the investigated flows, notably the statistical approach and the LES, are explained. Finally, the numerical methods used to solve the system of discretized equations and the particular aspects related to this thesis are exposed.

In the third chapter, the state of the art of draft tube numerical simulations is discussed. For instance, the different methods used to model the turbulent flow inside this equipment and the influence of the imposed mean and fluctuating inlet boundary conditions in this type of simulation are examined. In addition, the methodology followed to validate the numerical results is explained, including the description of the experimental setup used to obtain the experimental measurements for two operating conditions.

The initial numerical simulations of the draft tube are discussed in Chapter 4. The numerical setup is explained, including the computational domain, mesh, and inlet boundary conditions used for the simulations of the two operating conditions. The results obtained with both RANS and LES are compared with the available experimental measurements and the influence of injecting synthetic fluctuations in LES is investigated. While these fluctuations improved some aspects of the numerical results, their *unrealistic* nature negatively impact the head losses evolution inside the draft tube.

Given the unsatisfactory results obtained in Chapter 4, particularly due to inadequate inlet boundary conditions for the numerical simulations, an innovative approach to determine these conditions is proposed in Chapter 5. The approach is based on data-driven techniques, such as Machine Learning, and a brief review of previous applications of these methods in the context of draft tube simulations is given at the beginning of the chapter. After that, the basic concepts about Machine Learning algorithms are quickly discussed and the strategy behind the proposed approach is explained.

Given the high computational cost associated of the proposed Machine Learning strategy, it is initially applied to a simpler flow configuration, as discussed in Chapter 6. The swirling flow inside the ERCOFTAC conical diffuser studied by Clausen *et al.* [19] is investigated. After defining the baseline numerical results using basic inlet boundary conditions (similarly to the draft tube case), the proposed Machine Learning strategy is thoroughly applied to yield proper mean and fluctuating inlet boundary conditions for RANS and LES computations. The numerical results obtained with both baseline and optimized simulations are compared to the experiments.

In Chapter 7, the problem of the turbulent flow inside a bulb turbine draft tube is revisited, but this time the proposed Machine Learning strategy is applied to generate the proper inlet boundary conditions for the computations. One of the operating conditions studied experimentally is analysed and the numerical results obtained with the proposed approach are compared to the experimental measurements and the reference simulations performed in Chapter 4. A detailed head losses analysis is also conducted and the importance of imposing proper inlet conditions highlighted.

Finally, in the last chapter of this thesis, the conclusions about this work are presented and the perspectives for future works, especially in the context of the proposed Machine Learning strategy, are described.

Chapter 2

Numerical methodology and turbulence modelling

Contents

2.1 Turbulent flows

2.1.1 Governing equations

In the domain of hydraulic machines, the considered flows are incompressible Newtonian flows where the continuum hypothesis is valid. In this kind of flows, the mass-conservation of continuity equation can be written, in index notation, as:

$$\frac{\partial u_i}{\partial x_i} = 0 \tag{2.1}$$

where u_i is the velocity component at the direction x_i. The implication of Eq. (2.1) is that the velocity field is solenoidal or divergence-free. The spatio-temporal evolution of the velocity $\vec{u}(\vec{x}, t)$ and pressure $p(\vec{x}, t)$ fields of the flow are determined by the Navier-Stokes equations, based on the conservation of momentum, given as:

$$\frac{\partial u_i}{\partial t} + \frac{\partial u_i u_j}{\partial x_j} = -\frac{1}{\rho}\frac{\partial p}{\partial x_i} + \nu\frac{\partial}{\partial x_j}\left(\frac{\partial u_i}{\partial x_j} + \frac{\partial u_j}{\partial x_i}\right) + g_i \tag{2.2}$$

where t is the time, ρ is the density, ν is the kinematic viscosity and g_i is the body force (e.g., gravity) component in the x_i direction. The momentum equation is based on Newton's second law and relates the fluid particle acceleration to the surface and body forces acting on the fluid. On left-hand side (l.h.s) of Eq. (2.2), in addition to the term defining the temporal evolution of the velocity u_i, there is also a term defining the advection of this velocity by the flow. On the right-hand side (r.h.s.), the forces acting on the fluid particle are listed, respectively: the pressure forces, the viscous forces responsible for diffusion of momentum and the gravity force. Due to the non-linear term in Eq. (2.2), there is no analytical solution for the Navier-Stokes equations, except for few very simple flow cases where they can be simplified. Most of the time, however, an approximate solution requires the modelling of certain terms and is normally obtained via the discretization (e.g., using finite volumes) and numerical resolution of these equations.

In Eq. (2.2), the diffusion term on the r.h.s. characterizes the viscous effects whereas the inertia effects are characterized by the advection term on the l.h.s. The time scales for these phenomena can be defined, respectively, as $T_v \sim L^2/\nu$, which is the characteristic time for an instability to be damped by the viscous effects over a distance L, and $T_i \sim L/U$, which is the time required for a fluid particle at a characteristic velocity U to travel a distance L due to its inertia. The ratio of the viscous timescale T_v to the inertial time scales T_i is equal to a dimensionless quantity called Reynolds number:

$$Re = \frac{T_v}{T_i} = \frac{UL}{\nu} \tag{2.3}$$

which characterizes the state of the flow. For instance, whenever the inertia effects are predominant over the viscous effects, i.e.,T_v is large compared to T_i, the Reynolds number $Re >> 1$. In this case, instabilities can develop inside the flow before being damped by the viscous effects and complex tridimensional motions will appear in addition to the main flow movement. The flow is then said to be in a turbulent regime. Conversely, if the viscous effects are predominant over inertia effects, i.e.,T_v is small compared to T_i and $Re << 1$, instabilities will not have enough time to develop within the flow and the flow is said to be in laminar regime. The system of equations formed by Eqs. (2.1) and (2.2) govern the behaviour of a flow. Due to the length and velocity scales involved in the domain of hydraulic machines, the considered flows are very turbulent and unsteady, with significantly high Reynolds numbers (in the order of 10^6). Before discussing the means used for modelling and studying these turbulent flows, some important aspects of their physics are present below.

2.1.2 Turbulence physics

Turbulence is a widely studied physical phenomena, present in many practical applications, either in nature or in the industry, but to which there is no rigorous definition. Rather, a turbulent flow is characterized by some important properties like its unsteadiness, randomness, and unpredictability. Indeed, even though Navier-Stokes equations are deterministic, they are very sensitive to the initial conditions and small perturbations in these conditions can lead to considerably different flow evolution. In addition to that, turbulent flows are also characterized by a wide range of motions scales, which are created by the instabilities that were not dissipated within the flow. Finally, as a consequence of these wide range of motions scales, turbulent flows also have an increased mixing capacity compared to laminar flows where the perturbations are damped by the effect of viscosity [85]. Figure 2.1 shows the evolution in time of the velocity measured at a point inside a turbulent flow. In this figure, the instantaneous velocity signal $u(x,t)$ is constantly fluctuating around a mean value $\langle u \rangle$. Statistically, a turbulent flow can

be described as the superposition of a mean field (deterministic) and a fluctuating field, which is very sensitive to external perturbations [126]. The velocity and pressure fields can thus be written as the combination of a mean and a fluctuating field, using what is called the Reynolds decomposition:

$$u_i(\vec{x},t) = \langle u_i \rangle(\vec{x},t) + u_i'(\vec{x},t) \tag{2.4}$$

$$p(\vec{x},t) = \langle p \rangle(\vec{x},t) + p(\vec{x},t) \tag{2.5}$$

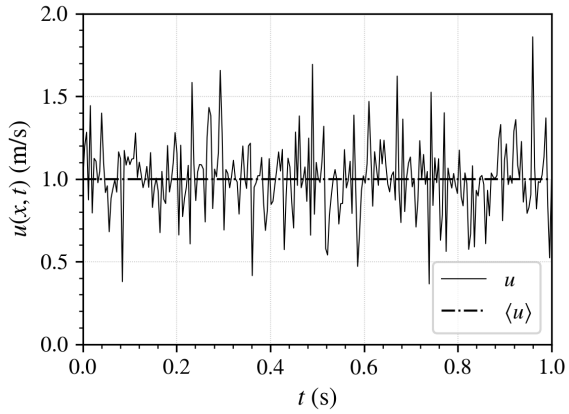

Figure 2.1: Evolution in time of the velocity signal measured a point inside a turbulent flow.

where the $\langle . \rangle$ operator corresponds to the statistical mean of the variable and, by definition, $u_i'(\vec{x},t) = 0$. Defining the *mean* kinetic energy per unit mass of the flow field as $K = (1/2)\langle u \rangle \langle u \rangle$, applying the average operator $\langle . \rangle$ to the momentum equation (2.2) and multiplying the result by $(1/2)\langle u_i \rangle$, yields the following equation for K:

$$\underbrace{\frac{\partial K}{\partial t}}_{I} + \underbrace{\langle u_i \rangle \frac{\partial K}{\partial x_i}}_{II} = \underbrace{\langle u_i' u_j' \rangle \langle S_{ij} \rangle}_{III} - \underbrace{\frac{\partial}{\partial x_j}\left(\langle u_i \rangle \langle u_i' u_j' \rangle + \frac{1}{\rho}\langle p \rangle \langle u_i \rangle - 2\nu \langle u_i \rangle \langle S_{ij} \rangle \right)}_{IV} - \underbrace{2\nu \langle S_{ij} \rangle \langle S_{ij} \rangle}_{V} \tag{2.6}$$

where $S_{ij} = (1/2)(\partial \langle u_i \rangle / \partial x_j + \partial \langle u_j \rangle \partial x_i)$ is the strain rate tensor of the mean field. Multiple terms appear in this equation. Terms I and II correspond, respectively, to the variation in time and advection of mean kinetic energy. Term III corresponds to the energy transfer between the mean and fluctuating flows. Often negative, this term represents a sink for K and is most usually represented by its opposite, $P = -\langle u_i' u_j' \rangle \langle S_{ij} \rangle$, called *turbulent kinetic energy production*. Term IV represents the diffusion of the mean kinetic energy and V is responsible for the viscous dissipation of K, which is converted into heat. Similarly, the turbulent kinetic energy per unit mass can be defined as:

$$k = \frac{1}{2}\langle u_i' u_i' \rangle \tag{2.7}$$

and a similar equation to (2.6) can be written for k:

$$\underbrace{\frac{\partial k}{\partial t}}_{I} + \underbrace{\langle u_i \rangle \frac{\partial k}{\partial x_i}}_{II} = - \underbrace{\langle u_i' u_j' \rangle \langle S_{ij} \rangle}_{III} - \underbrace{\frac{\partial}{\partial x_j}\left(\langle u_j' \frac{u_i' u_i'}{2} \rangle + \frac{1}{\rho}\langle p' u_i' \rangle - 2\nu \langle u_i' s_{ij}' \rangle \right)}_{IV} - \underbrace{2\nu \langle s_{ij}' s_{ij}' \rangle}_{V} \tag{2.8}$$

where $s'_{ij} = (1/2)(\partial u'_i/\partial x_j + \partial u'_j/\partial x_i)$ is the strain rate tensor of the fluctuating field. Similar terms explaining the variation of k are found in Eq. (2.8). For instance, terms I corresponds to the variation in time of the turbulent kinetic energy and term II to its advection by the mean flow. The turbulent kinetic energy production, P, is recovered as term III. Term IV corresponds to the turbulent kinetic energy diffusion. Finally, term V, which is equal to $-\epsilon$ or $\epsilon = 2\nu\langle s'_{ij} s'_{ij}\rangle$, represents the viscous dissipation of k that is converted into heat.

Equations (2.6) and (2.8) show that there is an energy transfer between the mean flow and the turbulent flow. Moreover, they also show that the mean and turbulent kinetic energies dissipate with time. These energy transfers are linked to the *energy cascade* first introduced by Richardson in 1922 and later completed by Kolmogorov in 1941 [126] for the case of a fully developed turbulent flow at a high Reynolds number. Turbulent production is responsible for the generation of turbulent kinetic energy from the mean flow. This kinetic energy is mostly contained in large flow scales and is characterized by an integral scale, l_I, which is close to the characteristic scale of the mean flow, L_s. As these scales do not feel the effect of fluid viscosity, their energy is transferred to the smaller scales of the flow passing through a range of inertial scales. The smallest turbulent scales are characterized by Kolmogorov's length scale, l_K. As they are affected by the fluid viscosity, they are the ones responsible for the viscous dissipation ϵ of turbulent kinetic energy, given by term V in Eq. (2.8). This energy cascade is usually represented by the Kolmogorov spectrum, illustrated in Fig. 2.2. In this figure, the turbulence is treated in a spectral form, where $E(\kappa)$ is the turbulent kinetic energy spectrum and κ is the wave number associated with a characteristic length l, such that $\kappa = 2\pi/l$. The energy is transferred from the large scales following a $\kappa^{-5/3}$ law up to the Kolmogorov scales, where it is dissipated by the fluid viscosity.

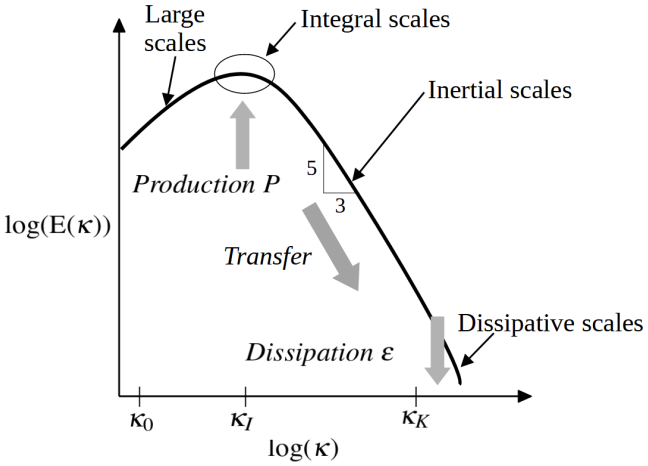

Figure 2.2: Energy cascade at high Reynolds number. Source: adapted from Wilhelm [160]

2.2 Turbulence modelling

2.2.1 The need for modelling the turbulence

As pointed out in Section 2.1.1, the system of equations governing the turbulent flow behaviour is non-linear and there is no analytical solution for it. However, it is possible to obtain an approximate solution by discretizing the Navier-Stokes equations over a mesh and then numerically solving the system of discretized equations, in which is commonly named Computational Fluid Dynamics (CFD). The complete resolution of these equations, i.e., without any modelling, is called Direct Numerical Simulation (DNS). In this approach, higher-order numerical schemes must be used to reduce the numerical errors when solving the system of discretized equations.

Moreover, the time step and mesh size must be sufficiently small to capture the smallest of the motion scales, that is, Kolmogorov's scale l_K. It can be shown that the ratio between the largest turbulent scales (e.g., the integral scale) and Kolmogorov's scale is proportional to $Re^{3/4}$ [135]. Thus, the number of points in the mesh required to solve a tridimensional flow is in the order of $Re^{9/4}$. Considering that, typically, the Reynolds number in the case of a turbulent flow inside a bulb turbine draft tube is in the order of 10^6, this implies that the mesh required to perform a DNS of such a flow would have approximately 10^{13} elements. The time step can also be estimated as being proportional to $Re^{1/2}$, resulting in a final computational cost for a DNS in the order of Re^3. That is the reason this type of numerical simulation is only applicable to simple flows configurations at low and moderate Reynolds number. In the case of more complex flows at higher Reynolds numbers, it is necessary to model *at least* a portion of the turbulent flow. In this thesis, two approaches are used: the *statistical turbulence modelling*, where all turbulent scales are modelled, and the *large-eddy simulations*, where only a small portion of the turbulent scales are modelled and all the rest is explicitly resolved.

2.2.2 Statistical turbulence modelling

The statistical turbulence modelling is based on the Reynolds Averaged Navier-Stokes (RANS) equations explained in Section 2.1.2 and is the most frequently used approach to study turbulent flows in engineering, particularly due its low computational cost. In this approach, the mean flow field is explicitly solved while the effects of the turbulent flow on the mean field are modelled by some statistical model.

Reynolds equations and Reynolds stress tensor modelling

The application of the Reynolds decomposition shown in Eqs. (2.4) and (2.5) to the Navier-Stokes equations (2.1) and (2.2) results in the following Reynolds equations:

$$\frac{\partial \langle u_i \rangle}{\partial x_i} = 0 \tag{2.9}$$

$$\frac{\partial \langle u_i \rangle}{\partial t} + \frac{\partial \langle u_i \rangle \langle u_j \rangle}{\partial x_j} = -\frac{1}{\rho}\frac{\partial \langle p \rangle}{\partial x_i} + \nu \frac{\partial}{\partial x_j}\left[\left(\frac{\partial \langle u_i \rangle}{\partial x_j} + \frac{\partial \langle u_j \rangle}{\partial x_i}\right) - \langle u_i' u_j' \rangle\right] + g_i \tag{2.10}$$

Therefore, the goal with the RANS approach is to solve this system of equations to obtain the mean velocity $\langle \vec{u} \rangle(\vec{x}, t)$ and pressure $\langle p \rangle(\vec{x}, t)$ fields. In the case of a statistically steady flow, the statistical mean can be replaced by the time averaging and the resolved fields are independent of time, i.e.,$\langle \vec{u} \rangle(\vec{x})$ and $\langle p \rangle(\vec{x})$, reducing thus even further the computational cost of the simulation. Nevertheless, it is possible to resolve the unsteady terms of the Reynolds equations based on what is called the unsteady Reynolds Averaged Navier-Stokes (URANS). This approach is particularly suited for turbulent flows where the macroscopic variations of the flow are at a much lower frequency compared to the turbulent fluctuations [103].

Due to the non-linear advection term in the original Navier-Stokes equations, the term $R_{ij} = -\langle u_i' u_j' \rangle$ appears in Eq. (2.10). This term, called Reynolds stress tensor, adds six unknowns to the system of equations, which is no longer closed as a consequence. Physically, the Reynolds stress tensor can be interpreted as an additional stress tensor that explains the influence of the turbulent flow field onto the mean flow field. Looking at the kinetic energy equations (2.6) and (2.8), the Reynolds stress tensor acts particularly on the mean turbulent kinetic energy production $P = -\langle u_i' u_j' \rangle \langle S_{ij} \rangle$. Indeed, the energy balance discussed in Section 2.1.2 shows that the kinetic energy is transferred from the mean field to turbulent field. Therefore, the main role of the turbulent fluctuations is to dissipate part of the kinetic energy of the mean flow field through mean turbulent kinetic energy production, whereas the viscous stresses dissipate the

mean kinetic energy through molecular viscosity. Based on that, Boussinesq [13] introduced the concept of an eddy-viscosity, ν_t, on which most of the turbulence models are based. By this hypothesis, the Reynolds stress tensor vary linearly with the mean strain rate tensor and can be expressed as:

$$-\langle u_i' u_j' \rangle = 2\nu_t \langle S_{ij} \rangle - \frac{2}{3} k \delta_{ij} \tag{2.11}$$

where δ_{ij} is the Kronecker delta and k is the turbulence kinetic energy defined in Section 2.1.2. According to Boussinesq's hypothesis, the six unknowns introduced by the Reynolds stress tensor can be replaced by a single scalar variable, ν_t. As a result, the Reynolds equation (2.10) can be rewritten as:

$$\frac{\partial \langle u_i \rangle}{\partial t} + \frac{\partial \langle u_i \rangle \langle u_j \rangle}{\partial x_j} = -\frac{1}{\rho}\frac{\partial \langle p^* \rangle}{\partial x_i} + \frac{\partial}{\partial x_j}\left[(\nu + \nu_t)\left(\frac{\partial \langle u_i \rangle}{\partial x_j} + \frac{\partial \langle u_j \rangle}{\partial x_i}\right)\right] + g_i \tag{2.12}$$

where $\langle p^* \rangle = \langle p \rangle + (2/3)k$ is a modified pressure.

Conversely to the molecular viscosity, ν, the eddy-viscosity, ν_t is a *flow* property and not a *fluid* property, meaning that it can vary with space and time, i.e.,$\nu_t(\vec{x}, t)$. A simple dimensional analysis shows that ν_t is proportional to the product between a characteristic length l_m and velocity u_t:

$$\nu_t(\vec{x}, t) \propto l_m u_t \tag{2.13}$$

Thus, to determine the unknown eddy-viscosity ν_t, it is necessary first to evaluate these two scales for the considered flow. In general, the models based on the concept of an eddy-viscosity will distinguish themselves by the number of additional equations required to evaluate l_m and u_t, which usually varies between zero and three. More details about these eddy-viscosity models can be found in the book of Pope [126], but in this thesis, we focus only on the most common two-equation eddy-viscosity models. In these models, the characteristic velocity u_t is usually determined from the turbulence kinetic energy k, after assuming that $u_t \propto \sqrt{k}$. Moreover, Boussinesq's hypothesis, shown in Eq. (2.11), is used to solve the turbulence kinetic energy equation (2.8). Different models propose distinct ways of determining the mixing length, l_m, with the two most commonly used being the k-ϵ and k-ω.

The k-ϵ model

In the k-ϵ model [71, 81], the mixing length is assumed to be proportional to the turbulence length scale introduced in Section 2.1.2, which in turn can be expressed as a function of the characteristic velocity u_t and a turbulence dissipation ϵ;

$$l_m \propto l_t = \frac{u_t^3}{\epsilon} \propto \frac{k^{3/2}}{\epsilon} \tag{2.14}$$

Therefore, from the dimensional analysis Eq. (2.13) and the assumption that $u_t \propto \sqrt{k}$, the eddy-viscosity can be evaluated as:

$$\nu_t(\vec{x}, t) = C_\mu \frac{k^2}{\epsilon} \tag{2.15}$$

where C_μ is a constant that should be determined. Thus, the k-ϵ turbulence model is based on one equation for the turbulence kinetic energy k and another for the turbulence dissipation ϵ. Thanks to its relatively good performances, simple implementation and numerical robustness,

this model has been used in a wide range of applications, including to study the flow inside draft tubes (as will be discussed in the next chapter). However, one of the main weaknesses of the k-ϵ turbulence model is its lack of sensitivity to adverse pressure gradients and consequent poor performance in predicting the flow near the walls. For instance, the model can overestimate the shear stress in this region of flow and the boundary layer separation can be delayed or not even take place [123]. Moreover, solving the transport equations for this turbulence model in the viscous sub-layer can be difficult and requires the inclusion of additional terms in the ϵ equation that can ultimately alter the model's robustness [102].

The k-ω model

Wilcox [158] took another approach to determine the eddy-viscosity and proposed to solve a transport equation for a turbulence characteristic frequency, ω, such that $\omega \propto \epsilon/k$. Therefore, the eddy-viscosity is given by:

$$\nu_t(\vec{x}, t) = \frac{k}{\omega} \tag{2.16}$$

The advantage of Wilcox's k-ω turbulence model is that, compared to k-ϵ, its near-wall formulation is simpler and it yields better results in this region of the flow, especially in the presence of adverse pressure gradients. However, it is also very sensitive to values of ω imposed at the boundaries of the numerical domain and a slight variation can significantly alter the final results of the simulation [102].

The k-ω SST model

Menter [102, 101] proposed to combine the good numerical performance of Wilcox's k-ω turbulence model in the near-wall region with the independence of Jones and Launder's k-ϵ turbulence model to the imposed boundary conditions away from the walls to create the k-ω SST turbulence model. In this model, the transport equation for the dissipation ϵ is rewritten in terms of ω such that $\epsilon \propto \omega k$. A blending function F_1, which smoothly transitions from $F_1 = 1$ near the walls to $F_1 = 0$ away from them, is used to combine the two turbulence models. For instance, Wilcox's k-ω equations are multiplied by F_1, whereas Jones and Launder's k-ϵ equations are multiplied by $(1 - F_1)$, and they are both added together afterwards.

Two-equation linear eddy-viscosity models are based on the assumption of a balance between turbulence kinetic energy production P and dissipation ϵ. However, in the cases where the boundary layer is subjected to an adverse pressure gradient, the production can be larger than dissipation leading to the overestimation of the Reynolds stress tensor and the eddy-viscosity. In this context, Menter also proposed to improve the model's performance over separation points by considering the transport of *Shear Stress Transport* (SST). Bradshaw hypothesis considers that, in a bidimensional boundary layer subjected to an adverse pressure gradient, the Reynolds stresses are proportional to the turbulence kinetic energy k. Therefore, the eddy-viscosity can be redefined as:

$$\nu_t = \frac{a_1 k}{S} \tag{2.17}$$

where a_1 is a constant and $S = \sqrt{2\langle S_{ij}\rangle\langle S_{ij}\rangle}$. Based on that, Menter proposes to limit the eddy-viscosity as follows:

$$\nu_t = \frac{a_1 k}{\max(a_1\omega, F_2 S)} \tag{2.18}$$

where F_2 is a second blending function used to constraint the eddy-viscosity limitation describe by Eq. (2.18) to the boundary layers. For instance, $F_2 = 1$ on these regions of the flow and 0 outside, which results in the original Wilcox's formulation for ν_t, Eq. (2.16). On the boundary layers, where $F_2 = 1$, if the turbulence kinetic energy production P becomes way larger than the dissipation ϵ, then $S > a_1\omega$ and Bradshaw's formulation for ν_t, Eq. (2.17) is recovered.

Final considerations on linear eddy-viscosity models

Eddy-viscosity models can be particularly unsuited for the prediction of highly anisotropic flows, such as rotating flows, since they are based on the hypothesis of an isotropic Reynolds stress tensor. For instance, the turbulent production P does not take into account the influence of streamlines rotation and curvature [142, 139]. Moreover, these models also generate excessive turbulence energy in the vicinity of stagnations points [74]. Nevertheless, corrections for these problems have been developed, particularly for the k-ω SST turbulence model, to render it more sensitive to streamline curvature and limit turbulent production at stagnation points [3].

In addition to the aforementioned limitations, linear eddy-viscosity models have a multitude of parameters that need to be calibrated prior to their implementation. Nevertheless, these models have been successfully applied to a variety of flows and, due to their relatively low computational cost and good numerical robustness, these methods are still widely used in industry. In the case of this thesis, we use the k-ω SST turbulence model to perform steady RANS simulations of the investigated flows, especially due to its better performance to predict the flows under strong adverse pressure gradients [123].

2.2.3 Large-Eddy Simulations

In addition to only having access to the information about the mean flow field, all the turbulent scales in RANS simulations are modelled. This limits the analysis of the flow, especially in the cases where it is important to have access to its fluctuating field information. Since the computational cost to perform a DNS of the industrial flows considered in this thesis are still prohibitive, one alternative to overcome the limitations observed in RANS consists in dividing the flow according to its turbulent scales, using an approach called Large-Eddy Simulation (LES). This approach is based on the fact that the large scales carry most of the energy in the flow but are also more sensitive to the boundary conditions and the geometry of the numerical domain, whereas small scales carry only a small portion of the energy of the flow and their behaviour can be considered as universal [126]. Thus, instead of modelling all turbulent scales or explicitly solving all of them, in LES, the large scales are resolved while the small dissipative scales are modelled.

Filtered conservation equations

For LES, the resolved and modelled scales separation is achieved by applying a high-pass filter to the Navier-Stokes equations (2.2). If G_Δ is a low-pass filter of width Δ, the filtered velocity field in the considered domain $\mathcal{D}$ is defined as:

$$u_i(\vec{x},t) = \iiint_{\mathcal{D}} u_i(\vec{y},t) G_\Delta(\vec{x}-\vec{y}) d\vec{y} = u_i(\vec{x},t) * G_\Delta \tag{2.19}$$

where $*$ represents the convolution product. The component of the unsteady velocity field at the x_i direction, $u_i(\vec{x},t)$, is decomposed in to two parts: one for the velocity associated with the large motion scales of the flow (i.e., larger than Δ), $\overline{u}_i(\vec{x},t)$, and another associated with the motion scales smaller than the filter width, $u_i''(\vec{x},t)$,

$$u_i(\vec{x},t) = \overline{u}_i(\vec{x},t) + u_i''(\vec{x},t) \tag{2.20}$$

The filter width, Δ, also called the *cut-off* scale, determines the minimal size of the motion scales explicitly resolved. Details about different filtering approaches can be found in Sagaut [135] and Pope [126], but the most commonly used is implicit filtering, where the filter width Δ is determined by the local size of the grid used to discretize the numerical domain [57], as illustrated in Fig. 2.3. Since the modelled scales in this approach are those smaller than the grid, they are also called subgrid scales (SGS). Although the implicit filtering is essentially a spatial operation, it also implies in an implicit temporal filtering since a characteristic timescale is associated with a characteristic length scale [135]. Moreover, as the filter is a linear operator that commutes with derivation, the Navier-Stokes equations (2.1) and (2.2) can be filtered to obtain:

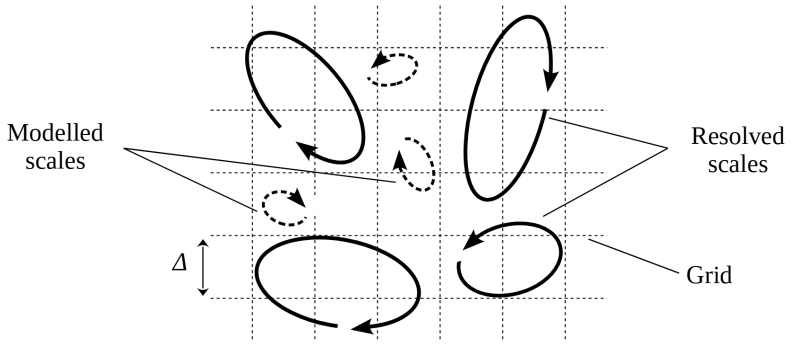

Figure 2.3: Spatial representation of the large (resolved) and small (modelled) motion scales in LES.

$$\frac{\partial \overline{u}_i}{\partial x_i} = 0 \tag{2.21}$$

$$\frac{\partial \overline{u}_i}{\partial t} + \frac{\partial (\overline{u}_i \overline{u}_j)}{\partial x_j} = -\frac{1}{\rho}\frac{\partial \overline{p}}{\partial x_i} + \nu \frac{\partial^2 \overline{u}_i}{\partial x_j \partial x_j} - \frac{\partial \tau_{ij}}{\partial x_j} + g_i \tag{2.22}$$

Similarly to RANS, the filtering operator applied to the non-linear advection term in the l.h.s. of Eq. (2.2) leads to the apparition of a new term, $\tau_{ij} = \overline{u_i u_j} - \overline{u}_i \overline{u}_j$, which is called the subgrid stress tensor and represents the influence of the small unresolved subgrid scales on the large resolved scales in the flow. In the case of LES, it is this term which needs to be modelled.

Subgrid scales modelling

Similar to the turbulence viscosity approach in RANS, this energy transfer between large and small turbulent scales of the flow can be modelled using Boussinesq's hypothesis and a subgrid scale viscosity, ν_{sgs}, i.e.,

$$\tau_{ij} = -2\nu_{sgs}(\vec{x},t)\overline{S}_{ij} + \frac{1}{3}\tau_{kk}\delta_{ij} \tag{2.23}$$

and the filtered momentum equation (2.22) can be rewritten as:

$$\frac{\partial \overline{u}_i}{\partial t} + \frac{\partial (\overline{u}_i \overline{u}_j)}{\partial x_j} = -\frac{1}{\rho}\frac{\partial \overline{p^*}}{\partial x_i} + \frac{\partial}{\partial x_j}\left[(\nu + \nu_{sgs})\left(\frac{\partial \overline{u}_i}{\partial x_j} + \frac{\partial \overline{u}_j}{\partial x_i}\right)\right] + g_i \tag{2.24}$$

where $\overline{p^*} = \overline{p} + \frac{1}{3}\tau_{ij}$ is the modified pressure. The subgrid scale viscosity is evaluated based

on the mixing length hypothesis, where its valued is proportional to the product between a characteristic length and velocity. This length is taken as equal to the filter width, Δ, such that:

$$\nu_{sgs} \propto \Delta u^{\star} \tag{2.25}$$

Therefore, the SGS viscosity models distinguish themselves by the way the characteristics velocity $u^{\star}$ is calculated. In this thesis, two models are used. For instance, in the simple case of the swirling flow inside a conical diffuser discussed in Chapter 6, the widely used Dynamic Smagorinsky model [58, 88] is employed. This model is based on the original Smagorinsky's [137] approach and ν_{sgs} is given by:

$$\nu_{sgs} = C_s \Delta^2 |\overline{S}| \tag{2.26}$$

where $|\overline{S}| = \sqrt{2\overline{S}_{ij}\overline{S}_{ij}}$ and C_s is a constant that should be determined. In the case of the Dynamic Smagorinsky model, this constant is dynamically evaluated to adjust the model's dissipation to the different regions of the flow, particularly near the walls.

In the case of LES computations of the more complex flow inside a bulb turbine draft tube, the more advanced σ-model [114] is used. This model is an evolution of the WALE (Wall-Adapting Local Eddy-viscosity) model introduced by Nicoud and Ducros [115] and is more adapted to complex flows and geometries. For instance, the model yields a better behaviour near solid boundaries and is more capable of handling solid rotation and pure shear. In the σ-model, the subgrid scale viscosity is equal to:

$$\nu_{sgs} = (C_\sigma \Delta)^2 \mathcal{D}_\sigma \tag{2.27}$$

where C_σ is a constant and $\mathcal{D}_\sigma$ is given by:

$$\mathcal{D}_\sigma = \frac{\sigma_3(\sigma_1 - \sigma_2)(\sigma_2 - \sigma_3)}{\sigma_1^2} \tag{2.28}$$

and σ_1, σ_2 and σ_3 are the three singular values of the local velocity gradient tensor.

2.3 Numerical resolution of the governing equations

The mass and momentum equations presented up to this point of the chapter are analytical and the system of partial differential equations (PDE) that they form need to be discretized to obtain a system of algebraic equations that can be numerically solved. In this section, the discretization methods and numerical schemes used to perform the simulations in this thesis are briefly discussed.

2.3.1 Spatial discretization

The tridimensional space defining the numerical domain where the previous conservation equations will be solved is discretized in a finite number small volumes, called elements, to form a mesh. The vertices of these volumes are called the nodes and depending on the way these nodes are connected, the mesh can be divided into two categories: structured or non-structured.

The nodes in a structured mesh are regularly connected and its topology and indexation are relatively simple. In 3D, these meshes form hexahedral elements, which renders their utilization in complex geometries particularly difficult and local refinement complicated. Nevertheless, these meshes can limit the number of elements for a given geometry, especially in the case where the flow has a preferred direction (e.g., near the walls). In these cases, the elements can be

deformed to precisely capture the important gradients on the flow. While this may result in highly anisotropic (deformed) low quality elements, this type of mesh are used in all RANS simulations in this thesis, notably due to the good performance of the numerical algorithms used for these simulations in this type of mesh.

In the case of the LES computations conducted in this thesis, higher-order numerical schemes are used, and better quality meshes are required. Non-structured meshes are more flexible, can be locally refined and usually produce higher quality elements in complex geometries compared to structured meshes. In 3D, the elements in this type of mesh are tetrahedrons. The weakness of non-structured meshes, though, is their higher computational cost, since the total number of elements is normally more important than in the case of structured mesh.

2.3.2 Finite Volume Method

The system of partial differential equations governing the flow is discretized using the finite volume method (FVM). One of the main advantages of this method is the fact the conservation principles (mass and momentum) of the governing equations is maintained after their discretization. The method is briefly explained in this section, but further details can be found in Ferziger and Perić [45] and Moukalled *et al.* [105].

The first step in the FVM is to integrate the governing equations over the small volumes (elements) created by the spatial discretization of the numerical domain. Volume integrals of the convection and diffusion terms are transformed into surface integrals thanks to the application of Green-Ostrogradski's theorem. The different fluxes through each surface of the control volume are then evaluated using spatial discretization schemes and a matrix system containing the balance of the fluxes at each control volume is obtained. Notice that, in addition to the spatial discretization, a temporal discretization scheme is also used in LES due to the unsteady nature of the solution.

The control volumes created by the mesh can be either cell-centred or vertex-centred, depending on their variable arrangement. Both flow solvers used in this thesis and discussed in Section 2.3.3 uses vertex-centred control volumes, which is schematically shown in Fig. 2.4 for a 2D mesh composed by triangular elements. In this case, these volumes are defined by the segments connecting the centre of the mesh edges and the centre of the elements. Since the centre of the control volume does not necessarily coincide with the node where the values are actually stored, this can lead to some numerical errors, especially in the case of highly skewed elements.

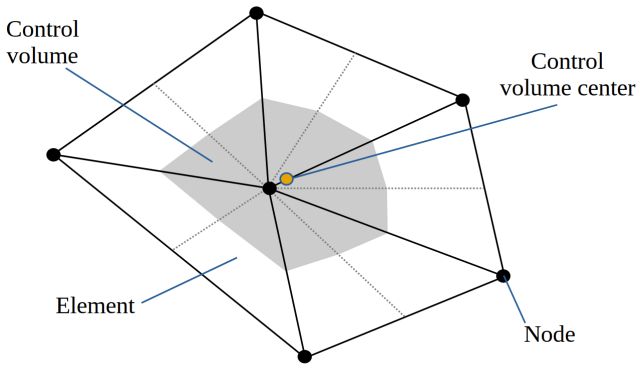

Figure 2.4: Scheme of a vertex-centred arrangement of a control volume in the mesh.

2.3.3 Numerical schemes and flow solvers

RANS

All the steady RANS simulations in this thesis were performed in the commercial code ANSYS CFX 19.0, a general-purpose CFD software particularly suited for the numerical resolution of the flow inside turbomachinery. It uses a *coupled solver* strategy, meaning that the system of discrete equations for the three velocity components and pressure are solved simultaneously. This strategy has the advantage of being more efficient, simple and robust, but it also requires more storage capacity to store all the coefficients for the system of equations. Further details about the different numerical schemes and the resolution of the system of equations in ANSYS CFX can be found in its documentation [3], but, in general, it will solve a linearized system of discrete equations of the form:

$$[A][\phi] = [B] \tag{2.29}$$

where $[A]$ is the coefficient matrix, $[\phi]$ is the solution vector composed by the pressure and different velocity components, and $[B]$ is the vector associated with the r.h.s. This equation is solved iteratively by starting from an approximate solution $[\phi]^n$, which is improved by a correction vector $[\phi]'$ to yield a better solution $[\phi]^{n+1}$ for the next iteration, such that $[\phi]^{n+1} = [\phi]^n + [\phi]'$. The correction vector $[\phi]'$ is evaluated from $[A][\phi]' = [R]^n$, where $[R]^n = [B] - [A][\phi]^n$ is the residual. This iterative process is repeated until the value of the residual $[R]^n$ associated to $[\phi]^{n+1}$ is inferior to a predetermined value.

Multiple spatial discretization schemes for the advection term are available in CFX. For the case of the steady RANS simulations conducted in this thesis, the *high resolution scheme* is used [3]. In general, the integrated value of a scalar ϕ at an integration point, *ip*, is evaluated as follows:

$$\phi_{ip} = \phi_{up} + \beta \nabla\phi \cdot \Delta\vec{r} \tag{2.30}$$

where ϕ_{up} is the value at the upwind node, $\nabla\phi$ is the gradient of ϕ on the element, and $\vec{r}$ is the vector from this upwind node to *ip*. If $\beta = 0$, the scheme is decentred and of order 1 (upwind), and if $\beta = 1$, the scheme is centred and of order 2. In the *high resolution scheme*, β (also called *blend factor*) is evaluated in each node of the mesh and it can vary between 0 and 1. The goal with this scheme is to use a value for β as close as possible to 1, while keeping the solution bounded. For the two extra transport equations for k and ω required for the k-ω SST turbulence model, a first order spatial discretization scheme is used.

LES

All the LES computations in this work were conducted using YALES2 [106], a multi-physics and multiphase fluid flow solver able to dynamically adapt meshes with billions of elements and particularly designed for High-Performance Computing (HPC) architectures and massively parallel computations. While the code was mainly developed at CORIA in the beginning, nowadays, many laboratories, including LEGI, use it and contribute to its constant improvement.

Conversely to ANSYS CFX, pressure and velocity are not simultaneously solved in YALES2. Indeed, a projection method allowing to decompose the velocity field into an irrotational and a solenoidal (divergence-free) part is used to solve the discrete Navier-Stokes equations. First, in the *prediction step*, a fictitious velocity u^* is determined from the velocity and pressure fields at the previous iteration, respectively u^n and p^n. Then, the pressure p^{n+1} can be determined from this fictitious velocity and Poisson's equation, obtained after taking the divergence of the momentum equations (2.2) in the case of an incompressible fluid:

$$\nabla^2 \left(\frac{p^{n+1}}{\rho} \right) = \frac{\nabla \cdot u^*}{\Delta t} \tag{2.31}$$

Finally, in the *correction step*, the velocity u^{n+1} is evaluated from the pressure p^{n+1} and the fictitious velocity u^* to verify the incompressibility. Poisson's equation 2.31 is solved using the Deflated Preconditioned Conjugate Gradient (DPCG) method, which details about its implementation in YALES2 can be found in Malandain *et al.* [94].

A centred 4^{th} order spatial discretization scheme is used, as well as a 4^{th} order temporal scheme adapted from the Runge-Kutta RK4 scheme called TFV4A [151]. To ensure the stability of the numerical solution, the time Δt has to be determined such that it is smaller than the time required for a fluid particle at speed u to travel more than the distance of one mesh element of size Δx. This condition is represented by the Courant–Friedrichs–Lewy (CFL) condition,

$$\text{CFL} = \frac{u \Delta t}{\Delta x} < 1 \tag{2.32}$$

In all LES computations performed in this thesis, CFL is always lower than 0.9.

2.3.4 Wall treatment

Predicting the near wall flow behaviour is crucial in wall bounded flows since it can have a major impact on the overall dynamics of the flow. Due to the no-slip condition, the velocity gradients normal to the walls in this region of the flow are notoriously important, especially in the case of highly turbulent flows, i.e., at high Reynolds numbers, as is illustrated in Fig. 2.5. To properly capture these important velocity gradients with the numerical simulations, the height of the first element at walls must be sufficiently small. The problem is that this would increase the computational cost associated with the simulation, since more elements would be necessary o cover the whole surface of the wall.

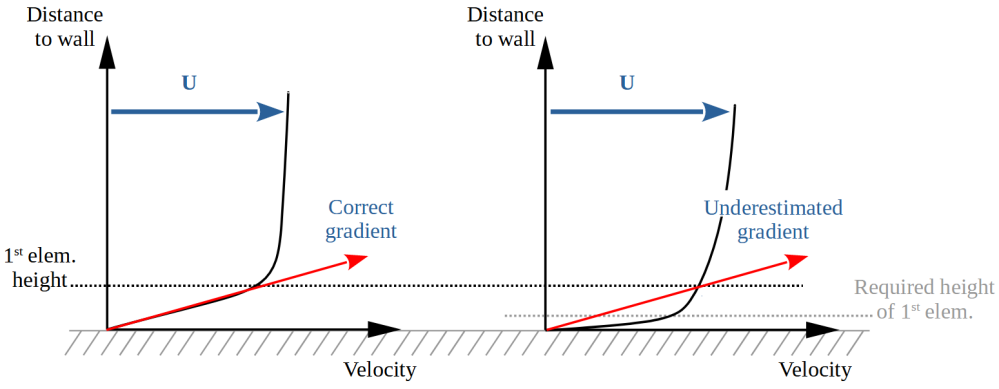

Figure 2.5: Near-wall velocity profiles at (left) low Reynolds number and (right) high Reynolds number. Illustration of the height of the first element at the wall to correctly capture the velocity gradient at this region. Source: adapted from Wilhelm [160].

In the case of RANS, the dissipation due to the turbulence model is such that it is not necessary to use higher order numerical schemes. As a result, highly deformed elements can be used at the walls, reducing thus the height of the first element at the walls while covering its whole surface area with a reasonably sized mesh. Conversely, in the case of LES, the dissipation induced by the turbulence model is low and higher order numerical schemes (as the 4^{th} used in YALES2) are required to limit the numerical dissipation and to obtain a better solution. As a

consequence, elements should have a good quality (e.g., low skewness, low growth rate) to keep the numerical stable, and the computational cost of the simulation can be prohibitively high due to the total number of elements in the mesh. To avoid having to explicitly resolve these velocity gradients, one solution consists in model the near-wall flow behaviour with the aid of some algebraic function or wall-law.

The near-wall flow behaviour can be described by some dimensionless quantities, notably a distance, y^+, and a velocity, u^+. For the case of a boundary layer in equilibrium, i.e., not subjected to adverse pressure gradients, these quantities are given by:

$$y^+ = \frac{u_\tau y}{\nu} \tag{2.33}$$

$$u^+ = \frac{U}{u_\tau} \tag{2.34}$$

where $u_\tau = \sqrt{(\tau_w)/\rho}$ is the friction velocity, τ_w is the wall-shear stress, y is the normal distance to the wall and U is the mean velocity parallel to the wall. As illustrated in Fig. 2.6, it is possible to establish a relation between y^+ and u^+ in the case of a turbulent boundary layer not-subjected to adverse pressure gradients. Indeed, the boundary layer can be divided into three main regions: (i) at $y^+ < 5$, called the viscous sublayer, the viscous effects are more important and the velocity profile varies linearly with the distance to the walls, i.e.,$u^+ = y^+$; (ii) at $y^+ > 30$, called log-law region, the inertial effects are more important and the velocity profile follows a logarithmic law, $u^+ = C_1 \ln(y^+) + C_2$ (where C_1 and C_2 are constants experimentally determined); (iii) at $5 \leq y^+ \leq 30$, called buffer-layer, the flow behaviour transitions between the two other regions. A wall-resolved numerical simulation requires the first node on the wall to be positioned at $y^+ \leq 1$, otherwise the velocity gradients can be underestimated. Nevertheless, based on this universal behaviour of the velocity profile near the walls shown in Fig. 2.6, it is possible to evaluate τ_w even if $y^+ \geq 1$.

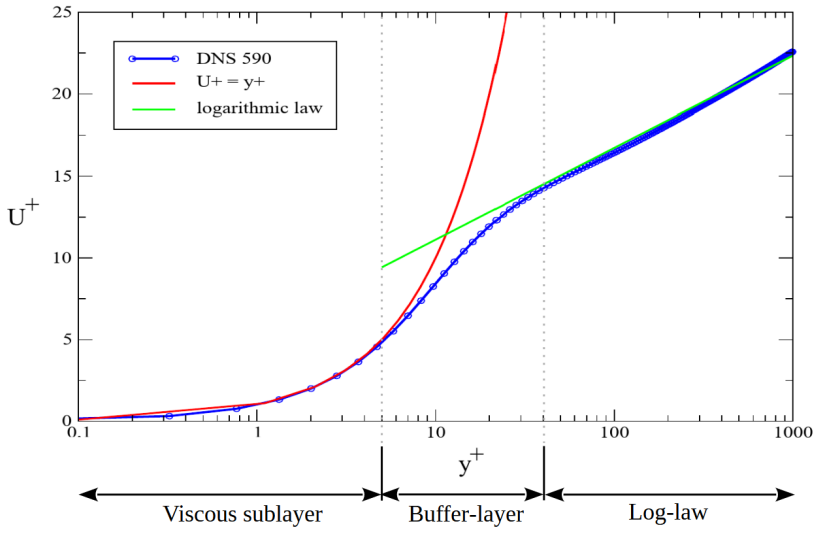

Figure 2.6: Mean velocity profile near the wall for a boundary layer in equilibrium. Source: adapted from Duprat [36].

RANS

The steady RANS simulations using the k-ω SST turbulence model presented in this thesis were all performed using the *automatic wall-treatment* available in ANSYS CFX [3]. This method

allows for the solver to automatically switch between the Wilcox's k-ω near wall formulation if the mesh is sufficiently fine (i.e., if $y^+ \leq 2$ according to CFX's manual [3]) and a logarithmic wall-function proposed by Launder and Spalding [81] if not. It should be noticed that, as demonstrated by Payette [123] and Taheri [149] when studying the turbulent flow inside a conical diffuser, the fact these wall-laws were developed based on the hypothesis of a boundary layer in equilibrium can delay or even prevent the boundary layer separation, particularly in the cases where y^+ is high.

LES

Being able to model the flow behaviour near the walls is even more critical in LES than in RANS, since the already higher computational cost of the simulation is affected by the total number of elements in the mesh as well as their minimum size (which controls the maximum Δt of the simulation; see Eq. (2.32)). It is possible to use a wall-law to model the flow behaviour near the walls in LES, through what is called *Wall Model Large Eddy Simulation* (WMLES). In the case of all large-eddy simulations performed in this thesis, the wall-law proposed by Duprat *et al.* [37] is used. This model is especially appropriate for draft tube (and diffuser) flows as it takes into account the strong adverse pressure gradients which the boundary layers are subjected to. If the near-wall mesh is sufficiently refined, the model will tend to a wall-resolved LES. However, even if the first node is not positioned inside the viscous sublayer, the model can evaluate the wall-shear stress.

2.4 Turbulent inflow boundary conditions for LES

As will be discussed in the following chapters, one of the main aspects of this thesis is the imposition of *proper* inlet boundary conditions for the numerical simulation of the turbulent flow inside a draft tube. Indeed, it is a well known fact that they can have a major impact on the accuracy of the final results, but it is still challenging to specify proper inlet boundary conditions in the case of spatially developing flows (e.g., jets, mixing layers, wall-bounded flows etc.), in spite of the many advancements over the past few decades in this regard. In the case of RANS, explained in Section 2.2.2, inlet boundary conditions are easier to prescribe and normally consist in Reynolds average mean quantities, turbulent length scale(s) and Reynolds stresses. However, in the case of more advanced DNS and LES, imposing only time-averaged quantities at the inlet of a simulation means that the deterministic information about the inflow is definitely lost and that the final numerical solution is possibly compromised. The problem is that high resolution (spatially and temporally) flow information at the inlet plane of a simulation is rarely available, particularly in complex industrial flow configurations, like the draft tube studied in this thesis. Therefore, realistically determining the fluctuating quantities at this location is a major challenge for LES and multiple solutions have been proposed along the years. Usually, these solutions are normally classified into three groups [76, 135, 148, 161, 30]: synthetic turbulence, precursor simulations and recycling methods.

2.4.1 Methods to generate turbulent inflow

Synthetic turbulence

Synthetic turbulence is possibly the most economical method to create the fluctuating inflow field for LES and the main idea behind this method is to superimpose artificially generated fluctuations to the mean inlet velocity field. The easiest way to achieve that is to generate and superimpose a random noise (such as white-noise) with an amplitude determined by the turbulent intensity level, however, since these random fluctuations completely lack spatial and temporal correlations, they are instantly destroyed by the Navier-Stokes solver [2, 36]. For this

reason, more advanced synthetic turbulence methods must include some way of reconstructing these correlations and therefore preventing them from quickly vanishing, such as the Random Flow Generation (RFG) method [138, 6, 23, 24], the Digital Filters (DF) method [79, 31], or even the Synthetic-Eddy Method (SEM) [68, 69, 121, 125]. Despite their relatively low computational cost, the synthetic methods still depend on flow information that is often hard to obtain, especially in complex flow configurations (e.g., Reynolds stresses components to determine turbulence anisotropy) and, more importantly, systematically produce a transition region close to their injection plane where the synthetic turbulent inflow is still developing, mostly because the fluctuations are not *completely* turbulent in nature. The problem is that, if the injection plane is close to the area of interest of the flow (i.e., the region we want to analyse), the decay of these unrealistic fluctuations can affect the mean velocity field via the production term.

Precursor simulations

Precursor simulations, on the other hand, are particularly better in producing realistic fluctuating inflow conditions, as they give more time and space for these fluctuations to develop before reaching the important portion of the computational domain and rely on turbulent data extracted from fully-developed regions of the flow. However, since these simulations are performed in a separate numerical domain, which represents only a fraction of the main domain, and are often launched before the main simulation, they require thus a considerable amount of storage for the generated inflow data. Beside the obviously higher computational cost compared to synthetic methods, the fact a precursor simulation is performed in a separate computational domain means that no feedback information from the main domain is possible. As a result, this approach is limited to very simple flow configurations, notably where the considered geometry yields fully-developed mean flow in the streamwise direction [44, 146, 124, 136, 54].

Recycling methods

Finally, a way to overcome this limitation of precursor simulations, specially for the case of spatially-developing boundary layers, consists in integrating the separate numerical domain into the main domain and recycling the information extracted in a downstream station as inflow conditions for the simulations. In this case, there is no more need for performing or storing the results of a separate precursor simulation. However, as the mean flow is not parallel in the case of spatially-developing boundary layers, the information extracted at the downstream station needs to be rescaled before being used at the inlet. Lund *et al.* [90] proposed such a rescaling technique that used different similarity laws for the inner and outer regions of the boundary layer. This technique produced turbulent boundary layer flows with the expected physical features, but still could lead to some transitional region near the inlet [70, 83] and (similarly to synthetic methods). Moreover, it suffered from inherent flaws [121], such as the need for injecting some kind of synthetic fluctuations to the inlet plane at the beginning of the simulation (which can affect the final results) and spurious coupling in the computed solution if the extraction station is not far enough from the inlet. Other techniques using forcing terms have been developed to improve the control over the rescaling over the inlet plane [143], however, these recycling methods are still restricted to very simple flow configurations.

Data-based methods

More recently, data-driven techniques (e.g., Machine Learning and adjoint methods), have been used to generate synthetic turbulent inlet boundary conditions for DNS and LES [49, 153, 21, 77]. Instead of generating the synthetic fluctuations from basic equations and some scaling and/or orthogonal transformations like in most of the synthetic turbulence methods, the fluctuating field at the inlet of the computational domain is determined by a non-linear model constructed from the data gathered after performing significantly large number of realizations

of a turbulent flow. The computational cost associated with these approaches is particularly high, since the amount of data required to create the non-linear model is not negligible. As a result, their applications are still limited to very simple flow configurations, like in the case of precursor simulations and recycling methods.

2.4.2 Turbulent inflow generation and injection in YALES2

The swirling turbulent flow inside hydraulic turbine draft tubes are indeed very complex and precursor and/or recycling methods are not adequate for its numerical simulation [36, 149]. However, as will be discussed in Chapter 5, we do propose to use Machine Learning algorithms to generate proper inlet boundary conditions, including the injection of synthetic fluctuations, for our numerical simulations in both RANS and LES. The difference though is that, in the case of LES, the incoming fluctuations are generated using a simple synthetic turbulence method and the main role of Machine Learning is to properly adjust their properties (e.g., velocity and length scales), in addition to those from the mean inlet velocity field. In YALES2, these synthetic fluctuations are generated accordingly to the scheme shown in Fig. 2.7.

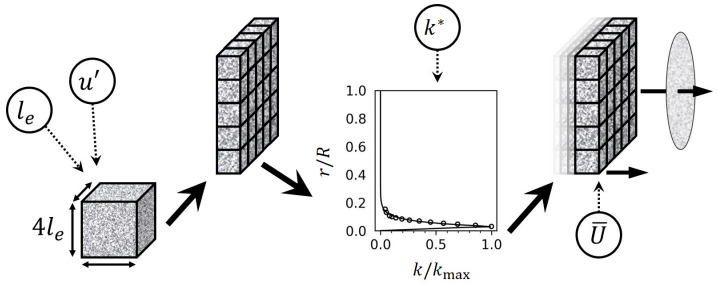

Figure 2.7: Scheme of the synthetic HIT filed generation and injection in YALES2.

Initially, the RFG method proposed by Smirnov [138] and based on the work of Kraichnan [80] is used to generate a divergence-free spatial and temporal correlated *homogeneous isotropic turbulence* (HIT) field of specified length scale l_e and velocity scale u' in a cube of edge length $4l_e$. These cubes are then replicated and positioned side-by-side until the injection plane (e.g., the inlet boundary) is fully covered by these synthetic fluctuations. They are then scaled by a specified normalized turbulence kinetic energy profile, $k/k_{\max}$, and finally injected into the domain at a specified speed, U_{inj}. It should be noticed that the RFG method is capable of introduce some anisotropy onto the synthetic fluctuations via a scaling and orthogonal transformations of the generated flow field, a procedure later simplified by Batten *et al.* [6] using a Cholesky decomposition of the Reynolds stress tensor. Nevertheless, determining the turbulence anisotropy of the flow leaving the runner and entering the draft tube is very hard experimentally and even numerically. Thus, the synthetic fluctuations injected in *all* LES computations in this thesis are *isotropic*, despite this definitely being a strong assumption.

2.5 Head losses equation in the context of numerical simulations

Another important aspect of this thesis is the analysis of the head losses inside the draft tube, since it determines the hydraulic performance of this equipment. Conversely to the experimental head losses, which are limited to integral quantities (see Section 3.2.2), numerical simulations give access to a more detailed information about the flow and the phenomena responsible for the head losses. Thus, starting from the definition of the head H given by Eq. (1.1) and the mean kinetic energy equation (2.6) derived from the Navier-Stokes equations for an incompressible fluid (2.2), Wilhelm *et al.* [159] developed an expression for the head losses in the context numerical simulations. In LES, this equation is given by:

$$
\begin{aligned}
gQ\Delta H_{i,e} &= \iint_{\mathcal{S}_i} \left(\frac{1}{2}\langle\overline{u}_i\rangle\langle\overline{u}_i\rangle + \frac{\langle\overline{p^*}\rangle}{\rho}\right)\langle\overline{u}_z\rangle d\mathcal{S} - \iint_{\mathcal{S}_e} \left(\frac{1}{2}\langle\overline{u}_i\rangle\langle\overline{u}_i\rangle + \frac{\langle\overline{p^*}\rangle}{\rho}\right)\langle\overline{u}_z\rangle d\mathcal{S} \\
&= \underbrace{-\iint_{\mathcal{S}} 2\langle\overline{u}_i\rangle\left(\nu\langle\overline{S}_{ij}\rangle + \langle\nu_{sgs}\overline{S}_{ij}\rangle\right)n_j d\mathcal{S}}_{I} + \underbrace{\iint_{\mathcal{S}} \langle\overline{u}_i\rangle\langle\overline{u'_i u'_j}\rangle n_j d\mathcal{S}}_{II} \\
&+ \underbrace{\iiint_{\mathcal{V}} 2\nu\langle\overline{S}_{ij}\rangle\langle\overline{S}_{ij}\rangle d\mathcal{V}}_{III} + \underbrace{\iiint_{\mathcal{V}} 2\langle\nu_{sgs}\overline{S}_{ij}\rangle\langle\overline{S}_{ij}\rangle d\mathcal{V}}_{IV} + \underbrace{\iiint_{\mathcal{V}} -\langle\overline{u'_i u'_j}\rangle\langle\overline{S}_{ij}\rangle d\mathcal{V}}_{V}
\end{aligned}
\tag{2.35}
$$

where the operator $\langle a\rangle$ corresponds to the time averaged value of a obtained from the flow statistics and $\overline{a}$ corresponds to the filtered value of a. Integrals are evaluated over the surface $\mathcal{S}$ and volume $\mathcal{V}$ of a control volume. Subscripts i and e, correspond, respectively, to the inlet and exit planes of the considered domain. While the head losses equation can be identified in the l.h.s. of Eq. (2.35), the r.h.s. contains the different mechanisms responsible for these losses. For instance, terms I and II correspond to the diffusion of mean kinetic energy, term III to the viscous dissipation mean kinetic energy, and terms IV and V to the modelled and resolved production of turbulent kinetic energy, respectively. Conversely to LES, all turbulent scales are modelled in RANS and, as a result, terms II and V are not available. In this case, the head losses equation is given by:

$$
\begin{aligned}
gQ\Delta H_{i,e} &= \iint_{\mathcal{S}_i} \left(\frac{1}{2}\langle u_i\rangle\langle u_i\rangle + \frac{\langle p^*\rangle}{\rho}\right)\langle u_z\rangle d\mathcal{S} - \iint_{\mathcal{S}_e} \left(\frac{1}{2}\langle u_i\rangle\langle u_i\rangle + \frac{\langle p^*\rangle}{\rho}\right)\langle u_z\rangle d\mathcal{S} \\
&= \underbrace{-\iint_{\mathcal{S}} 2\langle u_i\rangle(\nu+\nu_t)\langle S_{ij}\rangle n_j d\mathcal{S}}_{I} + \underbrace{\iiint_{\mathcal{V}} 2\nu\langle S_{ij}\rangle\langle S_{ij}\rangle d\mathcal{V}}_{III} + \underbrace{\iiint_{\mathcal{V}} 2\nu_t\langle S_{ij}\rangle\langle S_{ij}\rangle d\mathcal{V}}_{IV}
\end{aligned}
\tag{2.36}
$$

Similar equations have been used by MacIsaac *et al.* [93] and Cui *et al.* [22] to study the total pressure losses inside gas turbines and, in all studies, including Wilhelm's *et al.* [159], the turbulent kinetic energy production (terms IV and V) was the main mechanism responsible for losses in a turbulent flow. However, since only the modelled production is available in RANS due to the statistical nature of the numerical solution, the turbulence modelling has a more considerable impact on the final head losses prediction in this type of simulations [159].

Chapter 3

State of the art of draft tube simulations and validation data

Contents

3.1 State of the art of draft tube simulations

Given its importance in the overall hydraulic performance of a hydroelectric power plant, many experimental studies have been conducted along the years to study the complex flow behaviour inside draft tubes. Among them, we can mention the three Turbine-99 Workshops [55, 17] organized at Luleå University in Sweden, the Flow Investigation in Draft Tube (FLINDT) project [5], conducted at the EPFL in Switzerland, and both the AxialT [29] and BulbT [28] consortiums created by the Laval University in Canada. These projects have contributed to enhance the numerical simulations and create a strong knowledge base for the investigation of draft tube flows. In this section, an overview of some of these numerical studies is given to highlight its most important aspects.

3.1.1 Turbulence modelling

The flow inside a draft tube is very complex and difficult to simulate, in part, due to its highly unsteady and turbulent nature, but also as a result of swirling and adverse pressure gradients to which these flows are subjected. One of the first aspects to determine when performing numerical simulations of the flow inside a draft tube is the method chosen to model the turbulence on the flow. In industry, steady RANS simulations using two-equation linear eddy-viscosity turbulence models are traditionally used especially due to their low computational cost. Considering the machines operating close to their best efficiency point, the validity of two-equation turbulence models have been studied many times. For instance, Cervantes and Engström [16] studied the flow inside the Turbine-99 draft tube operating close the best efficiency point using RANS and three different turbulence models: zero equation (algebraic), k-ϵ and k-ω SST. Pressure recovery

and head losses predict by the three models were very similar, but only the two-equation models predicted a flow separation at the hub. Similarly, Marjavaara *et al.* [97] also utilized RANS and k-ϵ and k-ω SST turbulence models to study the same configuration and the results were again very similar, although this time no turbulence method was considered as more appropriate due to the lack of experimental data. More recently, Iovanel *et al.* [66] also used RANS and both k-ϵ and k-ω SST turbulence models to investigate the velocity field inside the Porjus U9 draft tube operating at the best efficiency point. The obtained results were all very similar, but the k-ω SST turbulence model with the streamlines curvature correction [142, 139] mentioned in Section 2.2.2 was slightly closer to the experiments. In spite of the similar results obtained with the k-ϵ and k-ω SST turbulence models in the aforementioned numerical works, the latter model is more adapted to flows subjected to adverse pressure gradients [104], like the ones found in draft tubes. Moreover, when studying the swirling flow inside a conical diffuser, Payette [123] demonstrated that the k-ϵ turbulence model tends to delay the boundary layer separation.

One of the problems with steady RANS simulations using two-equation linear eddy models is that they are not capable of capturing the unsteadiness of the flow inside draft tubes. To overcome these limitations, one solution is to use unsteady RANS (URANS) simulations. These methods have the advantage of resolving a small part of the turbulent structures on the flow, limiting thus the influence of the turbulence model. In the context of the FLINDT draft tube, URANS has been used by Vu *et al.* [154] to study the performance of this draft tube and, more recently, by Pasche *et al.* [122], who investigated the pressure fluctuations associated with the part load vortex rope. An evolution of URANS, called Scale-Adaptive Simulations (SAS) [39], is a hybrid method between URANS and LES based on the k-ω SST turbulence model, and has also been used to investigate the flow inside draft tubes. For instance, Mulu *et al.* [107] used RANS and the k-ϵ and k-ω SST turbulence models, as well as SAS to study the flow close to the inlet of the Porjus U9 draft tube. All turbulence methods predict similar drat tube performance, however, there was definitely an impact on the velocity field close to the inlet. Interestingly, in comparison to the other turbulence methods, the SAS method was not as good at predicting the phase-averaged velocity. A similar poor performance of the SAS was observed in Iovanel *et al.* [67], who studied the pressure fluctuations inside the same Porjus U9 draft tube. While the authors expected this method to be able to capture higher pressure fluctuations on the monitored points, the numerical results obtained with SAS did not converge and the signal could not be processed.

While URANS is less computationally demanding than more advanced turbulence methods, such as LES, its results are still dependent on the chosen turbulence model [134] and the turbulent structures produced by this approach can still be damped out [56]. Indeed, this is clearly shown in the master's thesis of Bélanger-Vincent [8], who performed Detached Eddy Simulations (DES) of the flow inside a Francis turbine draft tube, but who also initially compared the results of the central vortex rope with those predicted in RANS and URANS. While the vortex rope was mostly inexistent in RANS and very damped out in URANS, its helicoidal shape was clearly visible in DES. A very similar result was found in Foroutan and Yavuzkurt [48], who analysed the vortex rope behaviour inside a simplified Francis turbine draft tube using URANS with the k-ϵ and k-ω SST turbulence models, as well as DES. Given the superior description of the flow achieved with DES and its lower computational cost compared to LES, as it consists in a hybrid RANS/LES approach, it has been used in other numerical studies of the flow inside draft tubes. For instance, Beaubien [7] investigated the causes for a sharp performance drop in a draft tube close to its best efficiency point using URANS and DES. While the performance results obtained with both approaches ended up being very similar, they did not agree very well with the experimental data. Nevertheless, the resulting flow was much more detailed in DES.

The exact same draft tube studied in Beaubien [7] was initially investigated by Duprat [36] using LES. The results were compared to the experimental work of Tridon [150] and the sharp experimental performance drop was correctly recovered by the numerical simulations. However,

the recirculation zone associated with this drop persisted in other operating conditions in the numerical simulations, which was not the case with the experiments. Brugière [14] also used LES to study the flow inside a draft tube. The results were compared with RANS and the available experimental measurements. The goal was to investigate the uncertainty of the inlet profiles used in the simulations. While the near-wall region of these profiles was identified as having the most influence over the final results, they were not sufficient to explain the differences with respect to the experimental data. Finally, Wilhelm [160] has also analysed the flow inside a bulb turbine draft tube using LES, although URANS simulations were also performed to compare with the experimental measurements. A head losses equation was developed and the accurate description of the flow obtained with LES allowed for a precise determination of the mechanisms responsible for the head losses inside the draft tube.

3.1.2 Inlet boundary conditions

Mean velocity profiles

In addition to modelling the complex nature of the turbulent flow inside the draft tube, it is also crucial to define proper inlet boundary conditions for the numerical simulations. These conditions usually consist in the specification of the three velocity components measured downstream the runner, at the inlet of the draft tube. Moreover, depending on the turbulence method utilized, turbulent inlet boundary conditions *must* be imposed too to close the system of equations. However, the flow downstream the runner is complex (e.g., rotating, highly turbulent, unsteady etc.) and *comprehensive* experimental measurements at this region are delicate to perform and thus rarely available.

In industry, it is common to limit these measurements to *mean* flow quantities measured at a single radial line positioned just downstream the runner and, in this case, the standard approach to perform draft tube simulations consists in assuming a sufficiently high mixing of the flow between the runner and the draft tube and consider axisymmetric inlet boundary conditions. However, steady RANS simulations of draft tube flows using this approach showed an important sensitivity to the imposed mean velocity profiles and turbulent parameters (e.g., turbulence intensity and length scale) on the overall performance of the draft tube. For instance, in the context of steady RANS k-ϵ simulations of the FLINDT draft tube, Mauri [98] studied the influence of multiple inlet parameters (mean radial velocity profile, near wall velocity interpolation, turbulent dissipation length scale etc.) onto the performance and flow behaviour inside the draft tube. Among these parameters, the inlet mean radial profile had an important impact on the results. A similar investigation was conducted by Cervantes and Engström [18] in the context of the Turbine-99 draft tube. They used a method called *factorial design* to investigate the influence of some unknown inlet conditions (in particular, the radial velocity profile, turbulence length scale and wall-roughness) on the pressure recovery coefficient of the draft tube. Once again, the radial velocity profile was found to have an important impact on the downstream results. Payette [123] also demonstrated the importance of properly imposing this velocity component when studying the swirling flow inside a conical diffuser using RANS and the k-ω SST turbulence model. Recently, Brugière [14] performed a sensitivity analysis of the mean inlet velocity profiles imposed at a RANS simulation of a bulb turbine draft tube using k-ω SST turbulence model and showed that a correct characterization of these profiles near the walls is very important.

Assuming axisymmetric inlet boundary conditions can be particularly unsuitable for turbines with a few blades due to the fairly inhomogeneous flow just downstream the runner [119, 50, 157, 84]. Thus, another approach to determine the inlet conditions for a draft tube simulation consists in conducting separate RANS simulations of one guide vane and one runner blade passage, using periodic conditions and a *stage* interface [3] between the two, which applies a circumferential averaging of all fluxes between the two sides of the boundary. This approach

allows to recover a complete bidimensional inlet field that can be imposed at the inlet of the draft tube. It was compared to the previously axisymmetric one in the work of Marjavaara *et al.* [97] in the context of steady and unsteady RANS simulations of the Turbine-99 draft tube. Overall, the results are very similar, though the pressure recovery coefficient was slightly better predicted by the bidimensional inlet. Taheri [149] also compared these two approaches when investigating the flow inside a bulb turbine using DES. While the mean profiles and pressure recovery coefficient predicted by both methods were very similar, the bidimensional inlet boundary conditions allowed for a better characterization of the turbulent structures inside the draft tube. This was also observed in the case of LES, where the numerical simulations of a bulb turbine draft tube conducted by Brugière [14] imposing axisymmetric inlet boundary conditions did not show any signs of runner blade tip vortices along the external walls, whereas they were very clear in the simulations conducted in Wilhelm [160], who imposed bidimensional inlet conditions.

However, one problem with determining the inlet boundary conditions from a separate guide vane and runner blade simulation is that the results are dependent on accurate descriptions of runner blade geometries, which can have an important impact on the downstream flow behaviour inside the draft tube [113, 156]. Moreover, in the case of double regulated low head turbines, a proper description of the gaps between the runner blades and the hub and shroud walls is crucial to properly capture the vortices being formed in this region of the flow [118, 120, 62, 155]. Furthermore, the interface between the two turbine elements can have an impact on the obtained results [95, 64]. For instance, if the draft tube is coupled to the guide vanes and runner blades steady RANS simulations, a second stage interface between the runner and draft tube has to be used implying a circumferential averaging of the fluxes and an axisymmetric draft tube inlet boundary condition. Conversely, if the draft tube is simulated separately from the runner, other flow quantities (e.g., turbulence length scale, dissipation rate etc.) can still have an important impact on the final results [25].

Turbulent quantities

RANS simulations using two-equation linear eddy viscosity turbulence models also require the specification of turbulent inlet boundary conditions. In the case of draft tube simulations, it is common to impose a combination of a turbulence intensity, I_t, and a turbulent length scale, l_t. The turbulence intensity is defined as the ratio between the root-mean-square of the turbulent velocity fluctuations u' and the mean velocity $\langle u \rangle$ (in the sense of Reynolds decomposition):

$$I_t(\vec{x}) = \frac{u'(\vec{x})}{\langle u \rangle(\vec{x})} \tag{3.1}$$

The turbulence intensity can be determined experimentally as long as the fluctuations are measured. Conversely, the length scale, l_t, represents the size of the most energetic eddies and is not easy to measure experimentally. It is usually considered to be between 5% to 10% of the draft tube inlet diameter [123, 160]. However, small variations in these values can have an important influence on the downstream flow behaviour inside a draft tube simulated using RANS. This was discussed in Mauri [98] and Cervantes and Engström [18], but was also observed in Payette [123] and de Henau *et al.* [25]. In all these cases, modifying, for instance, the turbulent length scale impacted the overall performance of the draft tube. Brugière [14], on the other hand, evaluated the uncertainty of the velocity profiles inside a bulb turbine draft tube predicted using RANS k-ω SST based on the uncertainty of the I_t and l_t values. In that case, it was the length scale which influenced the most the results. Unsteady draft tube flow simulations using DES also require the specification of the turbulent inlet boundary conditions, though they are slightly different from RANS and usually depends on the definition of a turbulent viscosity at the inlet of the domain. Nevertheless, Bélanger-Vincent [8], who performed DES computations of the

flow inside a Francis turbine draft tube, showed a strong sensitivity of the downstream flow behaviour due to the imposed turbulent inlet conditions.

In the case of LES, however, turbulent inlet conditions are not required to solve the system of discretized equations and previous studies simply did not inject any turbulent fluctuations at the draft tube inlet. Instead, they would let the instabilities naturally appear relying on the very unstable nature of the downstream swirling flow. For instance, a simple axisymmetric inlet boundary condition without inlet turbulence has been used by Brugière [14] to simulate the flow inside a bulb turbine draft tube in LES. Wilhelm *et al.* [159] used a separate guide vane and runner RANS simulations to obtain a complete flow field description at the inlet of a draft tube but also did not impose any turbulent inflow. On the other hand, Duprat [36] imposed an axisymmetric mean velocity field at the inlet and a turbulent field issued from white-noise fluctuations. However, these fluctuations are quickly destroyed by the flow solver due to their lack of correlations [2]. To overcome these issue, Taheri [149] reconstructed part of the experimental data obtained in Lemay *et al.* [84] using machine learning to impose a synthetic fluctuations based on the method of Davidson and Bilsson [23] with *proper* anisotropy and spatio-temporal scales in the case of a complete inlet flow field description for his DES computations of the flow inside a bulb turbine draft tube. Nevertheless, compared to a simpler inlet conditions without any synthetic turbulence injection, the impact of the proposed approach in the velocity profiles and draft tube performance was very limited.

3.1.3 Final considerations about the numerical simulations

The discussion of these previous numerical works that investigated the flow inside draft tube highlighted some important aspects which should be considered in *our* numerical simulations. For instance, when performing steady RANS simulations using two-equation linear eddy viscosity models of the bulb turbine draft tube considered in this thesis, the k-ω SST turbulence model should be utilized. First, this model is more adequate for the prediction of flows subjected to adverse pressure gradients. Second, they are also better than k-ϵ in predicting the boundary layer behaviour, particularly because they do not show a tendency to delay flow separation in this region of the domain. In the case of LES, all the numerical works that investigated the flow inside a bulb turbine draft tube used the Dynamic Smagorinsky to model subgrid scale viscosity. However, while this method will be used in the investigations of the conical diffuser in Chapter 6, we decided to use the σ-model for our draft tube flow simulations, especially due to its superior performance in more complex flows and geometries.

In addition to the turbulence modelling, the previous discussions shown that special attention should be given to the specification of the inlet boundary conditions, especially because the obtained results can be strongly affected by them. For instance, while bidimensional mean velocity fields had no significant effect on the main results of previous draft tubes simulations, the characterization of these profiles, particularly near the walls, had a major impact on downstream flow behaviour. In the case of RANS k-ω SST simulations, standard turbulent inlet boundary conditions can indeed yield satisfactory results. However, the influence of turbulent inlet conditions in LES has not been particularly explored, mostly because it was previously thought that they were not required in this type of simulations.

It is important to verify the quality of the numerical solutions. For instance, the modelling and discretization errors must be identified and addressed prior to validate any of the results. Considering that the two flow solvers used in this thesis, ANSYS CFX and YALES2, were already validated and that the numerical methods used in both were shown to be sufficiently precise for our applications, the spatial and temporal discretization of the solutions still need to be verified. To ensure an adequate spatial resolution of the flows studies in this thesis, spatial discretization analyses are conducted prior to the validation of the numerical results. For instance, in the case of the bulb turbine draft tube, this step is thoroughly explained in Section 4.3. The temporal resolution, on the other hand, particularly in the case of LES, was ensured by performing a

series of simulations with the intent to first stabilize the flow inside the numerical domain and only then accumulate the desired statistics. Therefore, in the case of the draft tube discussed in Chapters 4 and 7, a fully converged solution is obtained after three runs of the numerical simulation, each corresponding to approximately ten flow passages through the draft tube. An initial run to stabilize the flow inside the domain is conducted and just then a second run is performed to compute all the flow statics necessary for the automatic mesh adaptation (see Section 4.3). Once the adaptation is finished, a third and final LES is performed to evaluate the final flow statistics and results. Similarly, for the case of the conical diffuser investigated in Chapter 6, in all LES cases, an initial simulation is run to stabilize the flow field within the diffuser and only then a second simulation is run to accumulate the statistics used in the final analysis of the flow during the equivalent of ten complete flow passages throughout the domain.

3.2 Experimental data for numerical simulations validation

To validate the numerical results obtained with the simulations in the following chapters, these are compared with experimental measurements to verify the good representation of the flow dynamics inside the computational domain. For the numerical simulations of the draft tube flow conducted in the context of this thesis, these experimental measurements were carried out by the engineers at GE Hydro, in France, and GE Global Research Center (GRC), in the United States. Several measurements have been performed at two different operating conditions. Their main characteristics are discussed in this section.

3.2.1 Experimental setup

The experimental setup of the draft tube studied in this work is schematically shown in Fig. 3.1. The geometry of the draft tube is similar to that investigated by Wilhelm *et al.* [159], but it is attached to a closed loop where a constant *air* flow is forced through. Flow temperature and humidity are controlled and the Reynolds number evaluated at the first measurement station (R0, in Fig. 3.1) is around 1.5×10^6, which is similar to real draft tube configurations [123, 159]. Although the working fluid is not water, the flow is considered as incompressible since the maximum Mach number is kept under 0.2. The *key aspect* of the current setup though is that, conversely to real bulb turbines (see Section 1.3), the guide-vanes and runner were *replaced* by a grid and a set of 34 *fixed* blades, shown in details in Fig. 3.2.

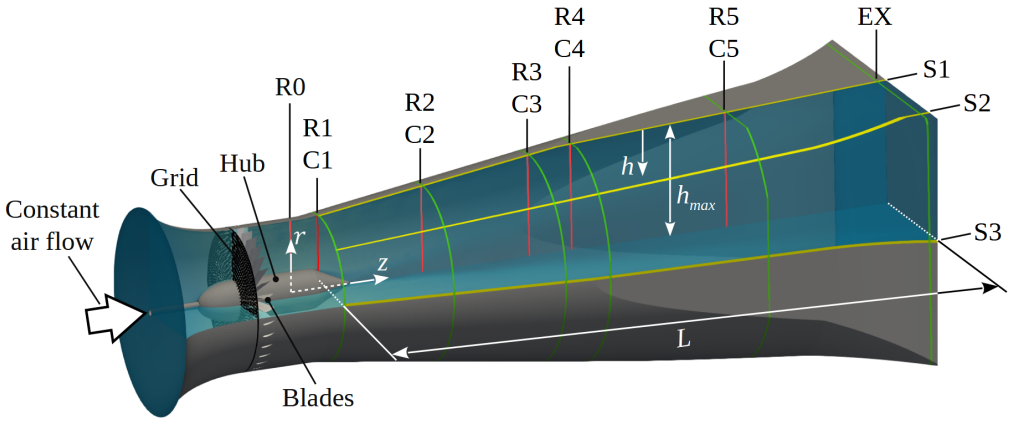

Figure 3.1: Scheme of the experimental setup used to study the flow inside a bulb turbine draft tube. In (red) the radial traverses R0 to R5; (green) circumferential distribution of wall-mounted pressure taps, C1 to C5 and EX; (yellow) streamwise distribution of wall-mounted pressure taps, S1 to S3.

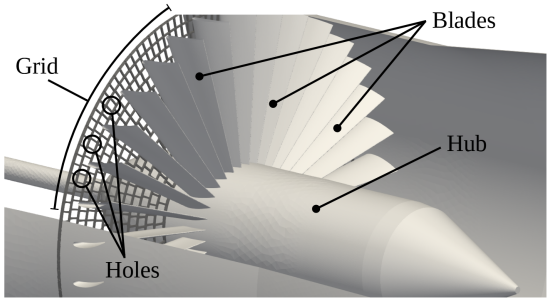

Figure 3.2: Details of the grid and fixed blades used to generate the turbulent swirling flow for the draft tube.

As pointed out at the beginning of this chapter when discussing previous numerical works that investigated the flow inside draft tubes, it is crucial to accurately determine the characteristics of the flow at the inlet of the computational domain. Therefore, replacing the guide-vanes and runner by a grid and a set of fixed blades allowed for a better control over the flow entering the draft tube and to a better characterization of the simulations' inlet boundary conditions. For instance, the large number of blades decreased the variations in the azimuthal direction, which is a real problem in the case of bulb turbines due to their reduced number of runner blades (as previously mentioned in Section 3.1.2). The size and distribution of the holes in the grid shown in Fig. 3.2 is used to control the total pressure profile at the inlet of the draft tube by allowing or restricting the flow passage. However, they also generate a fairly homogeneous turbulent field just behind the blades. These blades, on the other hand, divert the mean flow leaving the grid and generate flow swirl for the draft tube, creating thus even more instabilities in the already turbulent upstream flow. As a consequence, the turbulence at the inlet of the draft tube (station R0) has an intensity (as defined in Eq. (3.1)) of approximately 5% with a wide range of motion scales.

3.2.2 Experimental measurements

Mean velocity and static pressure profiles

Five-hole pressure probes measured the three components of the mean velocity profiles, as well as the static pressure profiles inside the draft tube. These probes were positioned at the end of radial traverses corresponding to stations R0 to R5 in Fig. 3.1. The profiles were measured with respect to radial distance to the external walls of the draft tube, h, but in the following chapters, this distance will be normalized by the maximum distance between the external wall and the axis of the draft tube (or the internal wall, in the case of stations R0 and R1), h_{max}. As the head losses inside the draft tube are greatly affected by the near-wall flow behaviour [14, 160], special attention was given to this part of the flow during the experiences, particularly to capture the boundary layer behaviour in this region. Indeed, this was a limitation of the experimental data used by Wilhelm [160] to validate her numerical results.

One important aspect of these measurements is that, in the case of the first operating point, OP1 (see Section 3.2.3), the results of two *distinct* experimental campaigns had to be combined to obtain a profile extending from the external walls of the draft tube up to the centre of the flow. Indeed, an initial experimental campaign, OP1(1), measured the mean velocity and static pressure profiles close to the external walls, covering approximately 40% of h_{max}. While these results were precise in terms of spatial discretization and description of the boundary layer, a second campaign, OP1(2), was later conducted to measure the complete velocity and pressure profiles (i.e., covering the whole length of h_{max}). However, as the results in OP1(2) were not as precise as in OP1(1) and the boundary layer was not as accurately described, the profiles obtained in both experimental campaigns were combined using OP1(1) as a reference. The combination process consisted in shifting the profiles obtained in OP1(2) until their values close

to the walls were consistent with OP1(1). As will be discussed in Chapter 4, most of the combined profiles coherent with each other, but, particularly in the case of the mean tangential velocity, some inconsistencies may have been caused by this combination process.

Turbulence kinetic energy profiles

In addition to the mean velocity and pressure profiles, hot-wire probes measured the turbulence intensity, I_t, and mean velocity magnitude, $\langle u \rangle$, at the six radial traverses presents in the experimental setup, i.e., stations R0 to R5. From these measurements, the turbulence kinetic energy profile can be estimated assuming isotropic turbulence and the definition of turbulence kinetic energy, k, and turbulence intensity, I_t, respectively Eqs. (2.7) and (3.1):

$$k(\vec{x}) = \frac{3}{2}\langle u \rangle^2(\vec{x}) I_t^2(\vec{x}) \tag{3.2}$$

Although the assumption of isotropic turbulence is not necessarily realistic, it allows us to have an idea of the turbulence kinetic energy profiles inside the draft tube and to compare these results with the experimental measurements at the respective locations.

Static pressure distribution at the walls

Wall mounted pressure taps measured the distribution of static pressure at the walls of the draft tube. They were positioned either in the streamwise direction (stations S1 to S3), or circumferentially (stations C1 to C5 and EX). The importance of these measurements, particularly the ones at stations S1 to S3, is that they give an indication about the pressure recover. Moreover, as these stations follow the geometry of the draft tube, it is possible to see its influence on the static pressure distribution on the walls. Finally, since the last circumferential station, EX, is positioned very close to the exit of the draft tube, it is used as a reference to evaluate the experimental head losses.

Evaluation of the experimental head losses

The final experimental results used to validate the numerical simulations consist in the experimental head losses inside the draft tube. The procedure followed to determine these losses is explained in the Standard International Electrotechnical Commission (IEC) 60193 [145]. The experimental head losses, henceforth called IEC losses, are measured between the inlet plane of the draft tube (e.g., section R0 in Fig. 3.1) and another plane close to its exit, which in the case of the experimental setup shown in Fig. 3.1, corresponds to section EX. They are given by the following equation:

$$\Delta H_{IEC} = \frac{1}{Q} \iint_{S_{in}} \left(\frac{\langle p \rangle}{\rho g} + \frac{1}{2g} \langle u_i \rangle \langle u_i \rangle \right) \langle u_z \rangle dS + \frac{1}{\rho g} \left[\langle p_{\mathrm{IEC}} \rangle + \frac{1}{2} \rho \left(\frac{Q}{A_{\mathrm{IEC}}} \right)^2 \right] \tag{3.3}$$

In the equation above, the influence of gravity is considered negligible inside the drat tube. The static and dynamic heads at the inlet plane of the draft tube are calculated from the mean velocity and pressure profiles measured by the five-hole pressure probes at this location. However, since such measurements are not available at the exit plane, EX, the static head at this location is equal to the average static pressure measured by the wall-mounted pressure taps, $\langle p_{\mathrm{IEC}} \rangle = \langle p_{\mathrm{EX}} \rangle$. This means that the static pressure distribution inside the draft tube in this plane is considered uniform and its value can be determined from the pressure at the walls. In addition to that, the dynamic head is evaluated from the bulk velocity at this plane, Q/A_{IEC}, meaning that the mean flow is uniform and purely axial at the exit plane. Due to these considerations about the static and dynamic heads at the exit plane of the draft tube,

IEC losses can be different from the *real* head losses between the inlet and exit planes, which is given by Eq. (3.4), below. Nevertheless, in an industrial perspective, the IEC losses is of extreme importance as it defines the hydraulic performance of the draft tube and can be used to compare the experimental and numerical results.

$$\Delta H = \frac{1}{Q}\iint_{S_{in}} \left(\frac{\langle p\rangle}{\rho g} + \frac{1}{2g}\langle u_i\rangle\langle u_i\rangle\right)\langle u_z\rangle dS - \frac{1}{Q}\iint_{S_{exit}} \left(\frac{\langle p\rangle}{\rho g} + \frac{1}{2g}\langle u_i\rangle\langle u_i\rangle\right)\langle u_z\rangle dS \tag{3.4}$$

3.2.3 Operating points

The experimental measurements were conducted into two different operating conditions, OP1 and OP2. The holes in the upstream grid shown in Fig. 3.2 as well as the flow rate in the closed loop to which the draft tube is attached were modified in each case, resulting in different inlet conditions and flow behaviour inside the draft tube. For instance, Figure 3.3 compares the results of the three mean velocity components and turbulence kinetic energy profiles measured at the inlet of the draft tube (station R0) for each of these operating conditions. The results are normalized by the average axial velocity measured at OP1, $V_{b,in,OP1}$, and the same location, and their radial distribution is given in terms of the normalized distance to the external wall, h/h_{max}. Notice that, since there is no guide-vanes or runner to control the flow at the inlet of the draft tube, the velocity profile distribution is controlled by the disposition of the holes at the upstream grid (see Fig. 3.2).

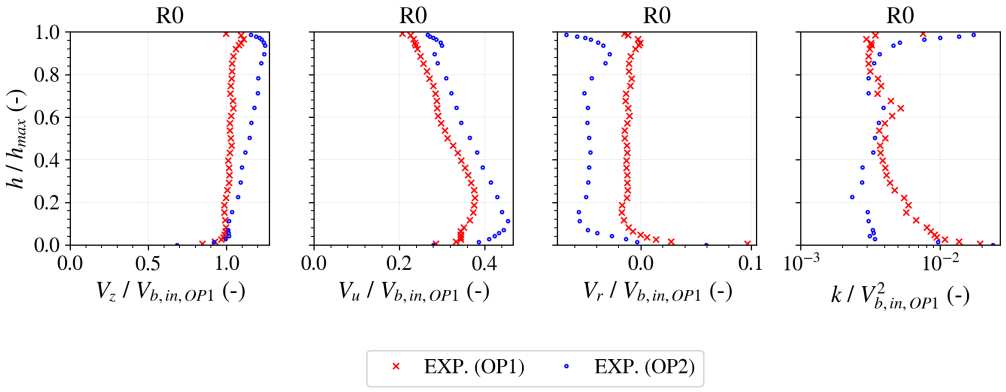

Figure 3.3: Mean velocity and turbulence kinetic energy profiles measured at the inlet of draft tube (station R0) at both operating points, OP1 and OP2.

It is clear from Fig. 3.3 that the mean axial velocity, V_z, is higher in OP2 compared to OP1, and its distribution is relatively different. For instance, in OP1, V_z is mostly constant along the inlet radius, except for a small peak observed very close to the hub (the centre of the flow, $h/h_{max} = 1.0$). In OP2, V_z values slowly increase towards the centre of the flow, to the point where its values are almost 30% higher close to the hub compared to the external walls ($h/h_{max} = 0.0$). Considering that the fluid density, ρ, is similar in both operating points, the mass flow in OP2 is about 10% higher than in OP1.

Another important difference between the two operating conditions is the mean tangential velocity profiles, V_u. Once again, their values are higher in OP2 compared to OP1 and, despite a similar distribution, the peak value is closer to the external walls, $h/h_{max} = 0.0$, at the second operating point. Defining the swirl number, S_w, as the ratio between the axial flux of angular momentum and the axial flux of axial momentum multiplied by the radius, its value at the inlet of the draft tube (station R0) is given by:

$$S_w = \frac{1}{R_{max,R0} - R_{min,R0}} \frac{\iint_{S_{R0}} V_z V_u r dS}{\iint_{S_{R0}} V_z^2 dS} \tag{3.5}$$

where $R_{max,R0}$ and $R_{min,R0}$ are, respectively, the maximum and minimum radius at station R0, and S_{R0} its area. The S_w values are respectively $S_w = 0.327$ for OP1 and 0.344 for OP2.

The mean radial velocity profile, V_r, distribution is similar in both operating conditions, but the values measured in OP2 are considerably more negative than in OP1. Finally, looking at the turbulence kinetic energy profiles, the modification of the upstream grid and flow rate resulted in higher values of k close to the external walls of the draft tube (between $0.0 \leq h/h_{max} \leq 0.5$) in OP1 compared to OP2.

Chapter 4

Reference simulations of the draft tube

Contents

4.1 Introduction

In this chapter, the turbulent flow inside the draft tube shown in Section 3.2.1 is investigated using the both RANS and LES turbulence methods. It starts with the definition of the basic numerical domain and boundary conditions used in these initial simulations. The spatial discretization of the numerical domain is verified and the results for the first operating point are examined. Synthetic fluctuations are then injected in LES and the influence of the turbulent inlet boundary conditions is discussed. A more detailed analysis of the head losses evolution inside the draft tube is conducted and the problems with inadequate inlet boundary conditions is explained. Finally, a similar analysis is performed for the second operating point, where the same problems are observed.

4.2 Numerical setup

4.2.1 Numerical domain

The numerical domain used in the reference RANS and LES computations of the draft tube is show in Fig. 4.1. It consists in the draft tube portion of the experimental setup shown in Fig. 3.1 followed by a straight extension downstream its exit. The inlet of the domain is defined by the first measurement station, i.e., station R0, however, since this station is positioned right downstream the set of 34 blades, a portion of the hub is still present within the numerical domain. With respect to its outlet, while the air flow passing through the real experimental setup discharges into a large cylindrical tank after a sudden expansion, simulating this complete geometry is computationally expensive and not necessarily required. For instance, Mauri [98] compared three downstream extension configurations (no extension, with a straight extension and with a large cylindrical extension) while investigating the flow inside a Francis turbine draft tube, Payette [123] investigated multiple downstream extension configurations in the context of a simple conical diffuser [19], Wilhelm [160] compared the flow behaviour inside a bulb turbine draft tube using either a straight extension or a large cylindrical extension and, more recently, Véras [152] thoroughly investigated the influence of different downstream extension geometries (e.g., a straight extension, a cylinder or an asymmetric box etc.) in the case of a bulb turbine. In all cases, it was found that a simple straight extension was more computationally efficient than simulating the whole downstream geometry and had a negligible influence on the flow inside the draft tube. Moreover, it helped with both the convergence and stability of the numerical solution, especially in the case where there is a recirculation at this location. Therefore, the outlet of the numerical domain is positioned at the end of a straight extension downstream the draft tube.

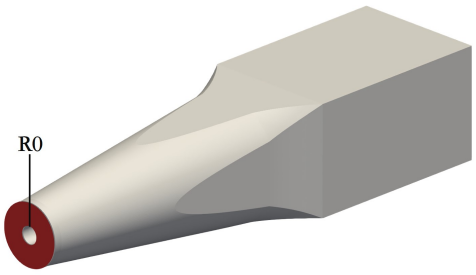

Figure 4.1: Numerical domain of the draft tube used in the reference RANS and LES computations.

4.2.2 Boundary conditions

As discussed in the description of the experimental setup used for this thesis (see Section 3.2.1), especial attention was given to the control and characterization of the flow at the inlet of the draft tube. One major difference of the current configuration compared to real turbines and previous numerical studies of draft tube flows is the replacement of the guide-vanes and runner by a grid and a set of 34 *fixed* blades, which together generate the desired turbulent swirling flow for the draft tube. The elevated number of blades used in the current experimental setup reduced the flow variations in the azimuthal direction and, as a result, the generated inflow is closer to an axisymmetric 2D distribution, allowing for better characterization of the simulations' inlet boundary conditions. Experimental mean axial, tangential and radial velocity profiles (V_z, V_u, V_r, respectively), as well as the turbulence kinetic energy profile (k) measured at the inlet of the numerical domain (station R0) are imposed as inlet conditions for these reference simulations. These profiles are shown in Fig. 4.2 normalized by the average axial velocity at the inlet, $V_{b,in}$, and as a function of the normalized height, h/h_{max}. For the moment, we consider only the first

operating point, OP1. Their distribution over the inlet plane is considered as axisymmetric due to the high number of blades used to generate the swirling flow entering the draft tube. RANS simulations using the k-ω SST turbulence model require turbulent inlet boundary conditions to close their system of equations. For that, the profiles of k estimated from the turbulence intensity measurements at station R0 and shown in Fig. 4.2 are used. Moreover, a turbulence length scale equal to 10% of the inlet channel height (i.e., the difference between the external and internal radius of the draft tube) is assumed, as it is a typical value in this type of simulation [123, 25, 160, 152]. In the case of LES, however, as turbulent inlet boundary conditions are not required, these initial reference simulations are run imposing only the axisymmetric mean inlet velocity profiles as boundary conditions. Indeed, this is the simplest and most commonly used approach in draft tube flow computations using LES, since in this swirling flow, instabilities would naturally develop inside the numerical domain [14, 160].

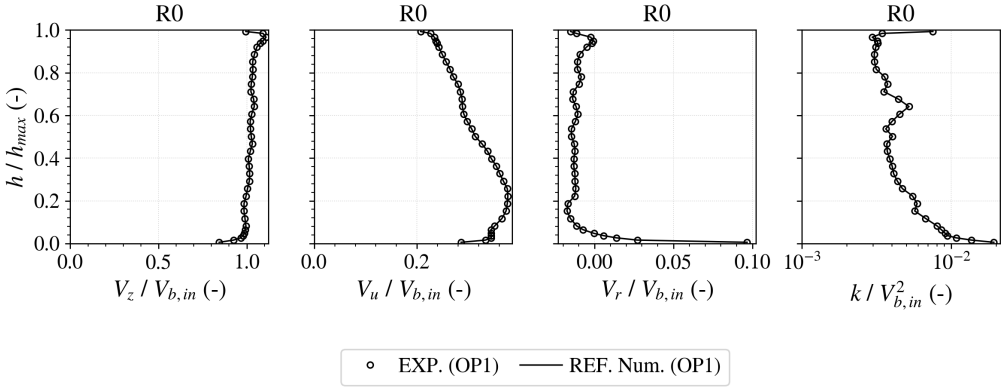

Figure 4.2: Mean velocity and turbulence kinetic energy profiles imposed at the inlet of the reference draft tube simulations (station R0) at OP1.

Finally, an average static pressure equal to 0 is imposed at the outlet plane of all RANS simulations, whereas, in LES, the solver imposes a velocity field which is normal to the outlet plane, avoiding thus any recirculation at this location. At the walls of the numerical domains, which are all fixed, a no-slip condition is imposed. Due to the high Reynolds number of the flow being investigated, and the prohibitive computational cost associated with a wall-resolved LES, the wall model proposed by Duprat *et al.* [37] and specifically developed to handle wall-bounded flows subjected to adverse pressure gradients is applied to these simulations. In the case of RANS, the automatic wall treatment implemented in ANSYS CFX is used (see Section 2.3.4).

4.3 Spatial discretization study

Prior to launch the reference draft tube simulations, a mesh convergence study is performed to ensure that the numerical results are independent of their spatial discretization level. In RANS, this discretization can have a major impact on the numerical errors associated with the predicted mean flow gradients, whereas in LES, the discretization also determine which portion of the turbulent scales of the flow are going to be explicitly resolved, as the filter width depends on the local mesh size [86] (see Section 2.2.3).

4.3.1 RANS

A classic spatial discretization study was performed in RANS by manually and gradually refining a block structured mesh of the reference numerical domain shown in Fig. 4.1. The meshes were generated in ANSYS ICEM and refinement was applied in all directions of the

geometry, e.g., radial, circumferential and longitudinal directions. Four meshes were considered, as shown in details in Fig. 4.3. In Tab. 4.3, the main characteristics of these meshes are resumed.

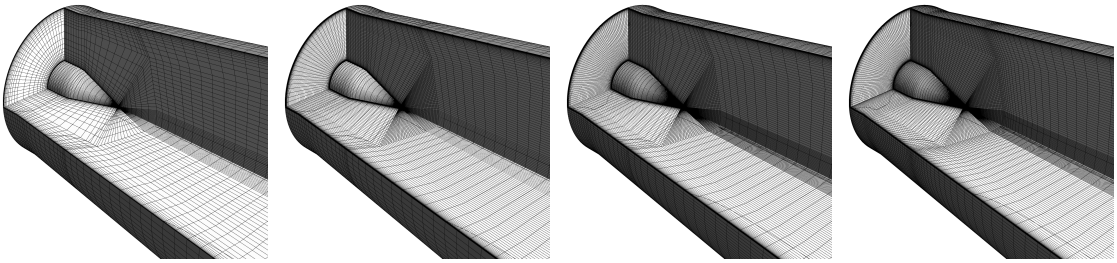

(a) (b) (c) (d)

Figure 4.3: Detail of the four meshes used for the spatial discretization study in RANS. (a) M0; (b) M1; (c) M2; (d) M3.

Table 4.1: Characteristics of the four meshes used for the spatial discretization study in RANS.

Mesh	M0	M1	M2	M3
Number of elem. ($\times 10^6$)	0.49	0.96	2.19	3.01
Number of nodes ($\times 10^6$)	0.50	0.98	2.22	3.06
Maximum y^+	2.90	2.94	3.03	3.19

As shown in Tab. 4.1, special attention was given to the near wall mesh refinement since the k-ω SST turbulence model implementation in ANSYS CFX requires y^+ values below to 2 to ensure an adequate application of the automatic wall treatment and a good resolution of the boundary layer flow [3]. Figure 4.4 shows the distribution of y^+ at walls for the coarsest mesh, M0.

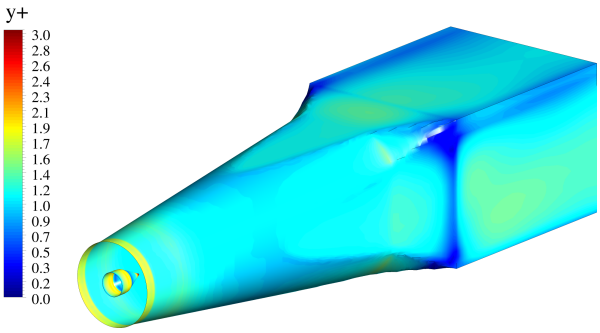

Figure 4.4: Distribution of y^+ on the coarsest reference RANS mesh, M0.

Comparisons of the mean axial and tangential velocity profiles inside the draft tube are shown in Figs. 4.5, 4.6. Results are again normalized by the average axial velocity at the inlet, $V_{b,in}$, and as a function of the normalized height, h/h_{max}. Overall, mean velocity results are very similar and almost independent of the spatial discretization level of mesh. Still, small differences can be seen between mesh M0 and the other three meshes, especially in the mean velocity profiles at stations R2, R3 and R4. For instance, the coarser mesh consistently underestimates V_z and V_u, and it is not sufficiently refined to correctly capture the mean tangential velocity peak at $h/h_{max} = 0.8$ at station R2. Moreover, looking at the turbulence kinetic energy profiles, shown in Fig. 4.7, M0 results are clearly overestimated in the three last stations compared to the other meshes. In terms of head losses, however, convergence is only attained after the second mesh refinement, i.e., with mesh M3, which predicted values are only 0.3% higher than those predicted

with M4, against 1.5% and 3.0% with meshes M1 and M3, respectively. For these reasons, the following draft tube simulations in this thesis using RANS and the k-ω SST turbulence model are performed with mesh M3.

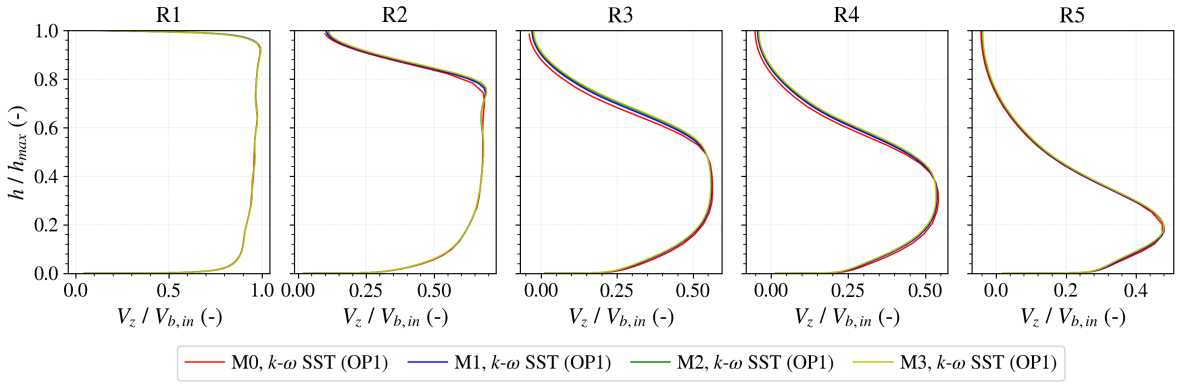

Figure 4.5: Normalized mean axial velocity profiles obtained with meshes M0 to M3 in RANS.

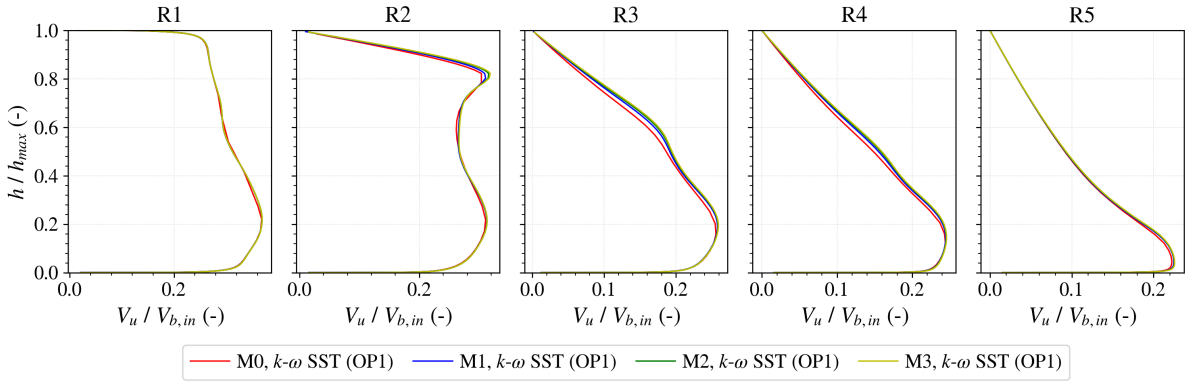

Figure 4.6: Normalized mean tangential velocity profiles obtained with meshes M0 to M3 in RANS.

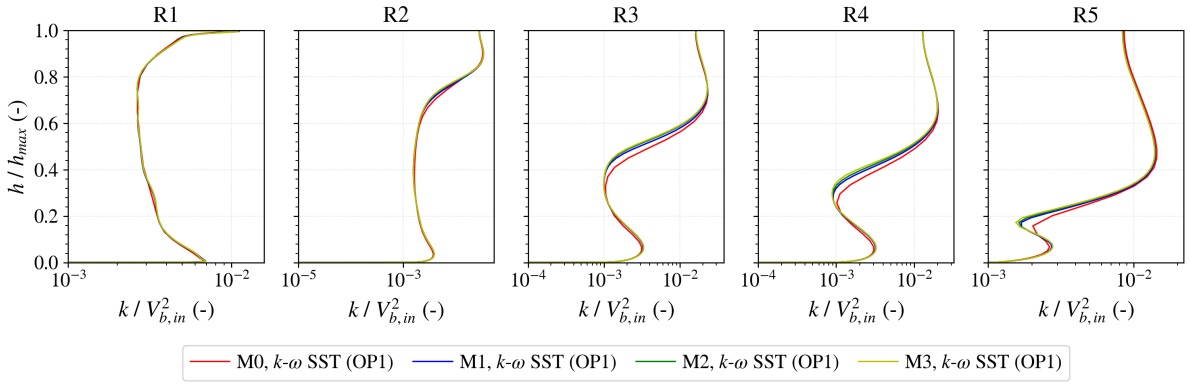

Figure 4.7: Normalized turbulence kinetic energy profiles obtained with meshes M0 to M3 in RANS.

4.3.2 LES

Previous DES and Zonal LES computations of the flow inside draft tubes followed the same classic procedure used in the previous RANS spatial discretization study and systematically refined the mesh until the convergence of the numerical results was attained [8, 73, 149]. However,

conversely to RANS, the spatial discretization of the numerical domain in LES affects not only the mean flow gradients but also which portions of the turbulent flow are going to be modelled by the sub-grid scale model and which portions are going to be explicitly resolved [86]. Moreover, as the computational cost is considerably higher in this method, a global approach for the mesh refinement is not ideal as it does not consider which portions of the flow are more important to be refined. Therefore, determining *what* is a good spatial discretization in LES is considerably more difficult than in RANS. Following the same procedure described in Wilhelm [160], the mesh convergence study in LES was divided into two parts: first, we shall consider the near-wall resolution of the draft tube and, then, the discretization of the internal flow.

Near-wall discretization

The first step in the spatial discretization study in LES consisted in analysing the effect of the near-wall mesh discretization on the results. Due to the prohibitively high computational cost associated with wall resolved LES, a few layers of prismatic elements was used to reduce the overall mesh size and to keep reasonable y^+ values at the walls. Conversely to Wilhelm [160], each prismatic element was later converted into six tetrahedrons due to a requirement of the Laplacian operator used for the projection step. One key element in the discretization of the near-wall mesh was the aspect ratio of the first element at the walls, i.e., the ratio between its length and height. While higher values of aspect ratio reduce the total number of elements for a given y^+, they also increase the skewness and therefore degrade the mesh quality and computation performance. Wilhelm [160] used an aspect ratio of 30 in the cone of the draft tube to obtain average $y^+ \approx 10$, but she did not have to convert the prismatic elements on the walls into tetrahedrons. In our case, such high aspect ratio values would result in extremely poor quality elements and potentially unstable numerical simulations. Thus, y^+ values were sacrificed in detriment of lower aspect ratios and better quality meshes in LES. Table 4.2 show the main characteristics of the three near wall mesh refinements used in our spatial discretization studies. Notice that for mesh M3, the aspect ratio had to be increased slightly, otherwise the total number of elements in the mesh would be prohibitively high. Furthermore, the high y^+ values justify the use of a wall-model, as explained in Section 4.2.2.

Table 4.2: Characteristics of the three meshes used for the *near-wall* spatial discretization study in LES.

Mesh	M1	M2	M3
Number of elem. ($\times 10^6$)	6.63	13.5	23.0
Number of nodes ($\times 10^6$)	1.22	2.45	4.11
1^{st} elem. Aspect Ratio	5	5	8
Maximum y^+	185	156	77
Average y^+	105	81	41

Mean axial and tangential velocity profiles obtained with the three meshes are shown in Figs. 4.8 and 4.9. The influence of the near-wall discretization on the mean velocity field is negligible since the obtained profiles are very similar in this region of the flow. Although small differences exist in the centre region of the flow, i.e., away from the walls, they can be due to the internal discretization of the numerical domain, which will be discussed next. Anyway, these conclusions are in accordance with Wilhelm [160], who performed LES of a similar draft tube configuration, using the same wall-model, but with high quality fully tetra meshes of up to 1.4 billion elements and y^+ between 10 and 750. Indeed, despite the significant y^+ values, the wall-model is still able to correctly capture main flow because the boundary layer is subjected to a quasi constant adverse pressure gradient inside the draft tube and flow swirl acts in the sense of stabilizing it, which renders it less controlled by the wall friction compared to the classical boundary layer over a flat plate. Given the considerably lower computational cost associated with the coarsest

mesh, M1, all following LES computations in this thesis use this near-wall spatial discretization.

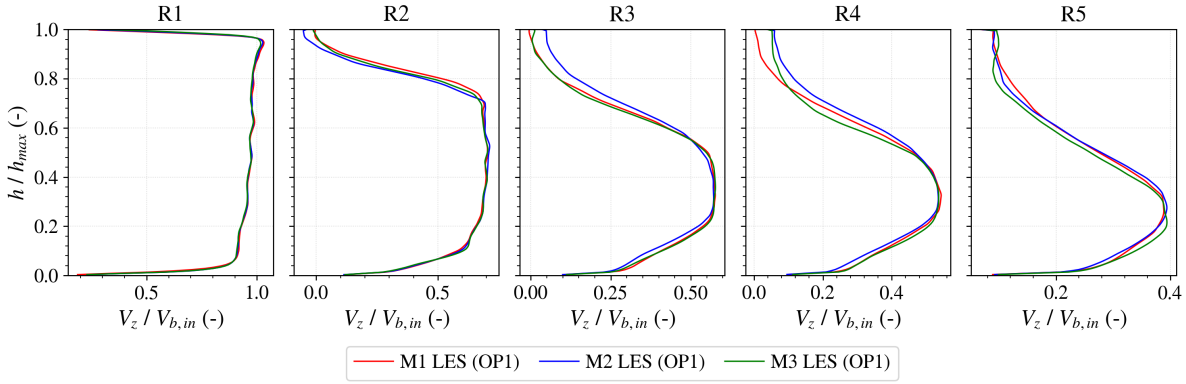

Figure 4.8: Normalized mean axial velocity profiles obtained with meshes M1 to M3 in LES.

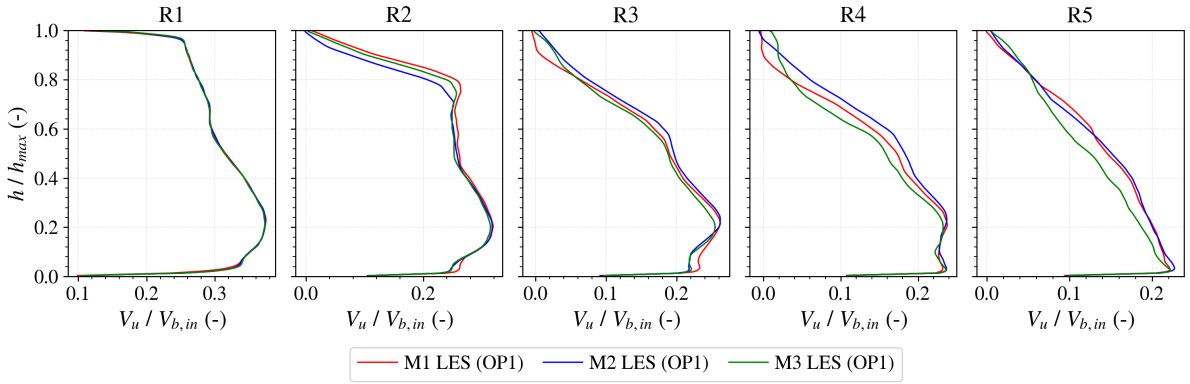

Figure 4.9: Normalized mean tangential velocity profiles obtained with meshes M1 to M3 in LES.

Interior discretization and automatic mesh adaptation strategy

For the interior mesh, an *automatic* mesh adaptation procedure proposed by Benard *et al.* [9] is used to efficiently discretize the domain. The goal of this procedure is twofold: first, to guarantee an accurate resolution of the mean flow field and, second, to ensure that enough turbulent scales motions are explicitly resolved. This automatic procedure is implemented in YALES2 and generates a mesh refinement ratio field (i.e., the ratio between the original and the refined mesh sizes), which is then used by MMG3D [32] to automatically refine the mesh based on two different criteria. The first criterion, Q_{C1}, is based on the minimization and homogenization of the discretization error of the mean velocity gradients in the solution, similar to what is done in RANS. The error associated with the interpolation $\mathbf{u}^*$ of velocity $\mathbf{u}$ on a mesh of size Δ is limited by a quantity Q_{C1} and can be estimated by Eq. (4.1):

$$Q_{C1} = \Delta^2 \max_{i=1,2,3} \left(\left| \frac{\partial^2 u_j^*}{\partial x_i^2} \right| \right) \tag{4.1}$$

Since most SGS models are based on the assumption that the smallest scales are far from the largest and most anisotropic scales of the flow, these small scales must be located in the inertial range, where a universal behaviour for the scales transfer is expected. The second criterion, Q_{C2}, ensures that enough turbulent scales are explicitly resolved to guarantee the validity of the LES approach inside the domain. For the case of a fully developed turbulence with a classic

Kolmogorov spectrum, it can be shown that enough scales are resolved if more than 80% of the total turbulent kinetic energy is explicitly resolved [126]. Thus, Q_{C2} is defined by Eq. (4.2), where E_{sgs} and E_R are, respectively, the SGS and resolved total turbulent kinetic energy.

$$Q_{C2} = \frac{E_{sgs}}{E_{sgs} + E_R} \leqslant 0.2 \tag{4.2}$$

The local mesh size, Δ, is directly found in the equation defining Q_{C1}, whereas it can be estimated from the term E_{sgs} in the equation defining Q_{C2} [1]. These two criteria are evaluated from the mean flow quantities in the LES solution, meaning that the flow must be statistically converged before any adaptation being applied. Once these two criteria are determined all over the numerical domain, a refinement ratio field is calculated and used to determine which portions of the mesh should be refined (or coarsened) and by what amount. MMG3D then uses this information to automatically generate a high quality tetra mesh which replaces the old *not adapted* mesh. Brugière [14] and Wilhelm [160] used this same procedure to perform LES of the flow inside a bulb turbine draft tube. However, while they controlled the adaptation process by informing a desired number of elements in the adapted mesh, our implementation is slightly different, and it is Q_{C1} which is defined in the beginning of the adaptation. The final number of elements in the adapted mesh is thus a consequence of this Q_{C1}.

MMG3D implementation's in YALES2 generates high quality (i.e., mostly isotropic) tetra meshes. Since Q_{C1} is greatly affected by the important velocity gradients near the walls, any prismatic layers of elements used to control y^+ values and to keep the simulation at a reasonable computational cost (even if converted into tetrahedrons, like the ones discussed in Section 4.3.2) are destroyed by the adaptation process. As a consequence, prohibitively large meshes are required otherwise y^+ are too high and even the application of a wall model can be compromised. For instance, in addition to a mesh containing a few layers of prismatic elements at the walls, Wilhelm [160] also investigated fully tetra meshes in LES, which have been notably adapted by the procedure described above. While the original mesh with prismatic layers had only 16 million elements and average $y^+ \approx 10$, the finest fully tetra mesh had 1.4 billion elements and an average y^+ of approximately 50. It is thus crucial for our simulations to preserve the prismatic layers of elements discussed in the previous section, at the risk of having an extremely high computational cost. A masking strategy schematically shown in Fig. 4.10 was therefore used in the context our LES. It allowed for just the part of the mesh away from the walls, i.e., outside the layers of prismatic elements, to be adapted during the adaptation process, whereas the region close to the walls remained untouched.

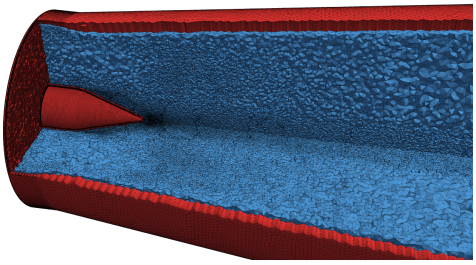

Figure 4.10: Detail of the masking applied to the automatic mesh adaptation. In red, the masked region unable to adapt; in blue, the region able to adapt.

With both masking and adaptation strategies in place, and starting with the *not*-adapted version of the mesh M1 discussed in the previous section, three more meshes were generated by changing the value of Q_{C1}. Table 4.3 resumes the main characteristics of the four meshes (one *not*-adapted and three adapted), while Fig. 4.11 show the details of the adaptation in the cone

[1] For more details, see Bernard *et al.* [9].

of the draft tube, just downstream the hub.

Table 4.3: Characteristics of the four meshes used for the *interior* spatial discretization study in LES.

Mesh	M1	M1A	M1B	M1C
Q_{C1}	-	20	10	5
Number of elem. ($\times 10^6$)	6.63	10.6	12.6	17.6
Number of nodes ($\times 10^6$)	1.22	2.02	2.39	3.34

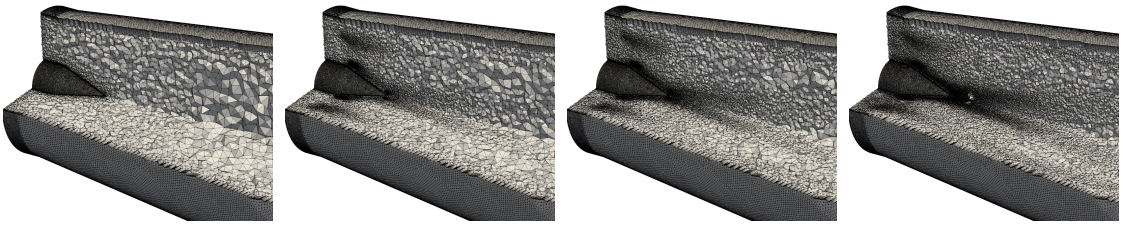

(a) **(b)** **(c)** **(d)**

Figure 4.11: Detail of the automatic mesh adaptation strategy near the hub of the draft tube. (a) M1 not adapted; (b) M1A; (c) M1B; (d) M1C.

As expected, most of the adaptation occurs in the regions of high velocity gradients and turbulence due to the two adaptation criteria. In the case of the draft tube flow, these regions are mainly located near the walls and behind the hub, where a large vortical structure (central vortex) is formed as a result of the interaction between the hub and the swirling flow entering the draft tube [108]. To illustrate the impact of the automatic mesh adaptation on these structures, Fig. 4.12 show the iso-surfaces of Q-criterion [86] inside the draft tube coloured by the vorticity in the z-axis direction. While all four meshes are able to capture the large central vortex inside the draft tube, smaller structures are observed around this vortex and close to the hub as the mesh is refined and the flow resolution improved. These small structures interact with the large vortical structure at the centre of the flow to the point where, in the most refined case, mesh M1C, its helical shape is no longer easily identifiable downstream.

Of course, refining the mesh has an important impact on the final computational cost in LES, which not necessarily translates into better results. Looking at the mean velocity field inside the draft tube, Figs. 4.13 and 4.14 shown the mean axial and tangential velocity profiles obtained with these three adapted meshes compared to the original *not*-adapted mesh M1. In spite of the differences in terms of turbulent structures captured in each case, the impact of the automatic mesh adaptation procedure on the mean flow is limited, especially in the case of axial velocity. Still, V_z values predicted by the coarse *not*-adapted mesh in the centre of the flow at station R5 are quite overestimated in comparison with to the other adapted meshes. In the case of V_u, the original mesh M1 underestimated the values near the centre of the flow ($h/h_{max} = 1.0$) at station R1. This result is amplified and the peak value of V_u at station R2 and $h/h_{max} = 0.8$ is clearly underestimated by the *not*-adapted mesh. This is expected and is a consequence of the poor central vortex prediction in this case shown in Fig. 4.12. The adapted meshes are clearly better in predicting this peak value, but at station R3, the coarsest of them, mesh M1A, underestimated V_u between $0.6 \leq h/h_{max} \leq 0.8$ in comparison with M1B and M1C. Indeed, it does not seem necessary to use a refinement level equivalent to M1C since the results with M1B are sufficiently close at a considerably lower computational cost. For this reason, the following LES computations in this thesis are run using a near-wall mesh refinement equivalent to M1, but an interior mesh discretization level equal to M1B. It should be emphasized, however, that the different operating conditions will lead to different interior mesh refinement, as the adaptation process is strongly dependent on the flow characteristics.

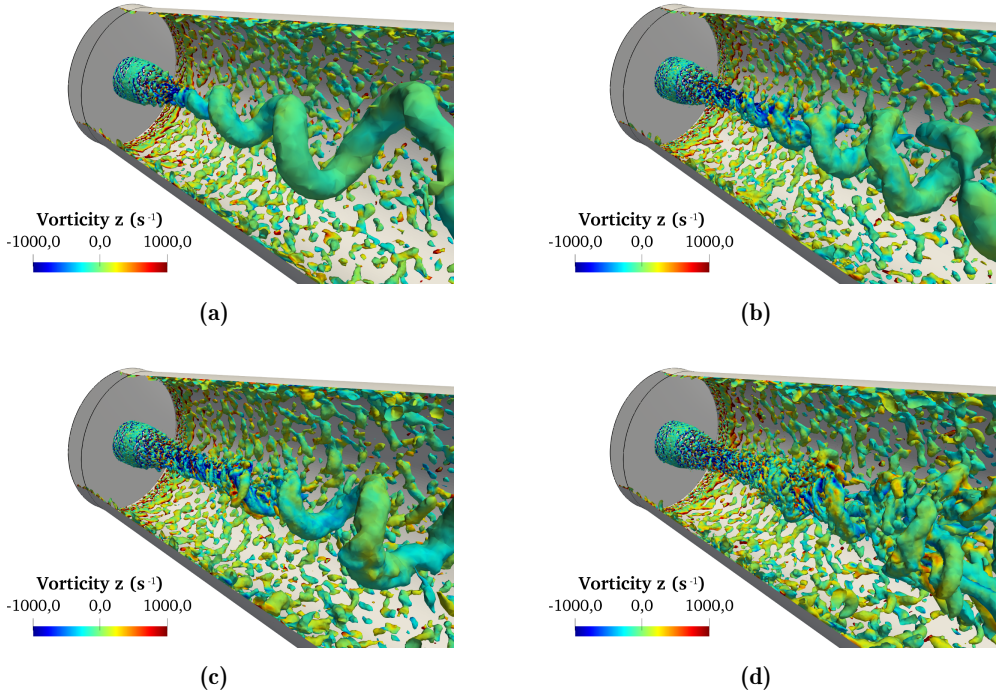

Figure 4.12: Turbulent structures inside the draft tube visualized by iso-surfaces of Q-criterion and coloured by their vorticity z. (a) M1 not adapted; (b) M1A; (c) M1B; (d) M1C.

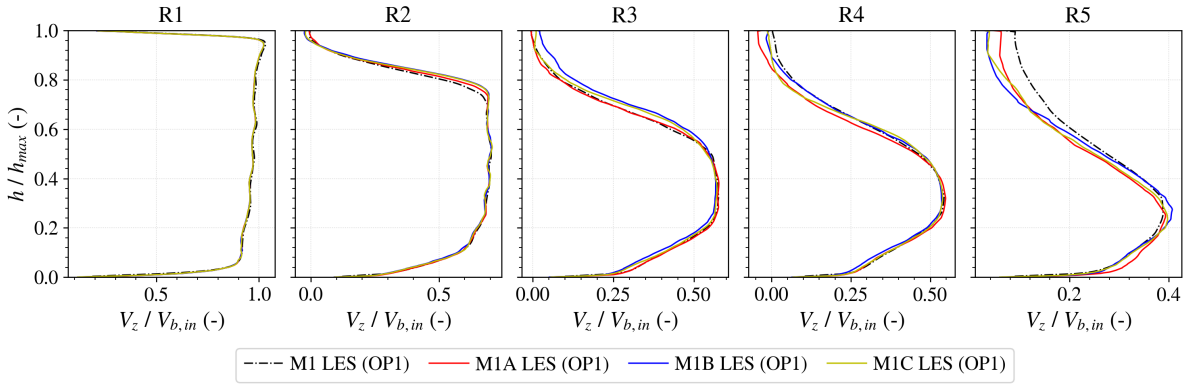

Figure 4.13: Normalized mean axial velocity profiles obtained with meshes M1A to M1C in LES.

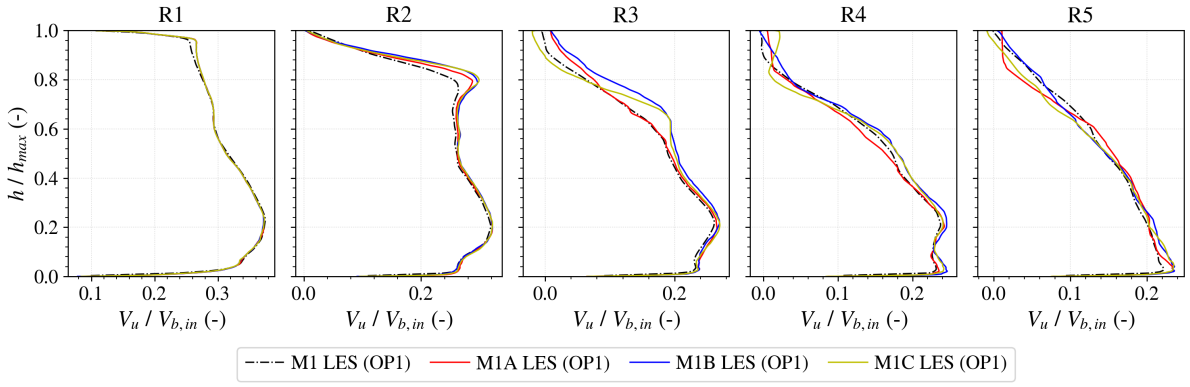

Figure 4.14: Normalized mean tangential velocity profiles obtained with meshes M1A to M1C in LES.

4.4 Comparison with experimental data at OP1

4.4.1 Velocity and turbulence profiles

Figure 4.15 show the comparison of normalized mean axial velocity profiles at the five measurement stations inside the numerical domain. At station R1, both reference RANS simulations and LES predict very similar results, though V_z values are mostly overestimated compared to the experiments between $0.1 \leq h/h_{max} \leq 0.8$. Towards the centre of the flow ($h/h_{max} = 1.0$), a rapid increase in the mean axial velocity values is observed in the experiments, which is by the LES solution, though the peak values of V_z are still underestimated. Conversely, the RANS simulation using the k-ω SST turbulence model does not predict this rapid increase, which is compensated by slightly overestimated mean axial velocity values near $h/h_{max} \approx 0.0$. At stations R2 and R3, the very low V_z values in the centre of the flow and associated with the large central vortex shown in Fig. 4.12 are very well captured in LES, whereas in RANS they are overestimated at R2 and underestimated at R3. Indeed, at station, RANS simulation using the k-ω SST turbulence model underestimates the mean axial velocity in this region of the flow and predict the start of a recirculation region (due to negative values of V_z), which extends until the last measurement station, R5. This same superiority of LES in capturing the central vortex behaviour was observed previously in Brugière [14] and Wilhelm [160] and is one of the reasons simple steady and unsteady RANS simulations using two-equation linear eddy viscosity models are unsuitable for the type of flow found inside a draft tube [134, 56]. Starting at station R2, LES results consistently underestimates V_z near the external walls, i.e., close to $h/h_{max} = 0.0$, indicating a faster thickening of the boundary layer compared to the experiments. In RANS, this behaviour is not as pronounced as in LES, possibly due to the overestimation in this region of the flow at station R1, but V_z are still underpredicted compared to the experiments. As a consequence of the underestimated flow rate close to the walls, both numerical results overestimate the mean axial velocity values in the intermediate region of the flow. This is actually seen since station S1, but as the central vortex grows wider, the difference between numerical and experimental V_z values increase. For instance, at station R3, experimental measurements show a small axial velocity peak near the walls and another one close to $h/H = 0.6$. Conversely, numerical profiles show no mean axial velocity peak but rather a constant and overestimated V_z value between $0.3 \leq h/H \leq 0.5$.

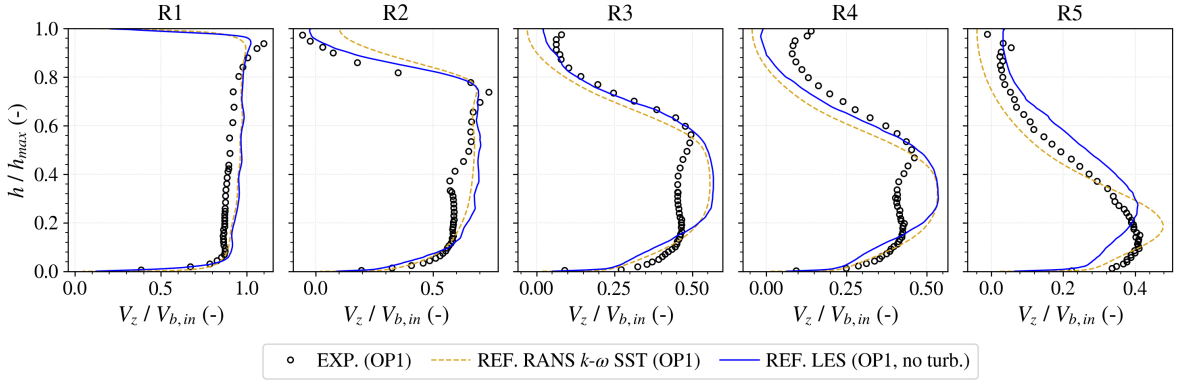

Figure 4.15: Normalized mean axial velocity profiles for the reference simulations of the draft tube at OP1 using RANS and LES.

The results for normalized mean tangential velocity profiles are shown in Fig. 4.16. Like in the previous profiles, both turbulence methods yielded very similar results at station R1 and agree quite well with the experimental data, except for the small variation at $0.8 \leq h/h_{max} \leq 0.9$ which is not captured numerically, and the tangential velocity near the external walls ($h/h_{max} = 0.0$), which is very underestimated in both RANS and LES. At station R2, however, numerical

results are mostly overestimated compared to the experiments, especially towards the centre of the flow. At $h/h_{max} = 0.8$, both reference simulations predict a peak in the profile of V_u, which is not seen experimentally. Indeed, experimental measurements even predict negative mean tangential velocity values at $h/h_{max} \geq 0.9$. While this indicate the presence of counter-rotating vortex rope and is normally associated with turbines operating at high-load configurations [72], it is possible that the corrections applied to the experimental data in OP1 (see Section 3.2.3) be the real cause for this behaviour and the reason it is not captured by the numerical simulations. By station R3, the mean tangential velocity peak is completely dissipated in RANS, whereas it is still observed in LES at $h/h_{max} = 0.7$. Numerical results are also closer to the experimental values, though the predicted V_u near the walls is very underestimated. This near-wall behaviour is improved at station R4, but a small peak is predicted in LES, which is not observed in the experiments neither in RANS. Finally, at station R5, V_u varies almost linearly from the walls and towards the centre of the flow, however, LES results are overestimated compared to RANS and experimental measurements.

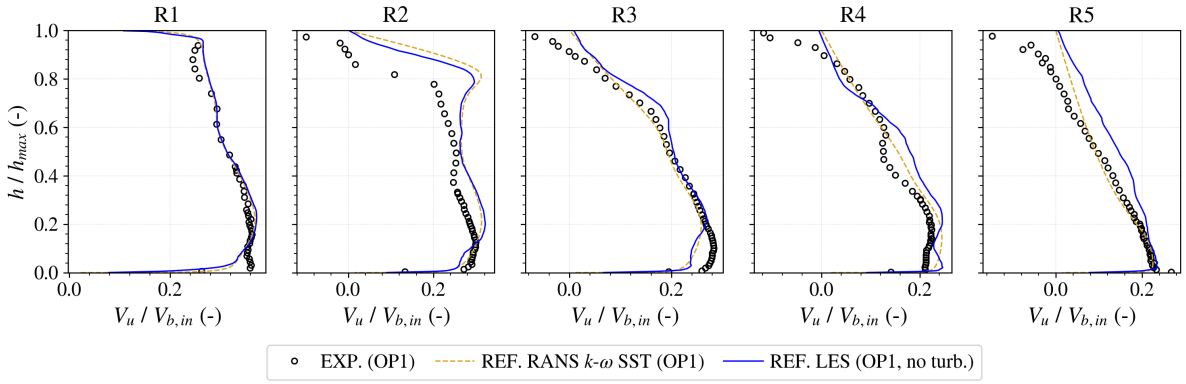

Figure 4.16: Normalized mean tangential velocity profiles for the reference simulations of the draft tube at OP1 using RANS and LES.

Turbulence kinetic energy profiles are shown in Fig. 4.17. The results are normalized by the square of the average axial velocity at the inlet of the domain, $V_{b,in}$. Experimental measurements are limited to the near wall region because they were taken in only one of the two campaigns that produced the results for OP1. RANS results using the k-ω SST turbulence model predict quite well the turbulence kinetic energy level at the between stations R1 and R3, but ultimately underestimate its values at the last two stations, R4 and R5. Conversely, LES results are mostly underestimated at stations R1 and R2, which is expected since no turbulent inlet conditions are being imposed at the domain. However, as flow instabilities naturally develop along the draft tube, the turbulence kinetic energy results obtained between stations R3 and R5 are at the same level of the experiments.

4.4.2 Static pressure profiles and distribution along the walls

Figure 4.18 show the results for the static pressure, P_s, profiles inside the draft tube. The static pressure measured middle height ($h/h_{max} = 0.5$) at station R0, $P_{s,\text{mid,R0}}$, is used as reference for the measurements. Furthermore, the results are also normalized by the dynamic pressure evaluated from the average axial inlet velocity, i.e., $q_{in} = 0.5\rho V_{b,in}^2$. Overall, numerical results are very similar at station R1 and seems at the good level compared to the experiments. However, the static pressure peak near $h/h_{max} = 0.0$ is captured neither in RANS nor LES, and the same goes for the depression towards $h/h_{max} = 1.0$. At station R2, LES results are slightly underestimated between $0.0 \leq h/h_{max} \leq 0.7$ compared to RANS and experiments. As a consequence of the central vortex prediction, RANS consistently predicted the lowest static pressure values right at the centre of the flow ($h/H = 1.0$). Conversely, the position of this

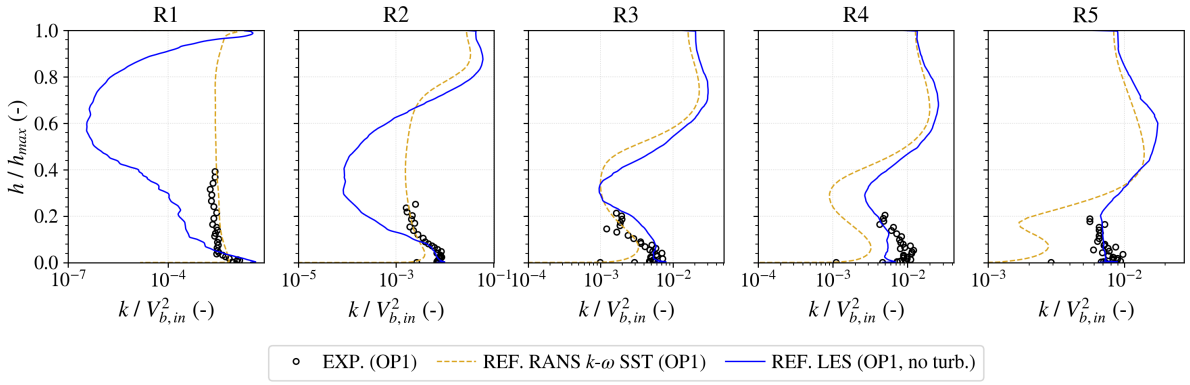

Figure 4.17: Normalized turbulence kinetic energy profiles for the reference simulations of the draft tube at OP1 using RANS and LES.

depression varies in LES depending on the station, going from $h/H \approx 0.9$ at R2 to $h/H \approx 0.6$ at R4. This behaviour is very similar to what has been measured during the experiences and are a result of the divergent shape of central vortex rope (see Fig. 4.12). Nevertheless, the magnitude of this depression is still underestimated numerically. Between stations R3 and R5, both numerical results seem shifted with respect to the experiments, although LES follows the experimental distribution of P_s compared to RANS.

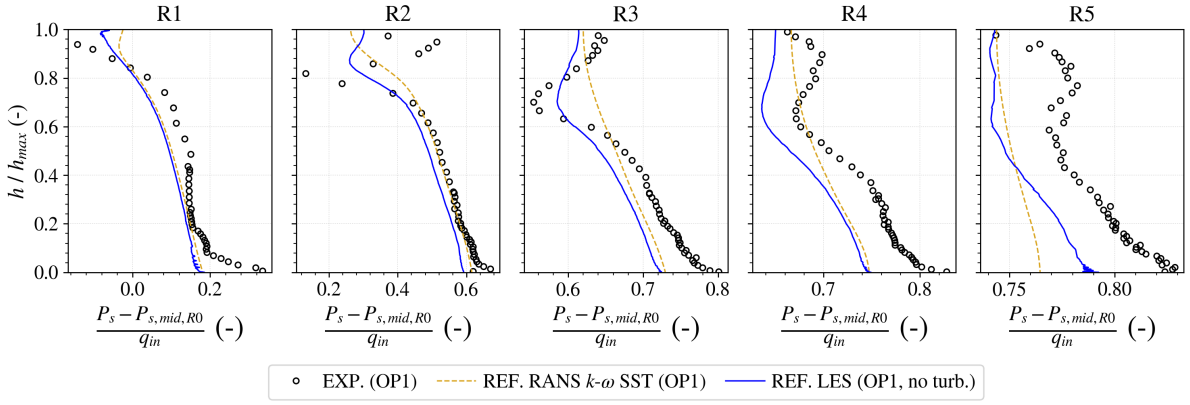

Figure 4.18: Normalized static pressure profiles for the reference simulations of the draft tube at OP1 using RANS and LES.

The static pressure evolution along the walls of the draft tube and measured at stations S1, S2 and S3 are shown in Fig. 4.19. The static pressure at the first measurement point, located at the same axial position of station R1, $P_{s,\text{wall,R1}}$, is used as a reference, and the results are again normalized by the dynamic pressure q_{in}. From the results, it is clear that most of the static pressure recovery takes place in the cone of the draft tube, i.e., between $0.0 \leq z/L \leq 0.4$. Both reference simulations capture very well this behaviour, and the smaller pressure recovery downstream the cone, although LES results are overestimated at station S2. It should be to noticed how the geometry of the final portion of the draft tube modifies the static pressure evolution along the walls, especially at stations S2 and S3. For instance, $P_{s,\text{wall}}$ follows almost a straight line between $z/L = 0.4$ and 1.0 in the case of station S1, whereas a small valley is observed at $z/L = 0.8$ in station S2 and a peak at $z/L \approx 1.0$ in station S3. Both RANS and LES captured these small variations downstream the draft tube.

Finally, the static pressure distribution measured circumferentially at stations C1 to C5 and EX (see Fig. 3.1) on the draft tube are compared. Initially, the static pressure measured middle height at station R0, $P_{s,\text{mid,R0}}$, is used as reference, however, as shown in Fig. 4.20, the

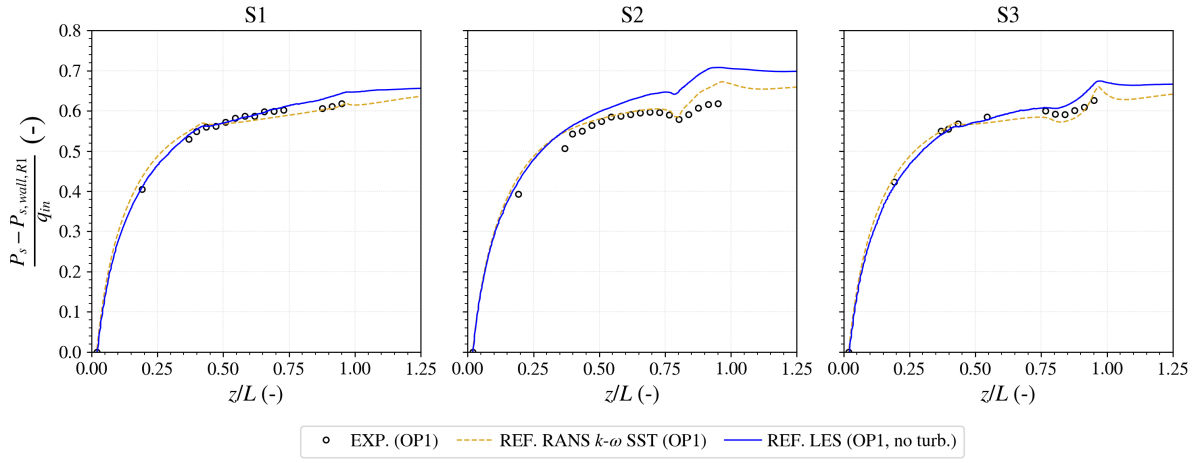

Figure 4.19: Normalized streamwise static pressure evolution at the walls for the reference simulations of the draft tube at OP1 using RANS and LES.

experimental and numerical results are systematically shifted with respect to each other. This is possibly due to the fact that different probes have been used to measure the values of P_s on the walls and $P_{s,\mathrm{mid,R0}}$ during the experiments, respectively a wall-mounted pressure tap and a five-hole pressure probe. A different reference pressure taken with the same type of probe is thus chosen, notably the average static pressure on the walls measured at station C1, $\overline{P_{s,\mathrm{C1}}}$. Figure 4.21 shows the results obtained with this new reference pressure. While numerical results are slightly overestimated between the circumferential stations C2 and C4, reference RANS result agree quite well with the experimental at station C5, whereas LES overestimate P_s values. Conversely, at station EX, LES results yield a very good match with the experimental while RANS underestimate the static pressure at the walls.

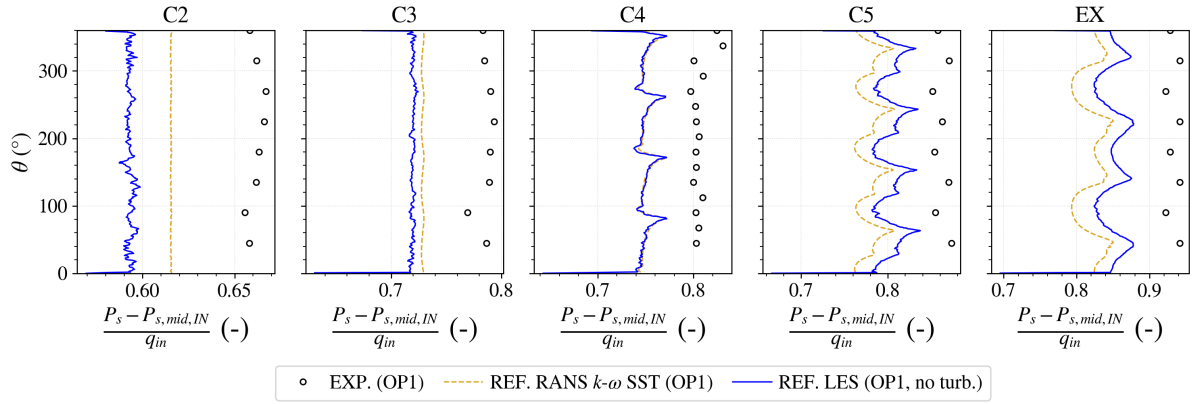

Figure 4.20: Normalized circumferential static pressure distribution at the walls for the reference simulations of the draft tube at OP1 using RANS and LES. Reference as the static pressure measured middle height at station R0, $P_{s,\mathrm{mid,R0}}$.

4.4.3 Head losses analysis

The importance of well predicting the static pressure evolution at the walls of the draft tube, especially at the circumferential stations, is to evaluate the head losses inside the draft tube according to the IEC standard [145], as explained in Section 3.2.2. Normally, these losses are measured between the inlet and exit of the draft tube, stations R0 and EX, respectively. By decomposing the total head losses, ΔH_{tot}, into their static, ΔH_{sta}, and a dynamic, ΔH_{dyn},

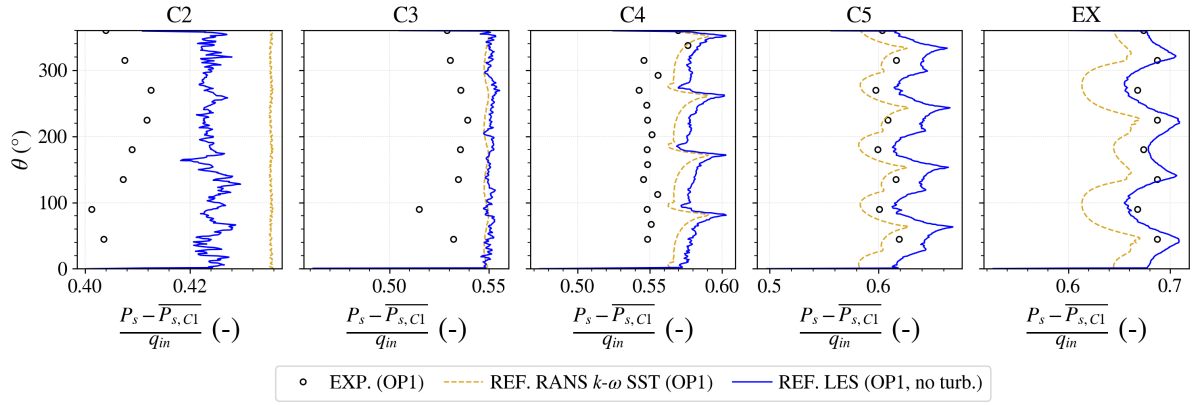

Figure 4.21: Normalized circumferential static pressure distribution at the walls for the reference simulations of the draft tube at OP1 using RANS and LES. Reference as the average static pressure on the walls measured at station C1, $\overline{P_{s,\mathrm{C1}}}$.

heads, we have Eq. (3.3):

$$\Delta H_{tot} = \Delta H_{sta} + \Delta H_{dyn} \tag{4.3}$$

where, ΔH_{sta} is the difference between the mass flow averaged static pressure at the plane R0 and the average static pressure at walls at EX, i.e.,

$$\Delta H_{sta} = \frac{1}{Q} \iint_{S_{R0}} \frac{\langle P_s \rangle}{\rho g} \langle u_z \rangle dS - \frac{1}{\rho g} \langle \overline{P_{s,\mathrm{EX}}} \rangle \tag{4.4}$$

and ΔH_{dyn} is the difference between the mass flow averaged dynamic pressure at plane R0 and the dynamic pressure calculated using the average axial velocity at the plane EX, i.e.,

$$\Delta H_{dyn} = \frac{1}{Q} \iint_{S_{R0}} \left(\frac{1}{2g} \langle u_i \rangle \langle u_i \rangle \right) \langle u_z \rangle dS - \frac{1}{\rho g} \left(\frac{1}{2} \rho \left(\frac{Q}{A_{EX}} \right)^2 \right) \tag{4.5}$$

Experimental and numerical results are shown in Fig. 4.22. Since ΔH_{dyn} values are independent of the case due to the axisymmetric mean velocity profiles imposed as inlet conditions, differences in total head losses come exclusively from static head, which is negative due to the increase in static pressure caused by the divergent shape of the draft tube [61, 99]. Although the two turbulence methods yield similar results for ΔH_{sta}, experimental static head variation is significantly lower and therefore the numerical ΔH_{tot} values are greatly overestimated.

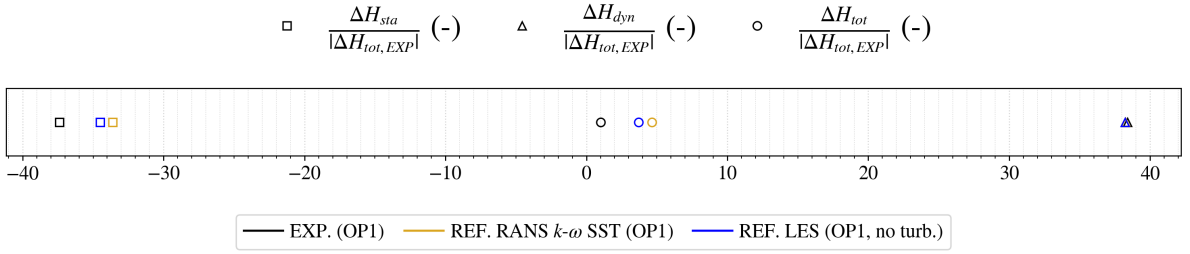

Figure 4.22: IEC losses between stations R0 and EX for the reference simulations of the draft tube at OP1 using RANS and LES.

This difference can be explained, however, by the static pressure shift between the five-hole pressure probes and wall-mounted pressure taps, as discussed in Figs. 4.20 and 4.21. For instance, while the former are used to evaluate the first element on the r.h.s. of Eq. (4.4), the latter is used to evaluate the second element on the r.h.s. on this same equation. Thus, as the experimental measurements coming from these probes are systematically shifted, ΔH_{sta} is definitely impacted. To mitigate this issue, only the static pressure measurements coming from the wall-mounted pressure taps are used to evaluate the static pressure evolution along the walls using, keeping the consistency on the utilized data. Indeed, this is the same approach used to create the graphs in Fig. 4.21, where $\overline{P_{s,\mathrm{C1}}}$ was used as reference static pressure for the rest of the draft tube. As a result of this modification, the first element on the r.h.s. in Eq. (4.4) is given by:

$$\Delta H_{sta} = \frac{1}{\rho g}\langle\overline{P_{s,\mathrm{C1}}}\rangle - \frac{1}{\rho g}\langle\overline{P_{s,\mathrm{EX}}}\rangle \tag{4.6}$$

Accordingly, the first element on the r.h.s. in Eq. (4.5) is also measured at station R1 (same axial position of C1), instead of R0, i.e.,

$$\Delta H_{dyn} = \frac{1}{Q}\iint_{S_{R1}}\left(\frac{1}{2g}\langle u_i\rangle\langle u_i\rangle\right)\langle u_z\rangle dS - \frac{1}{\rho g}\left(\frac{1}{2}\rho\left(\frac{Q}{A_{EX}}\right)^2\right) \tag{4.7}$$

The results with these modified equations are shown in Fig. 4.23. Small differences in the velocity profiles at station R1 have an impact on the mass flow averaged dynamic pressure at this location and therefore ΔH_{dyn} depends on the case. However, conversely to the previous analysis, the numerical prediction of static head variation is much closer to the experimental measurements, especially in the case of LES. These results are in accordance with the static pressure results previously discussed and, as a consequence, total head losses, ΔH_{tot}, is very well predicted in LES, only 6% overestimated with respect to the experiments, whereas RANS the results are 25% overestimated.

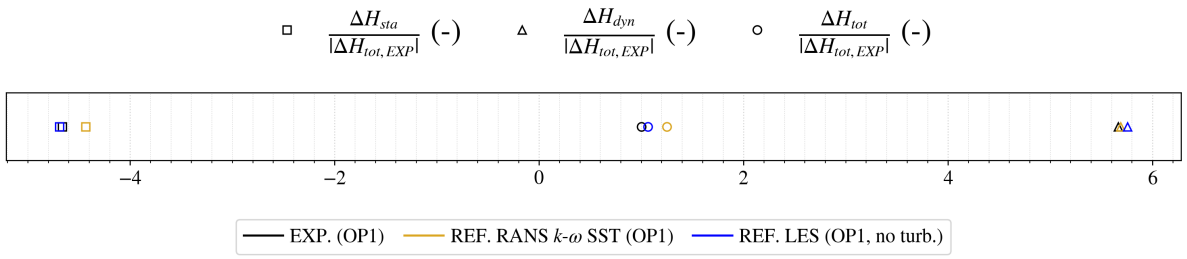

Figure 4.23: IEC losses between stations R1 and EX for the reference simulations of the draft tube at OP1 using RANS and LES.

4.5 Influence of turbulent boundary conditions in LES

Despite the very encouraging head losses results obtained for the first operating point, OP1, these values are based on integral quantities of the flow and do not properly reflect how these head losses are occurring on the flow. Indeed, as well demonstrated in Wilhelm *et al.* [159], the *real* head losses inside the draft tube are very dependent on internal distribution of both velocity and static pressure fields. In this regard, the reference numerical simulations of the draft tube at OP1 did not yield a very good match with the experimental data, especially in the case of mean velocity profiles. For instance, the numerical results underestimated the mean

axial velocity near the walls leading to overestimated V_z in the intermediate region of the flow. Moreover, both reference RANS and LES solutions failed to predict the two mean axial velocity peaks at stations R3 and R4 and consistently underestimated the static pressure, P_s, inside the draft tube. In their computations of the flow inside a bulb turbine draft tube, Brugière [14] and Wilhelm [160] also observed some discrepancies between numerical and experimental mean velocity profiles close to the walls, in particular. Brugière [14] then analysed the uncertainty of the inlet velocity profiles near the walls in RANS, but found that this was not sufficient to explain the differences on the flow behaviour downstream. Wilhelm [160], on the other hand, investigated the wall-roughness in LES and was able to partially improve the results. However, in both cases, the mean velocity near the draft tube walls was *overestimated* compared to the experiments, which is exactly the opposite of is observed in Figs. 4.15 and 4.16. Thus, increasing the wall-roughness, like in Wilhelm [160], would just worsen the numerical results.

Another aspect of the inlet boundary conditions, particularly in LES, which has not been investigated by Brugière [14] and Wilhelm [160], though, was the turbulence entering the domain. For instance, as explained in Section 4.2.2, the standard approach used in both works was to let the instabilities naturally develop within the draft tube, instead of imposing some sort of fluctuating field at the inlet of the domain. Nevertheless, the results in Fig. 4.17 clearly show that the turbulence kinetic energy predicted in the reference LES is quite underestimated in the beginning of the draft tube. Moreover, the fast thickening of the boundary layer in the mean axial velocity profiles shown in Fig. 4.15 indicate a lack of turbulence upstream the flow. The problem of imposing turbulent inlet conditions is to generate and impose a proper fluctuating field, as discussed in Section 2.4. Due to the very limited information about the turbulent flow at the inlet of the numerical domain (station R0), which goes down to the profile of k, essentially, a simple homogeneous isotropic synthetic turbulent field is generated in imposed in our LES of the draft tube discussed above. The method to generate and inject this field in YALES2 is explained in Section 2.4 and shown in Fig. 2.7, and depends on four inputs from the user: a normalized turbulent kinetic energy distribution, an injection speed at the inlet of the domain, a velocity scale, u', and a length scale, l_e. While the normalized profile of k is obtained directly from the experimental data, as shown in Figs. 4.2 and the injection speed is assumed to be equal to the average axial velocity at the inlet, $V_{b,in}$, determining the correct characteristic velocity, u', and length, l_e, scales is far more complicated and several combinations are tested to investigate their impact on the downstream flow behaviour. For instance, u' varies between 0.1, 0.6 and 1.2 of $V_{b,in}$, whereas l_e is either 0.2 or 0.4 of the inlet channel height, $h_{max,R0}$.

4.5.1 Velocity and turbulence profiles

The turbulence kinetic energy profiles inside the draft tube predicted in LES with/without the synthetic turbulence injection is shown in Fig. 4.24. Compared to the previous reference simulations, the cases with $u' = 0.1V_{b,in}$ still underestimate k at station R1, but are much closer to the experimental measurements between $0.1 \leq h/h_{max} \leq 0.4$. Conversely, stronger synthetic fluctuations overestimate k values at station R1 but are closer to the correct level at station R2, which can be explained by the quick dissipation of the synthetic fluctuations close to their injection plane. Indeed, a very good agreement is found between the LES case with $u' = 0.6V_{b,in}$ and $l_e = 0.2h_{max,R0}$ and the experimental data at this station. Further downstream, at station R3, all numerical results predict similar levels of turbulence close to the walls, including the reference case without synthetic turbulence injection. Interestingly, at station R4 and especially R5, the most turbulent cases, with $u' = 0.6V_{b,in}$ and $u' = 1.2V_{b,in}$, underestimate k near the walls, which can be explained by the different mean velocity gradients in this region of the flow.

The effect of the synthetic turbulence injection on the mean axial velocity profiles is shown in Fig. 4.25. Overall, the weakest injected fluctuations, i.e., $u' = 0.1V_{b,in}$, has no effect on the distribution of V_z inside the draft tube, in spite of the slightly modified turbulence kinetic energy profiles shown in Fig. 4.24. Conversely, in the case with $u' = 0.6V_{b,in}$ and $1.2V_{b,in}$, the

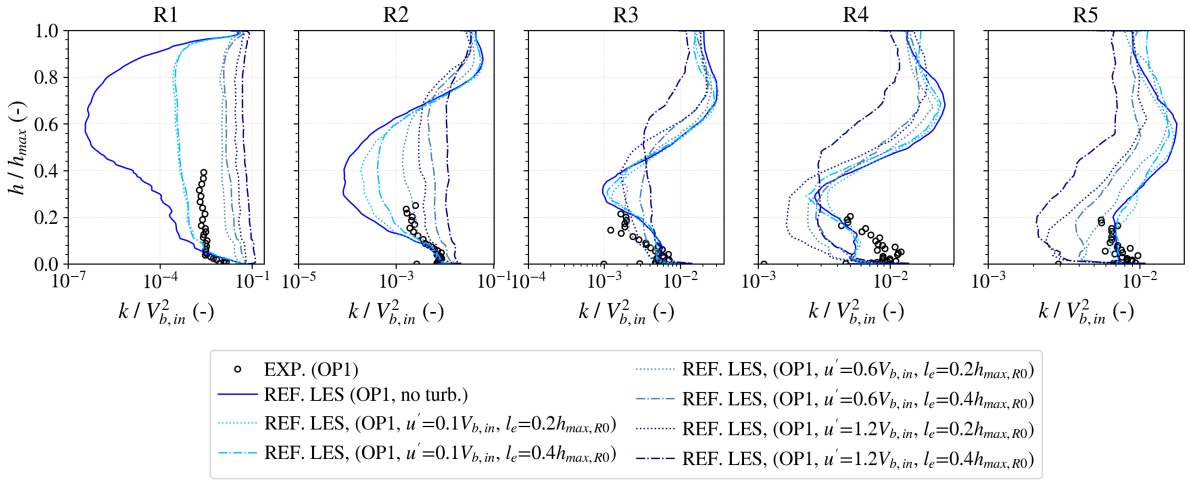

Figure 4.24: Normalized turbulence kinetic energy profiles for the reference simulations of the draft tube at OP1 using LES with/without synthetic fluctuations.

boundary layer prediction is improved as the mean axial velocity values are increased in this region of the flow ($h/h_{max} = 0.0$). As a consequence of the increased flow rate near the walls, V_z is reduced in the intermediate region of the flow between stations R2 and R4, which brings the results closer to the experimental measurements. Finally, increasing the characteristic length scale, l_e, improves the results at station R5, but increases the dissipation of the central vortex, which compromises the numerical prediction between stations R2 and R4.

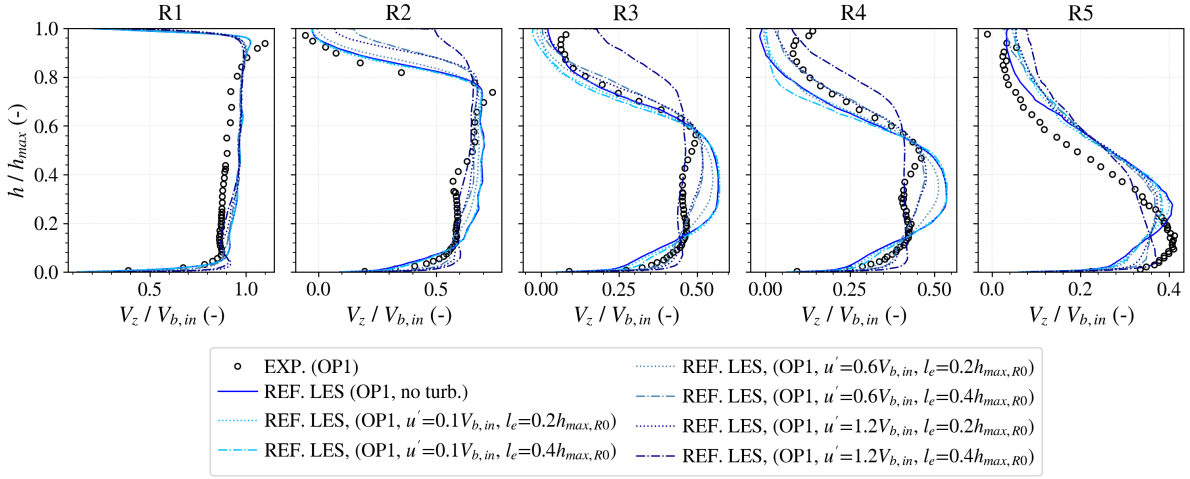

Figure 4.25: Normalized mean axial velocity profiles for the reference simulations of the draft tube at OP1 using LES with/without synthetic fluctuations.

4.5.2 Static pressure profiles and distribution along the walls

In addition to the velocity field, injecting synthetic fluctuations in LES also impacted the static pressure distribution inside the draft tube. This can be seen on Fig. 4.26, which shows the normalized static pressure profiles. At station R1, the cases with $u' = 1.2V_{b,in}$ are slightly shifted with respect to the LES cases, and the static pressure peak near $h/h_{max} = 0.0$ is captured by the case with $l_e = 0.4h_{max,R0}$. Between stations R2 and R5, however, P_s is overestimated by the cases with $u' = 1.2V_{b,in}$. Conversely, with $u' = 0.6V_{b,in}$, the numerical results agree very well with the experimental data, although a larger l_e dissipates too much the central vortex and

the position of the low pressure region is not well predicted. Finally, similarly to the previous results, weak synthetic fluctuations, i.e., $u' = 0.1V_{b,in}$ does not affect the results compared to the reference case without turbulence injection.

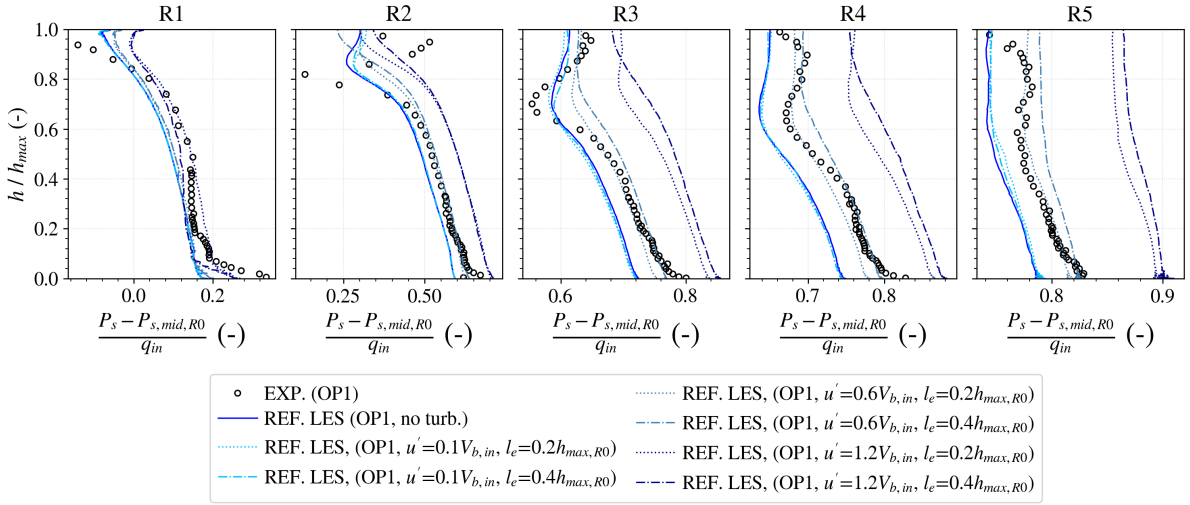

Figure 4.26: Normalized static pressure profiles for the reference simulations of the draft tube at OP1 using LES with/without synthetic fluctuations.

Comparing the streamwise evolution of normalized static pressure at the walls in LES, shown in Fig. 4.27, it is clear that injecting synthetic fluctuations increases P_s on the walls and overestimates its values compared to the experiments. The variation is small, though, and this behaviour is more pronounced between $0.2 \leq z/L \leq 0.75$, especially at station S1. Pressure recovery in this region of the flow is therefore modified by the synthetic fluctuations, but close to the exit of the draft tube, $z/L = 1.0$, results are almost independent of the turbulence level, indicating that the overall performance of the draft tube is not so affected. Similarly, as shown in Fig. 4.28, the circumferential static pressure distribution is also shifted by the injection of synthetic fluctuations in LES. Like in the previous streamwise results, P_s increase as the injected turbulence gets stronger, especially between stations C2 and C5. At the station close to the exit of the draft tube, EX, differences between the cases with/without synthetic turbulence injection are small, and the results agree very well with the experimental data.

4.5.3 Head losses analysis

Figure 4.29 compares the IEC losses inside the draft tube using the modified Eqs. (4.6) and (4.7). The cases with synthetic turbulence injection are grouped by the length scale to facilitate the analysis. Starting with the smallest l_e, equal to $0.2h_{max,R0}$, the impact of the injected synthetic fluctuations is small, although ΔH_{tot} values are still improved as u' increases. For instance, the 6% difference between experimental and numerical total head losses obtained with the reference LES without turbulence injection, is down to 1.8% in the case with $u' = 0.6V_{b,in}$ and 0.6% in the case with $u' = 1.2V_{b,in}$. This improvement is due to a better prediction of the variation in dynamic head, which is ultimately controlled by the mean velocity profiles at station R1. Interestingly, looking at the results for V_z at this location (see Fig. 4.25), injecting moderate and strong synthetic fluctuations dissipates the peak near $h/h_{max} = 0.9$ and overestimates the mean axial velocity near $h/h_{max} = 0.0$. In the cases with $l_e = 0.4h_{max,R0}$, however, the impact of u' is more pronounced and ΔH_{tot} is underestimated in the cases with $u' = 0.6V_{b,in}$ and $1.2V_{b,in}$. This is a consequence of important variations of ΔH_{sta} and ΔH_{dyn} in these cases.

The problem with the IEC losses is that they do not take into account the distribution of velocity and static pressure profiles in the exit of the draft tube, and therefore they can differ

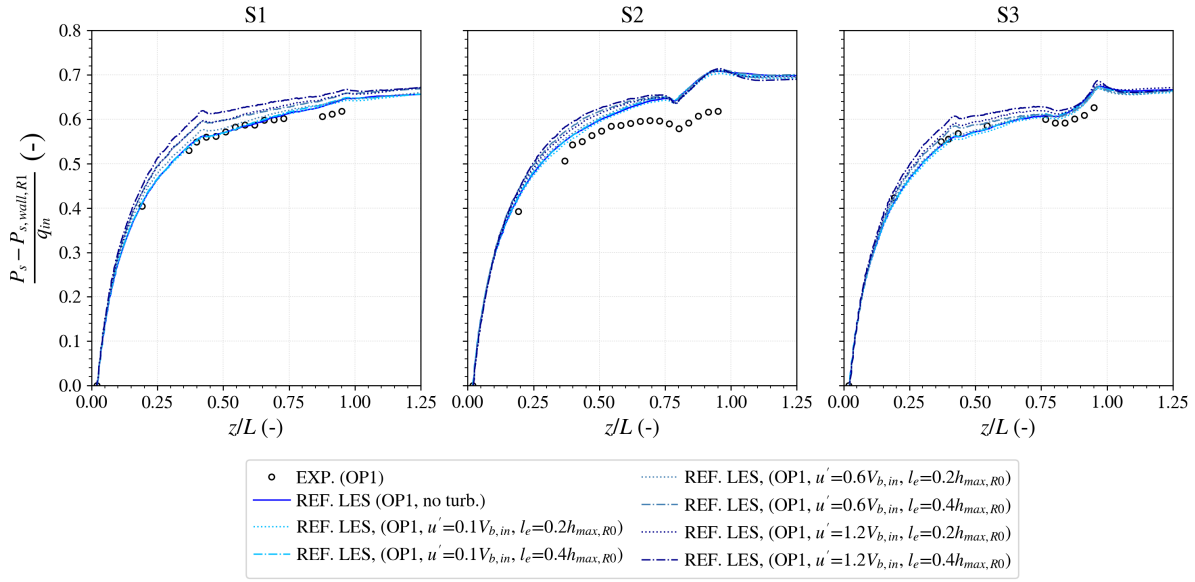

Figure 4.27: Normalized streamwise static pressure evolution at the walls for the reference simulations of the draft tube at OP1 using LES with/without synthetic fluctuations.

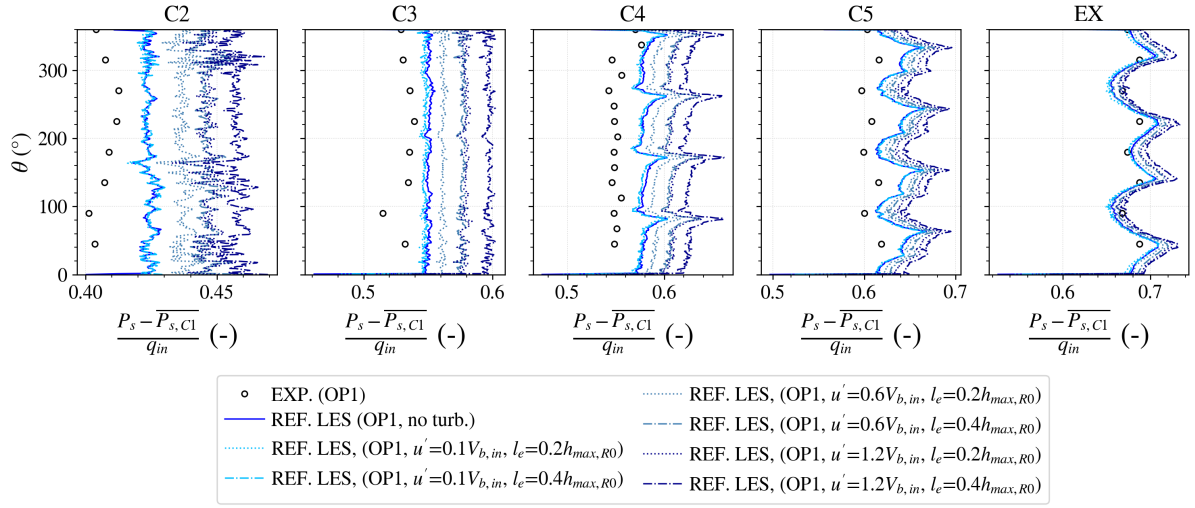

Figure 4.28: Normalized circumferential static pressure distribution at the walls for the reference simulations of the draft tube at OP1 using LES with/without synthetic fluctuations. Reference as the average static pressure on the walls measured at station C1, $\overline{P_{s,C1}}$.

from the *real* head losses. Starting from the same total head losses decomposition shown in Eq. (4.3), the real static and dynamic head variations inside the draft tube can be evaluated as the difference in mass flow averaged H_{sta} and H_{dyn} at the inlet and a given downstream plane, i.e.,

$$\Delta H_{sta} = \frac{1}{Q}\iint\limits_{S_{R0}} \frac{\langle P_s \rangle}{\rho g}\langle u_z \rangle dS - \frac{1}{Q}\iint\limits_{S_{sec}} \frac{\langle P_s \rangle}{\rho g}\langle u_z \rangle dS \tag{4.8}$$

and

$$\Delta H_{dyn} = \frac{1}{Q}\iint\limits_{S_{R0}} \left(\frac{1}{2g}\langle u_i \rangle\langle u_i \rangle\right)\langle u_z \rangle dS - \frac{1}{Q}\iint\limits_{S_{sec}} \left(\frac{1}{2g}\langle u_i \rangle\langle u_i \rangle\right)\langle u_z \rangle dS \tag{4.9}$$

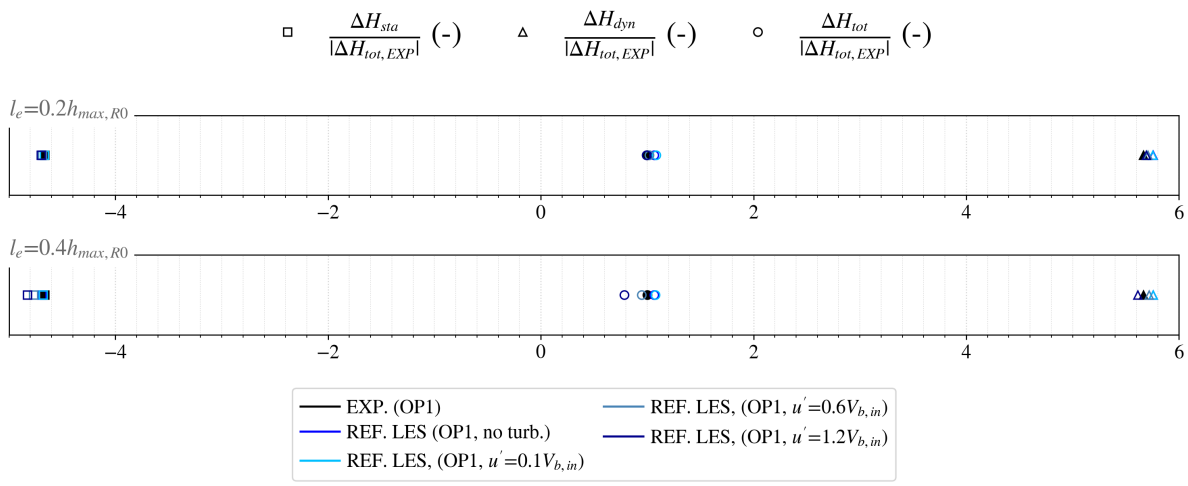

Figure 4.29: IEC losses between stations R1 and EX for the reference simulations of the draft tube at OP1 using LES with/without synthetic fluctuations.

By varying the position of the downstream cross-section, it is possible to evaluate the evolution of total head losses inside the draft tube, as shown in Fig. 4.30. The results are normalized by the total head losses between the inlet and outlet of the draft tube in the reference LES case without turbulence injection, $\Delta H_{REF.\ LES}$. Since the experimental data is limited to measurements at radial traverses at a few stations, it is not possible to evaluate the real head losses in this case. Nevertheless, it is clear from that figure that, despite the very similar IEC losses shown previously, real head losses vary significantly depending on the synthetic turbulence level. In the cases without synthetic turbulence, evolution of ΔH_{tot} is similar to what has been found in Wilhelm [160], with most of the head losses occurring in the first half of the draft tube. However, what is interesting on the curves shown in Fig. 4.30, is the evolution of ΔH_{tot} in the beginning of the draft tube, i.e., between $0.0 \leq h/h_{max} \leq 0.2$. As the incoming fluctuations become stronger (e.g., cases with $u' = 0.6V_{b,in}$ and $1.2V_{b,in}$), negative values of total head losses are found. This behaviour is not expected and indicate that the total mean kinetic energy of the flow, increases close to the inlet of the numerical domain, before gradually reducing further downstream. As explained in Section 2.4, the injected synthetic fluctuations are not necessarily correlated (temporal and spatially) with the mean flow and, as a result, a transition region is expected close to their injection plane. Indeed, within this transition region, the incoming fluctuations will adapt and develop, and it is possible that part of the energy contained in these turbulent structures be transferred to the mean flow via the production term, affecting thus the head losses.

To further understand the synthetic turbulence transition issue and the cause behind this *unexpected* head losses behaviour close to the inlet of the numerical domain, we can look at the turbulent structures being injected in this region of the flow. Figure 4.31 shows them using iso-surfaces of Q-criterion coloured by the vorticity in the z-axis direction. As expected, in the reference LES case without synthetic turbulence injection, there are no turbulent structures visible at the inlet plane, which will develop at the walls and further downstream in the centre of flow due to large vortex in this region. Conversely, a few structures are seen in the case with $u' = 0.1V_{b,in}$, but as demonstrated by the previous results, they are not strong enough to significantly modify the downstream behaviour of the flow. Increasing u' to $0.6V_{b,in}$ or $1.2V_{b,in}$ has an important effect and many turbulent structures are seen at the inlet of the domain. However, as the synthetic fluctuations get stronger, a rapid variation in vorticity values is observed close their injection plane, indicating thus that they need to adjust to the mean flow entering the draft tube.

The effect of the transition region due to *unrealistic* synthetic fluctuations is also observed in

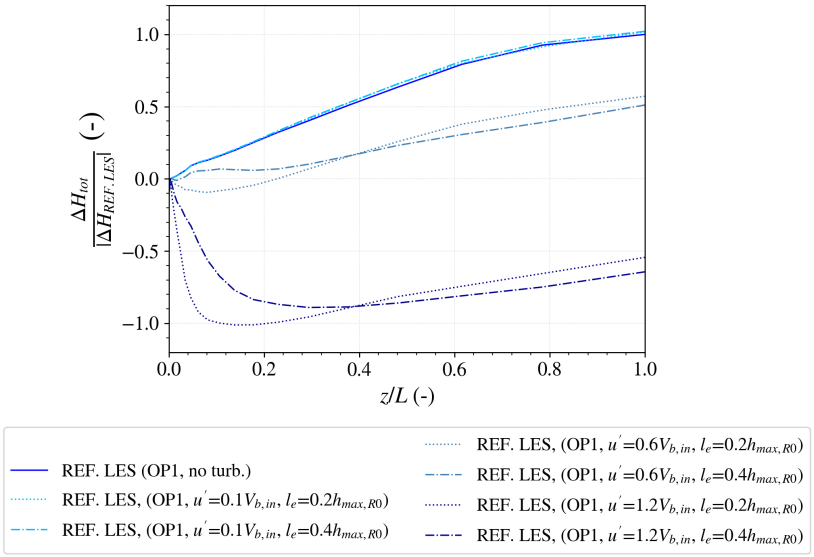

Figure 4.30: Real head losses evolution for the reference simulations of the draft tube at OP1 using LES with-/without synthetic fluctuations.

the distribution of resolved turbulent kinetic energy production, term V in Eq. (2.35), shown in Fig. 4.32. In the reference case without turbulence injection or with weak synthetic fluctuations (i.e., $u' = 0.1V_{b,in}$), resolved production is mostly zero close to the inlet of the draft tube, except at the walls and downstream the hub, where some turbulence is generated as a result of flow shear and the central vortex. In the cases with stronger synthetic turbulence injection, turbulent production is clearly affected by the incoming fluctuations. Like the vorticity in the previous figure, there is a rapid variation of term V close to the inlet of the domain, associated with the decay and adjustment of the *unrealistic* turbulence being injected. Indeed, depending on the case, negative values of turbulent kinetic energy production are observed in this region of the flow, which means that there is an inverse energy transfer from the turbulent flow field to the mean flow field. As the resolved turbulent kinetic energy production term is the most important source of head losses inside a draft tube [159], it is clear that the synthetic fluctuations are the main cause for the *unrealistic* behaviour of real ΔH_{tot} in Fig. 4.30.

4.6 Comparison with experimental data at OP2

Before exploring the issue with negative values of head losses caused by the decay of *unrealistic* synthetic fluctuations, the second operating point tested during the experimental campaign, OP2, is investigated in this section. The same numerical setup in the previous RANS and LES computations is used, except for the inlet profiles, which are now given by the curves shown in Fig. 4.33. In the case of LES, synthetic fluctuations are once again injected into the reference numerical domain to examine their influence on the velocity and pressure fields, as well as in the head losses evolution inside the draft tube. The same three levels of velocity scale, u', and length scale, l_e, are tested. Since most results are somehow normalized by the average axial velocity at the inlet of the draft tube, $V_{b,in}$, it should be noticed that this value is about 10% higher in OP2 compared to OP1.

4.6.1 Velocity and turbulence profiles

The normalized axial velocity profiles for the second operating point are shown in Fig. 4.34. Both reference RANS simulations and the LES without synthetic turbulence injection yield

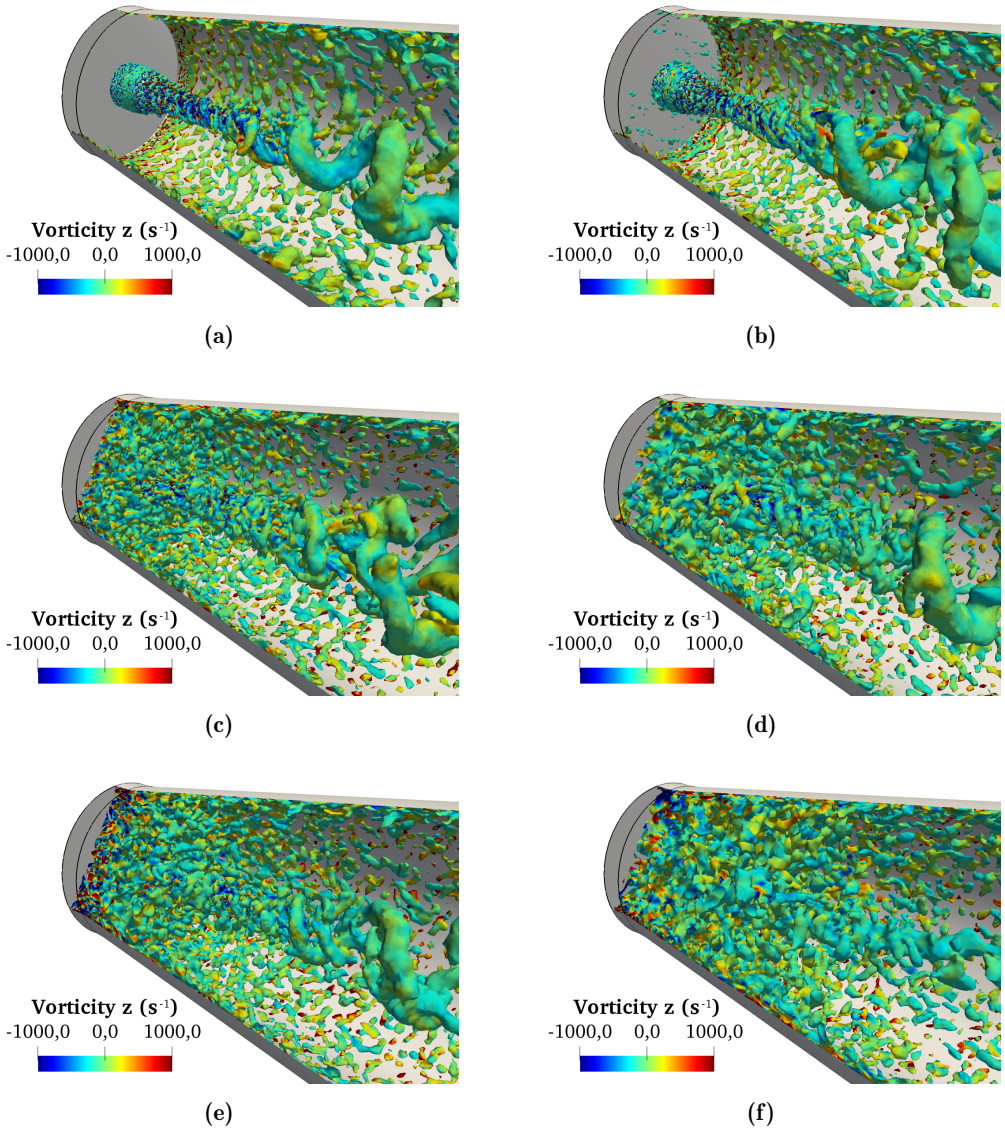

Figure 4.31: Turbulent structures inside the draft tube visualized by iso-surfaces of Q-criterion and coloured by their vorticity z. (a) REF. LES (OP1, no turb.); (b) REF. LES (OP1, $u' = 0.1V_{b,in}$, $l_e = 0.2h_{max,R0}$); (c) REF. LES (OP1, $u' = 0.6V_{b,in}$, $l_e = 0.2h_{max,R0}$); (d) REF. LES (OP1, $u' = 0.6V_{b,in}$, $l_e = 0.4h_{max,R0}$); (e) REF. LES (OP1, $u' = 1.2V_{b,in}$, $l_e = 0.2h_{max,R0}$); (f) REF. LES (OP1, $u' = 1.2V_{b,in}$, $l_e = 0.4h_{max,R0}$).

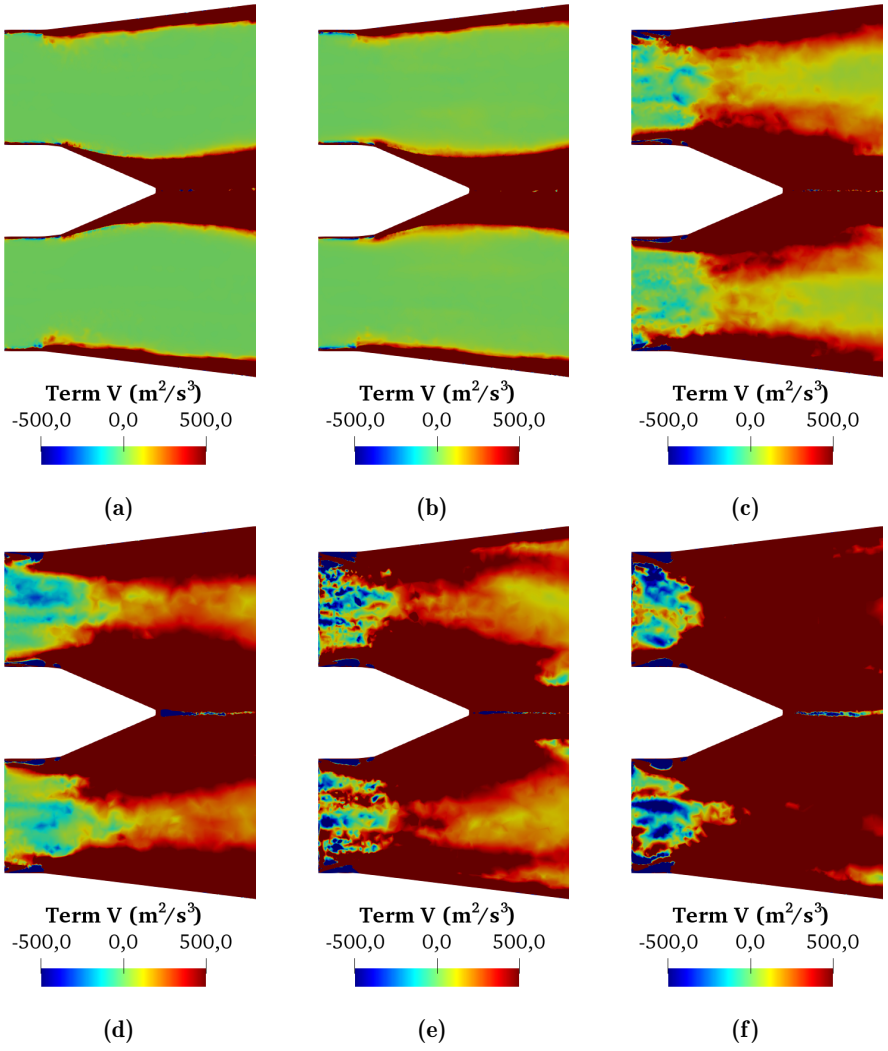

Figure 4.32: Distribution of resolved turbulent kinetic energy production, term V in Eq. (2.35), close to the inlet of the draft tube. (a) REF. LES (OP1, no turb.); (b) REF. LES (OP1, $u' = 0.1V_{b,in}$, $l_e = 0.2h_{max,R0}$); (c) REF. LES (OP1, $u' = 0.6V_{b,in}$, $l_e = 0.2h_{max,R0}$); (d) REF. LES (OP1, $u' = 0.6V_{b,in}$, $l_e = 0.4h_{max,R0}$); (e) REF. LES (OP1, $u' = 1.2V_{b,in}$, $l_e = 0.2h_{max,R0}$); (f) REF. LES (OP1, $u' = 1.2V_{b,in}$, $l_e = 0.4h_{max,R0}$).

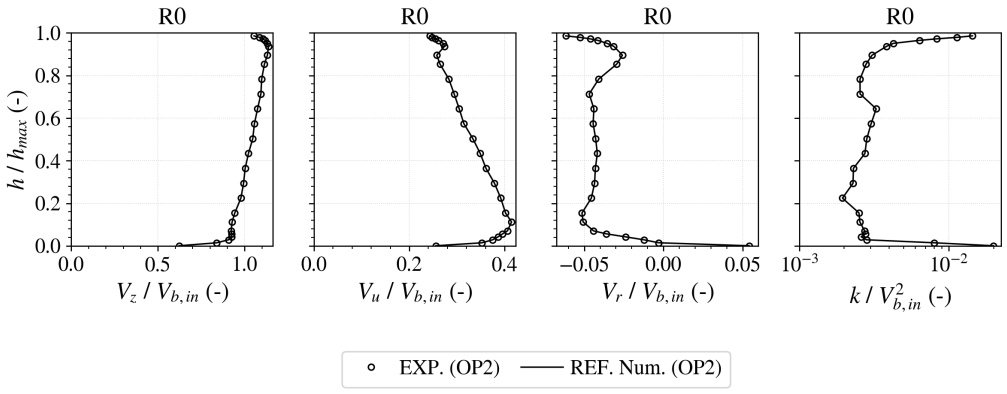

Figure 4.33: Mean velocity and turbulence kinetic energy profiles imposed at the inlet of the reference draft tube simulations (station R0) at OP2.

very similar results at station R1. Agreement with the experimental data near the external walls ($h/h_{max} = 0.0$) is good, but, in spit of the proximity of station R1 to the domain's inlet (station R0), the numerical results are overestimated towards the centre of the flow ($h/h_{max} = 1.0$). Between stations R2 and R4, the influence of the central vortex formed downstream the hub is once again observed as mean axial velocity values are very low near $h/h_{max} = 1.0$. Like in OP1, RANS results using the k-ω SST turbulence model are overestimated in this region of the flow, whereas a very good agreement is found in the case of LES. Near the walls, however, both turbulence solutions underestimate V_z and the boundary layer is not well predicted. As a result, the mean axial velocity values in the intermediate region of the flow ($0.2 \leq h/h_{max} \leq 0.8$) are overestimated to compensate for the reduced mass flow elsewhere. At stations R4 and R5, RANS simulation predicts negative values of V_z near the walls ($h/h_{max} \approx 0.0$), indicating a recirculation and consequent boundary layer separation in this region of the draft tube. Conversely, this behaviour is not observed in LES neither in the experimental measurements at these stations. Indeed, at stations R3 and R4, i.e., where the draft tube transitions from a circular to a squared shaped cross-section, a strong mean axial velocity peak is visible in the experiments, but no numerical simulation is able to capture it. Similarly to the first operating point, injecting synthetic fluctuations improves LES results. For instance, as the velocity length scale, u', increases, the boundary layer is better predicted between stations R2 and R5. Consequently, the values of V_z in the intermediate region of the flow are also reduced and are now closer to the experiments. At station R1, however, a mean axial velocity peak is observed near the external walls of the draft tube in the cases with $u' = 1.2V_{b,in}$. In addition to the velocity scale, the length scale of injected synthetic fluctuations, l_e, also affects the downstream flow behaviour. For instance, $l_e = 0.4h_{max,R0}$ flattens the mean axial velocity profile at station R5 and improves the LES results at this location. However, it also increases the dissipation of the central vortex and V_z values near $h/h_{max} = 1.0$ are overestimated between stations R2 and R4 in the case with $u' = 1.2V_{b,in}$. For those reasons, the turbulent LES case with $u' = 0.6V_{b,in}$ and $l_e = 0.4h_{max,R0}$ seems a good compromise to yield satisfactory results.

Figure 4.35 shows the normalized tangential velocity profiles inside the draft tube. At station R1, numerical results are very different from experimental measurements. For instance, instead of a peak value near the external walls of the draft tube ($h/h_{max} = 0.0$), experimental measurements predict a strong peak near the centre of the flow ($h/h_{max} = 1.0$). Due to its proximity with the inlet plane (station R0), it seems very improbable that such a different profile is recovered at station R1, especially because the results for OP2 have been obtained from a single experimental campaign, unlike OP1. Another simulation with an inverted (with respect to h/H) inlet mean tangential velocity profile has been performed, but the results did not improve. At stations R3 and R4, experimental measurements predict a strong reduction in

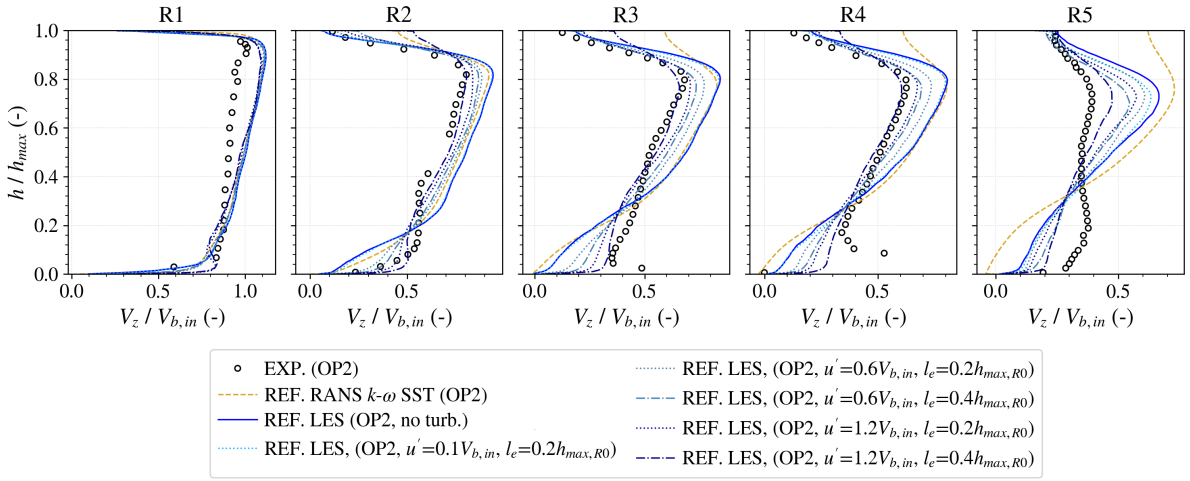

Figure 4.34: Normalized mean axial velocity profiles for the reference simulations of the draft tube at OP2 using RANS and LES with/without synthetic fluctuations.

V_u close to $h/h_{max} = 0.9$ whereas numerical results predict a peak in this region of the flow. Moreover, after slowly decrease towards the walls, experimental V_u profiles indicate the presence of a counter-rotating flow near the walls of the draft tube (due to the negative values of V_u), while numerical results predict a rather constant *and* positive V_u between $0.0 \leq h/H \leq 0.8$. At station R2, the experimental and numerical distribution of mean tangential velocity profiles are similar and follows the same behaviour observed numerically at stations R3 and R4. For instance, there is a peak close to the centre of the flow, at $h/h_{max} = 0.9$, which is well captured in RANS and in LES, depending on the synthetic turbulence levels. In the case without turbulence injection or weak synthetic fluctuations ($u' = 0.1V_{b,in}$), the peak is overestimated compared to the experiments. This is slightly improved by increasing u', but if l_e is also too large, the peak ends up being underestimated (e.g.,$u' = 1.2V_{b,in}$ and $l_e = 0.4h_{max,R0}$). Between $0.0 \leq h/h_{max} \leq 0.8$, experimental values are underestimated compared to numerical simulations. Nevertheless, looking only at the distribution of V_u in this region of the flow, the reference LES case without turbulence injection predicts a secondary peak near $h/h_{max} = 0.2$ followed by a rapid decrease until $h/h_{max} = 0.1$. This is not observed in the experiments neither in the other numerical simulations. Indeed, injecting moderate and strong synthetic fluctuations leads to a secondary peak very close to $h/h_{max} = 0.0$. Finally, at station R5, experimental measurements present two mean tangential velocity peaks, at $h/h_{max} = 0.0$ and $h/h_{max} = 0.8$, respectively. The reference RANS simulation using the k-ω SST turbulence model overestimates V_u all along this station, whereas LES is able to correctly capture the experimental profile behaviour. Indeed, the two peaks are already observed in the LES results at stations R3 and R4. Moreover, like the profiles at station R2, increasing the synthetic fluctuations intensity improves the numerical results.

Figure 4.36 shows the turbulence kinetic energy profiles normalized by the square of the average axial velocity at the inlet, $V_{b,in}^2$. Conversely to the first operating point, OP1, turbulence measurements in OP2 are not limited to the region close to the walls at the radial stations inside the draft tube (i.e., R1 to R5). In RANS, the imposed turbulent inlet boundary conditions yield a good match with the experimental measurements between stations R1 and R4. At the last stations, however, k values are mostly underestimated. In the reference LES case with no synthetic turbulence injection, turbulence kinetic energy profile is mostly underestimated compared to the experiments at stations R1 and R2, and partially underestimated at station R3 (at $h/h_{max} \leq 0.1$ and between $0.4 \leq h/h_{max} \leq 0.8$). At station R4, numerical results agree well with the experimental data, but end up slightly overestimated at station R5 between $0.0 \leq h/h_{max} \leq 0.5$. Injecting weak synthetic fluctuations, with $u' = 0.1V_{b,in}$, slightly improves

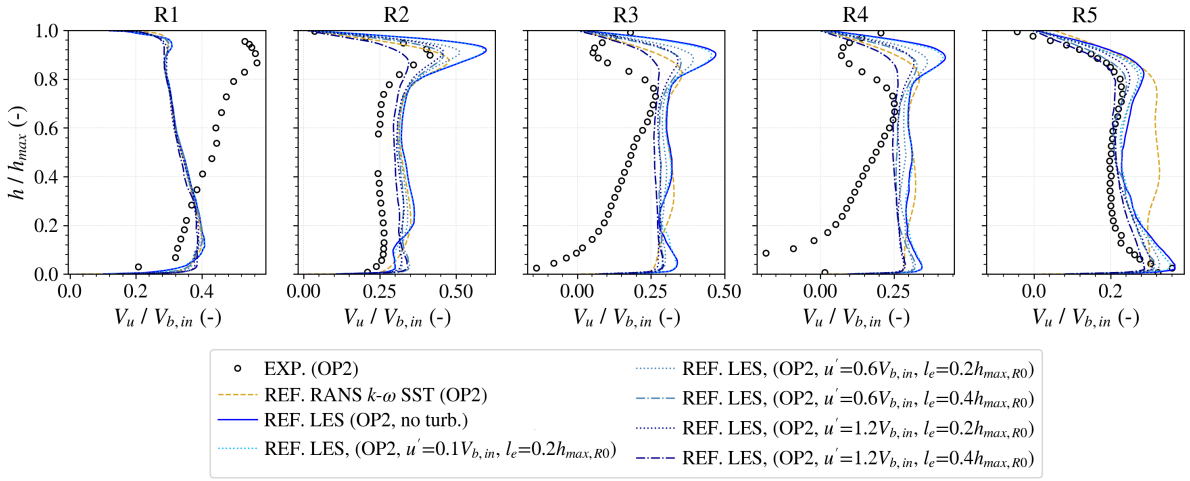

Figure 4.35: Normalized mean tangential velocity profiles for the reference simulations of the draft tube at OP2 using RANS and LES with/without synthetic fluctuations.

the profiles of k at stations R1 and R2, but they remain underestimated compared to the experiments. However, since these weak synthetic fluctuations quickly decay inside the draft tube, the turbulence kinetic energy profiles predicted in LES without turbulence injection and with synthetic turbulence with $u' = 0.1V_{b,in}$ are identical between stations R3 and R5. Increasing u' to $0.6V_{b,in}$ and $1.2V_{b,in}$ results in more intense injected fluctuations and overestimated values of k at stations R1 and R2. Further downstream, between stations R3 and R5, the cases with $u' = 0.6V_{b,in}$ agree well with the experimental measurements. Interestingly, like in OP1, the cases with the most intense synthetic fluctuations, i.e., $u' = 1.2V_{b,in}$, underestimate the turbulence kinetic energy profiles at the last measurement station, R5.

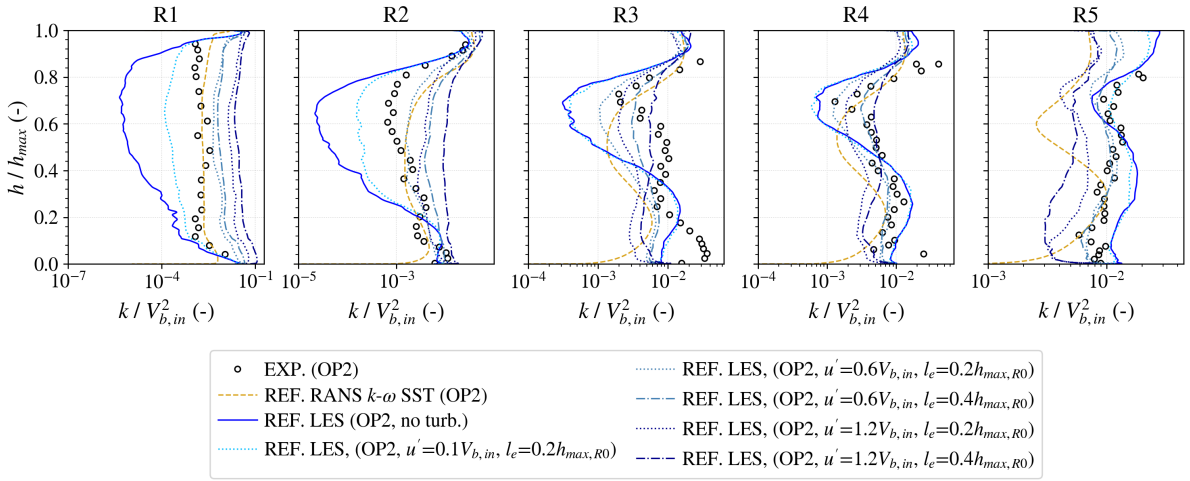

Figure 4.36: Normalized turbulence kinetic profiles for the reference simulations of the draft tube at OP2 using RANS and LES with/without synthetic fluctuations.

4.6.2 Static pressure profiles and distribution along the walls

Following in the analysis of the flow inside the draft tube operating at OP2, the static pressure profiles are shown in Fig. 4.37. Like in OP1, the static pressure measured in the middle height at station R0 is used as a reference and the results are normalized by the dynamic pressure q_{in}. Overall, the results of the reference RANS and LES without turbulence injection are very

similar and underestimated compared to the experimental measurements. However, P_s values near $h/h_{max} = 1.0$ are considerably lower in LES between stations R1 and R4, in spite of the good prediction of the mean velocity profiles in this region of the flow. Injecting synthetic fluctuations in LES improved the static pressure results. For instance, as u' increased and the injected fluctuations intensified, the profiles of P_s move towards the experimental measurements. While in the first operating point, $u' = 0.6V_{b,in}$ yielded the best results compared to the experiments, in OP2, it is the case with $u' = 1.2V_{b,in}$ and $l_e = 0.2h_{max,R0}$ which delivers the best agreement between stations R2 and R5. Nevertheless, all simulations underestimate P_s between $0.0 \leq h/h_{max} \leq 0.8$ at station R1.

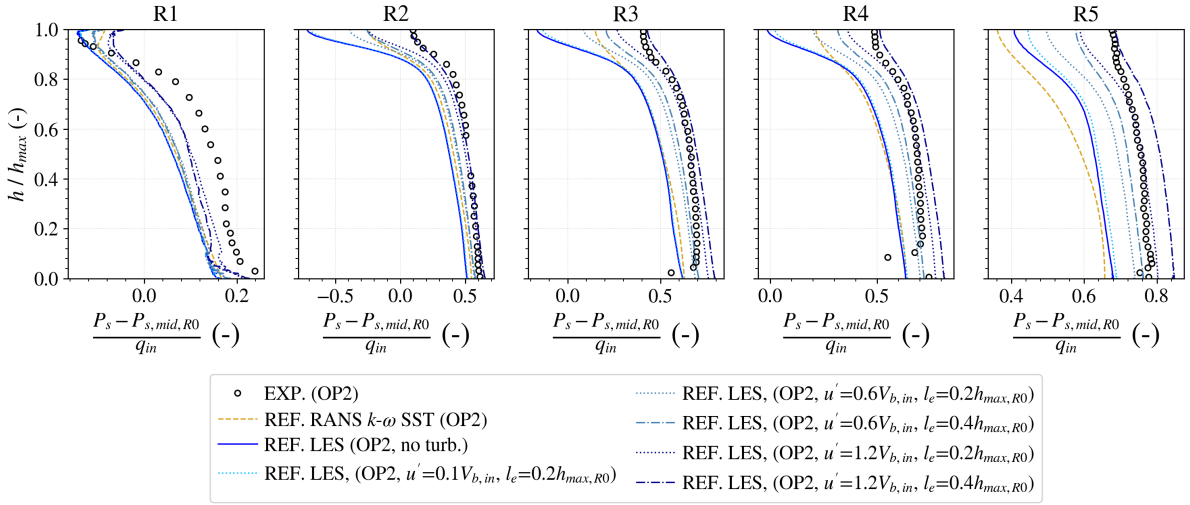

Figure 4.37: Normalized static pressure profiles for the reference simulations of the draft tube at OP2 using RANS and LES with/without synthetic fluctuations.

The evolution of normalized static pressure along the draft tube walls in the streamwise direction for the second operating point is shown in Fig. 4.38. Conversely to OP1, the reference RANS simulations using the k-ω SST turbulence model and the LES without turbulence injection underestimate the pressure recovery at the beginning of the draft tube, which compromise the downstream results. However, while RANS predicts a very small pressure recovery downstream the draft tube cone, i.e., $z/L \geq 0.4$, similar to what has been measured during the experiments, the reference LES case with no synthetic fluctuations predicts a relatively important pressure recovery at $z/L \geq 0.5$. Like in the first operating point, OP1, injecting a synthetic turbulence field reduced the pressure recovery at the final portion of the draft tube but increased it inside the cone. As a result, P_s values evolution along the walls are closer to the experiments, particularly in the LES case with $u' = 1.2V_{b,in}$ and $l_e = 0.4h_{max,R0}$ at stations S1 and S3. At station S2, in spite of the good agreement between $0.0 \leq z/L \leq 0.6$, LES results at the end of the draft tube are overestimated with respect to the experiments.

Figure 4.39 compares the normalized circumferential distribution of static pressure at the draft tube walls. Like in OP1, there is a shift between static pressure values measured by the wall-mounted pressure taps and the five-hole pressure probes, which is why the average static pressure at circumferential station C1, $\overline{P_{s,\mathrm{C1}}}$, is used a reference. Overall, the results follow the same trend observed in Fig. 4.38, which is expected given that they are measured at similar locations. At station C2 ($z/L = 0.2$), RANS simulation using the k-ω SST turbulence model predicts higher P_s values at the walls compared to the reference LES case without turbulence injection or with synthetic weak fluctuations, i.e., $u' = 0.1V_{b,in}$. At station C3 ($z/L = 0.4$), the three numerical results are very similar, but RANS predicts a slower increase in static pressure at the walls towards the exit of the draft tube, i.e., between stations C4 and EX. Compared to the experiments, the results are all underestimated, which is in agreement with the observations

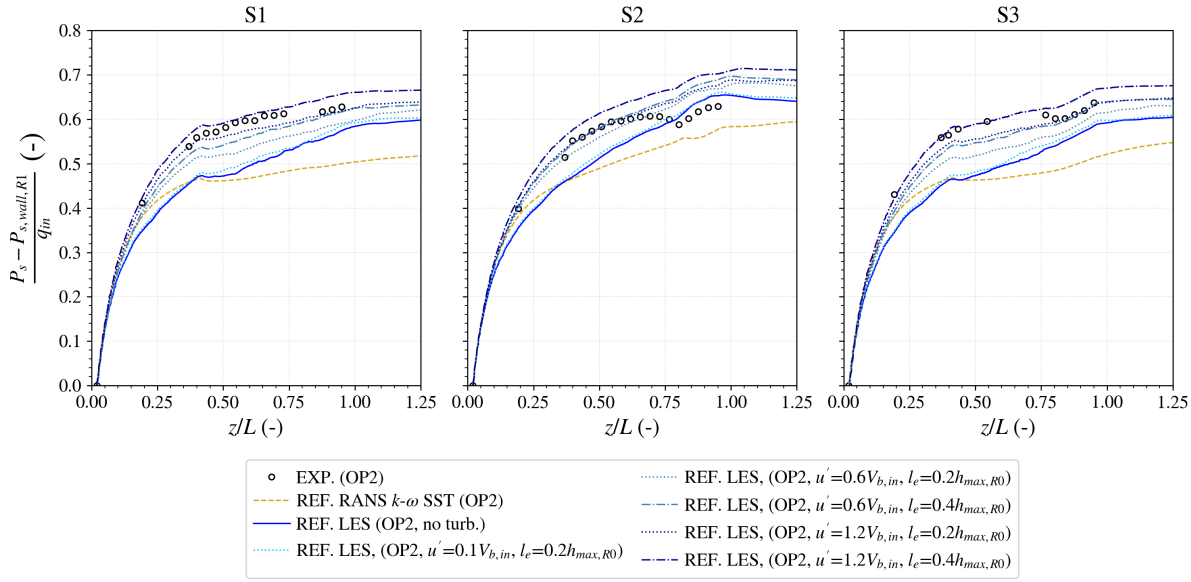

Figure 4.38: Normalized streamwise static pressure evolution at the walls for the reference simulations of the draft tube at OP2 using RANS and LES with/without synthetic fluctuations.

in the previous analyses. The increased pressure recovery after injecting moderate and strong synthetic fluctuations in LES improves the circumferential P_s distribution at the draft tube walls. However, conversely to the results at stations S1 to S3, it is the cases with $u' = 0.6V_{b,in}$ and $l_e = 0.4h_{max,R0}$, and $u' = 1.2V_{b,in}$ and $l_e = 0.2h_{max,R0}$ which yield the best agreement with the experimental measurements. The case with $u' = 1.2V_{b,in}$ and $l_e = 0.4h_{max,R0}$ mostly overestimates the static pressure at the walls, except in the last station, EX.

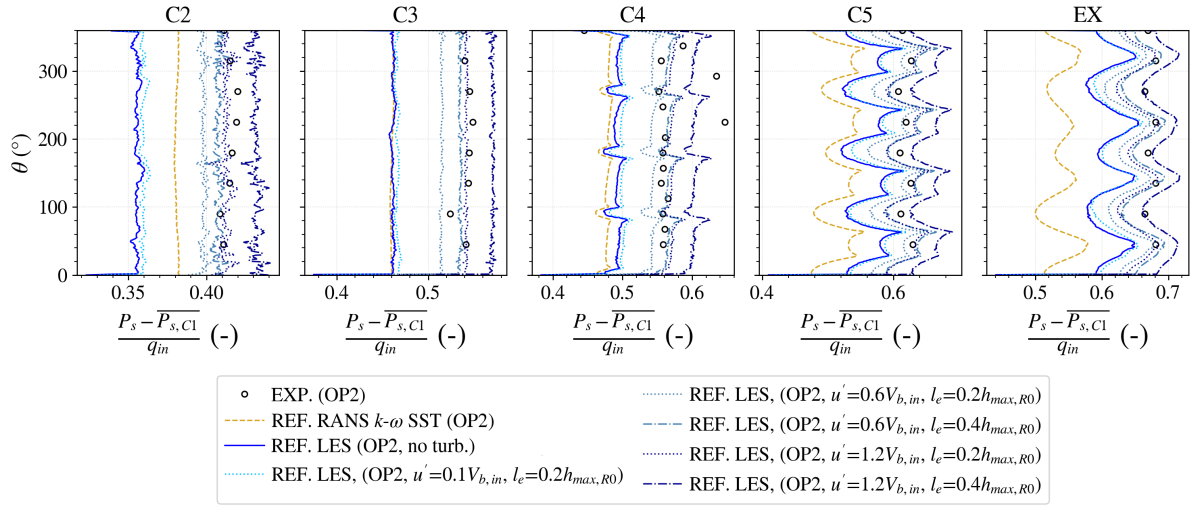

Figure 4.39: Normalized circumferential static pressure distribution at the walls for the reference simulations of the draft tube at OP2 using RANS and LES with/without synthetic fluctuations. Reference as the average static pressure on the walls measured at station C1, $\overline{P_{s,C1}}$.

4.6.3 Head losses analysis

The first approach to evaluate the IEC losses inside the draft tube for its second operating point used the modified ΔH_{sta} and ΔH_{dyn} calculated between stations R1 and EX, and defined in Eqs. (4.6) and (4.7). The results are shown in Fig. 4.40 and LES cases with turbulence

injection are separated by the length scale of the synthetic fluctuations, l_e. Total head losses predicted in RANS are considerably higher compared to experiments and LES results, which can be explained by the poor prediction of ΔH_{sta} with this turbulence model. In LES, injecting synthetic fluctuations reduced the total head losses inside the draft tube and numerical results got closer to the experimental ΔH_{tot} values as u' and l_e increased. While ΔH_{dyn} is slightly affected by the synthetic turbulence parameters, it is ΔH_{sta} which is mostly affected by the turbulent inflow. In the cases with $u' = 0.6V_{b,in}$ and $1.2V_{b,in}$, the static head variation agree very well with the experiments. However, the numerical values of ΔH_{dyn} are systematically overestimated with respect to the experimental measurements, which can explain the overestimation of ΔH_{tot} in these cases. Indeed, this problem can be traced back to the underestimated mean axial and unreliable mean tangential experimental velocity profiles at station R1 shown in Figs. 4.34 and 4.35. Therefore, the modified ΔH_{dyn} equation used to evaluate the IEC losses are not suitable for the analysis of OP2.

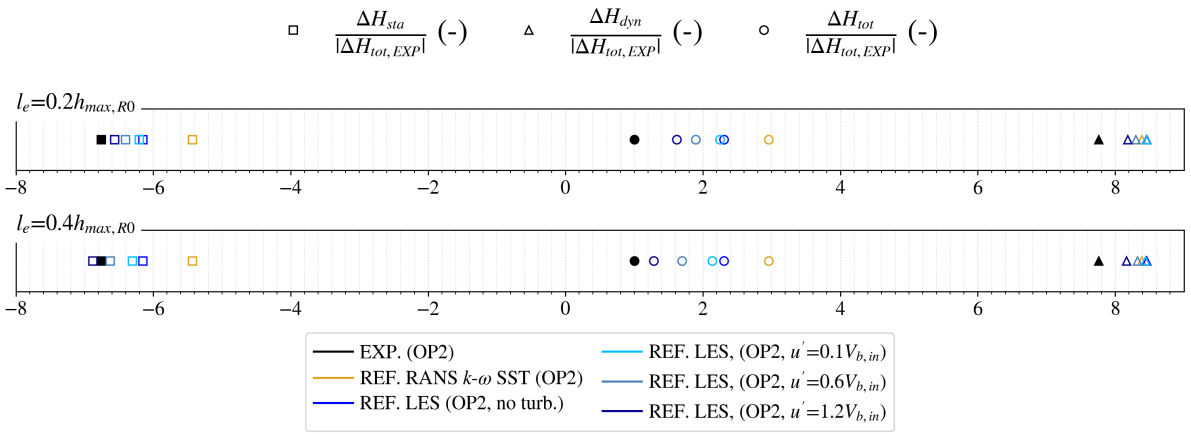

Figure 4.40: IEC losses between stations R1 and EX for the reference simulations of the draft tube at OP2 using RANS and LES with/without synthetic fluctuations.

To circumvent this issue with the dynamic head at station R1, we decided to use the original Eq. (4.5) to evaluate ΔH_{dyn}, while the modified Eq. (4.6) is used to evaluate ΔH_{sta}. Although the different components of the total head losses are not measured between the same two locations inside the draft tube, the experimental measurements used in their evaluation are more *reliable*. The results with this approach are shown in Fig. 4.41. As expected, ΔH_{dyn} values are independent of the case, since they are based on the mean axial velocity profiles at station R0 (the inlet of the computational domain), which are imposed in the numerical simulations, and the flow rate at station EX, which is fixed. Therefore, differences in ΔH_{tot} are due to the static head, ΔH_{sta}, which are determined by the circumferential static pressure distribution at stations C1 and EX. In RANS, the total head losses are 51% overestimated compared to the experiments, which is expected given the poor pressure recovery prediction obtained by this turbulence method. The reference LES without turbulence injection improves these results but still overestimates ΔH_{tot} by approximately 23%. At $l_e = 0.2h_{max,R0}$, it is the case with $u' = 1.2V_{b,in}$ that yields the best ΔH_{tot} results compared to the experiments, *only* 9% over its value. However, at $l_e = 0.4h_{max,R0}$, both $u' = 0.6V_{b,in}$ and $u' = 1.2V_{b,in}$ cases yield similar results. The former overestimates the experimental total head losses inside the draft tube by 3.5%, whereas the latter underestimates it by 3.8%.

The normalized *real* head losses evolution inside the draft tube for the reference LES cases are show in Fig. 4.42. Similar to the first operating point, the real ΔH_{tot} values vary significantly depending on the synthetic turbulence levels, much more than what has been observed with the IEC losses (see Fig. 4.41). In addition to that, the same problem of negative values of total head losses are observed in the beginning of the draft tube in the cases with $u' = 0.6V_{b,in}$ and

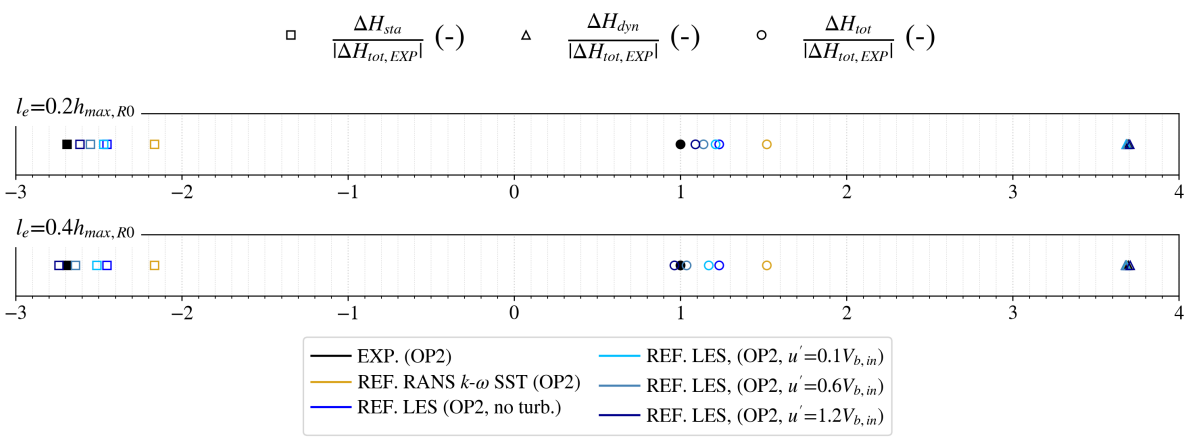

Figure 4.41: IEC losses between stations R0/C1 and EX for the reference simulations of the draft tube at OP2 using RANS and LES with/without synthetic fluctuations.

$u' = 1.2V_{b,in}$, indicating an *unexpected* increase in the total energy in this region of the flow.

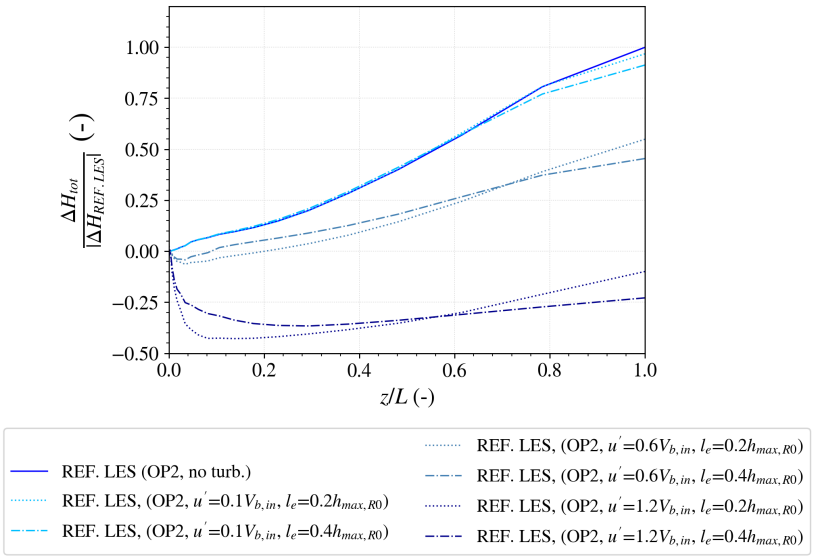

Figure 4.42: Real head losses evolution for the reference simulations of the draft tube at OP2 using LES with-/without synthetic fluctuations.

Figure 4.43 shows the turbulent structures, identified by the Q-criterion, inside the draft tube and close to its inlet for the second operating point, OP2. The topology of the flow, especially the central vortex, is slightly different from OP1 (see Fig. 4.31). For instance, instead of a helical vortex that gradually increase in diameter downstream the draft tube, the central vortex in OP2 is narrower and remains like this throughout the draft tube. Injecting synthetic fluctuations to the inlet of the computational domain has a similar effect, though. While no turbulent structures are observed in inlet plane of the reference LES case without turbulence injection, they are numerous in the cases with $u' = 0.6V_{b,in}$ and $u' = 1.2V_{b,in}$. This *unrealistic* turbulent inflow has to transition, i.e., adapt and adjust to the surrounding flow, right after entering the draft tube. This can be visualized by the rapid variation in vorticity values close to the synthetic fluctuations' injection plane, particularly in the cases $u' = 1.2V_{b,in}$.

As explained in the case of OP1, this *unrealistic* turbulence transitioning process affects the energy balance of the flow, in particular the resolved turbulent kinetic energy production, term

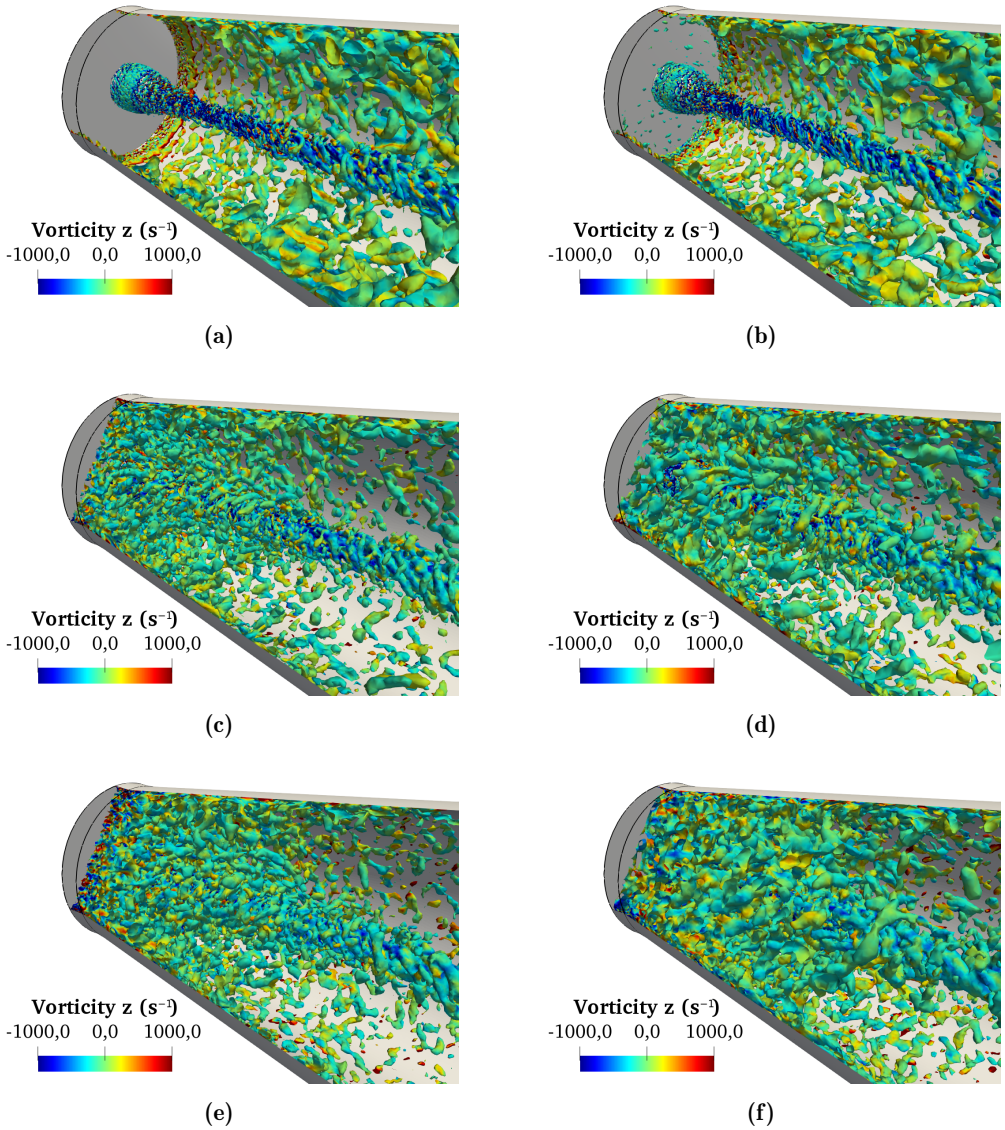

Figure 4.43: Turbulent structures inside the draft tube visualized by iso-surfaces of Q-criterion and coloured by their vorticity z. (a) REF. LES (OP2, no turb.); (b) REF. LES (OP2, $u' = 0.1V_{b,in}$, $l_e = 0.2h_{max,R0}$); (c) REF. LES (OP2, $u' = 0.6V_{b,in}$, $l_e = 0.2h_{max,R0}$); (d) REF. LES (OP2, $u' = 0.6V_{b,in}$, $l_e = 0.4h_{max,R0}$); (e) REF. LES (OP2, $u' = 1.2V_{b,in}$, $l_e = 0.2h_{max,R0}$); (f) REF. LES (OP2, $u' = 1.2V_{b,in}$, $l_e = 0.4h_{max,R0}$).

V in Eq. (2.35), close to the inlet of the numerical domain, which can explain the negative values of real head losses, ΔH_{tot}, observed in Fig. 4.42. The distribution of resolved turbulent kinetic energy production in the reference simulations of the second operating point is shown Fig. 4.44. As expected, in the cases without synthetic turbulence injection or with weak fluctuations, i.e., $u' = 0.1V_{b,in}$, term V is mostly zero close to the inlet of the draft tube, except on the walls, where turbulence is constantly being generated by the flow shear. In the cases with $u' = 0.6V_{b,in}$ and $u' = 1.2V_{b,in}$, a transition region is clearly visible close to the inlet of the numerical domain. More importantly, a few zones of strong negative values of resolved turbulent kinetic energy production are also observed. These negative values are associated with an inverse energy transfer from the turbulent flow to the mean flow, confirming thus our initial suspicion that the decay of the synthetic fluctuations *unrealistically* increased the total energy of the flow close to the inlet of the draft tube.

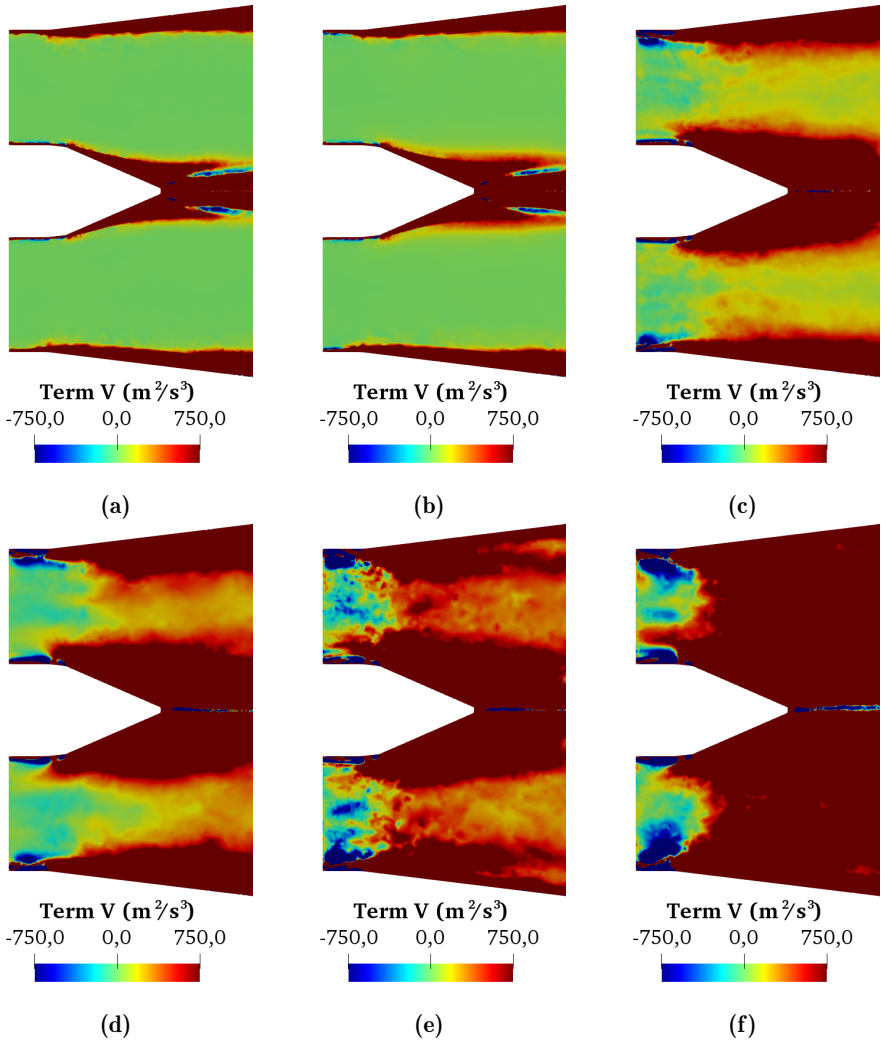

Figure 4.44: Distribution of resolved turbulent kinetic energy production, term V in Eq. (2.35), close to the inlet of the draft tube. (a) REF. LES (OP2, no turb.); (b) REF. LES (OP2, $u' = 0.1V_{b,in}$, $l_e = 0.2h_{max,R0}$); (c) REF. LES (OP2, $u' = 0.6V_{b,in}$, $l_e = 0.2h_{max,R0}$); (d) REF. LES (OP2, $u' = 0.6V_{b,in}$, $l_e = 0.4h_{max,R0}$); (e) REF. LES (OP2, $u' = 1.2V_{b,in}$, $l_e = 0.2h_{max,R0}$); (f) REF. LES (OP2, $u' = 1.2V_{b,in}$, $l_e = 0.4h_{max,R0}$).

Chapter 5

Optimal inlet conditions based on Machine Learning

Contents

5.1 Introduction

The results obtained in the previous chapter demonstrate the importance of imposing proper inlet boundary conditions in the numerical simulation of draft tube flow. For instance, neither RANS nor LES turbulence method was capable of providing satisfactory results using commonly used inlet conditions. In LES, injecting simple synthetic fluctuations into the draft tube domain had a positive effect and the numerical mean velocity and static pressure field were improved in comparison with the experimental data. As a consequence, the prediction of IEC losses was also enhanced. However, since generating a proper fluctuating field for LES is not a trivial task, the *unrealistic* nature of the injected synthetic fluctuations creates a transitional region close to their injection plane that, ultimately, affects the energy balance of the flow and compromises *any* real head losses and efficiency analysis of the draft tube. As the complexity of the flow leaving the runner (or the set of 34 fixed blades, in our case) renders it particularly difficult to obtain accurate and extensive experimental measurements at the inlet of the draft tube, the real challenge to perform such simulations consists thus in determining proper mean and fluctuating inlet boundary conditions based on limited and *potentially* unreliable experimental data. In this chapter, we propose an approach based on Machine Learning algorithms and Artificial Neural Networks (ANN) to solve the inverse problem of determining the optimal inlet conditions for a numerical simulation based on the downstream flow information. Before detailing the proposed approach in Section 5.4, though, previous works in the context of draft tube optimization are discussed Section 5.2 to understand the types of problems and optimization algorithms that have been employed in the past, and, in Section 5.3, some basic concepts of Machine Learning are explained to facilitate the comprehension of the method applied in the following chapters.

5.2 Optimization in the context of draft tubes

Given its importance to the overall performance of the machine, multiple numerical works investigated ways of optimizing the flow inside hydraulic turbine draft tubes. Eisinger and Ruprecht [40] compared improve the shape of a simple conical diffuser, a circular draft tube proposed in the GAMM Workshop [141] and a typical low head draft tube for vertical-axis turbines. The goal was to maximize the static pressure recovery coefficient between its inlet and outlet while only a few geometrical parameters were allowed to vary during the optimization (the area ratio of different cross-sections inside the draft tube). Numerical simulations of the flow inside the draft tube were carried using RANS simulations and the k-ϵ turbulence model [81]. The performance of three optimization algorithms was compared and, while all of them were able to improve the pressure recovery in the three draft tubes, the evolutionary method presented a more robust behaviour. The same conclusion was obtained by Puente *et al.* [127] after performing a very similar analysis of the typical low-head draft tube investigated in Eisinger and Ruprecht [40], but this time using CFX and an interactive optimization solution called iSIGHT. Marjavaara *et al.* [96], on the other hand, compared two surrogate models (polynomial Response Surfaces and Radial Basis Neural Networks) used in conjunction with evolutionary algorithms to maximize the static pressure recovery coefficient of a draft tube operating at two different conditions. The investigated geometry consisted in a simplified version of the Turbine-99 draft tube [55], which contained its inlet cone followed by a straight extension. Only four design parameters, which controlled the cross-sectional shape at different axial positions of the simplified draft tube, were allowed to vary. Once again, numerical simulations were carried using RANS simulations and the k-ϵ turbulence model. The proposed optimization framework using surrogate models reduced the computational costs compared to solely utilizing an evolutionary algorithm and the hydraulic performance of the simplified draft tube was increased in both operating conditions. The static pressure recovery coefficient and evolutionary algorithms were used by Fares *et al.* [42] to optimize the shape and performance of a simple conical diffuser and a real hydraulic turbine draft tube. The difference to the previous works, however, is that both diffuser and draft tube shapes were parametrized using Bézier curves [15], instead of the just a few geometrical parameters.

Draft tube shape optimizations algorithms are not limited to a single objective function though, and Nakamura and Kurosawa [110] used the total head loss between across the runner and draft tube a Francis turbine, as well as the height of the latter, to optimize the shape of both components using evolutionary algorithms. Approximately 30 design parameters were used to define the geometry runner, whereas for the draft tube, this number was approximately 50. RANS simulations are performed using the k-ϵ turbulence model and the overall performance of the turbine was greatly improved by the proposed multi-objective optimization algorithm. However, the computational cost was extremely high as Nakamura and Kurosawa [110] had to run almost three thousand simulations of the runner and four thousand of the draft tube. Lyutov *et al.* [91] conduct a very similar analysis of a different Francis turbine runner and draft tube, but the simulations were coupled and both geometries varied simultaneously during the optimization process. The overall performance of turbine over a wide range of operating conditions was improved and the total number of simulations required to reach an optimal solution was greatly reduced compared to Nakamura and Kurosawa [110] (*only* 720, to be precise). However, it should be noticed that the amount of parameters being optimized was also smaller, with only 24 for the runner and 20 for the draft tube. More recently, Demirel *et al.* [26] used both the static pressure recovery coefficient and the total head losses across a draft tube as objective functions for its multi-objective optimization algorithms. Like in Marjavaara *et al.* [96], different surrogate models used in conjunction with evolutionary algorithms have been compared and the hydraulic performance of the draft tube was considerably increased at the end, however, geometrical parameters were very limited though, as only 5 design variables were allowed to vary during the optimization process. McNabb *et al.* [100] also investigated the use of evolutionary

algorithms in the draft tube shape optimization based on multi-objective functions, however, very recently, Fleischli *et al.* [47] revisited their draft tube optimization problem to compare the performance of the gradient-free evolutionary algorithm with a gradient based adjoint method. As already pointed out in the work of Eisinger and Ruprecht [40], the advantage of gradient based methods is that they are more computationally efficient than evolutionary algorithms, requiring significantly less numerical simulations to achieve an optimal solution. For instance, Fleischli *et al.* [47] performed 300 numerical simulations to attain an optimal draft tube design using adjoint methods, whereas the evolutionary algorithm using *only* 47 geometrical parameters required approximately 2500 simulations. However, in spite of this reduced number of simulations, the adjoint method was only 30% less demanding in terms of calculation time. Indeed, in addition to the flow solver, an adjoint solver must be directly integrated into the CFD code, which increases the computational cost per simulation and renders the general application of these methods more complex.

While all the aforementioned works modified the shape of the draft tube to optimize its hydraulic performance at a given operating condition, other works focused on optimizing the inlet velocity profiles for a given draft tube geometry. For instance, Galván *et al.* [52, 53] proposed an optimization methodology for maximizing the performance of the Turbine-99 draft tube [55] as a function of the inlet velocity profile. An evolutionary algorithm was implemented using iSIGHT and three different objective functions were considered: the normalized head losses inside the draft tube, the normalized static pressure recovery measured at the walls and the area averaged static pressure recovery measured at the inlet and outlet planes. Steady RANS simulations were conducted using the k-ϵ turbulence model and comparisons were made with respect to the best operating point of the machine. An important aspect of the work, however, was the parametrization of the imposed inlet profiles. Since the total amount of design parameters can have an important impact on the final number of optimization iterations, it was essential to simplify the description of these profiles. This was achieved by the swirling flow model described in Susan-Resiga *et al.* [147], which produced realistic inlet velocity profiles while reducing the overall number of design parameters to only 8. Still, approximately 3000 optimization iterations were required to obtain a converged optimal solution. Galván *et al.* [51] also used a similar approach to study the inlet velocity profiles at a simplified conical diffuser. Although the results were once again very promising, even in that rather simple flow configuration, the number of numerical simulations required to obtain an optimized solution was close to 1000.

It is clear from the previous discussions that evolutionary algorithms are the preferred method to optimize the performance of hydraulic turbine draft tubes. However, although they are robust and have been successfully applied to different flow configurations and types of problems, one common issue with this method is the relatively high computational cost given the small number of design parameters utilized in the optimization. Indeed, while all the numerical simulations discussed previously were performed in less computationally demanding RANS using two-equation linear eddy viscosity models, our goal is to optimize the inlet conditions for both steady RANS *and* LES of the draft tube. Moreover, as will be discussed in Chapters 6 and 7, our optimized inlet profiles are not simplified as in Galván *et al.* [52, 53, 51] and the number of design parameters surpasses the 200. Gradient based adjoint methods, on the other hand, are more computationally efficient and could obtain optimal solution with much less numerical simulations, as has been demonstrated in Fleischli *et al.* [47]. However, implementing such methods is not trivial as they need to be directly integrated to the CFD code. To solve the problem with proper inlet boundary conditions for the numerical simulations of a draft tube flow, a different approach, based on Machine Learning and Artificial Neural Networks, is therefore proposed in this thesis.

5.3 Introduction to Machine Learning algorithms

The term Machine Learning, which is just a branch of Artificial Intelligence (AI), is very broad and normally associated with the design of algorithms and techniques that enable computers to *learn* by identifying and extracting patterns from raw data. Before discussing the proposed approach, the basic aspects of Machine Learning algorithms are explained in this section. However, although the field of Machine Learning is indeed extremely prolific and numerous sources exist, most of the discussions were taken from Goodfellow *et al.* [60] and Nilsen [116].

5.3.1 Learning algorithms for regression

The Machine Learning algorithms is a technique that allows computer programs to learn some class of *task* executed with a given *performance* from *experience*. Many tasks can be solved by Machine Learning algorithms, such as classification, transcription, translation, anomaly detection etc. As the goal of the proposed approach is to determine the correct inlet profiles (a sequence of numerical values) from the ensemble of experimental measurements (another sequence of numerical values), as will be explained in Section 5.4, the main task of our Machine Learning algorithm consists in a non-linear regression, where the computer program must predict a numerical value given some input. For the actual *learning* process can take place, it is essential to evaluate the ability of the algorithm in realizing such a task, i.e., its *performance*. The model's *accuracy* is a common way of doing that, and it measures the proportion of examples for which the model produces the correct output. However, this is not well suited for regression problems as the *error* between the actual and predicted values should be continuous to determine the magnitude of the mistakes. In this case, a different metric should be used to take this effect into account. Finally, the kind of *experience* the Machine Learning algorithm will be allowed to have during learning can be broadly divided into two categories: *unsupervised*, when the hidden patterns in a given dataset are discovered without human intervention, and *supervised*, when each an example in a dataset is associated with a label or target, that is, when the algorithm learns the patterns from a set of inputs *and* outputs.

As will be explained in Section 5.4, the proposed approach is designed to learn the correlations between downstream flow field and upstream inlet boundary conditions in a supervised manner. In the case of a linear regression, this involves observing many examples of a vector $\mathbf{x} \in \mathbb{R}^n$ and an associated value $y \in \mathbb{R}$, then learning to predict y from $\mathbf{x}$, normally by estimating the probability of y given $\mathbf{x}$, i.e., $p(y|\mathbf{x})$. If $\hat{y}$ is the value of y predicted by the model, the output of a linear regression can be written as:

$$\hat{y} = \mathbf{w} \cdot \mathbf{x} + b \tag{5.1}$$

where $\mathbf{w} \in \mathbb{R}^n$ is a vector of parameters, also called *weights*, that determine how each feature x_i affects the prediction $\hat{y}$, while the intercept term b, often called *bias*, is used to affine the transformation. The task in the aforementioned Machine Learning algorithm can thus be defined as: to predict y from $\mathbf{x}$ by outputting $\hat{y} = \mathbf{w} \cdot \mathbf{x} + b$.

The relation in Eq. (5.1) can be represented in the form of a *perceptron* [131], a type of artificial neuron and one of the building blocks of more complex Artificial Neural Networks. A scheme is shown in Fig. 5.1, and it is possible to identify the features x_i being multiplied by the respective weights w_i and then summed with the bias b in a neuron to output a prediction $\hat{y}$ after being modified by an activation function f.

Given the simplicity of a single perceptron, its applications are limited to linear regression and classification problems. For more complicated tasks, such as non-linear regression problems, more complex *feedforward* neural networks, composed by multiple interconnected artificial neurons should be used. The term feedforward means that the information flows from the inputs $\mathbf{x}$, through the intermediate neural network to finally produce an output $\hat{y}$. A Multilayer

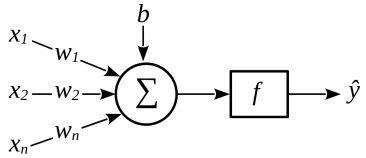

Figure 5.1: Representation of a single perceptron.

Perceptron (MLP) is one example of a feedforward neural network and is composed by a series perceptrons grouped in what is called layers. A scheme of a MLP is shown in Fig. 5.2 and, in addition to the input and output layers, a series of intermediate layers, also called *hidden* layers, are seen in the in between. In the application of the proposed Machine Learning approach to determine proper inlet boundary conditions discussed in Chapters 6 and 7, the ANN are mostly composed by MLP.

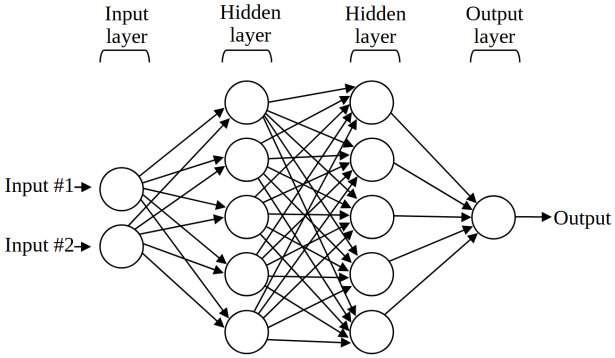

Figure 5.2: Representation of a Multilayer Perceptron.

5.3.2 Activation functions

In the scheme of the perceptron shown in Fig. 5.1, if the value of $\hat{y}$ is exactly equal to the weighted sum $\sum w_i x_i + b$, it is said that the *activation function* or *transfer function* f of the neuron in Fig. 5.1 is *linear*, and a perceptron composed only by this type of neuron is no different from a linear regression model. In the original conception of a perceptron, however, Rosenblatt [131] proposed to determine the neuron's output by whether the weighted sum is lower or greater than a threshold value:

$$\hat{y} = \begin{cases} 0 & \text{if } \mathbf{w} \cdot \mathbf{x} + b \leq \text{threshold} \\ 1 & \text{if } \mathbf{w} \cdot \mathbf{x} + b > \text{threshold} \end{cases} \tag{5.2}$$

The threshold value is *a priori* and in this case, the neuron is said to have a *binary step* activation function. While a perceptron with this type of activation function is different from a linear regression model, it is obvious that it is only suited for classification tasks. A neural network composed by multiple perceptrons that use non-linear activation functions is capable of learning more complex tasks, therefore, many works in the field of Machine Learning have been conduct with the goal of determining better activation functions. One of the earliest and most commonly used is called *sigmoid* function or *logistic* function and is defined as:

$$\sigma(z) = \frac{1}{1 + e^{-z}} \tag{5.3}$$

which, in the context of the single perceptron shown in Fig. 5.1 and equation Eq. (5.1), $z = \mathbf{w} \cdot \mathbf{x} + b$ and the predicted value $\hat{y}$ is equal to:

$$\hat{y} = \frac{1}{1 + \exp[-(\mathbf{w} \cdot \mathbf{x} + b)]} \tag{5.4}$$

Compared to a binary step, the sigmoid activation function yields similar results but, since its derivative is different from zero, weights can be updated during the backpropagation step (see Section 5.3.3) and the learning process can take place. Moreover, its derivative is not constant and the output value varies non-linearly depending on the inputs, distinguishing a perceptron with this activation function from a simple linear regression. The problem with sigmoid, in addition to limiting the outputs to $[0, 1]$, however, is that its derivative value tends to zero when the inputs are large, as shown in Fig. 5.3. This problem is called *vanishing gradients* and, much like in the case of a binary step, it prevents the weights for being updated during backpropagation and therefore no learning will occur.

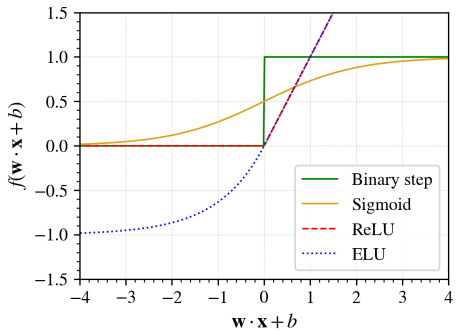

Figure 5.3: Comparison of the response of different activation functions.

The *Rectified Linear Unit* (ReLU) activation function [109], one of the most popular activation functions for Machine Learning [129], overcomes these problems and outperforms sigmoid and hyperbolic tangent functions in the training of deep neural networks [59, 82]. In the case of the perceptron shown in Fig. 5.1, its output, $\hat{y}$, using ReLU as an activation function is given by Eq. (5.5), which is a mix of binary step and linear activation functions. As shown in Fig. 5.3, the derivative of ReLU does not converge to zero, and therefore it does not suffer from the problem with vanishing gradients saw with sigmoid functions. However, if the weighted sum values are negative, the derivative is indeed constant and equal to zero, which prevents learning during the backpropagation step.

$$\hat{y} = \begin{cases} 0 & \text{if } \mathbf{w} \cdot \mathbf{x} + b < 0 \\ \mathbf{w} \cdot \mathbf{x} + b & \text{if } \mathbf{w} \cdot \mathbf{x} + b \geq 0 \end{cases} \tag{5.5}$$

Some modifications have been proposed to improve this behaviour of ReLU activation functions, such as *Leaky ReLUs* [92], which allows the values of $\hat{y}$ to slowly decrease whenever $\mathbf{w} \cdot \mathbf{x} + b < 0$. In the case of the ANN used in Chapters 6 and 7, we use Exponential Linear Unit (ELU) activation functions [20]. They are similar to Leaky ReLUs, however, instead of linearly varying on the negative side of the activation function, the output value, $\hat{y}$, is given by Eq. (5.6). Although ELU is slower to compute than ReLU due to the exponential function, it has no problems with zero valued derivatives and the learning process can continue during backpropagation since the weights, $\mathbf{w}$, are still updated even if the weighted sum values are negative.

$$\hat{y} = \begin{cases} a[\exp(\mathbf{w}\cdot\mathbf{x}+b)-1] & \text{if } \mathbf{w}\cdot\mathbf{x}+b<0 \\ \mathbf{w}\cdot\mathbf{x}+b & \text{if } \mathbf{w}\cdot\mathbf{x}+b\geq 0 \end{cases} \tag{5.6}$$

5.3.3 Learning: forward pass, cost function and backpropagation

During the learning process of the Machine Learning algorithm, information is passed in two directions over the neural network: forward and backward. The goal is to repeatedly adjust the weights $\mathbf{w}$ and biases b, so the predicted values $\hat{y}$ are as close as possible of their true values y. Thus, in the *forward pass*, the input vector $\mathbf{x}$ is fed into the network and the output $\hat{y}$ is evaluated after successive multiplications and additions by the weights, biases, and activation functions in the neurons. Mathematically, this can be written as:

$$\hat{y} = f(\mathbf{W}^L f^{L-1}(\mathbf{W}^{L-1}\cdots f^1(\mathbf{W}^1\mathbf{x}+\mathbf{b}^1)\cdots+\mathbf{b}^{L-1})+\mathbf{b}^L) \tag{5.7}$$

where L is the number of layers, f^l is the activation function at layer l, $W^l = w^l_{jk}$ are the weights between layers $l-1$ and l, where w^l_{jk} is the weight for the connection from the k-th neuron in layer $l-1$ to the j-th neuron in layer l, and $\mathbf{b}^l = b^l_j$ is the bias vector at layer l, where b^l_j is the bias added to the j-th neuron in layer l. Note that for the first forward pass over the neural network, an initial value has to be prescribed for weights and biases. In the case of the ANN discussed in Chapters 6 and 7, weights are initialized using independent Gaussian random variable, normalized to have mean 0 and standard deviation 1, whereas biases are set equal to zero.

From the output of the forward pass, it is possible to evaluate the performance of the current network in realizing the task of the predicting the true value y. In the case of non-linear regression problems, this can be achieved by calculating the *Mean Squared Error* (MSE) between the model's prediction $\hat{y}$ and the true value y, which for a dataset comprising m training examples, is given by:

$$\text{MSE}_{train} = \frac{1}{m}\sum_i^m (\hat{y}_{train} - y_{train})^2 \tag{5.8}$$

The next step in the learning process consists in performing a *backpropagation* [133] to understand how the loss function varies with small changes in weights and biases, i.e., to compute the partial derivatives $\partial C/\partial w^l_{jk}$ and $\partial C/\partial b^l_j$, where C is the value of the loss function (e.g.,MSE_{train}). While these individual derivatives (gradients) can be calculated using the chain rule, the goal with backpropagation is to *efficiently* compute the gradients vector associated with layer l and denoted by δ^l, which can in turn be used to evaluate $\partial C/\partial w^l_{jk}$ and $\partial C/\partial b^l_j$.

Based on these values, an optimization algorithm can be used to update the weights and biases to reduce the value of the loss function, that is, to improve the output prediction $\hat{y}$. Among the many types of optimization algorithms used in Machine Learning, Ruder [132] lists the most commonly used based on gradient descent. Depending on the amount of data used to evaluate the gradients of the loss function, standard gradient descent algorithms can be divided into three categories: batch gradient descent, mini-batch gradient descent and stochastic gradient descent (SGD). The first case uses the whole training set to evaluate the gradients, while a fixed portion of the training set in the second and a single training example is used in the third. In any case, the weights and biases are updated according to Eqs. (5.9) and (5.10):

$$w^{new}_{jk} = w^{old}_{jk} - \eta_l \frac{\partial C}{\partial w_{jk}} \tag{5.9}$$

$$b_j^{new} = b_j^{old} - \eta_l \frac{\partial C}{\partial b_j} \tag{5.10}$$

where η_l is the learning rate, which is fixed and must be defined *a priori*. The performance of SGD algorithms can be improved by adding some momentum [128] and Nesterov accelerated gradient (NAG) [111] to the update vectors in Eqs. (5.9) and (5.10). However, unlike more advanced optimization algorithms [35, 162, 78, 34] the fixed learning rate is a limiting factor as it does not distinguish frequent and infrequent parameters (weights and biases). In the neural networks discussed in Chapters 6 and 7, we utilize an optimization algorithm called NAdam [34], which combines NAG with Adam [78].

5.3.4 Generalization: underfitting, overfitting and regularization

An important aspect of Machine Learning algorithms is *generalization*, which measures the ability of the trained ANN model to perform well on previously unobserved data. For instance, during the training step described in the previous section, the ANN model is exposed to what is called a *training set*, which contains all the information (i.e., inputs and outputs) used to minimize the training error, i.e., the loss function, via successive adjustments of the model's weights and biases. While this is similar to a traditional optimization problem, Machine Learning algorithms are different because the *generalization error*, i.e., the expected value of the error on a *new* input, should also be low. This generalization error of a trained ANN model is typically estimated by measuring its performance on a *validation set*, i.e., a separate set of examples collected independently of the training set. For instance, in the cases discussed in Chapters 6 and 7, the generated databases are divided into a training and a validation sets, which are then used to evaluate the trained model's generalization capacity.

Indeed, the main challenges in Machine Learning are twofold: *underfitting* and *overfitting*. The first occurs when the model is not able to obtain sufficiently low training errors on a given database, while the second occurs when the gap between training and validation errors is too large, i.e., when the model does not generalize very well. The model's capacity is what controls whether it will tend to underfit or overfit, and a Machine Learning algorithm will normally perform better when this capacity is appropriate for the complexity of the problem it needs to solve and the amount of data available for training. *Regularization* is one way of controlling a model's capacity, particularly to avoid overfitting, and consists in modifying the Machine Learning algorithm to reduce the generalization error but not the training error. Simple regularization methods, like $L1$ and $L2$ regularization, consist in adding to the loss function a cost associated with having large weights, however, in the ANN models discussed in Chapters 6 and 7, a more effective and commonly used regularization called *dropout* [144] is used. It consists in randomly and temporarily *dropping out* (i.e., removing) some nodes of a layer, effectively deactivating its incoming and outgoing connections, as shown in Fig. 5.4. The *dropout rate* controls the amount of nodes affected by the dropout in a layer.

5.4 Machine Learning strategy

Based the Machine Learning algorithms discussed in the previous section, an approach is proposed in this thesis to overcome the issues with imposing basic inlet boundary conditions in the numerical simulations of the draft tube. Since the final goal of the simulations is to match as closely as possible the available experimental information inside the numerical domain, the task to be solved by the proposed approach consists in using any known information about the flow (e.g., experimental mean velocity, turbulence, and static pressure profiles), along with an appropriate database of numerical simulations to determine which boundary conditions should be imposed at its inlet plane, so the downstream flow behaviour is in *good* correspondence with

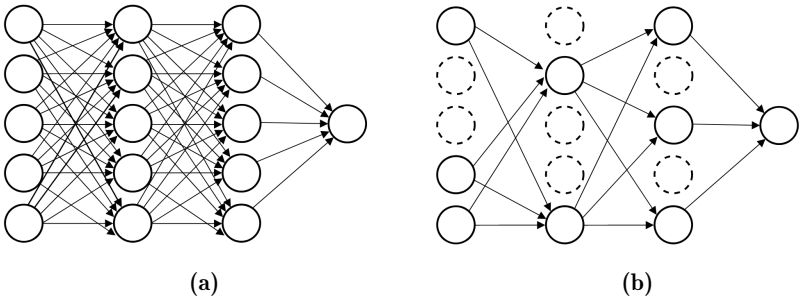

Figure 5.4: Schematic visualization of a dropout in an ANN. (a) standard Neural Network; (b) after applying dropout.

the experimental measurements. The Machine Learning strategy proposed in this thesis is shown schematically in Fig. 5.5 and it can be divided into three main steps:

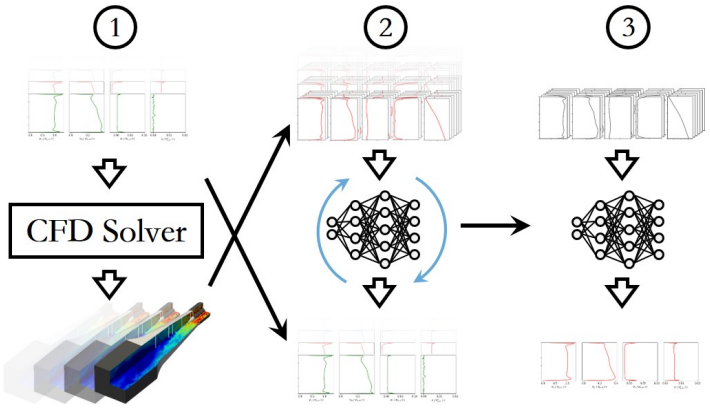

Figure 5.5: Scheme of the proposed Machine Learning strategy to determine optimal inlet boundary conditions for a numerical simulation.

1. **Creating the database**: in the first step of the proposed strategy, multiple numerical simulations are run to create an appropriate database which will be used to train an ANN. The numerical setup (computational domain, boundary conditions, turbulence model, wall-model etc.) of each simulation in this database *must* be identical to that from the case we want to optimize, *except* for a different set of *inlet* boundary conditions. For instance, in the case of RANS simulations of the bulb turbine draft tube discussed in Chapter 4 of this thesis, different V_z, V_u, V_r and k, as well a different turbulence characteristic length scales would be imposed at the inlet of each simulation. In the case of LES, the turbulence kinetic energy profile would be replaced by a normalized profile of k (see Fig. 2.7) and, instead of a single turbulence characteristic length scale, the two parameters required to define the synthetic fluctuations, a velocity, and a length scales (u' and l_e, respectively), would be varied in each simulation. As a result, any difference on the downstream flow field behaviour is exclusively due to the inlet boundary conditions and the ANN can be trained to establish a mapping between the two.

2. **Training the ANN**: the second step in the proposed Machine Learning strategy consists in training the ANN, i.e., creating a non-linear regression model that will correlate ANN inputs and outputs, using the database generated in the previous step. Inputs correspond to the downstream flow field results obtained from the database (e.g., mean velocity, turbulence kinetic energy and static pressure profiles etc.) whereas outputs consist in the set of inlet boundary conditions applied to each simulation of the database. Thus, the trained ANN model should be able to determine which set of inlet conditions is required

to yield a given downstream flow field behaviour. As it is going to be discussed in the next two chapters, the complexity of the flow and, eventually, the quality of the available experimental data play an important role in the amount and type of data used to train the ANN.

3. **Predicting the optimal inlet boundary conditions**: finally, once the ANN is successfully trained and the non-linear regression model is created, the third and final step in the proposed Machine Learning strategy consists in informing the ANN of the actual downstream flow results we want our numerical simulations to match (e.g., the experimental measurements) and, in return, it shall output the corresponding inlet boundary conditions required to obtain such a flow.

As will be discussed in the following chapters, the computational cost associated with Step 1 in the proposed Machine Learning strategy is *not* negligible since creating comprehensive databases may involve performing hundreds of numerical simulations. However, for the amount of parameters optimized (over 200) and the type of problems to be solved (i.e., the inverse problem in RANS *and* LES), the computational cost is considered inferior to previous optimization algorithms used in the context of draft tubes. Moreover, conversely to evolutionary algorithms and adjoint methods, the numerical simulations performed to create the database are not aimed to resolve a single task but rather to cover a large solution space (e.g., operating conditions and flow conditions), meaning that they can be *reused* to solve many types of problems. It should be noticed, however, that the proposed approach has some limitations, especially in terms of what can be used as inputs and outputs for the ANN. For instance, if the goal is to reproduce the experimental results inside the draft tube discussed in Chapter 4, ANN's inputs would be *limited* by what has been measured (both in terms of location and data type) during the experimental campaigns. Thus, even though numerical simulations give access to comprehensive information about the flow field inside the computational domain, we could *not* use, for example, the mean velocity field measured at station EX as an input because this quantity has not been measured this far downstream inside the draft tube. Similarly, we could *not* use any individual component of the Reynolds stress tensor as an input because it has not been measured anywhere on the flow. Conversely, ANN's outputs are not limited by the experimental data, but by the parameters that were modified during the creation of the database, meaning that it is not possible to optimize a quantity that was not varied when creating the database. Otherwise, the proposed approach is relatively flexible and can be easily applied to different types of problems and flow configurations.

Chapter 6

Test case: swirling flow inside conical diffuser

Contents

6.1 Introduction

As discussed in the previous chapter, the proposed Machine Learning strategy has a significant computational cost, particularly associated with the generation of the database used to train the ANN model. Moreover, due to its innovative nature, many important aspects of this strategy are not fully known *a priori* and must be investigated (e.g., the size of the database, the structure of the data used as inputs and outputs for the ANN, the architecture for the ANN etc.). Thus, before applying the proposed Machine Learning strategy to the complex and computationally demanding draft tube flow, a simpler case of the swirling flow inside a conical diffuser is examined in this chapter. This particular flow has been used many times in the past as a validation case for the numerical approaches in other studies due to its similar characteristics to draft tube flows (e.g., unsteady, swirling and subjected to adverse pressure gradients), especially those from bulb turbines. Despite its simplicity, the delicate balance between core flow recirculation and boundary layer separation renders accurate numerical simulations of this flow a real challenge to perform, while its relatively low computational cost and high sensitivity to inlet boundary conditions (which are only partially known) makes of the swirling flow inside the conical diffuser the ideal case to apply and explore the proposed Machine Learning strategy. The goal with this chapter is, therefore, to acquire some knowledge in this simpler yet challenging flow case and to use this knowledge in the more complex and computationally expensive draft tube configuration studied in Chapter 4. First, the characteristics of the conical diffuser are presented and the previous numerical works that investigated it are discussed.

Then, steady RANS and LES computations are performed using standard approaches to define both inlet boundary conditions and numerical domain in order to establish a baseline to which the proposed Machine Learning strategy can be compared to. Finally, the proposed strategy is thoroughly applied, first in RANS and then in LES, to different configurations of the test case and the obtained results are compared with the reference simulations and experiments.

6.2 Flow configuration

The test case chosen to explore the Machine Learning strategy consists in the swirling flow inside a conical diffuser experimentally studied by Clausen *et al.* [19] and which is part of the classic *European Research Community On Flow Turbulence And Combustion* (ERCOFTAC) database (Case 60: Swirling Boundary Layer in Conical Diffuser). As shown by the scheme in Fig. 6.1, the diffuser was 510mm long, had an inlet diameter of $D_0 = 260$mm and a 20° opening angle. A constant air flow, with kinematic viscosity $\nu = 1.5 \times 10^{-5}\text{m}^2/\text{s}$, was forced through the diffuser and discharged into the atmosphere at a flow rate $Q = 0.616\text{m}^3/\text{s}$, which corresponds to an average axial velocity at the inlet, $U_b = 11.6$m/s and a Reynolds number, Re, equal to 2×10^5.

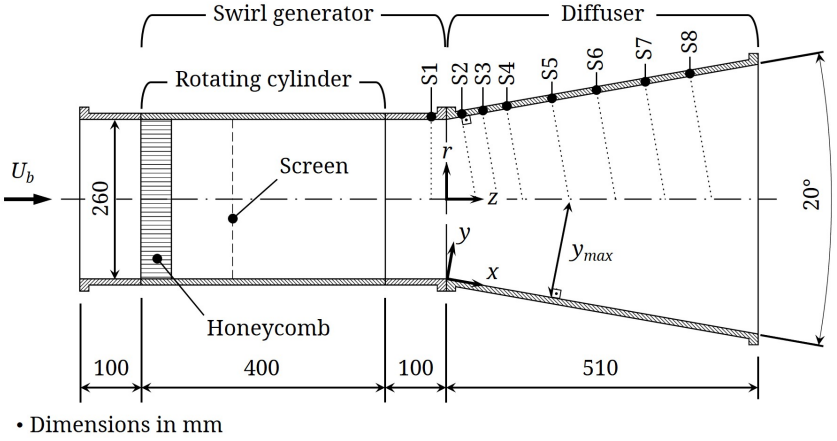

Figure 6.1: Scheme of the conical diffuser studied by Clausen *et al.* [19].

Flow swirl was generated by a 400mm rotating cylinder (including a honeycomb screen) positioned 100mm upstream the diffuser. The corresponding swirl number, S_w, given by Eq. (6.1) and defined as the ratio between the axial flux of angular momentum and the axial flux of axial momentum multiplied by the radius was taken equal to 0.295. It was finely adjusted, so the flow remains attached to the diffuser walls and, at the same time, no recirculation was created in its core.

$$S_w = \frac{\int_0^R r^2 \left|U_\theta\right| U_z dr}{R \int_0^R r U_z^2 dr} \tag{6.1}$$

Measurements are taken with respect to two coordinate system in the conical diffuser, as shown in Fig. 6.1. Inside the upstream swirl generator, U_z is the mean axial velocity of the flow, U_r is the mean radial velocity and U_θ is the mean circumferential velocity. However, inside the cone, Clausen *et al.* [19] used a local coordinate system composed by an x-axis and

y-axis, respectively parallel and normal to the walls, to measure the velocity profiles. In this coordinate system, U_x is the mean velocity component parallel to the walls (streamwise) and U_y is the mean velocity component perpendicular to the walls (normal). Notice that the mean circumferential velocity component is the same in both coordinate systems and that U_x and U_z, as well as U_y and U_r, are equivalent at the first measurement station, S1. The mean velocity profiles were measured using hot-wires at eight traverses perpendicular to the walls, shown as stations S1 to S8 in Fig. 6.1. The positioning of the traverses is accurate to 0.01mm, whereas the estimated error in the mean velocities is approximately 2%. Both mean streamwise (U_x and U_z) and circumferential (U_θ) velocity components were measured by Clausen *et al.* [19] during the experiments, but the mean velocity normal to the walls U_y as well as the mean radial velocity U_r components were not measured due to some technical difficulties. The six components of the Reynolds stresses were also measured at the same eight traverses, though they were limited to the region very close to the walls and their accuracy was estimated in 10%. Nevertheless, it is possible to determine the turbulence kinetic energy, k, from these measurements using Eq.(6.2):

$$k = \frac{1}{2}\left(u'^2_r + u'^2_\theta + u'^2_z\right) \tag{6.2}$$

Finally, in addition to the mean velocity and turbulence kinetic energy profiles, the evolution of static pressure at the walls was also measured in the form of the pressure coefficient, C_p, defined by (6.3), where P_w is the static pressure at the wall, P_{atm} is the atmospheric pressure and ρ is the density of the air.

$$C_p = \frac{P_{\text{wall}} - P_{\text{atm}}}{0.5\rho U_b^2} \tag{6.3}$$

6.3 Previous numerical studies of the case

The first numerical work to study the swirling flow inside the ERCOFTAC conical diffuser was conducted by Armfield *et al.* [4] in 1990. The performance of the standard k-ϵ and Algebraic Reynolds Stress (ASM) turbulence models were compared in a numerical domain that started at the second measurement station, S2 (see Fig. 6.1) and that was simplified by considering the flow as axisymmetric. A two-layer wall function was used, and inlet boundary conditions consisted in experimental U_x, U_θ and k profiles at S2. However, as U_r is unknown from the experiments, *it was assumed to be equal to zero.* The dissipation rate, ϵ, was also adjusted so the correct axial variation of k at the centre of the diffuser. At the end, both turbulence models yielded similar results and mean velocity and turbulence kinetic energy profiles agreed quite well with experiments.

A slightly modified version of the numerical domain studied in Armfield *et al.* [4] was investigated during an ERCOFTAC Workshop held in Karlsruhe in 1995 [130]. The numerical domain started at the first measurement station, S1 (instead of S2), but the flow was still considered as axisymmetric. Inlet boundary conditions came from the experimental mean velocity and turbulence measurements at this station, but, in their contribution to this workshop, Vu and Shyy argued that considering $U_r = 0$ at the inlet was not realistic as station S1 was too close to the divergence section of the diffuser. Therefore, they estimated this velocity component by moving the inlet section and extending the domain 100mm further upstream, imposing the same boundary conditions (including $U_r = 0$), performing a preliminary flow analysis for the conical diffuser and recover U_r at the original inlet position, station S1. Multiple turbulence models, such as Reynolds Stress Models (RSM), ASM, k-ϵ and k-ω, were tested during the Workshop and, when required, the dissipation rate, ϵ, was determined similarly to Armfield *et al.* [4]. In general, the results obtained during the workshop did not agree very well with the experimental data, especially because mean axial velocity profiles were systematically underestimated near

the walls and overestimated at the centre region of the diffuser.

A few years later, in 2002, Mauri [98] investigated a 3D version of the numerical domain proposed in the ERCOFTAC Workshop held in Karlsruhe [130] to validate his numerical methods for the simulations of the FLINDT draft tube [5]. Steady RANS simulations using the standard k-ϵ turbulence model coupled with wall functions were conducted with inlet boundary conditions coming from the experimental measurements at station S1. U_r at the inlet was considered equal to zero once again, but the major difference this time was the turbulence kinetic energy considered as 5% of the total energy, and the dissipation rate, considered as $\epsilon = k^{3/2}/0.04D_0$. Overall, the results did not agree with experimental measurements as the mean streamwise velocity peaks near the walls were underpredicted near the walls, leading thus to an overestimation of this velocity component at the centre of the diffuser. Moreover, due to the fairly arbitrary turbulent boundary condition imposed at the inlet, k values were very overpredicted at the initial portion of the draft tube and underpredicted at closer to its exit.

In 2006, Gyllenram and Nilsson [63] performed Very Large-Eddy Simulations (VLES) of the flow inside the conical diffuser using the k-ω turbulence model. To deal with the problem of unknown U_r, the numerical domain was extended upstream to include the cylindrical swirl generator shown in Fig. 6.1. The radial velocity component was considered equal to zero at this *new* inlet position, and the axial and circumferential velocity profiles were accordingly adjusted by a polynomial equation. Turbulent intensity was taken equal to 10% and the system of equations was closed by a turbulent length scale, $l_e = 3.2$mm, which corresponds to the size of a cell in the rotating honeycomb screen. However, the obtained results were very dependent on both the turbulence model and grid refinement. Moreover, in spite of limited comparisons with experimental data, U_x values were systematically underpredicted near the walls. Indeed, the boundary layer even detached from the walls in some cases.

Bounous [12] conducted an extensive study of the test case in the context of the Turbomachinery Working Group in the Third OpenFOAM Workshop organized in 2008 [117]. Simulations were conducted in RANS using both k-ϵ and k-ω SST turbulence models. Aside from the numerical domains studied in original ERCOFTAC Workshop [130] and in Gyllenram and Nilsson [63], another configuration containing a straight upstream and downstream extensions was investigated by Bounous [12]. Amongst the two turbulence models and other numerical parameters, many inlet boundary conditions were investigated in his study, although U_r was always set equal to zero at the inlet. Most of his simulations ended up underestimating U_x near the walls and, as a result, overestimating it at the centre of the diffuser. However, a relatively good agreement with the experimental data was obtained when using the extended numerical domain, turbulent inlet boundary conditions proposed in Gyllenram and Nilsson [63], a constant inlet mean axial velocity and a linearly varying inlet mean circumferential velocity.

Still in 2008, Payette [123] also conducted an extensive study of the ERCOFTAC conical diffuser using steady RANS, again as a mean of validating his numerical methodology for some draft tube flow simulations. Initial computations of the flow inside the numerical domain without upstream extension proved the k-ω SST turbulence model to be very susceptible to boundary layer separation inside the conical diffuser, conversely to previous simulations using the k-ϵ turbulence model. Indeed, Payette [123] argued that these early simulations were actually affected by the model's tendency to delay flow separation and that the problem with the k-ω SST simulations was caused by the specification of $U_r = 0$ at the inlet of the numerical domain (station S1). A separate simulation of the conical diffuser with a 500mm upstream extension was then performed to determine the correct level of U_r at this location, very similarly to what was proposed by Vu and Shyy in their contribution to the original ERCOFTAC Workshop [130]. Conversely to these authors though, the radial velocity profile recovered by Payette [123] along with the experimental U_z and U_θ and the turbulent inlet boundary conditions proposed by Armfield [4], yielded very good (arguably the best) results for the conical diffuser numerical domain without upstream extension.

A few years later, in 2010, again in the context of draft tube flow numerical simulations, Bélanger-Vincent [8] performed RANS, URANS, DES and Delayed DES (DDES) computations of the swirling flow inside the conical diffuser. The numerical domain had an upstream and downstream straight extensions (similarly to Bounous [12]) precisely to avoid some problems with proper inlet boundary conditions as discussed in Payette [123]. U_r was set equal to zero and the rest of the inlet boundary conditions came from Bounous [12], i.e., a constant mean axial velocity profile, a linearly varying circumferential velocity and, in the case of RANS and URANS, the turbulent inlet boundary conditions as proposed in Gyllenram and Nilsson [63]. Both turbulence models yielded identical results but underpredicted U_x and U_θ values near the walls. DES also did not predict very well the flow behaviour inside the conical diffuser and results were extremely sensitive to turbulent inlet conditions. Only DDES using the k-ω SST turbulence resulted in a good prediction of the mean streamwise velocity field inside the diffuser, although it depended on some *ad hoc* blending function to control the boundary layer separation at the walls.

A very similar investigation was conducted by Taheri [149], but instead of k-ω SST, he used Spalart-Allmaras turbulence model. Conversely to Bélanger-Vincent [8], though, Taheri [149] was not to obtain good DDES results. In addition to the extended numerical domain, Taheri [149] also investigated the numerical domain starting at station S1 and applied the exact same procedure discussed in Payette [123] to determine the optimal U_r profile at this location. However, his URANS simulations using Spalart-Allmaras turbulence model were once again in disagreement with the experimental data. The problem was that the flow behaviour inside the conical diffuser was very sensitive to small variations in the mean velocity profiles caused by the upstream extension and to the imposed turbulent inlet boundary conditions, which are more complex to define in DDES than in RANS.

Duprat [36] used the swirling flow inside the conical diffuser to investigate three synthetic turbulence techniques for his LES of a draft tube flow. The first technique consisted in introducing an extension upstream the diffuser and map the turbulent field at a downstream cross-section back into the inlet of the numerical domain. Despite adding a forcing term to ensure the appropriate flow rate and swirl number at the station S1, the correct mean velocity profiles distribution was not recovered, and the obtained results were very poor in comparison with the experiments. Thus, changing to a numerical domain starting at station S1 and imposing the experimental U_x and U_θ profiles measured at this location, the second and simplest technique explored by Duprat [36] consisted in introducing a white-noise random component to the mean inlet velocity field. However, as previously explained in Section 2.4 and actually observed by Duprat [36], the synthetic fluctuations generated with this method completely lack spatial and temporal correlations and, as a result, they are instantly destroyed by the Navier-Stokes solver, mostly dissipating close to the inlet of the domain. Finally, the third and last technique consisted in injecting the fluctuations issued from a separate precursor pipe flow simulation. The results were indeed improved compared to the simple white-noise case, but performing precursor simulations of more complex flows, such as draft tubes, is computationally expensive and the application of this technique is thus very limited. Moreover, these fluctuations would still create a transition region within the numerical domain, which potentially affects the energy balance of the flow (see the discussion of the draft tube in Chapter 4).

Based on these discussions, it is clear how important it is to impose proper inlet boundary conditions in the case of the swirling flow inside the ERCOFTAC conical diffuser. Moreover, in spite of the many efforts conducted along the years to correctly determining some unknown quantities for this case, particularly the mean radial velocity component, U_r, the proposed solutions do not work in multiple turbulence methods and/or rely on actually simulating the flow upstream the conical diffuser, which is simply not applicable in the case of a real draft tube due to the complexity of the flow coming from the guide-vanes and runner. Finally, while RANS and DES simulations are already quite sensitive to turbulent inlet conditions, LES adds

another difficulty due to the complexity of generating appropriate synthetic fluctuations, with proper intensity, characteristic length scale and the right anisotropy. Therefore, being able to determining a method capable of imposing proper inlet boundary conditions for the swirling flow inside the conical diffuser and that is applicable to multiple turbulence methods and flow configurations is indeed very relevant and a good benchmark for the proposed Machine Learning strategy discussed in Chapter 5.

6.4 Basic inlet boundary conditions

Before applying the proposed Machine Learning strategy to determine the inlet boundary conditions for the conical diffuser, it is necessary to establish a baseline to which its performance can be compared. The simplest approach to simulate this flow consists in following the recommendations given for the first ERCOFTAC Workshop [130] that studied this case. The numerical domain is shortened with respect to the original configuration shown in Fig. 6.1 since the upstream swirl generator is not considered and the available experimental data at the first measurement station is used as inlet conditions for the computations. As a result, this simplified approach has been used in many works that investigated this test case [98, 12, 117, 123, 36, 149].

6.4.1 Numerical setup

The numerical domains considered for the *reference* simulations are shown in Fig. 6.2. For the steady RANS simulations using the k-ω SST turbulence model, the flow statistical axisymmetry is assumed to restrict to 2D computations and therefore reduce the overall computational cost. Conversely, in LES, the complete 3D geometry of the diffuser has to be considered. In both cases, the domain consists in the conical diffuser, including a very short cylindrical extension upstream the cone. The inlet of the domain corresponds to the first measurement station, S1, whereas the outlet is positioned at the end of a 500mm straight extension downstream the diffuser exit. In the original configuration, the flow discharges directly to the atmosphere after passing through the diffuser, however, the downstream straight extension helps with the convergence and stability of the numerical solution without interfering with the flow behaviour inside the cone [123]. A classical mesh convergence study was conducted in RANS where different levels of refinement for a block structured hexahedral mesh were tested to guarantee that results were indeed independent of the spatial discretization. The final mesh had approximately 6×10^3 elements and $y^+ \approx 1$. In the case of LES, an automatic two-criteria based mesh adaptation [9] was used in the spatial discretization study of the domain and the final mesh was composed by 3.3×10^6 tetrahedral elements. Moreover, like in the draft tube case, 4 layers of prismatic elements of aspect ratio equal to 4 were positioned at the walls to reduce the maximum y^+ to approximately 20 and to keep the simulation at a reasonable computational cost.

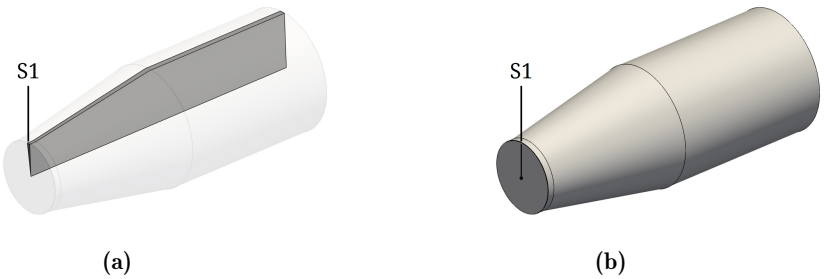

Figure 6.2: Numerical domains for reference simulations using (a) RANS and (b) LES.

Following the previous draft tube simulations in this thesis, the commercial flow solver ANSYS CFX is used to perform the steady RANS simulations using the k-ω SST turbulence model

[101], as it has been shown to be the most appropriate for this particular flow [123]. Due to the swirling nature of the flow, two corrections are applied to the production term in the k and ω transport equations, one to limit its values at stagnation points [74] and another to render it more sensitive to the effect of streamline curvature and system rotation [139]. The *high resolution scheme* of ANSYS CFX [3] is used for the advection term and a first order scheme is used for the two extra k and ω transport equations. LES are once again performed in YALES2 using its incompressible fractional step-solver, finite-volume formulation and 4^{th} order space and time numerical schemes. The Dynamic Smagorinsky turbulence model [58] is used to model the SGS effects on the flow and time steps are evaluated so CFL is always smaller than 0.9 in the whole numerical domain. In all LES cases, an initial simulation is performed to stabilize the flow field within the diffuser and only then a second simulation is run during the equivalent of ten complete flow passages throughout the domain to accumulate the statistics used in the final analysis of the flow.

6.4.2 Boundary conditions

As the inlet of the numerical domain corresponds to the first measurement station, S1, inlet boundary conditions consist in the experimental mean velocity and turbulence kinetic energy profiles measured at this location. These profiles are shown in Fig. 6.3 as a function of the normalized distance to the walls, y/y_{max}, where y is the normal distance to the walls, y_{max} is the maximum distance between the walls and the centreline of the diffuser at the i^{th} section, and $y/y_{max} = 1$ correspond to the axis of the conical diffuser. Their distribution over the inlet plane is considered as axisymmetric, similarly to the previous draft tube simulations conducted in this thesis. Mean velocity profiles are interpolated from the experimental data and an extra point is added to ensure that the velocity is actually zero at the walls. Since U_r was not measured during the original experiments conducted by Clausen *et al.* [19], it is set equal to zero at the inlet, which is indeed in accordance with most of the simulations conducted in the aforementioned ERCOFTAC Workshop that studied this case [130].

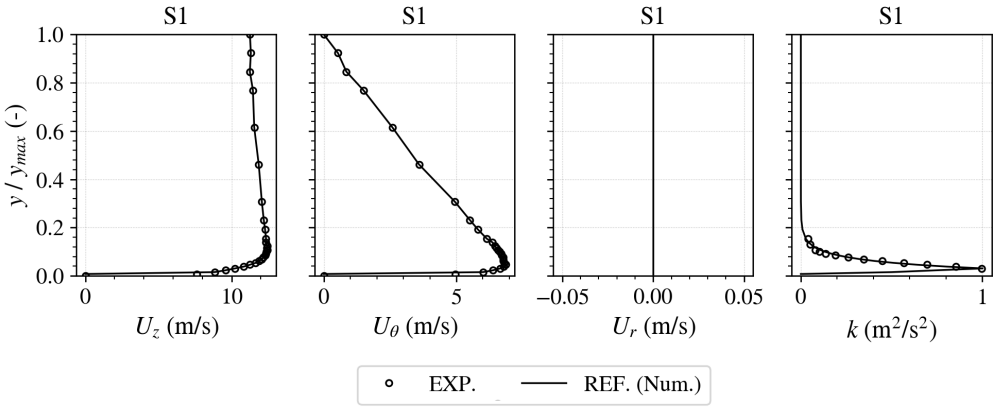

Figure 6.3: Mean velocity and turbulence kinetic energy profiles imposed at the inlet of the reference ERCOFTAC conical diffuser simulations.

For the RANS simulations using the k-ω SST turbulence model, turbulent inlet conditions are necessary to close the system of equations. The turbulence kinetic energy profiles obtained from the Reynolds stresses measurements can be used in this regard, however, since these measurements are limited to the region very close to the walls, between $y/y_{max} = 0.03$ and 0.15, as shown in Fig. 6.3, k is assumed to vary linearly between $k = 0$ at the walls and its value at the first experimental point (at $y/y_{max} \approx 0.03$). Moreover, an exponential regression curve [123] given by Eq. (6.4) is used to complete the profile between $y/y_{max} = 0.15$ and 1.0:

$$k = e^{29.2(r/r_{max})-28.3} \tag{6.4}$$

Finally, an equation for the dissipation rate, ϵ, given by Eq. (6.5) is used to close the system of equations. This equation was first proposed by Armfield [4] and $C_\mu = 0.09$ is the classical constant of the k-ϵ and k-ω models and D_0 is the diameter of the diffuser inlet. Most of the studies in the original ERCOFTAC Workshop [130] used a similar approach, but Payette [123] also used Eq. (6.5) to obtain his best results for the swirling flow inside the conical diffuser.

$$\epsilon = \frac{C_\mu^{3/4} k^{3/2}}{0.01 D_0} \tag{6.5}$$

In the case of LES, as no turbulent inlet boundary conditions are necessarily required and since we want to avoid the use of *ad hoc* solutions specific to the test case, two simple approaches are considered: no inlet turbulence or a homogeneous isotropic synthetic turbulent field at the inlet plane. The same synthetic turbulence generation scheme employed for the case of the draft tube case studied in Chapter 4 and available in YALES2 (see Chapter 2, Section 2.4) is used. The normalized turbulence kinetic energy profile follows the same construction applied in RANS, i.e., a linear variation between $y/y_{max} = 0$ and 0.03, and Eq. (6.4) for the rest of the profile, whereas the injection speed, $\overline{U}$, is assumed to be equal to the average axial velocity at the inlet, $U_b = 11.6$m/s. The synthetic turbulence length scale, l_e, is considered as being equal to 10% of the inlet diameter D_0, or 26mm, which corresponds to a classical characteristics turbulent length scale for pipe flows or channel flows, whereas the velocity scale, u', is approximately 0.82mm, or 7% of the average axial velocity, U_b, and is estimated from Eq. (6.6) and the maximum experimental value of k assuming isotropic turbulence:

$$u' = \sqrt{\frac{3}{2} k_{\max}} \tag{6.6}$$

Finally, an average static pressure equal to 0 is applied at the outlet of the numerical domain and no-slip condition is imposed at the walls. Following the previous draft tube simulations conducted in this thesis, an automatic wall treatment [3] is used in RANS k-ω SST simulations and the wall model proposed by Duprat *et al.* [37] is used in LES.

6.4.3 Comparison with experimental data

Figure 6.4 shows the comparison between the mean streamwise velocity profiles obtained by the numerical RANS and LES simulations of the reference conical diffuser configuration and the experimental measurements conducted by Clausen *et al.* [19]. Both turbulence models yield very similar results up to station S4 and are in relatively good agreement with the experimental data. At station S5, the k-ω SST turbulence model slightly underestimates U_x values close to the walls ($y/y_{max} = 0.0$) and, as a consequence, overestimates its values towards the centre of the flow ($y/y_{max} = 1.0$). Between stations S6 and S8, this behaviour is amplified and results in a boundary layer separation between stations S5 and S6, which is indeed confirmed by negative U_x values in vicinity of the walls. This separation was already observed in Payette [123] and is symptomatic of RANS simulations using the k-ω SST turbulence model and with zero inlet radial velocity. Conversely, LES results show no signs of separation and the near-wall behaviour of the flow inside the diffuser is well captured in both cases, i.e., with or without inlet turbulence. Nevertheless, U_x values are still overestimated in the centre of the diffuser, especially between stations S5 and S8. This is due to the poor prediction of the streamwise velocity peak, which is both underestimated and further away from the walls compared to the experimental data. In any case, injecting synthetic fluctuations had little effect on the profiles of U_x.

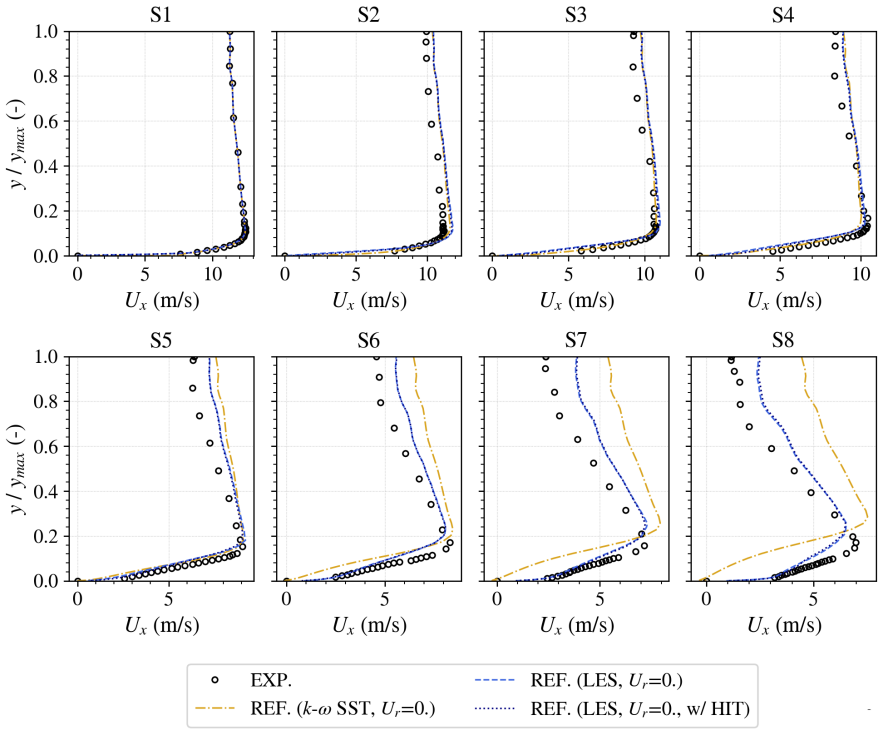

Figure 6.4: Comparisons of mean streamwise velocity profiles inside the conical diffuser for the reference simulations using RANS and LES.

The comparisons between mean circumferential velocity profiles obtained by the RANS and LES numerical simulations and the experiments conducted by Clausen *et al.* [19] are shown in Fig. 6.5. LES results match very well the experimental measurements, in spite of the discrepancies for U_x previously discussed. Moreover, injecting synthetic fluctuations had a negligible effect on U_θ profiles. RANS results, on the other hand, yield very similar results to LES up to station S4, but the boundary layer separation also interfered with the mean circumferential velocity profiles within the conical diffuser. Starting at station S6, the near wall peak of U_θ moves away from the walls and this velocity component is greatly overestimated towards the centre of the flow.

The turbulence kinetic energy profiles inside the diffuser for these reference simulations are shown in Fig. 6.6. Starting with the RANS k-ω SST results, the turbulent inlet boundary conditions are good at predicting the k values until station S4. At station S5, the turbulence kinetic energy peak is slightly underestimated compared to the experiments, though it is at the correct level at station S6. However, between stations S6 and S8, this peak moves away from the walls and its maximum numerical value is greatly overestimated at station S8, coinciding with the flow separation predicted by the k-ω SST turbulence model. In the case of LES, as expected, turbulence kinetic energy is equal to zero at the inlet of the numerical domain (station S1) in the case without synthetic fluctuations. In the case with imposed synthetic fluctuations, the profile of k matches the experimental data at station S1. However, as a result of flow shear at the walls and unrealistic turbulence decay close to the inlet of the numerical domain, both LES cases (with/without turbulent inflow) present very similar results by station S2. Indeed, their values are largely overestimated in comparison to the experimental measurements between stations S3 and S5, and slowly decrease until finally match the experimental results at stations S7 and S8. Another problem with these results is that, although the near-wall peak is well predicted, its profiles is wider in LES than in the experiments. Finally, it should be noticed that the inlet turbulence measured in the experiment is anisotropic. Indeed, both $\langle u'_r u'_\theta \rangle$ and $\langle u'_r u'_z \rangle$ components exhibit negative values near the wall due to the radial variations of the circumferen-

tial and of the axial mean velocity respectively. In the case of the LES with turbulence injection at the inlet, we have checked that these correlations are zero at station S1 due to the isotropic nature of the synthetic fluctuations.

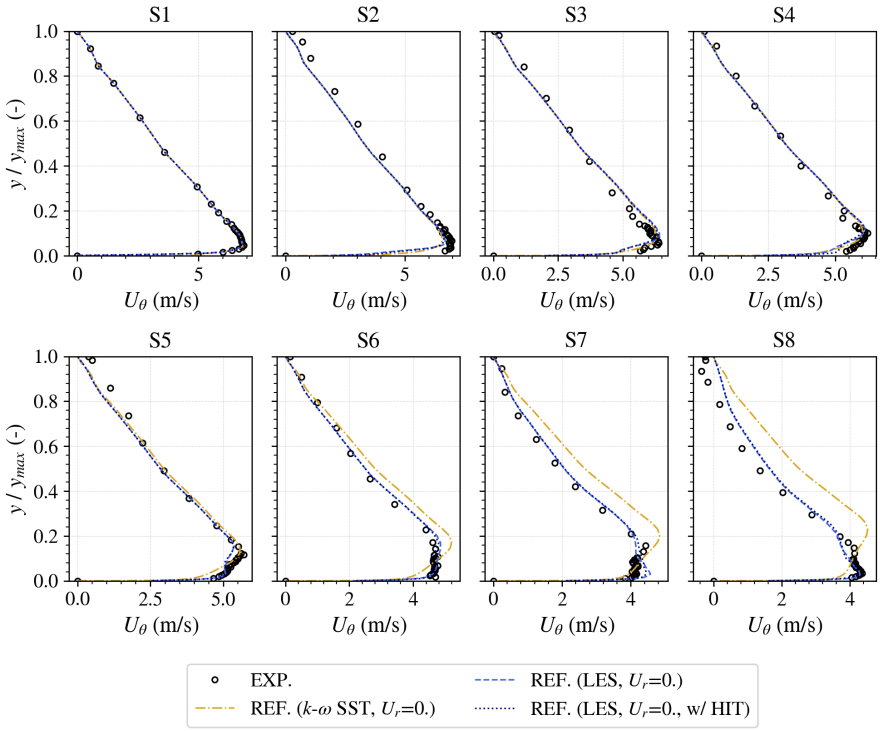

Figure 6.5: Comparison between mean circumferential velocity profiles inside the conical diffuser obtained experimentally by Clausen *et al.* [19] and the reference RANS k-ω SST and LES simulations.

6.5 Application of the proposed Machine Learning strategy

Similarly to the reference draft tube simulations discussed in Chapter 4, these results demonstrate that basic inlet conditions are not capable of providing satisfactory results for the simple case of the swirling flow inside the conical diffuser. Indeed, as pointed out in Section 6.3, this problem has been observed in previous numerical studies of this case and the main cause for these discrepancies comes from inadequate inlet boundary conditions, particularly the unknown U_r velocity component which is assumed to be zero. In LES, another key issue is the ability to generate and inject proper synthetic fluctuations into the simulation, with the right intensity and the right characteristic length scale and the right anisotropy. To circumvent these problems, the proposed Machine Learning strategy introduced in Chapter 5 is applied to the present ERCOFTAC conical diffuser case. The goal is to determine the optimal conditions that should be imposed at the inlet of the numerical domain (e.g., station S1) so the recovered downstream flow is in good correspondence with the experimental measurements by Clausen *et al.* [19]. In the following sections, a thorough application of this strategy will be presented and, at the end, the results compared to the previous reference simulations.

6.5.1 Step 1: Numerical setup and database generation

The first step in the proposed Machine Learning strategy is to create a database containing the results of multiple simulations of the case we want the inlet conditions to be optimized for. Prior to launch any of these simulations, it is necessary to define the numerical domain that is going to be used. In RANS, the reference domain starting at station S1 and shown in

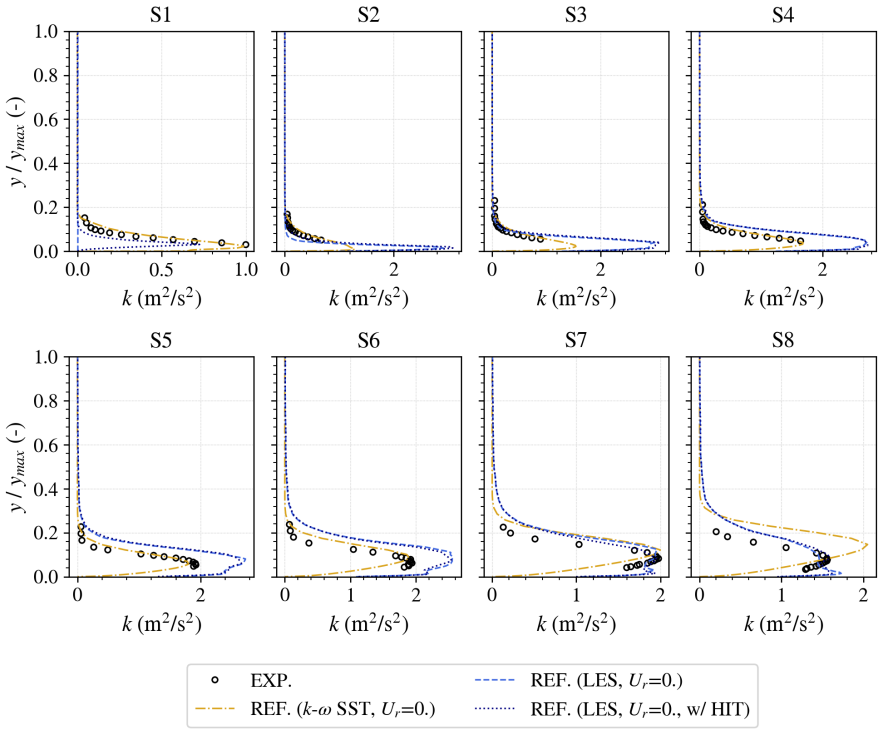

Figure 6.6: Comparison between turbulence kinetic energy profiles inside the conical diffuser obtained experimentally by Clausen *et al.* [19] and the reference RANS k-ω SST and LES simulations.

Fig. 6.2 can be employed since only mean quantities need to be prescribed and therefore no artificial upstream inlet extension are required to allow fluctuations correlations to build up. However, similarly to previous numerical works that simulated the upstream swirl generator [63, 12, 123, 8, 149], such an extension may improve the prediction of missing flow quantities like U_r. Conversely, in the case of LES, it will be shown that the upstream extension is important as it gives the incoming synthetic fluctuations the space and time required for them to develop before entering the diffuser.

To determine the length of the upstream extension, a first approach would be to it equal to the length of the swirl generator shown in Fig. 6.1, i.e., 500mm, as in several previous authors [63, 12, 123, 8, 149]. However, it is essential for the success of the proposed Machine Learning strategy that the downstream flow behaviour be dependent on the boundary conditions imposed at the inlet of this extension. A real concern for the case of the swirling flow inside the conical diffuser is that if the upstream extension is too long, the turbulence generated at the walls due to flow shear becomes the dominant effect on the downstream flow. Therefore, a parametric study has been conducted to evaluate the sensitivity of the downstream kinetic energy to the upstream synthetic turbulence parameters, specifically u' and l_e, using the two different extended numerical domains shown in Fig. 6.7, with upstream extension lengths equal to 500mm and 250mm.

In the parametric study, the velocity scale, u', is varied between $1.5\% \leq u' \leq 15\%$ of the average axial velocity at the inlet, U_b, whereas the length scale, l_e, is varied between $2\% \leq l_e \leq 40\%$ of the extension diameter, D_0. Mean velocity and turbulence kinetic energy profiles are held constant during the simulations. The results for the evolution of k between the inlet of the extended domains (station IN) and the first measurement station, S1, are shown in Fig. 6.8. It is clear that for the longer extension, with 500mm, the values of k in the vicinity of the walls at station S1 do not depend on the imposed u' and l_e. Indeed, the lines defining the minimum and maximum values of k overlap at the walls nearby station -200. Moreover, the numerical results at station S1 are *always* overestimated compared to the experiments. Conversely, the

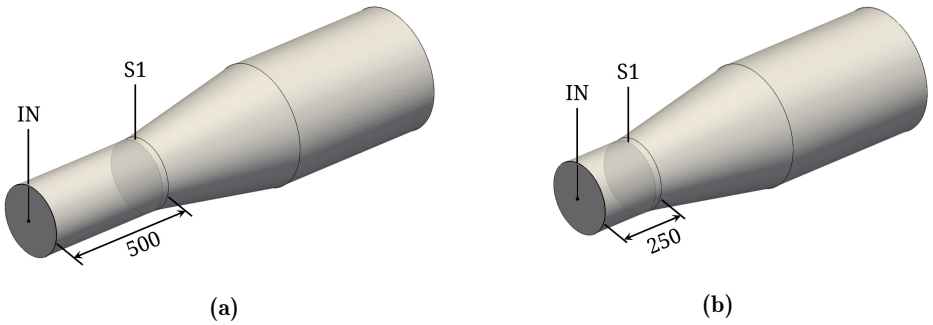

Figure 6.7: Numerical domains with upstream extension used for the parametric study in LES. (a) 500mm long extension; (b) 250mm long extension.

results for the turbulence kinetic energy profiles at station S1 obtained with the shorter 250mm extension are still dependent on the upstream inlet boundary conditions and, more importantly, experimental values are within the solution space of the parametric study. Thus, the proposed Machine Learning strategy is applied to the shorter extended numerical domain in LES. In RANS, in addition to the reference numerical domain discussed in Section 6.4, the proposed strategy is also applied to a simplified version of this shorter domain shown in Fig. 6.9

Another important aspect of the proposed Machine Learning strategy explained in Chapter 5 is that each simulation in the database is run with a different set of inlet boundary conditions. In RANS, these conditions are defined by four different profiles: three mean velocity components, U_z,U_θ and U_r, and one turbulence kinetic energy profile, k. The dissipation rate, ϵ, is not optimized and is defined by Eq. (6.5), as in the reference simulations. In the case of LES, the two synthetic turbulence parameters varied in the previous parametric study, notably u' and l_e, are also required to completely define the inlet boundary conditions for the simulation. One key aspect of these inlet boundary conditions is that they are able to cover a sufficiently large solution space, so the final ANN have enough information to deliver good solutions. Thus, each inlet profile for each simulation in the database was automatically generated by a Python script using B-splines [15] and a Sobol quasirandom sequence [140]. At the end, 1700 different sets of inlet boundary conditions have been generated and their mean, minimum and maximum distributions are shown in Fig. 6.10 compared to the experimental values measured at station S1.

With both numerical domain and sets of inlet boundary conditions well-defined, the simulations to create the database for the proposed Machine Learning strategy can be launched. In RANS, two databases containing 800 simulations each were created: one for the reference numerical domain without upstream extension and another for the domain with a 250mm long upstream extension (see Fig. 6.9). The computational cost per simulation in each case is very low, especially due to the simplified geometry (e.g., axisymmetric), and a simulation running in 12 CPU cores takes approximately a minute to complete. In addition to that, a typical RANS solution in the database occupies 4 Mb (megabytes), meaning that each database takes approximately 3.2 Gb (gigabytes) of storage. In LES, a single database for the case with a short upstream extension (see Fig. 6.7b) was created, but it is smaller and contains the results of *only* 450 simulations in total. The built-in tool called *Y2 Workflow* is used to automatically launch and post-process the simulations in YALES2, ensuring statistically converged solutions with minimum user interference. A typical LES computation in the database takes 400 CPUh to run (140 CPUh for the stabilization step and 260 CPUh for the flow statistics accumulation) and occupies 3.4 Gb. Therefore, the creation of the LES database required approximately 180 000 CPUh and 1.7 Tb (terabytes) of storage space. While these numbers refer to the databases containing the complete LES and RANS numerical solutions, these results are post-processed at the end of each simulation and all flow field information measured at the eight stations inside

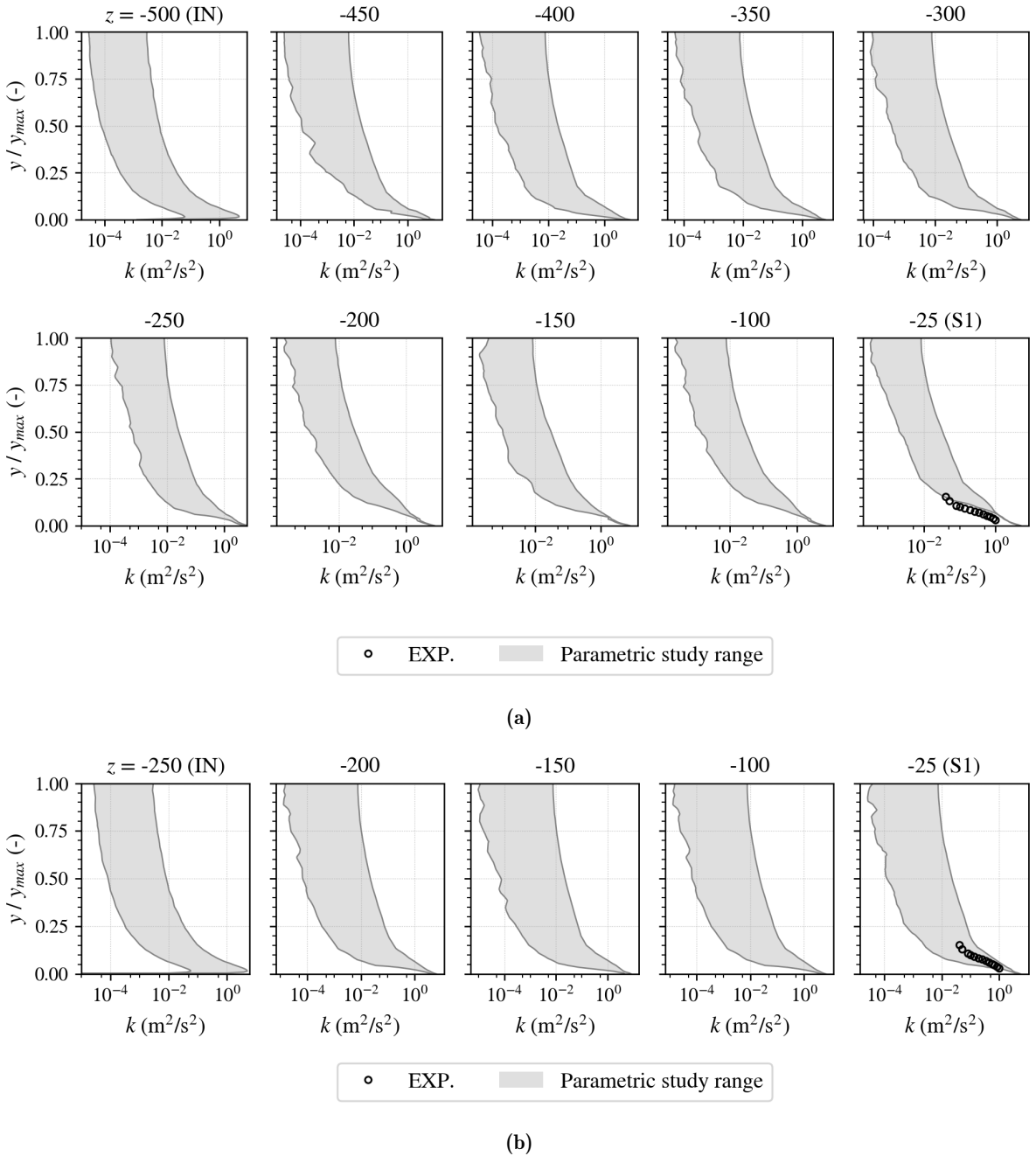

Figure 6.8: Evolution of turbulence kinetic energy profiles inside the upstream extension during parametric studies in LES. (a) 500mm long extension; (b) 250mm long extension.

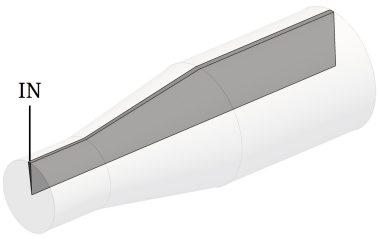

Figure 6.9: Simplified numerical domain with 250mm long upstream extension used in RANS.

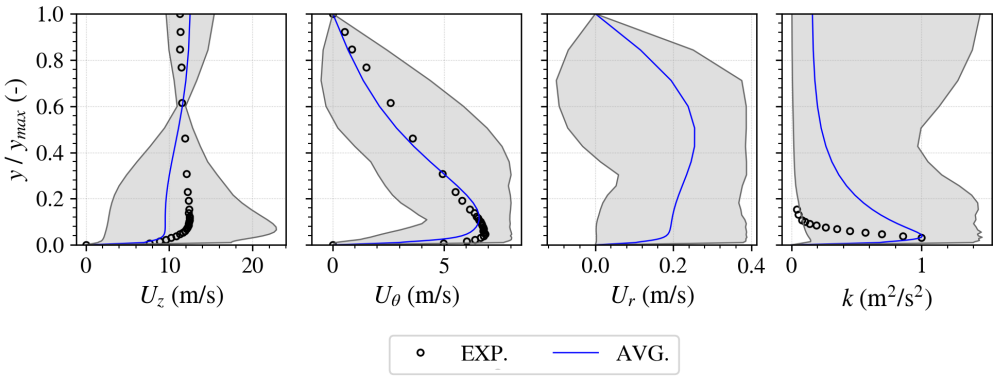

Figure 6.10: Distribution of the mean velocity and turbulence kinetic energy profiles generated for the proposed Machine Learning strategy.

the diffuser is stored along with the set of inlet boundary conditions that generated them. These profiles take only a few Mb of storage space and, as will be discussed in the following section, that is the only information required to create the ANN model.

6.5.2 Step 2: ANN architecture and training

Once the database is created, the second step in the proposed Machine Learning strategy consists in determining the non-linear model that will correlate the downstream flow field behaviour and the imposed inlet boundary conditions. This is achieved by training an Artificial Neural Network, ANN, specifically designed to *learn* these correlations in a supervised manner, i.e., by looking at examples of both inputs and outputs in the flow [60]. First, it is necessary to define the structure of the data used as inputs and outputs for the ANN. As already discussed in the presentation of the proposed Machine Learning strategy, inputs for the ANN are limited by the experimental data. In the case of the ERCOFTAC conical diffuser studied by Clausen *et al.* [19], this means that only mean streamwise and circumferential velocity profiles, as well as turbulence kinetic energy profiles at the eight stations inside the diffuser can be used in as inputs. However, since pre-processing these profiles can improve the training and performance of the ANN, each one of them is *scaled* by dividing their absolute values by their respective *area averaged value* at each section, i.e.,

$$\phi^* = \frac{\phi}{\dfrac{1}{S_{\text{sec}}} \displaystyle\iint_{S_{\text{sec}}} \phi dA} \tag{6.7}$$

where ϕ^* is the scaled variable (e.g., U_x^*, U_θ^* and k^*) and S_{sec} is the cross-section area. While this scaling regards each case in the database separately, a second pre-processing step, called *normalization*, is also applied to the ensemble of the inputs vectors [60], $\mathbf{X}$, so:

$$\mathbf{X}' = \frac{\mathbf{X} - \mu}{\sigma} \tag{6.8}$$

where μ and σ are a vector containing, respectively, the mean and the standard deviation of each variable. The goal of this second pre-processing step is to set the mean of the input vectors equal to 0 and its standard deviation equal to 1.

Outputs, on the other hand, are not limited by the experimental data, but by what was varied during the creation of the database. Indeed, since the goal of the proposed strategy is to determine the inlet boundary conditions, outputs consists in sets of inlet boundary conditions

imposed at each simulation of the database. In the case of RANS, this would correspond to the four inlet profiles (U_z, U_θ, U_r and k) and, in LES, we add the synthetic turbulence length and velocity scales (respectively, l_e and u'). Each profile was composed by 50 points, unevenly distributed along the inlet radius. For instance, points density is higher closer to the walls, where velocity and turbulence kinetic energy profiles gradients are more important. Finally, like the inputs, these profiles are also *normalized* before training.

With both inputs and outputs defined, the next step is to determine the architecture of the network, i.e., how the different layers will connect and what are the *hyperparameters* used in each one (e.g., the number of layers and its sizes, the activation functions, optimizer, learning rate etc.). Determining these different parameters is an optimization process by itself [10, 89, 46, 41], but in the context of this thesis, all of them have been determined manually. The final architecture of the ANN used in the optimization of the inlet boundary conditions for the three conical diffuser configurations considered in this chapter is shown in Fig. 6.11. The ANN consists in four or six MLP, one for each output, designed to learn in a supervised manner and composed only by fully-connected layers (FC). A concatenation layer is also used to concatenate the scaled and absolute inputs. Exponential Linear Units (ELU) activation functions [20] are used as, conversely to simpler and more commonly used Rectified Linear Units (ReLU) [109, 59], they can handle negative outputs, which turned to be important in our model. At the end of each fully-connected layer, a dropout rate of 50% is applied to reduce overfitting and improve the model's performance [144]. Moreover, as the problem being solved consists in a non-linear regression, the loss function is equal to the MSE between the training (true) set, $\mathbf{Y}$, and predictions, $\hat{\mathbf{Y}}$,

$$\mathrm{MSE} = \frac{1}{m}\sum_{i}^{m}\left(\hat{\mathbf{Y}} - \mathbf{Y}\right)^2 \tag{6.9}$$

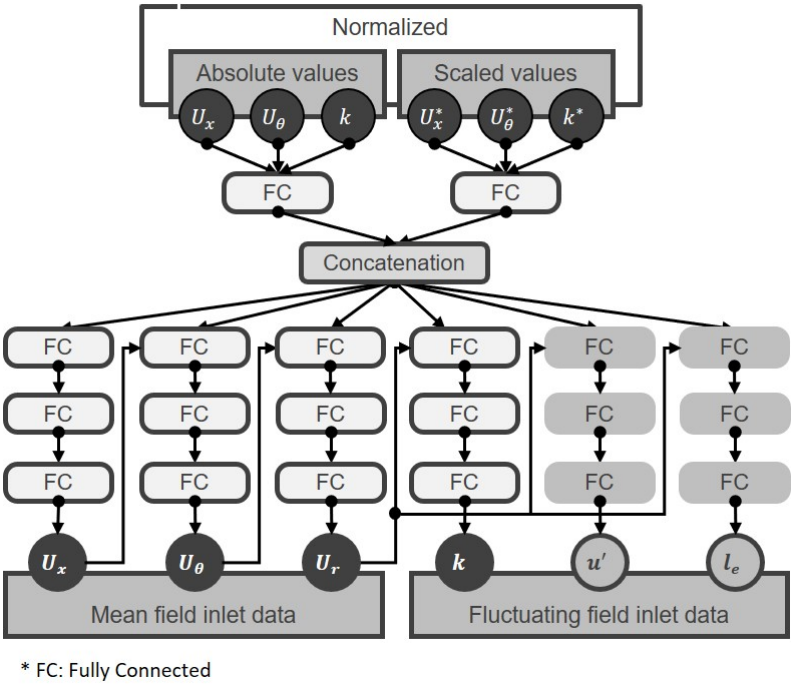

Figure 6.11: Scheme of the ANN architecture used to obtain optimized inlet boundary conditions for the conical diffuser case.

Finally, the machine learning algorithm is implemented in Python 3.7 using Tensorflow 2.1 and training is conducted for 5000 epochs using NAdam optimizer [34]. The results of these

trainings are discussed in Appendix A. In all three configurations investigated (two RANS and one LES), 400 cases from the database are used for training and 10% of it is used as validation for the model. The results from all stations are used as inputs for the ANN, except for station S2. At this location, the mean streamwise velocity profile seems underestimated with respect to the rest of the diffuser, which could potentially impact the performance of the ANN model. Moreover, since station S1 corresponds the inlet of the numerical domain without upstream extension, it is also not used in this particular case.

6.5.3 Step 3: Predicted inlet boundary conditions and results

RANS k-ω SST with/without upstream extension

Once training is finished, the last step in the proposed Machine Learning strategy consists in feeding the experimental data of the ERCOFTAC conical diffuser back into the trained ANN model and, as a result, it gives the optimized inlet boundary conditions for the numerical simulations. Starting with the numerical domain with upstream extension (see Fig. 6.9) simulated in RANS using the k-ω SST turbulence model, this case represents some previous attempts to recover the missing mean radial velocity profile at station S1 [63, 12, 123, 8, 149]. The boundary conditions imposed at the inlet of the upstream extension (station IN) and predicted by the proposed Machine Learning strategy is shown in Fig. 6.12. Experimental measurements are also shown in the figure for comparison, but it should be noticed that they are measured at station S1.

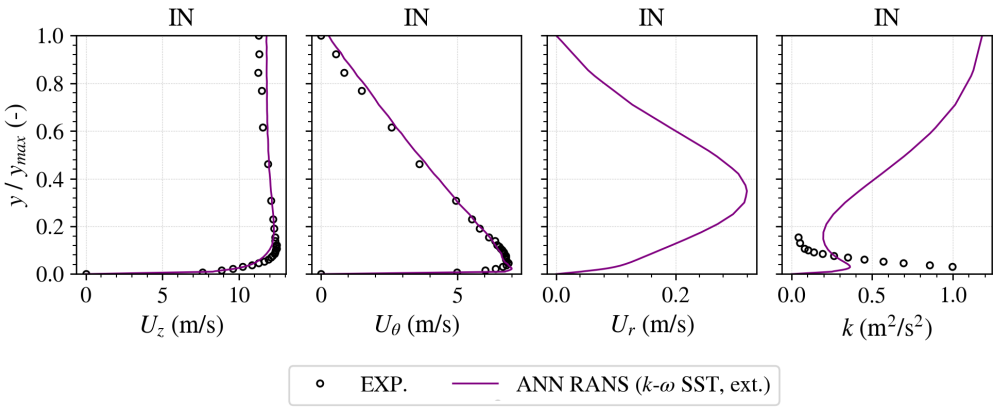

Figure 6.12: Inlet boundary conditions predicted by the Machine Learning strategy at station IN for the ANN-RANS simulation of the case with upstream extension, compared with the experimental measurements at station S1.

Mean velocity profiles predicted by the ANN model are similar to the experimental measurements at station S1, although the U_z distribution is flatter in the centre region of the flow ($y/y_{max} = 1.0$). Conversely, turbulence kinetic energy values are significantly lower at the walls but larger in the centre compared to the experiments. However, these adjustments are essential to recover the correct flow behaviour at station S1 and further downstream. For instance, previous attempts to simulate an extended conical diffuser domain failed because they underestimated U_z and U_θ at the walls at station S1 [12, 8, 149]. Considering the evolution of the mean axial velocity profile along the upstream extension, there are two opposite effects acting on it that must be taken into account by the ANN model: (i) the flow shear at the walls, which reduces U_z at the walls and, therefore, increases its values in the centre region, due to continuity; and (ii) flow swirl, which forces the flow towards the walls, increasing thus U_z values at this region and reducing it in the centre.

To evaluate the ability of the proposed Machine Learning strategy to correctly account for both effects and to match the experimental data at station S1 and inside the conical diffuser,

the profiles at station S1 are shown in Fig. 6.13. Moreover, to demonstrate the importance of the upstream extension, in addition to the extended case, the proposed strategy has also been applied to the reference domain shown in Fig. 6.2a. In this case, the predicted inlet boundary conditions are directly imposed at station S1. Both ANN-RANS results are compared with the experimental data measured at the same location and the standard inlet conditions used in the reference RANS case discussed in Section 6.4.

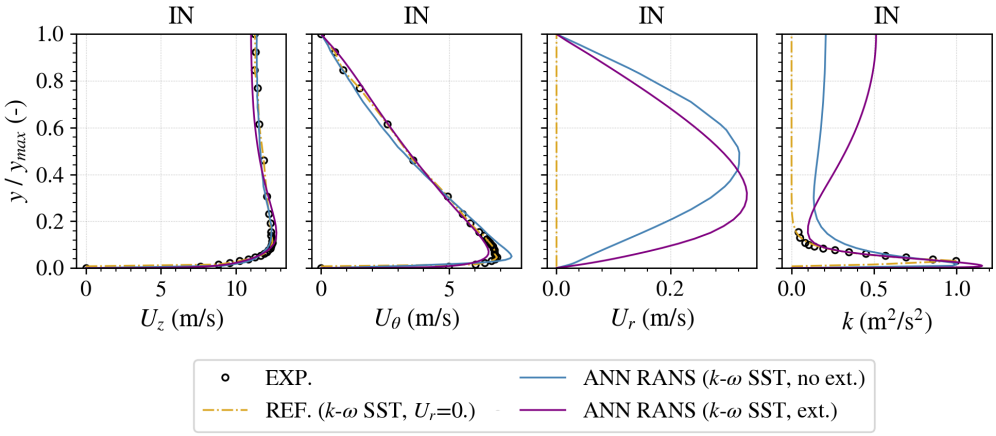

Figure 6.13: Comparison of experimental and numerical mean velocity and turbulence profiles at station S1 using the RANS and the Machine Learning strategy.

Overall, the predicted profiles agree very well with the experiments. In the case without upstream extension, the predicted mean axial velocity profiles, U_z, are very similar to the experimental measurements at station S1, whereas the mean circumferential velocity profile, U_θ, is overestimated close to the walls ($y/y_{max} \approx 0.0$) and slightly underestimated in the intermediate region of the flow ($0.5 \leq y/y_{max} \leq 0.8$). The turbulence kinetic energy profiles, k, is also very similar to the experiments near the walls, but it is overestimated towards the centre of the flow. Conversely, in the extended numerical domain case, the peak value of U_z is slightly overestimated and is located slightly further away from the walls, at $y/y_{max} \approx 0.2$ instead of 0.1, whereas the mean circumferential velocity profile agrees very well with the experimental measurements. Turbulence kinetic energy profile is also different in this case, as the peak is now closer to the walls and has a higher value, however, k is still overestimated towards the centre of flow. It should be noticed though that experimental measurements are not available between $y/y_{max} \approx 0.15$ and 1.0, which greatly restricts the amount of information the ANN has about the flow to infer good values of k in this region. Still, compared to previous works that imposed turbulent inlet boundary conditions based only on integral quantities [98, 123] (e.g., turbulence intensity and characteristic length scale), the proposed Machine Learning strategy predicts k profiles that are much closer to the experimental data at station S1. Indeed, for the case of the draft tube flow studied in this thesis, being able to deal with partial data can be a good characteristic of the proposed strategy, as experimental data in this case is harder to gather and potentially more unreliable. However, the real contribution of the proposed strategy is to obtain a more adequate mean radial velocity inlet profile at station S1, which is unknown from the original measurements in Clausen *et al.* [19]. It is clear from Fig. 6.13 that this velocity component is considerably smaller than the other two. However, as U_r profiles predicted by both ANN-RANS are positive, this means that the flow is being forced towards the walls at station S1, helping it to stay attached throughout the diffuser. Moreover, as explained in Payette [123], to impose an r varying profile of U_r at the inlet is equivalent to specify the rate of longitudinal variation of the axial velocity, U_z, at the inlet. This can be understood by looking at the continuity equation in cylindrical coordinates, Eq. 6.10:

$$\frac{\partial U_z}{\partial z} + \frac{1}{r}\frac{\partial U_\theta}{\partial \theta} + \frac{1}{r}\frac{\partial r U_r}{\partial r} = 0 \tag{6.10}$$

Since the flow is axisymmetric, $\partial/\partial\theta = 0$. Therefore, imposing a profile of U_r implies that $\frac{1}{r}\frac{\partial r U_r}{\partial r} \neq 0$ and sets an axial evolution for U_z due to the term $\frac{\partial U_z}{\partial z}$. However, the distribution of this radial velocity profile is also important, as it will, for instance, define the regions where the axial flow is accelerated and/or slowed down. This is illustrated by Fig. 6.14 which compares the inlet radial velocity profile at station S1 obtained by the proposed Machine Learning strategy and by the separate simulation of the swirl generator upstream the conical diffuser performed in Payette [123]. All profiles predict an accelerated axial flow close the walls and slowed down towards the centre due to the change in the sign of $\frac{1}{r}\frac{\partial r U_r}{\partial r}$, but the position of the peak is better captured in the case with upstream extension, which is explained by the effect of the circumferential velocity profile imposed at station IN.

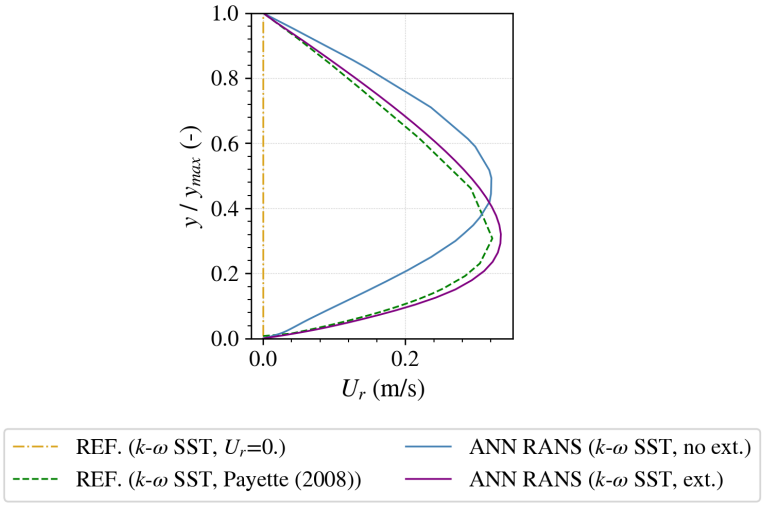

Figure 6.14: Comparison between the radial velocity profile at S1 obtained by the proposed Machine Learning strategy and the separate simulation in Payette [123].

Looking at the flow behaviour inside the conical diffuser, Fig. 6.15 compares the evolution of mean streamwise velocity profiles obtained with the proposed Machine Learning strategy, the reference RANS simulations discussed in Section 6.4 and the best result in Payette [123] using *ad hoc* solution and k-ω SST turbulence model. The proposed strategy has a great impact on the flow behaviour downstream the diffuser, especially due to the more appropriate radial velocity profile at station S1. For instance, the boundary layer is much better predicted in comparison to the reference simulations and stays attached to the walls throughout the diffuser. However, in the case with upstream extension, the slightly overestimated and higher peak of U_x at station S1 leads to a small difference in the prediction of the streamwise velocity peak further downstream compared to the case without extension and confirming thus the sensitivity of the test case to the boundary conditions at the inlet of the diffuser. Still, the magnitude and position of this velocity peak agrees very well with the experimental data, except for the last two stations, where it is slightly overestimated. In any case, the proposed Machine Learning strategy was able to properly adjust the upstream inlet conditions (imposed at station IN) to match the downstream flow field, which is its main goal. Moreover, compared to the best RANS solution obtained in Payette [123] using the k-ω SST turbulence model, the ANN-RANS profiles are very close, though they are not as good at capturing the small variations in U_x near the centre of the flow.

Figure 6.16 shows the results for mean circumferential velocity profiles. The results are much improved with respect to the reference simulations discussed in Section 6.4 and agree very

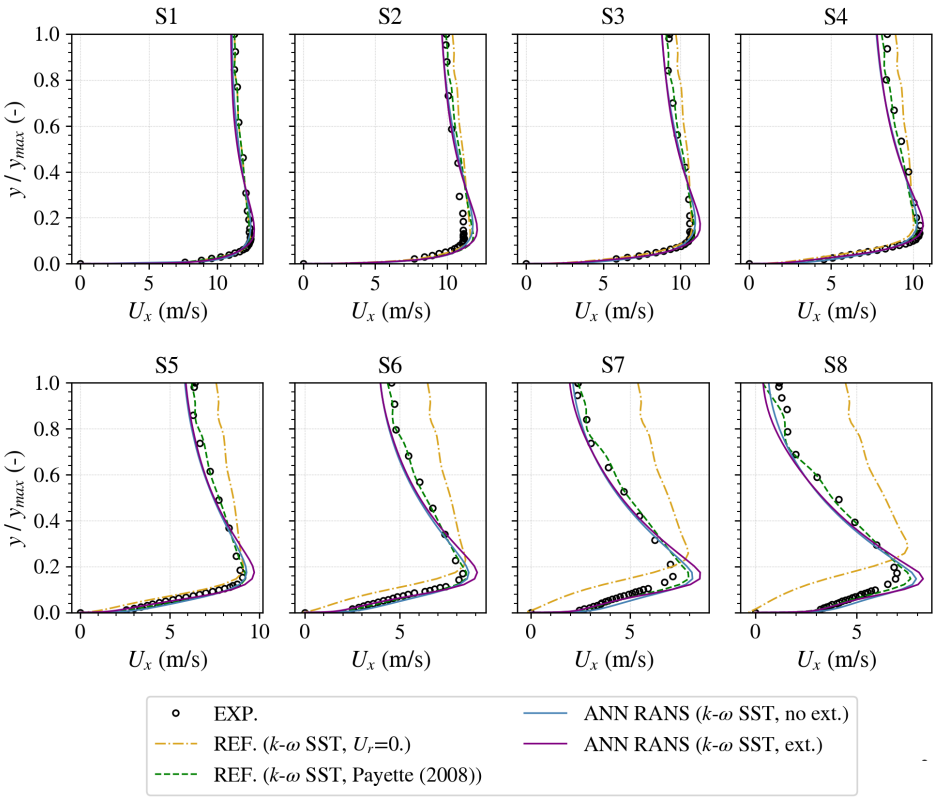

Figure 6.15: Comparisons of experimental and numerical mean streamwise velocity profiles inside the diffuser using RANS and the proposed strategy.

well with the experimental data and the best solution obtained in Payette [123]. In spite of overestimated U_θ values near the walls at station S1 in the case without upstream extension, the numerical results obtained with the proposed strategy agree well with the experimental measurements in this region along the diffuser. However, the slight underestimation between $0.5 \leq y/y_{max} \leq 0.8$ at the inlet of the domain (station S1) causes the circumferential velocity profile to be underestimated in the centre region of the flow compared to other cases.

The results for turbulence kinetic energy profiles are shown in Fig. 6.17. In the case without upstream extension, despite being overestimated between $0.1 \leq y/y_{max} \leq 0.2$ at station S1, the values of k slowly decrease and a very good agreement with the experimental data is found at station S4. However, while the maximum experimental value of turbulence kinetic energy is constant and $\approx 2\text{m}^2/\text{s}^2$ between stations S5 and S7 and is accompanied by a very slow displacement towards the centre of the diffuser followed by a strong decrease at station S8, numerical results keep reducing until the end of the diffuser and are quite underestimated at these last four stations. This is consistent though with previous studies that investigated the swirling flow inside the conical diffuser using two-equation linear eddy viscosity models [4, 98, 12, 123]. In this regard, steady RANS simulations using RSM predicted better turbulence kinetic energy profiles near the walls [4, 130]. However, due to the limited information about k inside the conical diffuser, is hard to determine how big its near-wall peak is the inlet of the numerical domain without upstream extension. Indeed, one characteristic of the extended domain results mentioned previously and shown in Fig. 6.13 is the higher peak value of k at this location.

One of the strengths of the proposed Machine Learning strategy compared to the *ad hoc* solution proposed in Payette [123] and many other previously discussed methods to determine proper inlet boundary conditions for the case of the swirling flow inside the conical diffuser and any other flow configuration, is that it relies *only* on the known experimental data to automatically reconstruct the inlet boundary conditions for a numerical simulation. Still, these

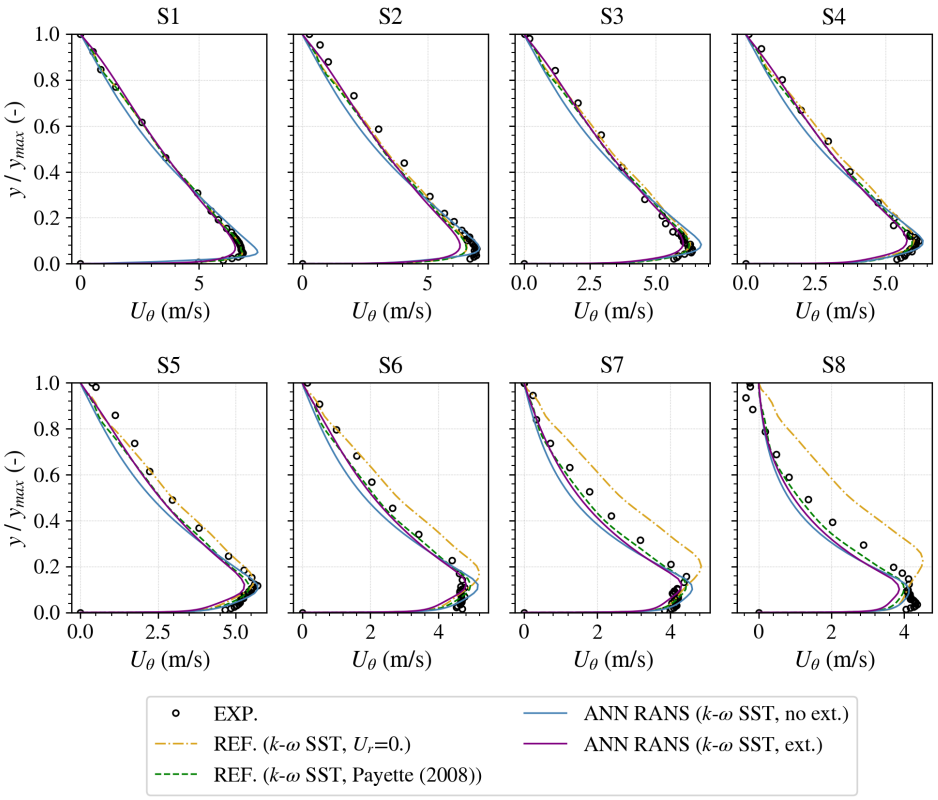

Figure 6.16: Comparisons of experimental and numerical mean circumferential velocity profiles inside the diffuser using RANS and the proposed strategy.

data *do* varies between cases, and it is important that the methodology can handle more or less information. In the case of the conical diffuser investigated in this chapter and particularly discussed using RANS above, seven out of eight measurement stations have been used to train the ANN. However, to evaluate the proposed Machine Learning strategy performance when less information is available, two stations (in particular S1 *and* S8) have been used to train another ANN for the extended RANS case just discussed. The results for mean streamwise velocity profiles are shown in Fig. 6.18 and they are compared with the previous ANN-RANS case with upstream extension. Overall, the ANN-RANS case trained with only two stations yields similar results to the one trained with seven downstream stations. Although the conical diffuser is far simpler than the draft tube studied in Chapter 4 of this thesis (constant opening angle, no centre flow recirculation or vortex rope, free flow outlet etc.), it is nevertheless a very challenging case and the fact the proposed Machine Learning strategy can still deliver good results with few stations is promising. Otherwise, at least it demonstrates the potential of the proposed Machine Learning strategy to be applied to cases with very limited experimental information.

LES with upstream extension

Following the application of proposed Machine Learning strategy in RANS, the next where it has been investigated consists in the numerical domain with upstream extension shown in Fig. 6.7b using LES. Conversely to the previous cases, the goal now is to reconstruct proper mean *and* fluctuating boundary conditions at the inlet of the extended numerical domain (station IN) so the downstream flow behaviour is as close as possible to the experiments. The challenge, however, is the considerably higher computational cost to generate a proper LES database for the ANN. Therefore, one possible solution to circumvent these costs would consist in using the inlet profiles predicted by the ANN-RANS procedure to initiate the LES simulation. However,

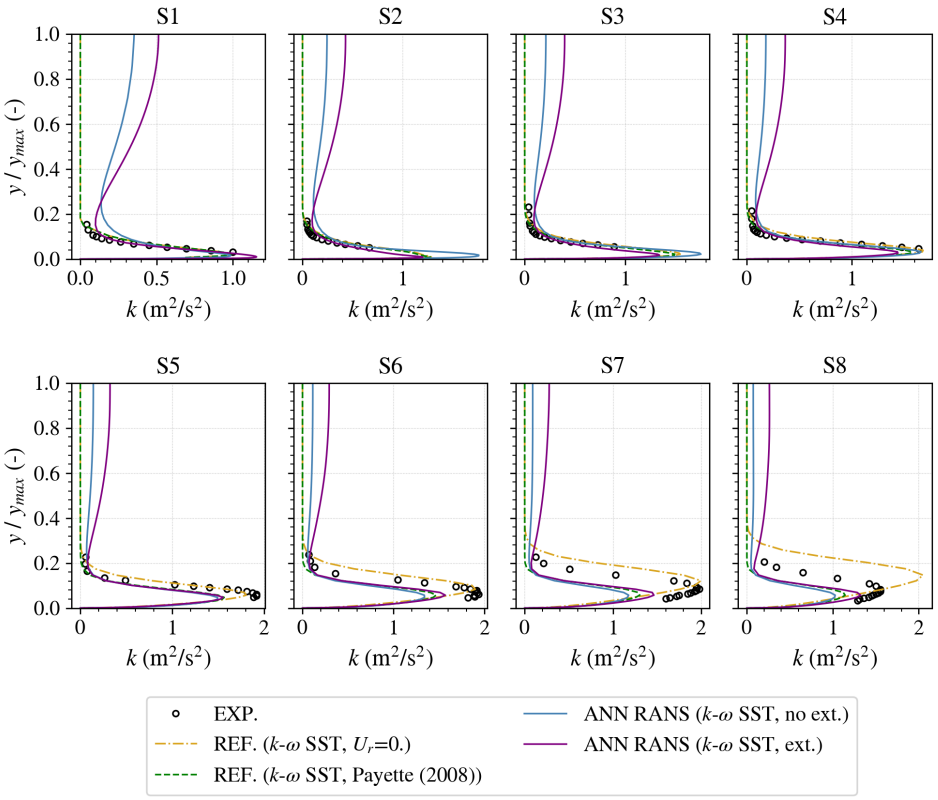

Figure 6.17: Comparisons of experimental and numerical turbulence kinetic energy profiles inside the diffuser using RANS and the Machine Learning strategy.

not only this does not solve the problem of determining the correct l_e and u' values for the injected synthetic turbulence at the inlet section (station IN), but also the inlet profiles issued from the ANN model takes into account all different errors (e.g., turbulence modelling, numerics etc.) which are distinct in RANS and LES. This is seen in Fig. 6.19, which compares the mean streamwise velocity profiles inside the conical diffuser obtained with both RANS and LES in the extended numerical domain and using the inlet conditions predicted by the ANN-RANS shown in Fig. 6.12. For the synthetic fluctuations, the velocity and length scales have been defined from generally used values [98, 123], i.e., $0.1U_b$ and $0.1D_0$, respectively. It is clear from Fig. 6.19 that the LES results are degraded with respect to the ANN-RANS, especially downstream station S4. This confirms that the database should reflect as much as possible the numerical case we want to optimize. In the case of the draft tube discussed in Chapter 4, this is definitely a disadvantage of the proposed strategy since the computational costs associated with LES (and even RANS) of that case are significant.

After training the ANN with the LES database discussed in Step 2 of this application and feeding the experimental data back to the trained model, the predicted inlet boundary conditions imposed at station IN are shown in Fig. 6.20. These profiles are compared to the equivalent extended RANS configuration discussed in the previous section and shown in Fig. 6.9. The various profiles predicted by both ANN-RANS and ANN-LES are noticeably different, specially near the walls. This confirms the previous assumption that the ANN procedure must include the multiple sources of errors (e.g., turbulence modelling, numerics etc.) into its predictions and therefore the final inlet profiles are specifically adapted to a given simulation, i.e., RANS or LES. The optimal parameters defining the injected synthetic fluctuations are, in addition to the normalized turbulence kinetic energy profile shown in Fig. 6.20, equal to $u' = 0.551$m/s, or $\approx 0.05U_b$, and $l_e = 0.042$m, or $\approx 0.16D_0$. Interestingly, these values are not far from the generally used values used earlier.

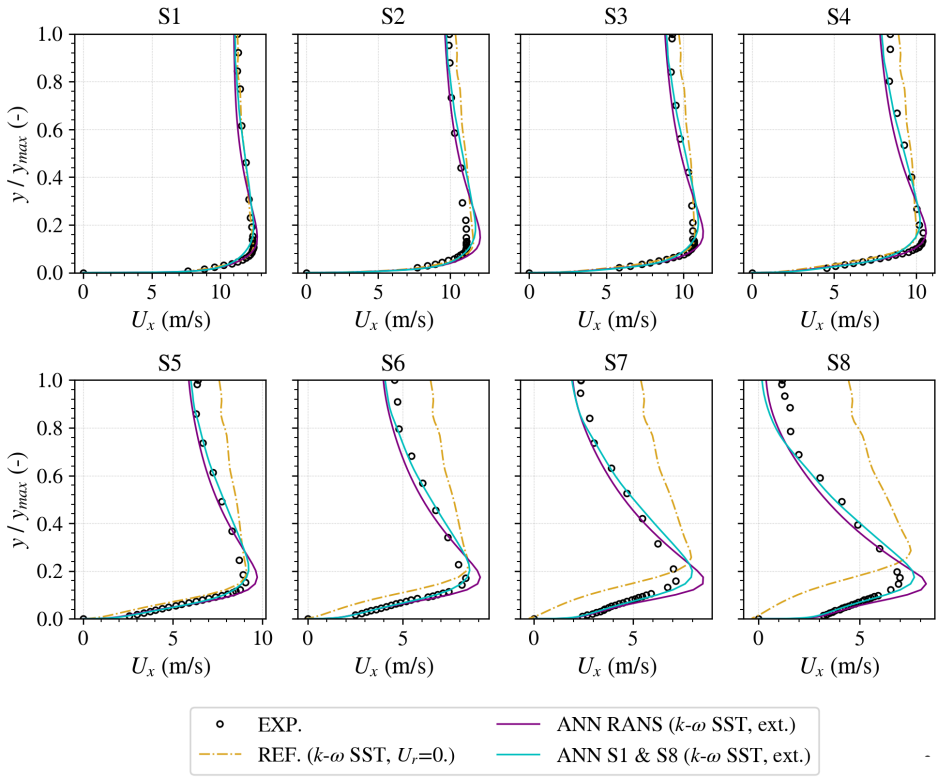

Figure 6.18: Comparisons of experimental and numerical mean streamwise velocity profiles inside the diffuser using RANS and different amount of stations for the ANN.

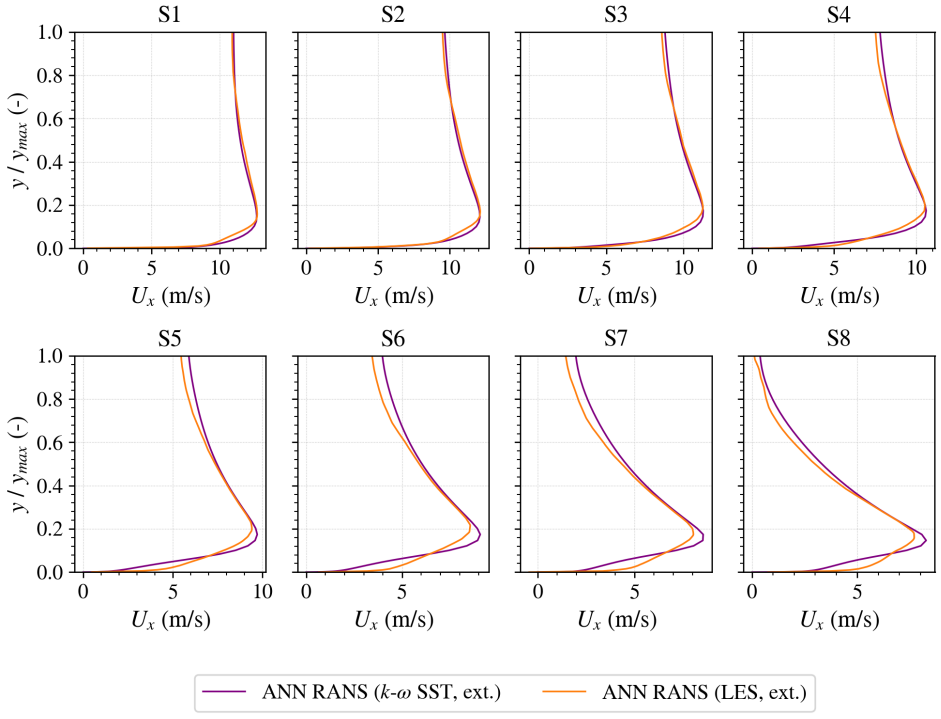

Figure 6.19: Comparisons of experimental and numerical mean streamwise velocity profiles inside the diffuser using the inlet boundary conditions predicted by the proposed strategy with a RANS database in LES and the proposed strategy.

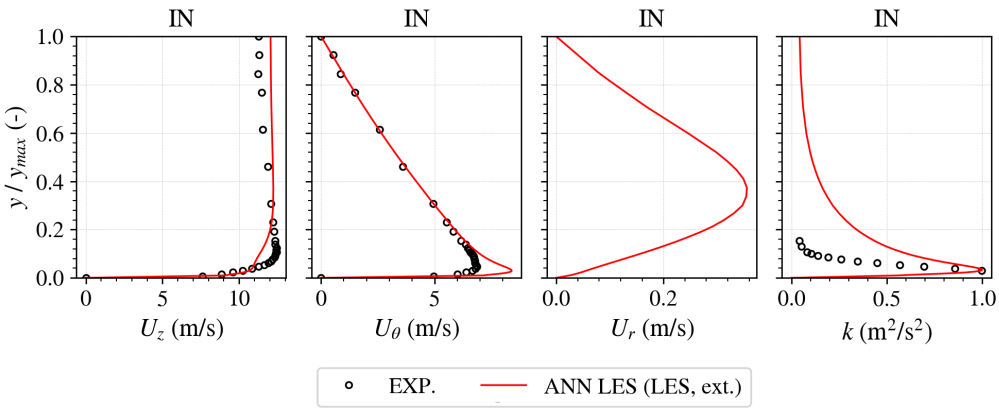

Figure 6.20: Inlet boundary conditions predicted by the proposed Machine Learning strategy at station IN using LES and the proposed strategy, compared with the experimental measurements at station S1.

Compared to the ANN-RANS case with upstream extension, the mean velocity profiles predicted in LES at station IN present some slight differences. For instance, U_z varies almost linearly after a rapid increase at the walls until it reaches its maximum value at $y/y_{max} \approx 0.2$. Moreover, while k values predicted in RANS are larger at the centre of the diffuser compared to its values at the walls, the normalized turbulence kinetic energy profile predicted in LES shows a single peak near the walls and decreases smoothly towards the centre. However, as in the RANS cases discussed in the previous section, the importance of these adjustments is to recover a good flow behaviour at station S1 and further downstream in the diffuser. This is initially shown in Fig. 6.21, which compares the mean velocity and turbulence kinetic energy profiles at the first measurement station, S1. Both mean axial and circumferential velocity profiles obtained by the ANN-LES agrees very well with the experimental measurements at this location. Although the mean radial velocity is not available from the experiments, the results are similar to what has been found in previously by the ANN-RANS and Payette [123]. Finally, the turbulence kinetic energy level near the walls is similar to the experiments, but the peak is considerably higher than in RANS.

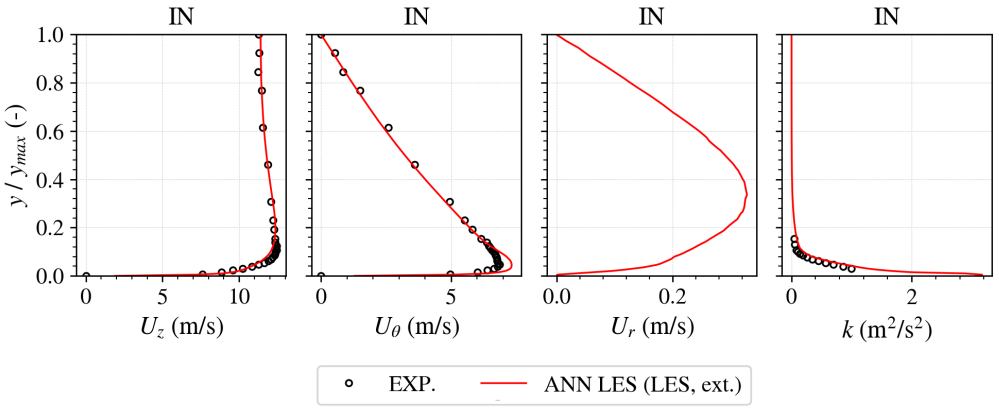

Figure 6.21: Comparison of experimental and numerical velocity and turbulence profiles at station S1 using the LES and the proposed strategy.

The evolution of the mean streamwise velocity profiles shown in Fig. 6.22. It is clear that the ANN-LES and the proposed Machine Learning strategy yields much better results compared to the reference LES cases discussed in Section 6.4. Even though the U_x values are slightly overpredicted at the walls, as if the boundary layer is more attached than it should be, the magnitude and position of the mean streamwise velocity peak is very close to the experimental

measurements. Indeed, while this peak value was notably overestimated in the previous ANN-RANS simulations, especially at stations S7 and S8 (see Fig. 6.15), ANN-LES results agree very well with the experiments at these locations. Interestingly, the correct levels of mean streamwise velocity at the centre of the flow is also obtained along the diffuser, except for stations S7 and S8, where they are slightly overpredicted.

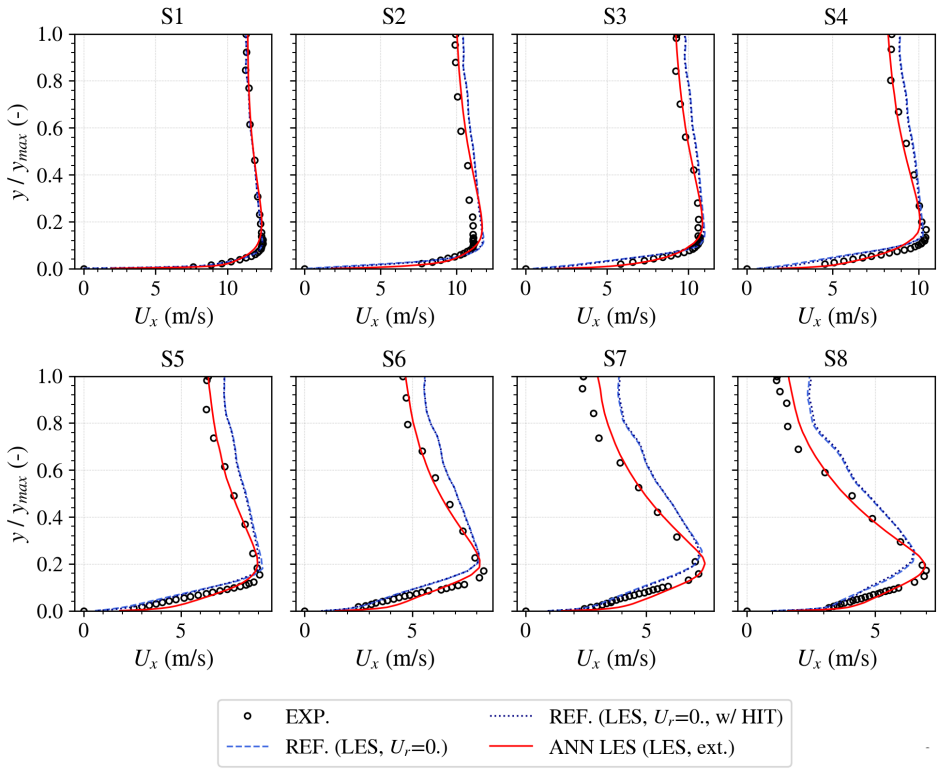

Figure 6.22: Comparisons of experimental and numerical mean streamwise velocity profiles inside the diffuser using LES and the proposed strategy.

The mean circumferential velocity profiles inside the conical diffuser are shown in Fig. 6.23. Similarly to the ANN-RANS cases and even the reference LES, numerical results obtained with the proposed Machine Learning strategy agree very well with the experiments, despite the overestimated U_θ values near the walls at station S1. Conversely to the previous simulations though, the correct level of mean circumferential velocity is recovered right to the walls between stations S2 and S4. However, a side effect is an overestimation of this velocity component in this region of the flow between stations S5 and S7. At station S8, ANN-LES results are slightly underestimated compared to the experimental measurements and the reference LES.

Figure 6.24 shows the turbulence kinetic energy profiles inside the conical diffuser. The parameters defining the synthetic fluctuations injected in the ANN-LES case yielded good levels of k compared to the experiments, with a strong peak near the walls and almost no turbulence towards the centre of the flow. However, conversely to the two reference LES cases, the turbulence kinetic energy is overestimated at stations S2 and S3, but is closer to the measurements of Clausen *et al.* [19] at stations S4 and S5. Between stations S6 and S8, the magnitude of the peak is underestimated, but the rest of the profile agree quite well with the experimental data. It should be noticed that, compared to previously discussed RANS simulations, y^+ values in LES are considerably higher, which could explain the strong peak of k near the walls. However, as the Machine Learning strategy required a significant number of simulations to be applied, computational cost is definitely a limiting factor, which is why increasing the near-wall mesh resolution to lower maximum y^+ values below 20 was not attempted.

As explained at the previous sections, the main reason to add an upstream extension in our

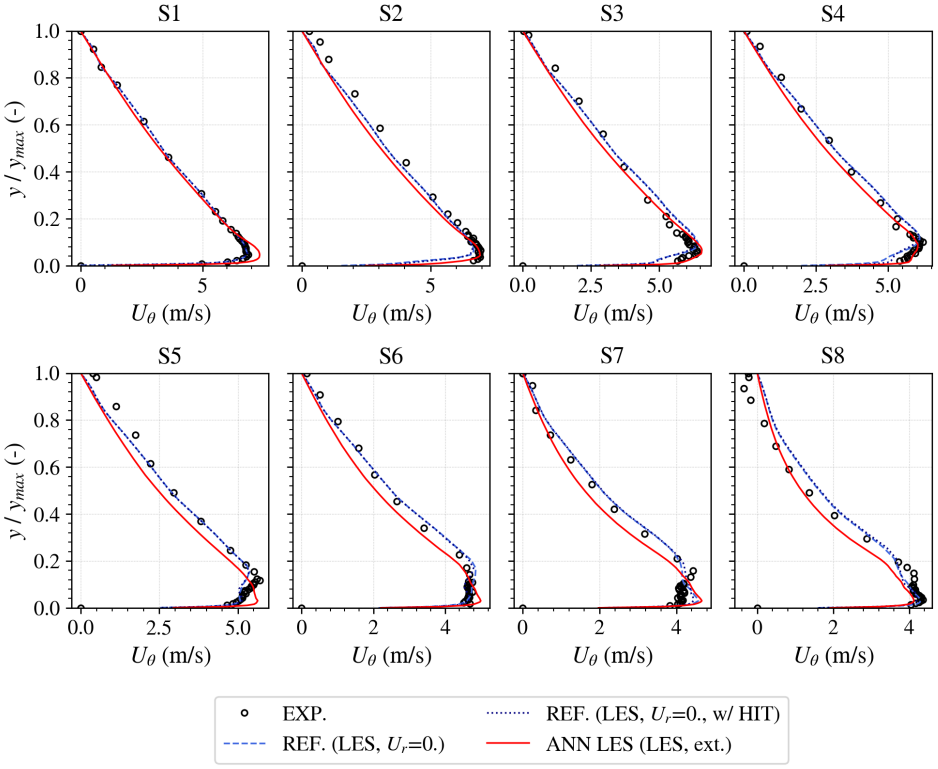

Figure 6.23: Comparisons of experimental and numerical mean circumferential velocity profiles inside the diffuser using LES and the proposed strategy.

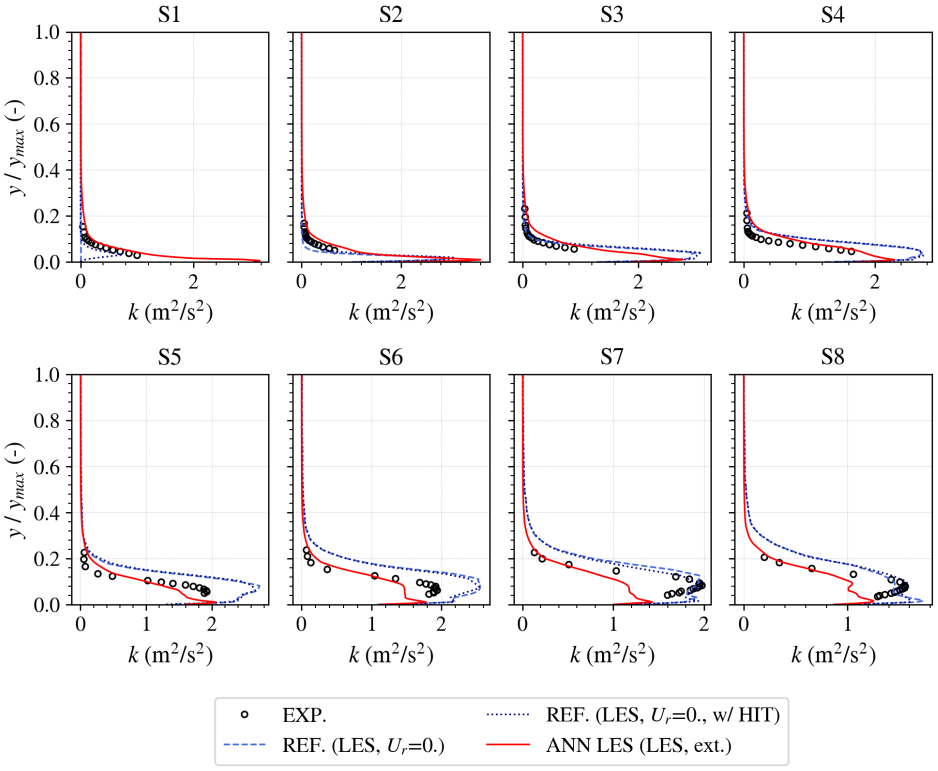

Figure 6.24: Comparisons of experimental and numerical turbulence kinetic energy profiles inside the diffuser using LES and the proposed strategy.

LES is to give the incoming synthetic fluctuations enough space and time for them to develop into more realistic turbulence before reaching the important portion of the numerical domain. Indeed, while easy to generate, one of the problems of the imposed synthetic fluctuations in this thesis is that they are isotropic, meaning that their correlations at the injection plane is equal to zero, which is not always necessarily the case. This is shown in Fig. 6.25, which compares the $\langle u'_r u'_\theta \rangle$ and $\langle u'_r u'_z \rangle$ correlations at station S1 of the conical diffuser. As expected though, in the ANN-LES case with upstream extension, these correlations are build-up upstream station S1 and by the time they reach this station, their values are in good agreement with the experimental measurements. It should be noticed, however, that regarding the turbulence characteristics at the inlet of the diffuser, the ERCOFTAC case is much more simple than the draft tube studied in this thesis. Nevertheless, as we will discuss in the following chapter, the artificial upstream extension is still as important in the draft tube.

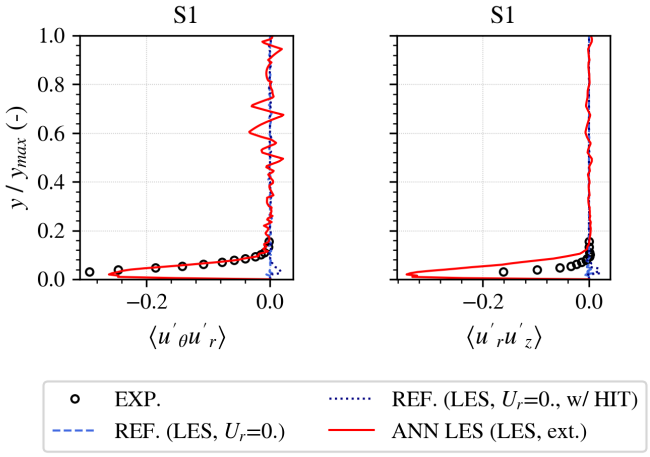

Figure 6.25: Comparisons of experimental and numerical Reynolds stresses profiles at station S1 using LES and the proposed strategy.

Another way to visualize the impact caused by the upstream extension on the flow consists in looking at the turbulent structures inside the conical diffuser. Figure 6.26 shows these structures using iso-surfaces of Q-criterion [86] coloured by the vorticity magnitude in the z-axis direction. In the reference case without synthetic fluctuations injection (see Fig. 6.26a), turbulent structures are not visible at the inlet plane, but they quickly develop at the walls as a result of flow shear in this region. Adding synthetic fluctuations to this reference case (see Fig. 6.26b) causes the turbulent structures to being seen from the beginning of the computational domain, but they are isotropic and still need to develop into more realistic turbulence downstream the diffuser, similarly to the results obtained in Duprat [36] and the draft tube case discussed in Chapter 4. However, in the ANN-LES case with an upstream extension (see Fig. 6.26c), the synthetic turbulence injected at station IN develop inside the extension and, by the time it arrives at station S1, it is more realistic. For instance, well-defined coherent structures can be observed at the beginning of the domain and consists in relatively long vortices aligned with the mean flow direction due to the centrifugal instabilities at the upstream extension.

Finally, as mentioned in the Section 6.2, Clausen *et al.* [19] also measured the static pressure evolution along the diffuser walls in the form of a pressure coefficient, C_p, defined in Eq. (6.3). These results are important as they give an indication of the pressure recovery inside the diffuser. Figure 6.27 shows the curves obtained for the three LES cases (two reference and one ANN-LES) in comparison with the experimental values. It should be noticed that the static pressure at station S8 is used as reference instead of the atmospheric pressure in the original C_p equation. Since the static pressure at the walls is greatly affected by the velocity distribution in this region of the flow, ANN-LES results are clearly improved with respect to the reference simulations

using standard inlet boundary conditions.

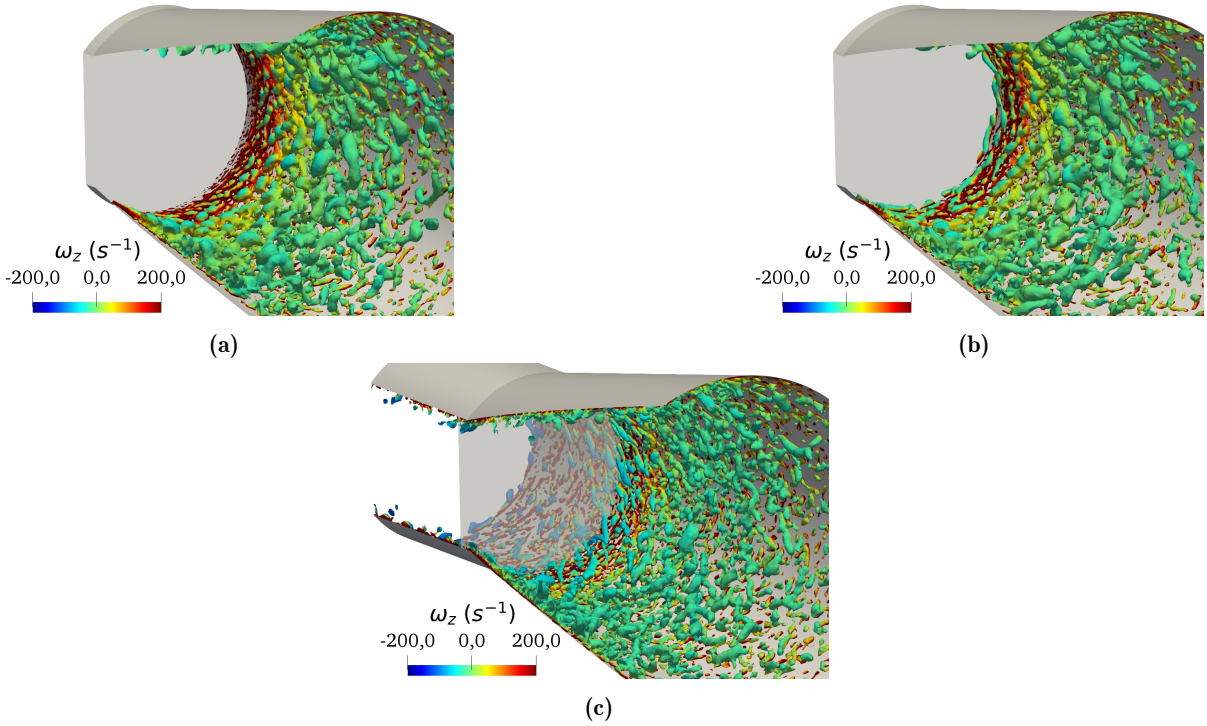

Figure 6.26: Turbulent structures inside the conical diffuser visualized by iso-surfaces of Q-criterion and coloured by their vorticity z. (a) reference LES w/o upstream extension and w/o synthetic fluctuations; (b) reference LES w/o upstream extension and w/ synthetic fluctuations; (c) ANN-LES w/ upstream extension and w/ synthetic fluctuations.

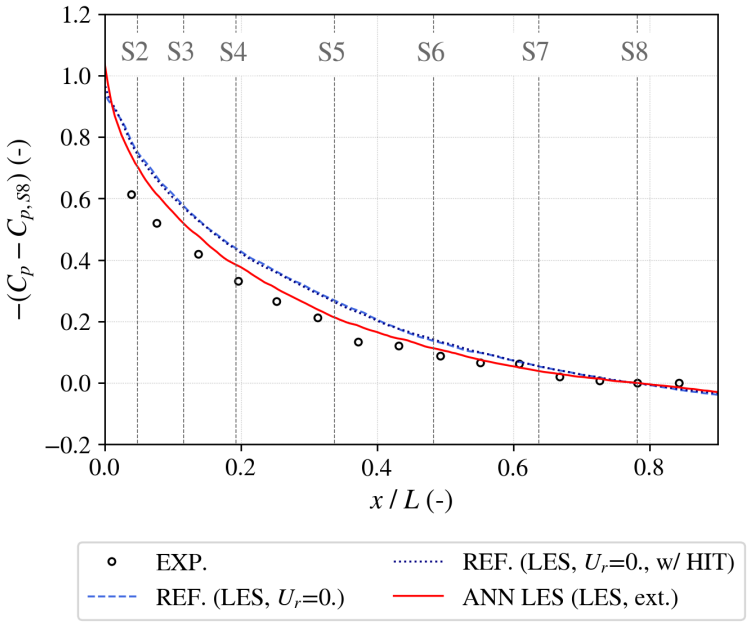

Figure 6.27: Comparisons of experimental and numerical C_p evolution using LES and the proposed strategy.

Chapter 7

Application to the bulb turbine draft tube case

Contents

7.1 Introduction

After the successful application of the proposed Machine Learning strategy to the canonical case of the swirling flow inside a conical diffuser, in the present chapter, we revisit the bulb turbine draft tube previously discussed in Chapter 4, but, this time, applying the same strategy to determine proper inlet boundary conditions for simulating its flow. As explained in the previous test case, the ANN can have some difficulties finding *physical* inlet boundary conditions for a simulation if the experimental data is *unreliable*. For this reason, the application to the draft tube case is limited to the second operating point, OP2, since the experimental data for OP1 have some inconsistencies (see Chapter 4). The application of the proposed Machine Learning strategy is once again divided into its three main steps, which are thoroughly explained in this chapter. In the first step, the numerical setup of the simulations used to create the database is explained. Overall, it is almost identical to that used in the reference simulations, except for the addition of an artificial extension upstream the *real* inlet of the draft tube (station R0) to give the incoming synthetic fluctuations more time and space for them to develop before reaching the important portion of the flow. RANS simulations are performed in ANSYS CFX using the k-ω SST turbulence model and the automatic near wall treatment, whereas LES are conducted in YALES2 using the σ-model to account for the SGS effects on the flow and Duprat's *et al.* [37] wall-model. In the second step, the architecture of the ANN used to determine the correlations between downstream flow behaviour and upstream inlet conditions, as well as the structure of its inputs/outputs are discussed. Finally, in the third and last step, the results obtained with the proposed Machine Learning strategy are presented and compared with the reference RANS and LES results from Chapter 4. A detailed head losses analysis is also conducted to show the importance of imposing proper inlet boundary conditions when evaluating a draft tube flow.

7.2 Step 1: Numerical setup and database generation

Similarly to the swirling flow inside the conical diffuser investigated in the precedent chapter, the first step in the application of the proposed Machine Learning strategy to the draft tube case explored in Chapter 4 consists in determining the numerical domain that is going to be used in our database computations. As discussed in Sections 4.5.3 and 4.6.3, injecting synthetic fluctuations directly at the inlet of the draft tube (station R0 in Figs. 3.1 and 4.1) have a positive effect on the downstream flow behaviour inside the draft tube but negatively impact its energy balance and head losses analysis. Thus, the key aspect of this new domain is the artificial upstream extension that gives these *unrealistic* fluctuations enough time and space for them to develop before reaching the *real* inlet plane (station R0). However, conversely to the previous test case, determining the length of this upstream extension is not obvious. For instance, in addition to the more complex downstream flow being generated by the set of 34 fixed blades, grid, and hub in the draft tube, turbulence measurements at the first station inside the diffuser studied by Clausen *et al.* [19] was relatively low and mostly concentrated at the walls, whereas in the case of the draft tube flow studied in this thesis, turbulence levels are significantly high all over its inlet plane (station R0), which means that the synthetic fluctuations take potentially longer (spatially and temporally) to develop. Therefore, based on the maximum distance in which the ΔH values were still decreasing and thus behaving unexpectedly in Figs. 4.30 and 4.42, which corresponds to $0.2L$ in the cases where $u' = 1.2V_{b,in}$ and $l_e = 0.2h_{max,\mathrm{R0}}$, a simple straight extension was added upstream the reference numerical domain of the draft tube, as shown in Fig. 7.1. Again, this extension is not required in RANS, as the problem with *unrealistic* synthetic fluctuations decay is not present in this turbulence method. Nevertheless, the extended domain is used because, similarly to the conical diffuser, RANS is a relatively inexpensive benchmark to test some proposed Machine Learning strategy aspects before passing to more computationally demanding LES. It should be noticed, however, that the numerical domain in RANS is not simplified as the draft tube geometry is not axisymmetric.

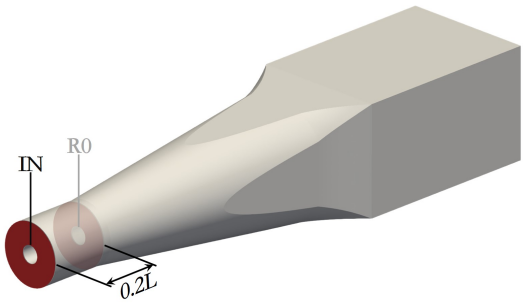

Figure 7.1: Extended numerical domain of the draft tube used in the application of the proposed Machine Learning strategy.

In addition to the numerical domain, it is also necessary to define the different sets of boundary conditions that should be imposed at the inlet of the upstream extension (station IN) in each simulation of the database. In both RANS and LES, four profiles are required to define these inlet conditions, notably the three mean velocity profiles (V_z, V_u and V_r) and one turbulence kinetic energy profile (k), which is normalized in LES. These profiles were generated by a Python script, similar to the one used in the ERCOFTAC case, using splines [15] and a Sobol quasiradom sequence [140]. At the end, 800 different sets of inlet boundary conditions have been generated, and their distributions are shown in Fig. 7.2. It should be noticed, however, that the distribution of these profiles is not the same as in the previous conical diffuser case because the downstream flow characteristics are notably different in both cases. Like in the previous case, experimental values measured at station R0 are shown for comparison, but the generated profiles are supposed to be imposed at the inlet of the upstream extension, station

IN.

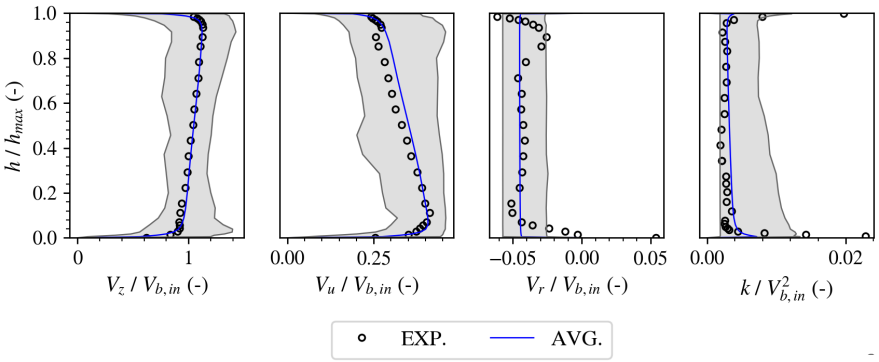

Figure 7.2: Distribution of mean velocity and turbulence kinetic energy profiles generated for the proposed Machine Learning strategy.

The parameters defining the incoming synthetic fluctuations characteristics (l_e and u') also needed to be determined prior to launch the simulation in the database. Like in the case of the swirling flow inside a conical diffuser, it is important that the downstream results be dependent on the imposed inlet boundary conditions. However, the decay of these synthetic fluctuations is greatly affected by these values and a parametric study is therefore necessary to evaluate the sensitivity of the downstream turbulence kinetic energy profile to them. Using the above extended numerical domain and keeping the four inlet profiles constant, the length scale was varied between $0.1h_{max,\mathrm{R0}} \leq l_e \leq 1.0h_{max,\mathrm{R0}}$, whereas the velocity scale varied between $0.1V_{b,in} \leq u' \leq 1.0V_{b,in}$. The results of this study are shown in Fig. 7.3 and it is clear that the turbulence kinetic energy profiles at station R0 are indeed dependent on the inlet boundary conditions. More importantly, the experimental values at this location are within the solution space of the parametric study. Conversely to the previous conical diffuser investigated in Chapter 6, the characteristic length scale of the imposed turbulence is also optimized by the proposed Machine Learning strategy in RANS. Thus, a similar study was carried out to determine its range, which was defined as $0.05h_{max,\mathrm{R0}}$ and $0.20h_{max,\mathrm{R0}}$.

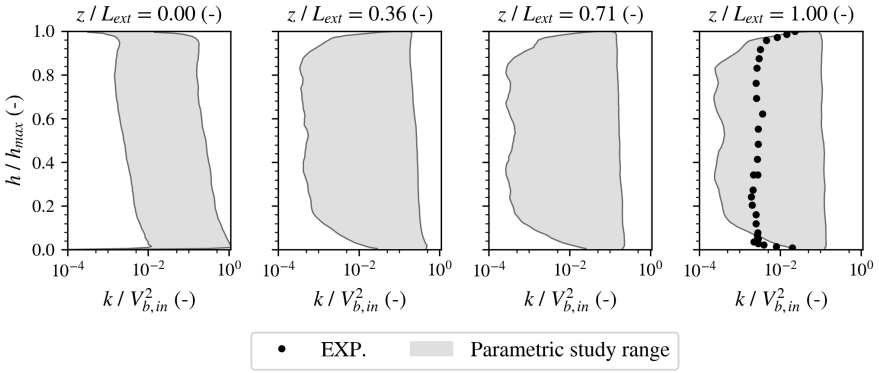

Figure 7.3: Evolution of turbulence kinetic energy profiles inside the upstream extension during the parametric study in LES.

With both numerical domain and sets of inlet boundary conditions defined, the simulations required to create the databases for the ANN could be launched. Each database, for both RANS and LES, were composed by 500 simulations. While the computational cost per simulation can vary depending on the imposed inlet conditions, a typical RANS solution of the flow inside the extended draft tube takes 60 CPUh to finish and 850 Mb (megabyte) of storage space. Thus, to run all 500 cases in the RANS database, approximately 30 000 CPUh and 425 Gb (gigabyte)

of storage were required. In the case of LES, simulations for the database were automatically launched and managed by a specific tool available in YALES2 to ensure that all steps required to obtain a statistically converged solution, including the mesh adaptation, were properly executed with minimum user intervention. The typical computational cost to perform the four steps required to obtain a converged LES solution (i.e., flow stabilization, flow statistics accumulation, mesh adaptation and final flow statistics accumulation) is around 6 200 CPUh, meaning that approximately 3 100 000 CPUh were required to run all 500 simulations. The storage space take by each LES varies depending on the final number of elements after the mesh adaptation step, but, together, the four numerical solutions occupy approximately 32 Gb of storage. This means that 16 Tb (terabytes) would be required for the complete LES database, however, this is raw data and not everything is useful in the long term, particularly the solutions other than the final flow statistics accumulation. As a result, *only* 4 Tb of data *need* to be stored. Post-processing in both RANS and LES was performed at the end of each simulation and all flow field information measured at all stations inside the draft tube were stored along with the corresponding set of inlet boundary conditions used to generate them. Similarly to the ERCOFTAC case, only these profiles (which occupy only a few megabytes) are treated by the ANN.

7.3 Step 2: ANN architecture and training

The second step in the proposed Machine Learning strategy consists in determining the non-linear model that correlates the downstream flow field behaviour with the upstream inlet boundary conditions. Again, an ANN specifically designed to learn these correlations in a supervised manner is used, however, compared to the test case discussed in the previous chapter, the draft tube has more experimental data that could be used as inputs for ANN. For instance, in addition to the mean axial (*streamwise*) and tangential (*circumferential*) velocity profiles, mean radial velocity and static pressure profiles are also available this time. Moreover, turbulence kinetic energy profiles are measured all the way up to the centre of the flow, instead of being limited to the boundary layer. However, while the reliability of this data was not a *real* issue in the conical diffuser, it definitely is in the case of the bulb turbine draft tube studied in this thesis [1]. Using this unreliable data could pose a problem for the ANN as no *physical* solution would exist for such an *unphysical* flow field. As a result, inputs had to be carefully selected this time, and they consisted *only* in mean axial and tangential velocity profiles, as well as turbulence kinetic energy and static pressure profiles, measured at stations R0, R2 and R5, for the second operating point tested during the experimental campaign, OP2. The data at stations R1, R3 and R4 are notably problematic at this operating condition, especially the mean tangential velocity profiles, which seems inverted at R1 and particularly different from the numerical results at R3 and R4 (see Fig. 4.35). It should be emphasized, however, that the proposed methodology has indeed been tested with the experimental data from OP1, but the results were mostly unsatisfactory and no converged inlet boundary conditions were obtained. Nevertheless, the strategy's relative success in the case of the swirling flow inside a conical diffuser and the draft tube flow operating at OP2 (as will be shown in the following section), indicates that the problem is possibly linked to the experimental data at OP1.

Similarly to the test case, inputs are pre-processed as it improves the training and performance of the proposed Machine Learning strategy. Mean axial velocity and turbulence kinetic energy profiles are *scaled* by dividing their absolute values by the respective bulk velocity at each section, i.e.,

[1] This problem has been discussed in Chapter 4, especially for OP1, but also for OP2, where it was argued that some of the experimental data is possibly unreliable and therefore should be analysed with caution (e.g., see Figs. 4.15, 4.16, 4.34, 4.35.

$$\phi^* = \frac{\phi}{\frac{1}{S_{\text{sec}}} \iint\limits_{S_{\text{sec}}} V_{z,\text{sec}} dS} \tag{7.1}$$

where ϕ^* is the scaled variable (i.e., V_z^*, k^*) and $V_{z,\text{sec}}$ is the mean axial velocity profile at a given station. Conversely, due to some problems with the magnitude of the experimental mean tangential velocity values, these profiles are scaled differently, where they are divided by the specific angular momentum and multiplied by the respective cross-section area:

$$V_u^* = \frac{V_u}{\frac{1}{S_{\text{sec}}} \int r V_{u,\text{sec}} dr} \tag{7.2}$$

Finally, the ensemble of inputs vectors, $\mathbf{X}$, which includes the static pressure profiles, are also *normalized* according to Eq. (6.8):

$$\mathbf{X}' = \frac{\mathbf{X} - \mu}{\sigma}$$

Outputs consist in the sets of inlet boundary conditions for each simulation of the database. In addition to the three mean velocity and turbulence kinetic energy profiles (V_z, V_u, V_r and k), the turbulence characteristics length scale was also varied in RANS using the k-ω SST turbulence model, while both length and velocity scales (l_e and u', respectively) were varied in LES. Each profile is composed by 70 points unevenly distributed along the inlet radius, following the same trend of the test case, where points density is higher close to the walls due to the more important velocity and turbulence kinetic energy gradients in this region. Finally, these profiles are also *normalized*, like the inputs.

Initially, the same network architecture used in the ERCOFTAC has been tested to predict the optimal inlet boundary conditions in the case of the draft tube. However, due to the complexity of the flow, the amount and type of experimental data, as well as its reliability, made that the obtained results were unsatisfactory, and a new ANN architecture had to be determined. The final network architecture used for the draft tube case is shown in Fig. 7.4 and, much like the previous test case, it was manually defined. In contrast to the scaled *and* absolute values used in the ERCOFTAC neural network (see Fig. 6.11), only scaled values are used as inputs for the ANN, except for the static pressure, P_s. Moreover, in addition to the five or six MLP used for each output of the ANN, a couple of separate fully-connected layers is added to the ANN, which are concatenated to the output of each MLP. In terms of activation functions, though, ELUs [20] are used once again due to their ability to handle negative values and a dropout rate of 50% is applied to reduce overfitting and improve the model's performance [144]. Moreover, the loss function is still the MSE between the training (true) set and predictions, given by Eq. (6.9).

The Machine Learning algorithm is implemented in Python 3.7 using Tensorflow 2.1. NAdam [34] is used as optimizer and training is conducted for 2000 epochs. The results of these trainings are discussed in Appendix A. All 500 cases from the database are used for training but 20% (i.e., 100 cases) is used for validating the model. As mentioned before, only the results at stations R0, R2 and R5 are used as inputs for the ANN.

7.4 Step 3: Predicted inlet boundary conditions and results

After finishing the training of the ANN and feeding the experimental data back into the trained model, the four inlet profiles predicted by the proposed Machine Learning strategy at

station IN for both RANS and LES of the *extended* draft tube domain are shown in Fig. 7.5. For comparison, the experimental profiles measured at station R0 are also shown in this figure. It should be noticed that the turbulence kinetic energy profile is normalized in LES (i.e., $k_{\max} \leq 1$) due to the way synthetic fluctuations are generated in YALES2 (see Section 2.4 and Fig. 2.7). In addition to these profiles, the ANN also predicted an optimal turbulence length scale equal to $0.13h_{max,\mathrm{R0}}$ to close the system of equations in RANS using the k-ω SST turbulence model, and $l_e = 0.21h_{max,\mathrm{R0}}$ and $u' = 0.37V_{b,in}$ for the injected synthetic fluctuations in LES.

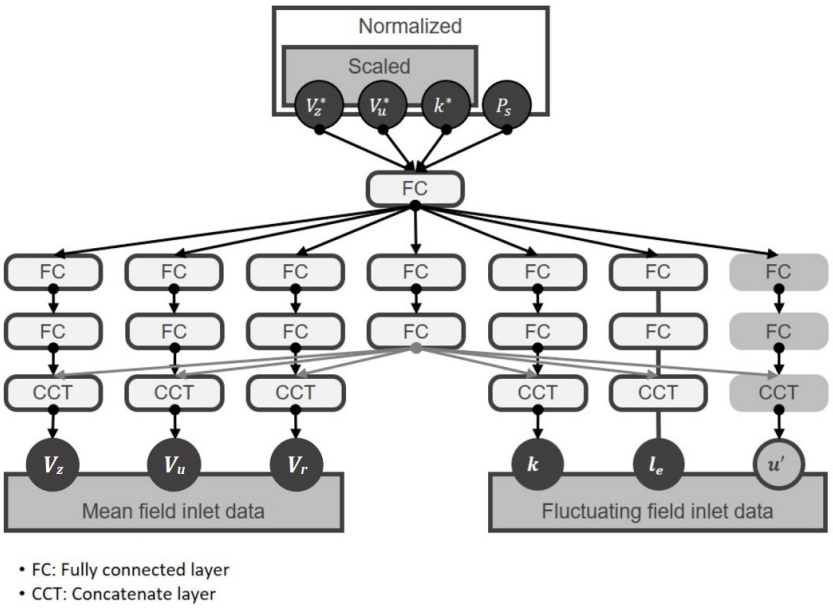

Figure 7.4: Scheme of the ANN architecture used to obtain the optimized inlet boundary conditions for the draft tube case.

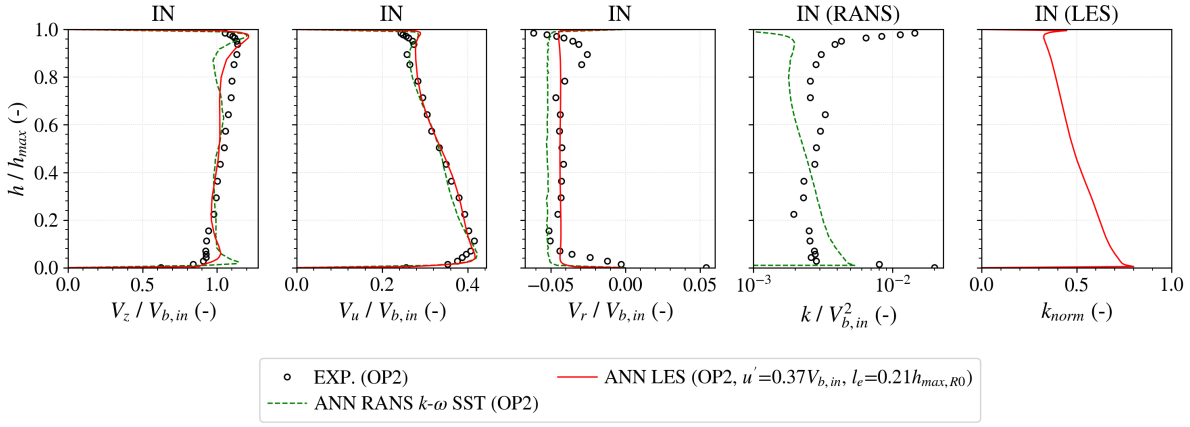

Figure 7.5: Normalized inlet boundary conditions predicted by the proposed Machine Learning strategy at station IN for both ANN-RANS and ANN-LES.

Compared to the ERCOFTAC case, mean axial and tangential velocity profiles are more complexes, especially due to the presence of a central hub in the draft tube, which adds another wall that must be taken into account by the ANN model. For instance, despite the being subjected to the same two opposite effects inside the upstream extension (see Section 6.5.3), the ANN has to compensate the axial velocity being reduced at both extremities of the inlet profile. Moreover, mean tangential velocity distribution is not as simple as a solid body rotation, although it gradually reduces from the external ($h/h_{max} \approx 0.0$) to the internal ($h/h_{max} \approx 1.0$)

region of the flow. As a result, two peaks are observed in the V_z profiles, particularly close to the walls, whereas a single peak can be observed in V_u close the hub ($h/h_{max} \approx 1.0$). Conversely to the conical diffuser though, mean radial velocity and turbulence kinetic energy profiles are mostly constant along the draft tube radius.

Overall, the inlet profiles predicted at station IN are similar to the experimental data measured at station R0. These small differences correspond indeed to the adjustments done by the proposed Machine Learning strategy and are essential for recovering the correct flow behaviour downstream the draft tube. This is illustrated in Fig. 7.6, which compares the numerical and experimental profiles measured at station R0. Starting with the mean axial velocity profile, the aforementioned peaks predicted at the inlet of the upstream extension (station IN) and close to the walls ($h/h_{max} = 0.0$ and $h/h_{max} = 1.0$) are mostly dissipated within the upstream extension. As a result, a very good agreement is found between the ANN results and the experimental measurements at station R0. The most noticeable difference is between $0.8 \leq h/h_{max} \leq 0.9$ where the ANN-RANS underestimate the values of V_z compared to the experiments while the ANN-LES overestimate it. The predicted mean tangential velocity profiles are also close to the experiments at station R0, although the peak near $h/h_{max} \approx 1.0$ is only captured by the ANN-RANS. Interestingly, both ANN models yield very similar V_u profiles at station IN, LES results being even overestimated with respect to RANS at this region of the flow, i.e., $h/h_{max} \approx 1.0$. However, as the flow in each case evolves differently inside the upstream extension (e.g., due to turbulence modelling, numerics etc.), downstream profiles end up being relatively different. Looking at the predicted mean radial velocity profiles, they are both much closer to zero compared to the experiments. While this velocity component is particularly difficult to measure and therefore experimental data *unreliability* is a plausible explanation, the influence due to the upstream blades and grid in the real draft tube configuration (see Fig. 3.1) can simply not be captured by the ANN in the extended domain (see Fig. 7.1), at least not with the current axisymmetric inlet boundary conditions. Finally, the distribution of both turbulence kinetic energy profiles are similar to the experimental measurements, but its values are mostly underestimated in the case of ANN-RANS and overestimated in the case of ANN-LES. It should be noticed, however, that the goal of the proposed Machine Learning strategy is not to *perfectly* match the numerical and experimental profiles at *every station* inside the draft tube. Rather, its main goal is to obtain the *best* correspondence with the experimental data *all over* the flow.

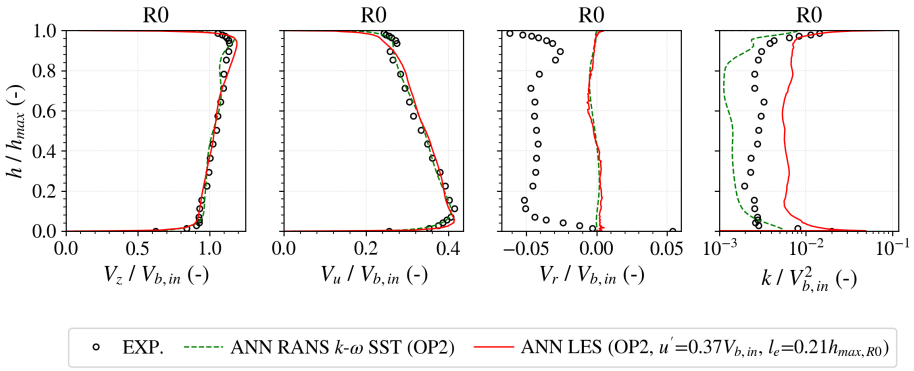

Figure 7.6: Experimental and numerical normalized mean velocity and turbulence kinetic energy profiles at station R0 using the proposed Machine Learning strategy.

7.4.1 Velocity and turbulence profiles

The downstream evolution of the normalized mean axial velocity profiles inside the draft tube is shown in Fig. 7.7. In addition to experiments, the results obtained with the proposed Machine Learning strategy are compared to both reference RANS and LES without synthetic

turbulence injection (i.e., the standard approach to draft tube simulations), as well as the overall best LES with synthetic fluctuations injection, case with $u' = 0.6V_{b,in}$ and $l_e = 0.4h_{max,R0}$. Starting with RANS using the k-ω SST turbulence model, V_z profiles are significantly improved by the proposed strategy. For instance, V_z values are closer to the experimental measurements at station R1 as they are increased near the external walls of the draft tube ($h/h_{max} = 0.0$) and slightly reduced towards the centre of the flow. This extra speed and energy in the boundary layer also result in a very good agreement between the ANN-RANS and experimental data at station R2. Indeed, even the central vortex behaviour at this station is better captured in the ANN-RANS, though still not as well as in reference LES. At stations R3 and R4, the influence of the turbulence model is more noticeable and the ANN-RANS does not capture either the near-wall or the central vortex behaviours very well. However, the slight increase in V_z values near $h/h_{max} = 0.0$ greatly improves the numerical results in the intermediate region of the flow, between $0.2 \leq h/h_{max} \leq 0.8$. Finally, a similar trend is observed at station R5, though the ANN-RANS predicts no boundary layer separation, in accordance with the experiments and conversely to the reference RANS simulations. In LES, the mean axial velocity values near $h/h_{max} = 0.0$ at station R1 predicted by the proposed strategy are also improved compared to the experiments and the reference simulations. As a result, the boundary layer behaviour ($h/h_{max} \approx 0.0$) is better captured at stations R2. The low V_z values at the central vortex is again well predicted in LES, but the enhanced boundary layer brings the ANN-LES results closer to the experimental measurements at the intermediate region of the flow. At stations R3 and R4, agreement with experimental data is very good, except for the high V_z values between $0.0 \leq h/h_{max} \leq 0.2$ at station R4, which is simply not captured numerically. At station R5, the small increase in boundary layer speed also reflects in the centre of the flow where ANN-LES results are closer to the experiments, though the relatively flat V_z profile is not recovered.

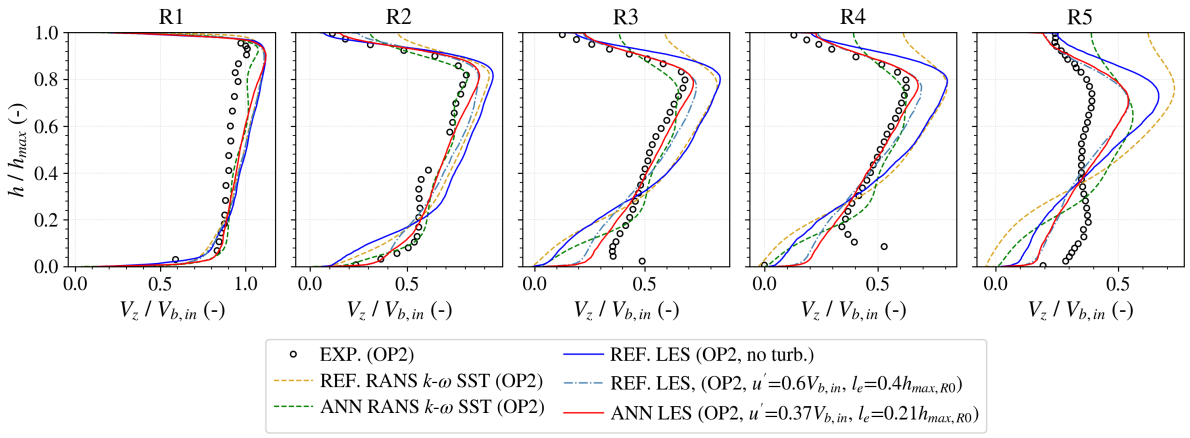

Figure 7.7: Normalized mean axial velocity profiles inside the draft tube predicted by the reference simulations of the draft tube at OP2 and the proposed strategy.

The normalized mean tangential velocity profiles are shown in Fig. 7.8. As previously discussed, experimental measurements at stations R1, R3 and R4 and noticeably different from the numerical results, which can be due to unreliable data at these three stations. Nevertheless, looking at the distribution of numerical profiles at station R1, they are all very similar, except for the peak near the hub (h/h_{max}=1.0), which is not captured by the ANN-LES. This is expected, however, since this same peak was not even captured at station R0, as shown in Fig. 7.6. Its impact on the downstream V_u profiles, however, is limited as ANN-LES results at stations R2 and R5 follows very well the experimental data. It should be noticed that, although the values of V_u near $0.0 \leq h/H \leq 0.8$ at station R2 are smaller than what has been experimentally measured, this is in consonance with the reference numerical results, especially the LES with moderate and strong synthetic fluctuations (i.e., $u' = 0.6V_{b,in}$ and $u' = 1.2V_{b,in}$). In RANS, both reference and

ANN-RANS simulations yield very similar results, which is expected given the good agreement with experimental measurements at station R0.

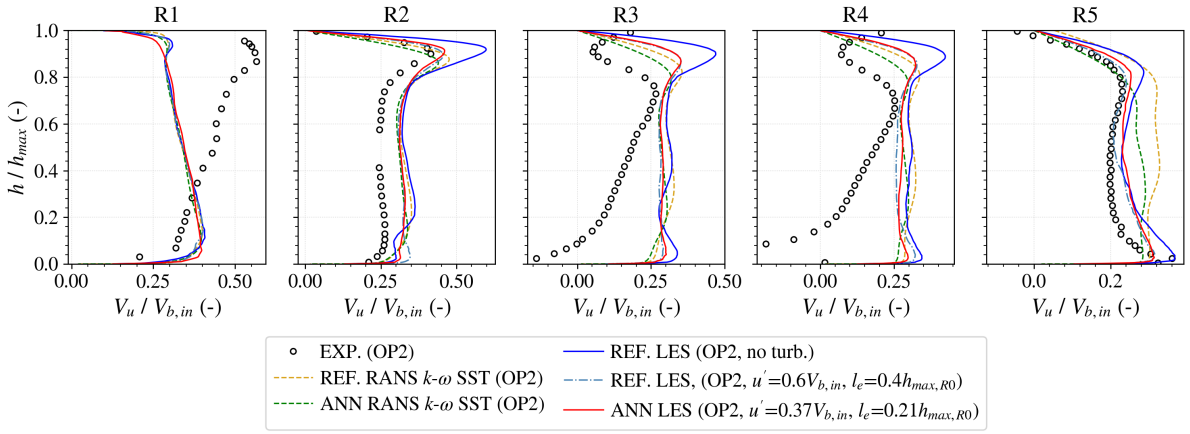

Figure 7.8: Normalized mean tangential velocity profiles inside the draft tube predicted by the reference simulations of the draft tube at OP2 and the proposed strategy.

While similar mean velocity results have been obtained previously using the reference numerical domain after injecting synthetic fluctuations in LES, those results depended on very strong synthetic fluctuations, which then affected the near wall mean velocity profile and, more importantly, the energy balance of the flow (see discussions in Chapter 4). With the proposed strategy and upstream extension, in addition to a more realistic turbulent inflow, the mean velocity profiles are also optimized at the *real* inlet of the draft tube (station R0). As pointed out by Brugière [14], these inlet profile distributions, especially near the walls, have a major impact on the downstream flow behaviour. Indeed, looking at the normalized turbulence kinetic energy profiles, shown in Fig. 7.9, the ANN-RANS results are only slightly underestimated with respect to the reference simulations at stations R1 and R2, but still close to the experimental data. Between R3 and R5, ANN-RANS results are underestimated, but the different velocity profiles (and thus gradients) lead to distinct k distributions near the walls ($h/h_{max} = 0.0$) compared to the reference simulations. Conversely, ANN-LES results are overestimated with respect to experiments at station R1, though not as much as the previous best LES case with turbulence injection discussed in Chapter 4 (i.e., the case where $u' = 0.6V_{b,in}$ and $l_e = 0.4h_{max,R0}$), but agree well with the experimental measurements at R2. Between stations R3 and R5, ANN-LES results are slightly underestimated compared to the experiments and the best reference LES.

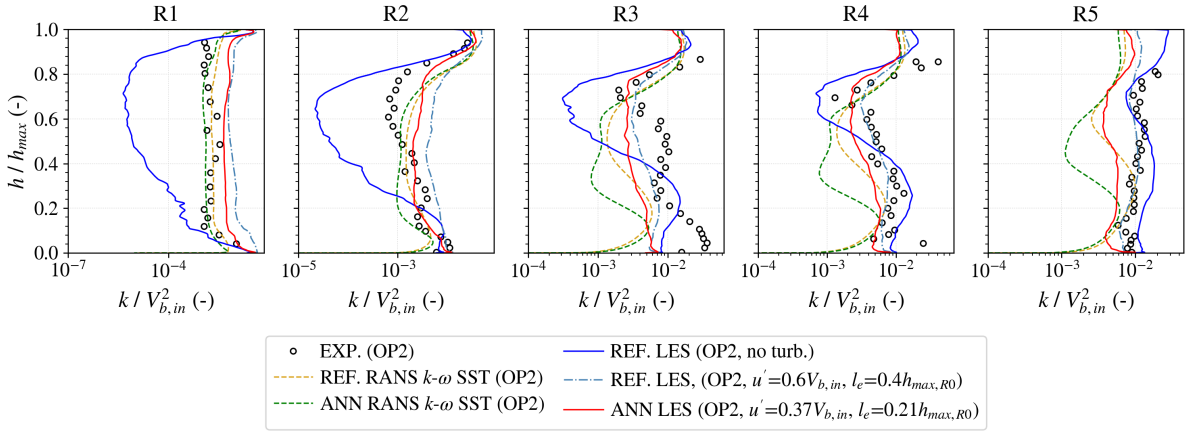

Figure 7.9: Normalized turbulence kinetic energy profiles inside the draft tube predicted by the reference simulations of the draft tube at OP2 and the proposed strategy.

7.4.2 Static pressure profiles and distribution along the walls

One of the most important contributions of the proposed Machine Learning strategy *and* upstream extension is observed in the static pressure evolution inside the draft tube, as illustrated by the normalized static pressure profiles shown in Fig. 7.10. These profiles are important as they indicate how efficiently is the draft tube converting the dynamic pressure into static pressure. Both ANN-RANS and ANN-LES results are shifted with respect to the reference simulations and agree very well with the experimental measurements at all stations. In LES, although this was also observed in reference LES cases with synthetic turbulence injection, though none of them captured the correct static pressure distribution near the walls at station R1 (see also Fig. 4.37). Indeed, this is just one indication of how imposing *unrealistic* synthetic fluctuations can affect the mean flow and therefore any analysis of the draft tube.

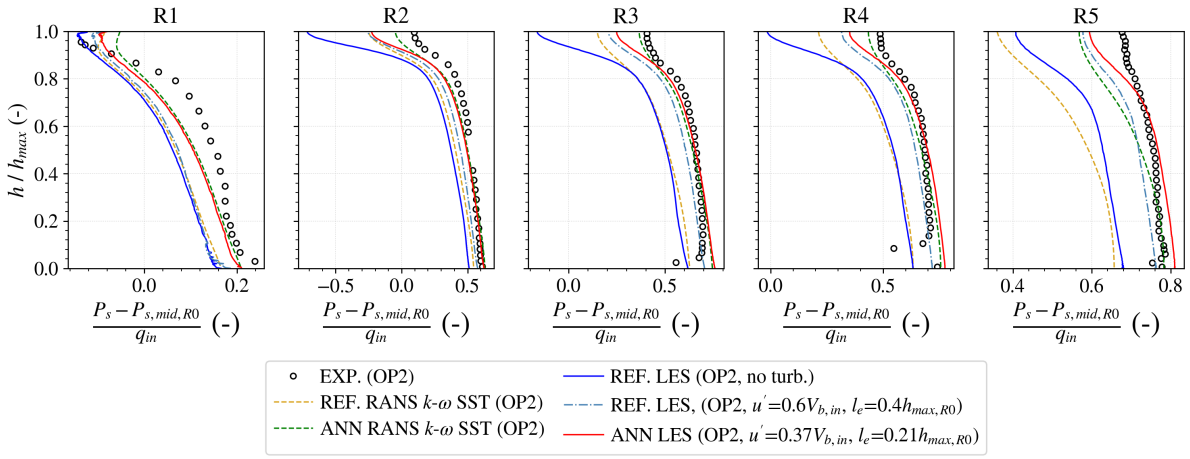

Figure 7.10: Normalized static pressure profiles inside the draft tube predicted by the reference simulations of the draft tube at OP2 and the proposed strategy.

In addition to the normalized static pressure profiles, the evolution of static pressure at the walls is also improved by the proposed Machine Learning strategy and upstream extension. Figure 7.11 shows these results measured circumferentially along the draft tube. Again, results are normalized by the dynamic pressure, q_{in}, and the average static pressure at the walls measured at station C1 is used as reference. As expected, both ANN-RANS and ANN-LES distributions are shifted with respect to the reference simulations and a very good agreement with the experimental data is found between stations C2 and C5. At station EX, however, ANN-RANS results no better than the reference LES without turbulence injection and static pressure values are underestimated with respect to the experiments. Conversely, ANN-LES results match the experimental points almost perfectly at station EX. This is important, as it shows that between stations C1 and EX, i.e., the inlet and outlet of the draft tube, static pressure evolution at the walls (and even inside the domain considering the profiles at Fig. 7.10) is very well predicted by the ANN-LES.

To further demonstrate the capacity of the proposed Machine Learning strategy and upstream extension to correctly predict the static pressure in the draft tube, Fig. 7.12 shows the evolution of P_s at the walls in the streamwise direction, i.e., at stations S1, S2 and S3. Starting with RANS simulations using the k-ω SST turbulence model, ANN results are again shifted with respect to the reference case, which increases the pressure recovery at the beginning of the draft tube and brings numerical results closer to experimental measurements. Downstream the cone of the draft tube ($z/L \geq 0.4$), however, pressure recovery is not as important as it should be and static pressure values at the walls predicted by the ANN-RANS are slightly underestimated with respect to experiments at stations S1 and S3. In LES, in addition to shifting the static pressure values up with respect to the reference case without turbulence injection, the pressure recovery

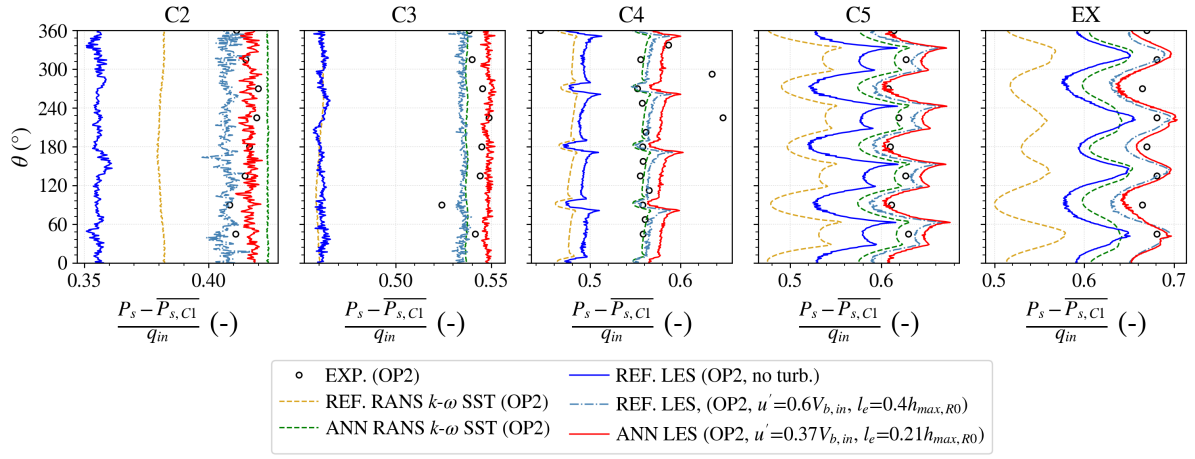

Figure 7.11: Normalized circumferential static pressure distribution at the walls for the reference simulations of the draft tube at OP2 and the proposed strategy. Reference as the average static pressure on the walls measured at station C1, $\overline{P_{s,\mathrm{C1}}}$.

downstream the cone of the draft tube is also modified in the ANN-LES case. At stations S1 and S3, numerical results match the experimental data very well all along its length and even the small variation between $0.75 \leq z/L \leq 1.0$ is captured at S3. Notice that the best reference LES case with synthetic turbulence injection underestimates the pressure recovery at the beginning of the draft tube and consistently underestimates P_s at the walls compared to the experiments.

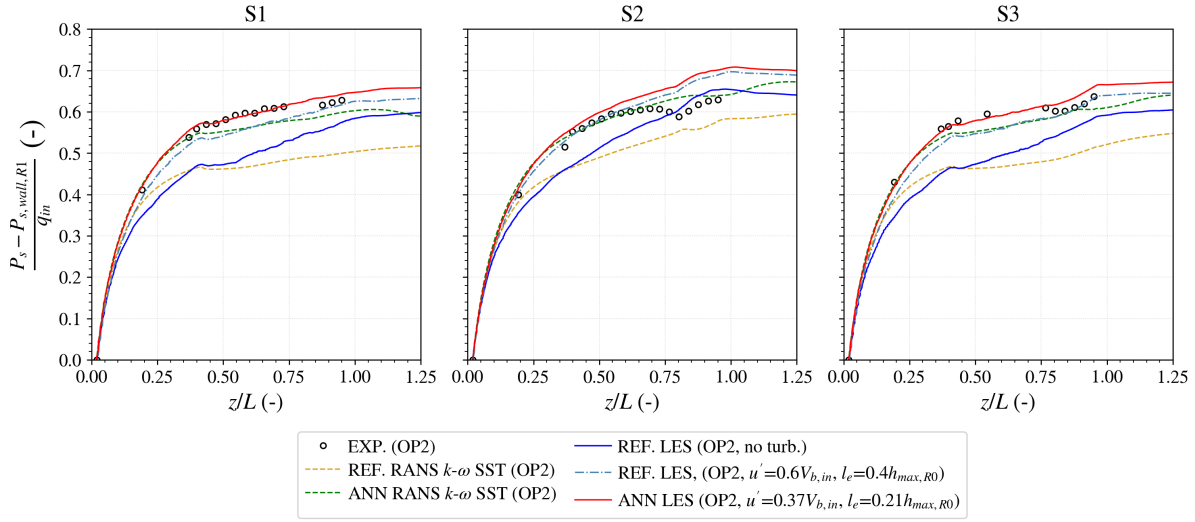

Figure 7.12: Normalized streamwise static pressure evolution at the walls for the reference simulations of the draft tube at OP2 and the proposed strategy.

7.4.3 Head losses analysis

The enhanced velocity and pressure field characterization obtained with the proposed Machine Learning strategy and the extended draft tube domain reflects, obviously, on its head losses. As discussed in Section 4.6.3, a few adaptations have to be made to the IEC losses equation to evaluate its experimental values in OP2, mostly due to *unreliable* mean velocity profiles at station R1 (which impacts the dynamic head) and a shift between five-hole pressure probes and wall-taps static pressure measurements (which impacts the static head). Therefore, the variation in total head inside the draft tube, ΔH_{tot}, is given by Eq. (4.3):

$$\Delta H_{tot} = \Delta H_{sta} + \Delta H_{dyn}$$

where the variation in static head, ΔH_{sta}, is given in Eq. (4.6):

$$\Delta H_{sta} = \frac{1}{\rho g}\langle\overline{P_{s,\mathrm{C1}}}\rangle - \frac{1}{\rho g}\langle\overline{P_{s,\mathrm{EX}}}\rangle$$

and the variation in dynamic head, ΔH_{dyn}, is given by Eq. (4.5):

$$\Delta H_{dyn} = \frac{1}{Q}\iint_{S_{IN}}\left(\frac{1}{2g}\langle u_i\rangle\langle u_i\rangle\right)\langle u_z\rangle dS - \frac{1}{\rho g}\left(\frac{1}{2}\rho\left(\frac{Q}{A_{\mathrm{EX}}}\right)^2\right)$$

From these equations, it is possible then to evaluate the total head losses inside the draft tube, shown in Fig. 7.13. Overall, the variation in dynamic head, ΔH_{dyn}, is very similar in all cases, which is expected given the very good agreement between numerical and experimental mean velocity profiles at station R0. Conversely, variation in static head, ΔH_{sta}, and consequently total head losses, ΔH_{tot}, are very dependent on the case. For instance, reference RANS simulations yield the worst results compared to the experiments, consequence of the poor prediction of static pressure evolution inside the draft tube in this case. The proposed Machine Learning strategy and the upstream extension considerably improves ΔH_{sta} and ΔH_{tot} values in RANS. Indeed, ANN-RANS results are comparable to the reference LES simulations without turbulence injection, and total head losses are 25% overestimated compared to the experiments, against more than 50% in the reference RANS case. On the other hand, ANN-LES results are even better, as ΔH_{sta} is very well predicted and total head losses, ΔH_{tot} are only 6% overestimated compared to the experiments. Although this is slightly above the 3.5% of the best reference LES with synthetic turbulence injection, this is solely due to ΔH_{dyn} and the velocity profiles at station R0. Nevertheless, even though important, the IEC losses are quite limited and do not reflect the *real* head losses inside the draft tube.

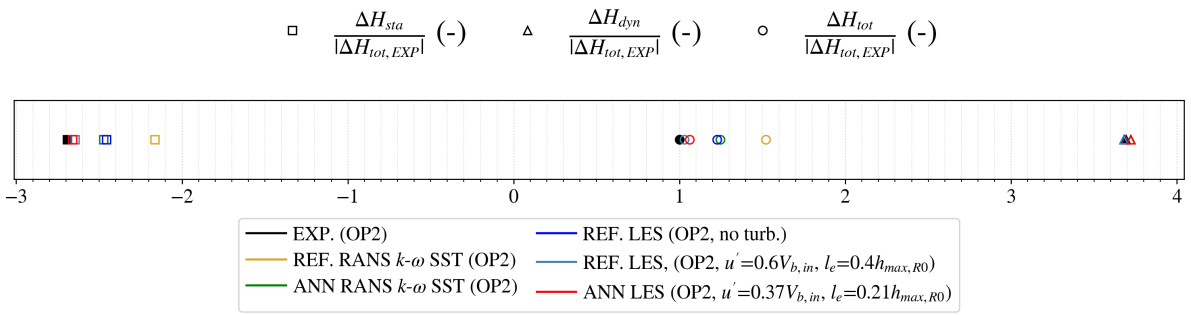

Figure 7.13: IEC losses between stations R0/C1 and EX predicted by the reference simulations and the proposed strategy.

Indeed, the original motivation for the artificial upstream extension and the proposed Machine Learning strategy was to correct the *unphysical* real total head losses evolution inside the draft tube in the reference LES with synthetic turbulence injection, as shown in Sections 4.5.3 and 4.6.3, for two different operating points. Conversely to the IEC losses, the *real* head losses are evaluated from the mass flow averaged evolution of static and dynamic heads in multiple cross-sections in the domain. For instance, the static head variation is given by Eq. (4.8):

$$\Delta H_{sta} = \frac{1}{Q}\iint_{S_{IN}} \frac{\langle P_s \rangle}{\rho g}\langle u_z \rangle dS - \frac{1}{Q}\iint_{S_{sec}} \frac{\langle P_s \rangle}{\rho g}\langle u_z \rangle dS$$

and the dynamic head variation is given by Eq. (4.9):

$$\Delta H_{dyn} = \frac{1}{Q}\iint_{S_{IN}} \left(\frac{1}{2g}\langle u_i \rangle \langle u_i \rangle\right)\langle u_z \rangle dS - \frac{1}{Q}\iint_{S_{sec}} \left(\frac{1}{2g}\langle u_i \rangle \langle u_i \rangle\right)\langle u_z \rangle dS$$

By varying the position of the downstream cross-section and using these two last equations, as well as Eq. 4.3, it is possible to plot *real* head losses evolution inside the draft tube. Although these analyses are restricted to the numerical results, which is important to compare is the ΔH_{tot} evolution predicted by the ANN-LES and the reference LES cases with/without synthetic fluctuations injection. As shown in Fig. 7.14, the issues with negative head losses are not seen in the case with an upstream extension and the proposed Machine Learning strategy. Indeed, ΔH_{tot} values in ANN-LES evolve similarly to the reference LES without synthetic fluctuations injection between $0.0 \leq z/L \leq 0.2$, whereas further downstream its evolution is close to the reference LES with moderate turbulence injection, i.e., $u' = 0.6V_{b,in}$. It should be noticed that, in spite of the relatively low u' values in the ANN-LES case, turbulence kinetic energy levels at station R1 are similar to the reference LES with moderate synthetic turbulence whereas mean velocity profiles are better than the reference LES with strong synthetic turbulence, both of which led to negative ΔH_{tot}.

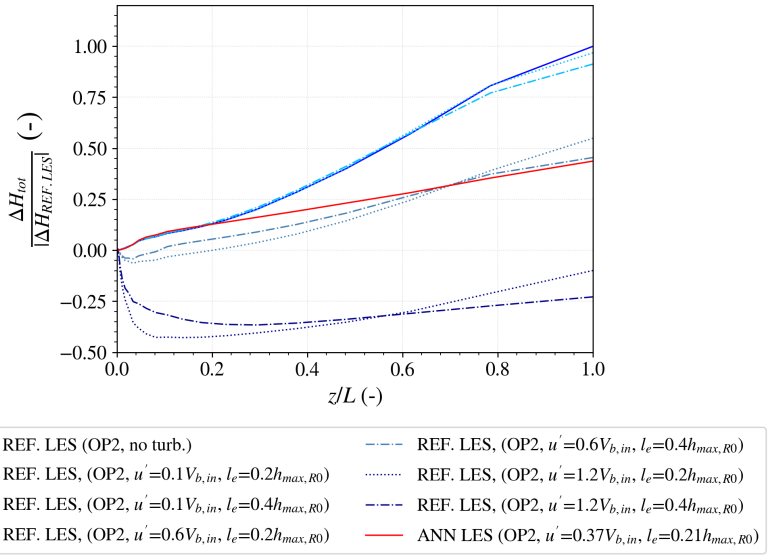

Figure 7.14: Real head losses evolution predicted by the reference simulations and the proposed strategy in LES.

To understand how the proposed Machine Learning strategy and upstream extension are able to improve the results of velocity and pressure fields inside the draft tube without negatively impacting its head losses, we compare the turbulent structures close to the inlet of the reference and extended numerical domains, as shown in Fig. 7.15. As a result of the synthetic fluctuations being injected at the inlet of the upstream extension (station IN), turbulent structures are seen at the *real* inlet of the draft tube (station R0), similarly to the reference LES with synthetic fluctuations injection. However, conversely to these cases, the upstream extension gives the incoming turbulence more time and space for it to develop before reaching the draft tube, impacting thus on the flow behaviour further downstream. For instance, it is hard to identify

any turbulent structure aligned with the mean flow in the reference cases with $u' = 0.6V_{b,in}$ and $u' = 1.2V_{b,in}$ close to the draft tube inlet. Moreover, many of these structures are quickly dissipated within the cone of the draft tube. The ANN-LES case, however, in spite of the low u' value, predicts relatively large turbulent structures at station R0. Indeed, most of these structures at R0 are not dissipated as quickly as before and, looking at the region close to the central vortex, many of them are actually aligned with the mean flow field. More importantly, the strong variation in vorticity values associated with the adaptation and transition of the incoming synthetic fluctuations is now limited to the upstream extension, conversely to the reference LES.

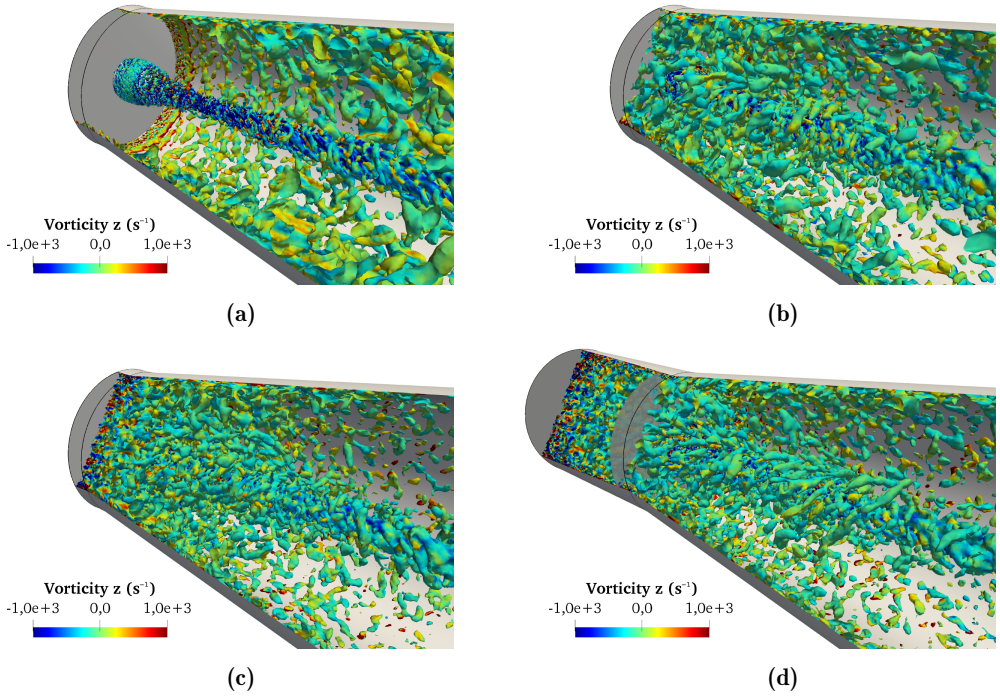

Figure 7.15: Turbulent structures inside the draft tube visualized by iso-surfaces of Q-criterion and coloured by their vorticity z. (a) REF. LES (OP2, no turb.); (b) REF. LES (OP2, $u' = 0.6V_{b,in}$, $l_e = 0.4h_{max,R0}$); (c) REF. LES (OP2, $u' = 1.2V_{b,in}$, $l_e = 0.2h_{max,R0}$); (d) ANN LES, (OP2, $u' = 0.37V_{b,in}$, $l_e = 0.21h_{max,R0}$).

Indeed, adding the upstream extension is crucial for the improved head losses evolution inside the draft tube, especially if we look at the resolved turbulent kinetic energy production, term V in Eq. (2.35). Figure 7.16 its distribution for the same four cases discussed above and, conversely to the reference LES cases with synthetic fluctuation injection, the strongly negative region near the inlet of the domain associated with the decay of the *unrealistic* synthetic turbulence is now far upstream station R0, therefore not interfering as much in the energy balance of the flow inside the draft tube. In the ANN-LES case, turbulent kinetic energy production seems well established at station R0 and there are no rapid variations close to the inlet of the draft tube, which is not the case with the reference simulations where synthetic fluctuations have been injected.

In addition to the upstream extension, the proposed Machine Learning strategy also adjusts the inlet boundary conditions (e.g., mean velocity profiles and synthetic turbulence parameters) to recover the correct downstream flow behaviour. Conversely to other numerical works that investigated the flow inside a bulb turbine draft tube [14, 149, 160], the current approach is able to circumvent some problems related with unknown and/or partially known inlet boundary conditions and its superiority is confirmed, for instance, by the very good agreement obtained with the numerous experimental measurements discussed previously. This is clearly seen in

RANS, where the proposed strategy significantly improved the numerical results using the k-ω SST turbulence model, even though the problems with synthetic fluctuations are *exclusive* to LES. These differences in the downstream flow field have an important impact on the head losses distributions inside the draft tube, especially the turbulent kinetic energy production, terms IV and V in Eq. (2.35). This is important because, as demonstrated in Wilhelm *et al.* [159], the distribution of these terms on the flow indicates the regions where head losses are more important and therefore that could be enhanced during the turbine design.

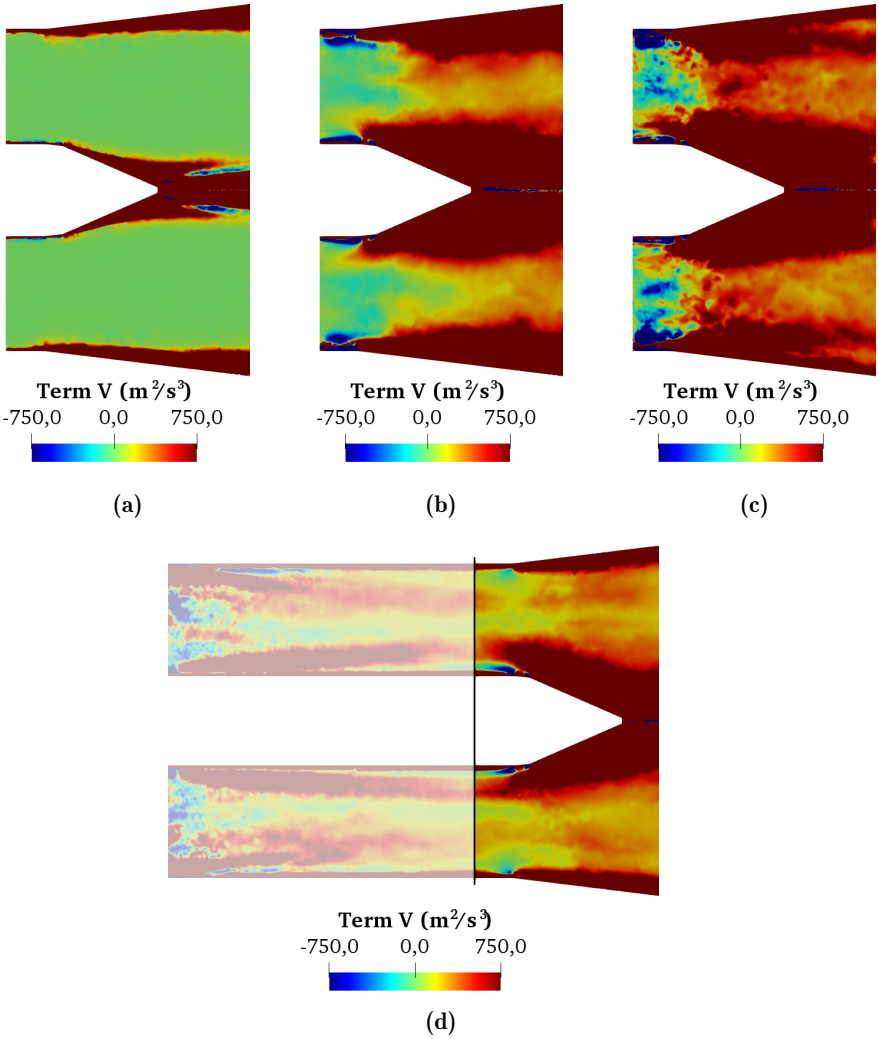

Figure 7.16: Distribution of resolved turbulent kinetic energy production, term V in Eq. (2.35), close to the inlet of the draft tube. (a) REF. LES (OP2, no turb.); (b) REF. LES (OP2, $u' = 0.6V_{b,in}$, $l_e = 0.4h_{max,R0}$); (c) REF. LES (OP2, $u' = 1.2V_{b,in}$, $l_e = 0.2h_{max,R0}$); (d) ANN LES, (OP2, $u' = 0.37V_{b,in}$, $l_e = 0.21h_{max,R0}$).

Figure 7.17 shows the distribution of *modelled* turbulent kinetic energy production, term IV in Eq. (2.35) inside the draft tube in both RANS cases. Overall, the results are very similar to what has been found in Wilhelm *et al.* [159], with two distinct regions of strong turbulent production: near the walls and in the centre region of the flow. The latter can be explained by the presence of a large vortex rope which is formed due to the interaction between flow swirl and the central hub. As the mean velocity gradients in this region of the flow are very similar in both RANS cases, modelled production is almost identical. Conversely, mean velocity gradients on the walls are quite different and so is the modelled turbulent kinetic energy production in this region of the flow. For instance, the more important mean velocity gradients in the reference RANS case leads a significant higher production near the walls, which can explain why

this case overestimated the head losses inside the draft tube by twice as much as the ANN-RANS. More importantly, the improved flow field characterization achieved with the proposed Machine Learning strategy considerably reduced the importance of the turbulent kinetic energy production near the walls in detriment of the central vortex region.

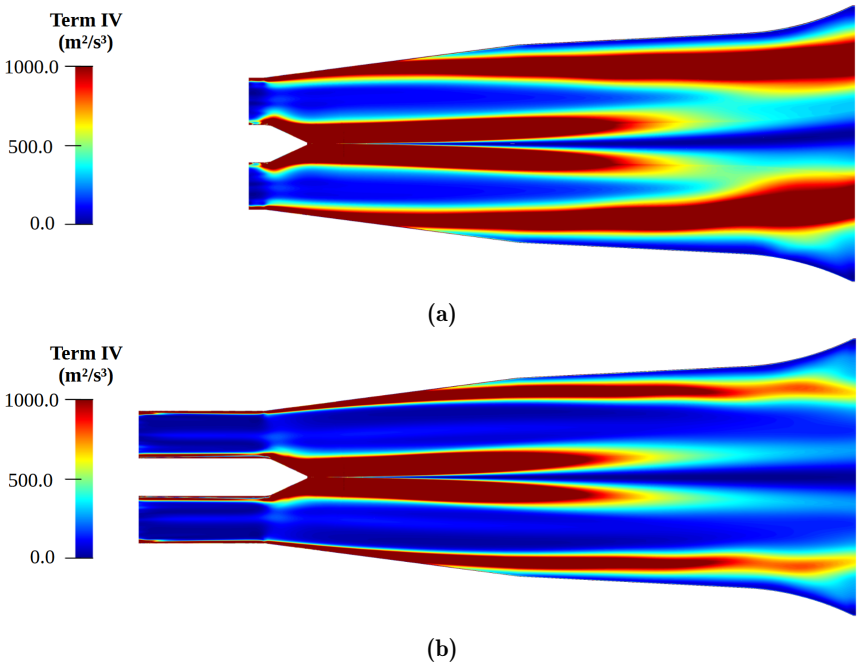

Figure 7.17: Distribution of modelled turbulent kinetic energy production, term IV in Eq. (2.35), inside the draft tube using RANS and k-ω turbulence model. (a) REF. RANS k-ω SST; (b) ANN RANS k-ω SST.

In the case of LES, turbulent kinetic energy production is divided in a modelled and resolved terms in Eq. (2.35), respectively terms IV and V. Due to the nature of the LES solution, modelled production in LES is considerably lower than resolved production. This has been demonstrated in Wilhelm *et al.* [159] and that is what makes of LES superior to RANS, since it is much less susceptible to turbulence modelling errors. In our case, the mesh adaptation process further reduced the modelled production as it ensures that at least 80% of the turbulent kinetic energy is actually resolved in LES. Finally, this is also confirmed by the distributions of modelled and resolved turbulent kinetic energy production inside the draft tube shown in Figs. 7.18 and 7.19 in the reference LES case without synthetic fluctuations injection and ANN-LES.

Analysing the modelled turbulent kinetic energy production distribution shown in Fig. 7.18, both reference and ANN LES cases predict high values in the centre of the flow, where a large central vortex is formed. This is a particularly turbulent region in the draft tube, with very important velocity gradients and where turbulent viscosity is high. The extension of these high values of modelled production goes slightly further downstream in the reference LES case, which can be explained by the lack of flow mixing upstream the draft tube. Indeed, modelled production values are nearly zero at the initial portion of the numerical domain in this case, especially far from both internal and external walls. In the ANN-LES case, the incoming fluctuations results in a fairly turbulent flow from the beginning of the draft tube. As a consequence, modelled production is low but far from zero away from the walls, and the central vortex is dissipated slightly faster due to the enhanced mixing. Another difference of the ANN-LES case to the reference LES without synthetic fluctuations is in the near-wall region of the flow, where the latter predicts a relatively high modelled turbulent kinetic energy production. The distribution of resolved turbulent kinetic energy production inside the draft tube, shown in Fig. 7.19, is similar to its modelled counterpart. For instance, both cases predict relatively high values near the centre of the flow due to the large vortex in this region. Moreover, in the case of the reference

LES without turbulence injection, almost no turbulent kinetic energy production is observed in a large portion of the draft tube. However, compared to the modelled production, the difference in turbulent kinetic energy production near the walls is considerably higher, which is expected given the very different mean velocity gradients in both reference and ANN LES cases.

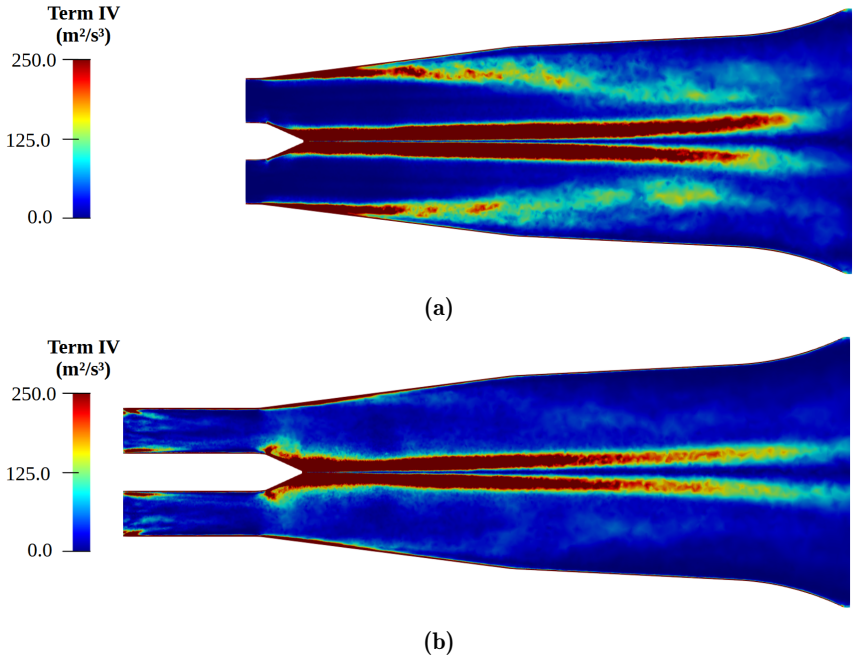

Figure 7.18: Distribution of modelled turbulent kinetic energy production, term IV in Eq. (2.35), inside the draft tube using LES. (a) REF. LES (no turb.); (b) ANN LES, $u' = 0.37V_{b,in}$, $l_e = 0.21h_{max,R0}$.

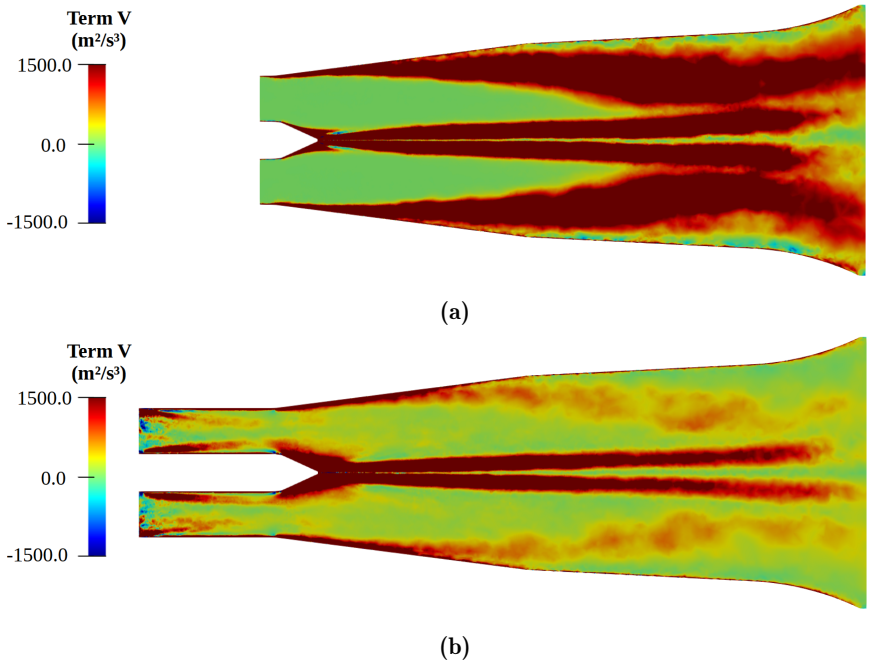

Figure 7.19: Distribution of resolved turbulent kinetic energy production, term V in Eq. (2.35), inside the draft tube using LES. (a) REF. LES (no turb.); (b) ANN LES, $u' = 0.37V_{b,in}$, $l_e = 0.21h_{max,R0}$.

In terms of head losses, the IEC losses results shown in Fig. 7.13 indicated that the reference RANS and LES cases overestimated the head losses inside the draft tube compared to their respective ANN cases and experimental measurements. A similar trend was then observed in

LES when tracing the *real* head evolution shown in Fig. 7.14. However, from these results, we could also determine that reference LES case predicted considerably more head losses in the final portion of the draft tube, as ΔH_{tot} values were very similar until approximately $0.2L$. Thanks to the head losses equation developed in Wilhelm *et al.* [159] and the access to extensive flow information provided by numerical simulations, particularly LES, the figures above just corroborate these previous head losses results, and we can identify the excess in turbulent kinetic energy production on the walls as the main source of head losses inside the draft tube and the main cause for the overestimation in the first place. However, such a precise analysis depended on accurate numerical results, which, in the case of the flow inside the current draft tube, was only possible after the development of a completely new approach to determine proper mean and fluctuating inlet boundary conditions for its numerical simulations.

Chapter 8

Conclusion and perspectives

Numerical simulations of the flow inside a bulb turbine draft tube have been conducted in this thesis. This flow is particularly challenging to simulate since it is highly unsteady, turbulent, with a wide range of motion scales, swirling and subjected to adverse pressure gradients. Two turbulence methods were used to model the turbulence on the flow: RANS using the k-ω SST turbulence model, and LES, using the σ SGS model. The main aspect of the simulations investigated in this work consisted in analysing the influence of the imposed inlet boundary conditions. For instance, accurate and comprehensive measurements of the flow at the inlet of the draft tube are often difficult to obtain, but the downstream flow behaviour is very sensitive to them. Therefore, a first objective in this thesis was to develop a method capable of determining proper mean and fluctuating inlet boundary conditions for these simulations. The proposed method was based on Machine Learning algorithms and its performance was initially verified in the simpler case of conical diffuser. This method is then used to improve the prediction of the flow inside the draft tube and, in particular, its head losses.

8.1 Summary of main results

The analysis of the flow inside the draft tube started with basic numerical simulations using standard approaches to simulate this type of problem. However, these simulations quickly evolved as the initial results were unsatisfactory and the injected synthetic fluctuations lead to an unexpected behaviour of the real head losses. A new approach to determine proper inlet boundary conditions for a numerical simulation was then developed and applied first to a simple test case and only then to the draft tube flow studied initially. The main conclusions of these results are presented in this section.

8.1.1 Reference simulations of the draft tube

Starting from the experimental campaign conducted by GE, the initial RANS and LES computations of the flow inside the draft tube were performed using basic inlet boundary conditions. In particular, the experimental mean velocity profiles measured at the inlet of the draft tube were imposed assuming an axisymmetric distribution. In addition to that, the turbulence kinetic energy profile and a commonly used value of length scale were used to define the turbulent inlet conditions in RANS, whereas in LES, only the mean velocity profiles are imposed initially.

The analysis started with the first operating point, OP1. After some adjustments to the equation, the IEC losses predicted in LES were very close to the experimental measurements. Indeed, these results were much better than RANS, in particular, due to the good prediction of the static pressure evolution at the walls. However, the static pressure profiles inside the draft tube were underestimated by both turbulence methods and, even though LES was able to capture the influence of the central vortex on the mean velocity field, both methods failed to

predict the correct boundary layer behaviour.

One of the issues observed in the LES was the underestimation of turbulence kinetic energy profiles closer to the inlet of the numerical domain. Although this was expected, given that only the mean velocity profiles were imposed at the inlet, the influence of these fluctuating inlet conditions was investigated to improve the mean velocity and static pressure profiles inside the draft tube. Simple synthetic fluctuations were first injected in the LES computations of the draft tube and depending on their intensity, positive effects were observed in the numerical results. For instance, the turbulence kinetic energy profiles were closer to the experiments and the boundary layer behaviour was improved. Moreover, the static pressure profiles were shifted towards the experimental measurements.

Injecting synthetic fluctuations in LES also improved the IEC losses predictions. However, as these losses are limited to integral values of the flow, the real head losses evolution inside the draft tube was also evaluated. The results showed negative head losses close to the inlet of the draft tube, an unexpected behaviour that indicated an increase in the total mean kinetic energy of the flow. This problem was linked to the unrealistic nature of the injected synthetic fluctuations. Moreover, a detailed analysis of the head losses mechanisms in this region of the flow allowed us to identify the resolved turbulent production as the main cause of these negative values.

In addition to OP1, the second operating condition tested experimentally, OP2, was also investigated using basic inlet boundary conditions, with/without synthetic fluctuations injection in LES. Similarly to the first case, the LES results were better in capturing the influence of the central vortex on the mean velocity profiles inside the draft tube. Moreover, the boundary layer behaviour was significantly improved by the synthetic fluctuations in LES. Conversely to OP1 though, IEC losses were not well predicted in RANS and in the LES case without synthetic fluctuations, but were much improved by their injection. However, as the real head losses evolution showed again an unphysical behaviour close to the inlet of the draft tube, it was clear that imposing basic inlet boundary conditions would not yield satisfactory numerical results.

8.1.2 Proposed Machine Learning strategy applied to a simple test case

An innovative approach to determine proper mean and fluctuating inlet boundary conditions for a numerical simulation is proposed in Chapter 5. It is based on Machine Learning algorithms and its goal is to use any downstream information about the flow to determine the proper inlet boundary conditions. Due to its high computational (associated with the generation of an adequate database) the problem of the swirling flow inside the ERCOFTAC conical diffuser was first investigated to understand some aspects of the proposed approach before passing to the more complex and computationally demanding draft tube case. The flow physics inside the conical diffuser is also very similar of a bulb turbine draft tube, in particular, there is a delicate balance between boundary layer septation and core flow recirculation which is very difficult to reproduce numerically. Moreover, while the flow is very sensitive to the imposed inlet boundary conditions, these are not completely known from the experiments.

Like in the initial draft tube simulations, basic inlet boundary conditions were utilized to define baseline results using RANS and LES. The results confirmed the previous numerical works that investigated this flow and the boundary layer in RANS using the k-ω SST turbulence model separated from the walls due to an inadequate inlet radial velocity profile. In LES, the problem was more complex due to the difficulty to generate proper synthetic fluctuations.

The three steps required in the proposed approach, notably the creation of a database, training of a specifically designed ANN and the determination of the optimized inlet boundary conditions were thoroughly explained. In the case of RANS, two numerical domains were investigated: with and without an upstream extension. In both cases, the proposed strategy was able to predict proper inlet boundary conditions, especially the mean radial velocity component. Inside the diffuser, the evolution of mean streamwise and tangential velocity profiles

was comparable to the experiments and the best previous RANS simulations that used *ad hoc* solutions to determine proper inlet conditions. In LES, an upstream extension was added to the numerical domain to give the incoming synthetic fluctuations more space and time for them to develop before reaching the inlet of the conical diffuser. Nevertheless, the proposed Machine Learning strategy was able to automatically adjust the upstream inlet boundary conditions in order to match the downstream flow behaviour. In addition to the mean velocity profiles inside the conical diffuser, the turbulence kinetic energy profiles and the turbulence correlations were also improved by the proposed approach.

8.1.3 Proposed Machine Learning strategy applied to the draft tube case

After the promising results obtained in the canonical case of the swirling flow inside the ERCOFTAC conical diffuser, we revisited the draft tube flow investigated in Chapter 4 and applied the proposed Machine Learning strategy to determine the proper inlet boundary conditions for these simulations. The three main steps of the proposed approach were once again thoroughly explained. To overcome the issues with the *unrealistic* synthetic fluctuations decay, an artificial extension was added upstream the draft tube computational domain. Due to some inconsistencies with the experimental data in OP1, only the second operating point was investigated and the architecture of the neural network had to be modified.

The proposed Machine Learning strategy was able to adjust the mean velocity profiles and turbulent inlet conditions at the inlet of the upstream extension to obtain a good correspondence between the numerical and experimental data inside the draft tube. For instance, in LES, the better characterization of the mean axial velocity profiles near the external walls at the inlet of the draft tube improved the boundary layer behaviour. In RANS, however, the results were clearly limited by the turbulence method. The static pressure profiles and evolution along the walls were shifted compared to the reference simulations and a very good match with the experimental measurements was found, especially in LES. As a consequence, the error in IEC losses prediction were reduced by half in RANS and, in the case of LES, they ended up being very close to the experimental measurements and as good as the best reference case with synthetic turbulence injection.

However, the motivation for the development of the proposed Machine Learning approach was to correct the negative values of real head losses evolution inside the draft tube in LES. In this regard, the artificial upstream extension gave the necessary space and time for the synthetic fluctuations to develop before reaching the draft tube. As a result, the real head losses evolution were improved by the proposed strategy. A detailed analysis of the turbulent kinetic energy production inside the draft tube, its main head losses mechanism, also allowed us to evaluate the impact of imposing proper inlet boundary conditions on the performance analysis. For instance, a strong reduction of the head losses was found near the external walls in the cases with proper inlet conditions. Indeed, most of the losses were concentrated in the central region of the flow (at the central vortex). This is a very important observation since it could change the analysis of which parts of the draft tube are more important to be optimized in order to improve its overall performance.

8.2 Future directions

Given the multiple aspects of the results presented in this thesis and briefly discussed in the previous section, three suggestions of future directions are given below.

8.2.1 Draft tube simulations

Starting with the numerical simulations of draft tubes, the results in the previous chapters just confirmed the importance of accurately determining and imposing the inlet boundary condi-

tions for these simulations. This is in agreement with previous observations [7, 149, 14, 160], but it is clear that the fluctuating field at the inlet of the draft tube is also very important to define. Therefore, one obvious future direction for this thesis is **to keep improving the characterization of the inlet boundary conditions for the draft tube**.

8.2.2 Proposed Machine Learning strategy

Although the geometry of the draft tube investigated in this thesis was already investigated in previous works [159, 160] and is similar to that found in a real bulb turbine, the elements generating the turbulent swirling flow at its inlet was considerably simplified for the current study. For instance, the generated inlet boundary conditions were more controlled in comparison to a real turbine and the flow was particularly uniform in the azimuthal direction. Since this behaviour is not necessarily equal to that found downstream a turbine runner [5, 157, 84], one first aspect of the proposed Machine Learning strategy that could be investigated is its **applicability to more representative draft tube flow configurations**. However, as the amount of experimental data required to feed the trained ANN model can be significantly lower than that from the draft tube investigated in this thesis, a second aspect of the proposed Machine Learning strategy that could be investigated is the possibility **to train a model with a limited amount of data while still being able to yield good inlet boundary conditions predictions**. Similar to that, given the high computational cost associated with the generation of the numerical database to train the ANN, one last aspect of the proposed strategy that could be explored is the **reduction of the amount of numerical simulations in the database**. For that, one could consider modifying the architecture of the current ANN (which was manually determined), performing a sensitive analysis to understand which inlet profiles control the most the downstream flow behaviour, or improving the inlet profiles automatic generation method to enhance their representativeness of a desired solution space.

8.2.3 Other applications of data-driven techniques

While we used machine learning algorithms to determine the proper inlet boundary conditions for the numerical simulations of the draft tube and conical diffuser, this is only one technique among many others that could have been applied. As explained in Chapter 5, previous numerical works that investigated draft tubes preferred adjoint methods and evolutionary algorithms as optimization techniques, which could be adapted to our problem and their performance compared against our proposed strategy. In addition to that, the inverse could also be done. For instance, the reason behind choosing machine learning algorithms was its relatively easy implementation and flexibility. Therefore, one possible continuation of this thesis would be to explore other problems using a similar approach such as the **optimization of the inlet profile based on the hydraulic performance of the draft tube** [52, 53, 51], which could potentially use the same databases already generated. In parallel with that, the proposed Machine Learning strategy could be adapted to **optimize the shape of the runner blades**, similarly to what have been done in previous works [27, 75, 87]. Finally, one last application our proposed Machine Learning strategy is the **optimization of the draft tube geometry**, something that has been investigated multiple times in the past but is still very computationally demanding with the use of adjoint methods and evolutionary algorithms [40, 127, 96, 42, 110, 91, 26, 100, 47].

Appendix A

ANN training performance

As discussed in Section 5.3, the *learning* process can only take place during training if we are able to measure the *performance* of the ANN in realizing the desired task. Similarly to a traditional optimization problem, this is achieved by calculating the value of some *loss function*. In the case of the problem discussed in the present work, the desired task consists in performing a non-linear regression since our goal is to determine the numerical values of the inlet profiles/parameters based on the numerical values of the downstream profiles. Therefore, the loss function used to evaluate the ANN performance is the *Mean Squared Error* (MSE) between the model's prediction $\hat{y}$ and the true value y. For the case of a dataset comprising m training examples, the MSE is given by Eq. (5.8):

$$\text{MSE} = \frac{1}{m}\sum_{i}^{m}(\hat{y} - y)^2$$

Based on this value, the weights and biases of the ANN are adjusted by an optimization algorithm after the *backpropagation* step to improve the model's prediction, i.e., to reduce the loss function. However, since one important characteristic of *machine learning* is that the trained ANN should perform well on the observed dataset as well as on previously unobserved data, i.e., since the trained ANN should be able to *generalize*, this loss function is typically evaluated into two datasets: a *training* and a *validation* datasets. The former contains the data that is observed by the ANN and is used during training to adjust its weights and biases. Conversely, the latter dataset contains unobserved data (i.e., data to which the ANN had no access to during training) that is used to evaluate the model's generalization capability.

As mentioned in Chapters 6 and 7, the databases used to train the multiple ANN discussed in the present work were divided into two, respectively a training and a validation dataset. For instance, from the 400 cases used to train the ANN in each conical diffuser problem, 10% of it (i.e., 40 cases) was used for validation (see Chapter 6). In the draft tube cases, 20% of the 500 cases (i.e., 100 cases) were used for validation (see Chapter 7). The evolution of the loss function MSE in each of these datasets during the training of the LES neural networks are discussed below.

A.1 ERCOFTAC conical diffuser

Figure A.1 shows the evolution of the loss function, MSE, for each of the four inlet profiles (U_z, U_θ, U_r and k) in the ANN LES case of the conical diffuser studied in Chapter 6. As expected, the value of MSE for both training and validation datasets continuously decrease as the ANN is trained, i.e., as the number of epochs increase and its weights and biases are adjusted. However, in the case of the validation dataset, the MSE quickly reaches a minimum value in all four cases. Continuing to train the ANN after this point increases the gap between the training

and validation MSE, meaning that the model is *overfitting*, and its generalization capabilities are *possibly* compromised.

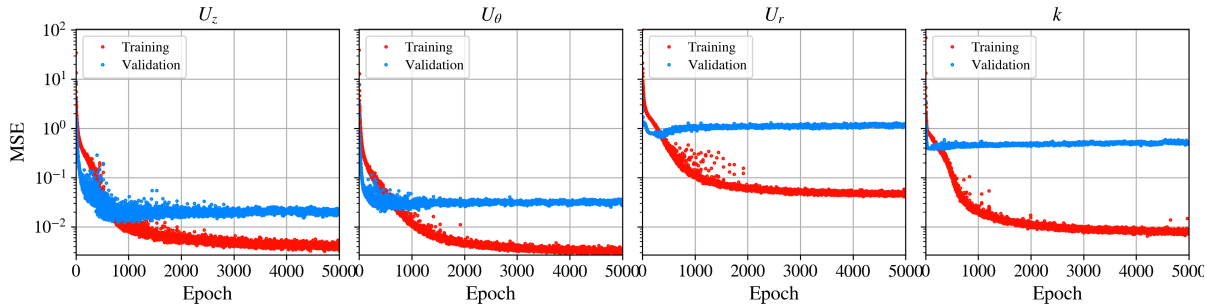

Figure A.1: Evolution of the training and validation loss function for each inlet profile in the ERCOFTAC conical diffuser case.

This *overfitting* behaviour can be improved by adding some *regularization* to the ANN, such as $L1$, $L2$ and dropout [144]. Indeed, this is done in all ANN discussed in Chapters 6 and 7, notably by using dropout. One difficulty though consists in the different MSE level attained by each inlet profile shown in Fig. A.1. For instance, both U_z and U_θ present similar MSE evolutions, and by the end of the 5000 epochs performed to train the ANN, the training MSE in both cases is approximately 2×10^{-3}, with the validation MSE being close to the training one. Conversely, the training MSE for the radial velocity profile, U_r, is considerably higher at the end of the 5000 epochs, at approximately 5×10^{-2}, but the validation MSE is further apart in this case. Looking at the turbulence kinetic energy profile, k, this difference between training and validation MSE is even more noticeable. Thus, adjusting the dropout rate for the different MLP that form the ANN is not straightforward, as each profile requires different levels of *regularization*.

Another difficulty of reducing the *overfitting* of the current ANN model is the impact that each inlet profile has on the downstream flow behaviour. For instance, it is *easier* for the ANN model to determine the correct mean axial velocity profile at the inlet as it is related to the flow rate (and, thus, U_x magnitude) inside the diffuser. Similarly, the mean tangential velocity profile at the inlet is related to the swirling level of the downstream flow, and controls in some sense the boundary layer inside the conical diffuser. However, as pointed out in Chapter 6, the proper mean radial velocity profile at the inlet of the diffuser is crucial to capture the correct behaviour of the boundary layer, in particular, to avoid that it detaches from the walls. Nevertheless, the sensitivity of the downstream flow bahaviour to its actual values seems to be less important as a significant variation on this profile still yields very good downstream results. Indeed, this is shown by the comparison of U_r at station S0 in Fig. 6.14 and the subsequent discussions. A similar analysis can also be performed for the turbulence kinetic energy profile, k, which was measured only very close to the walls.

It is important to note that both mean axial and tangential velocity profiles have been measured by Clausen *et al.* [19] and are used to train the ANN, whereas the mean radial velocity profile is not known anywhere on the conical diffuser, and the ANN has to *infer* its value at the inlet from other profiles. This, in addition to the weaker influence on the downstream flow, can explain the higher MSE values in this particular profile.

A.2 Bulb turbine draft tube

The MSE evolution for the ANN LES draft case studied in Chapter 7 is shown in Fig. A.2. The training MSE behaviour is very similar to what has been previously observed in the ERCOFTAC conical diffuser, showing once again the importance of this test case. However,

compared to the previous case, the validation MSE is considerably higher in the draft tube ANN and *overfitting* more important. While it is not easy to determine the exact reason behind this result, the higher complexity of the flow renders it more difficult for the ANN to *generalize*, at the same time that the access to the downstream profiles at fewer stations reduces the amount of information it has access during training. Nevertheless, similarly to the ERCOFTAC conical diffuser, mean axial and tangential velocity profiles yielded smaller validation MSE compared to mean radial and turbulence kinetic energy profiles.

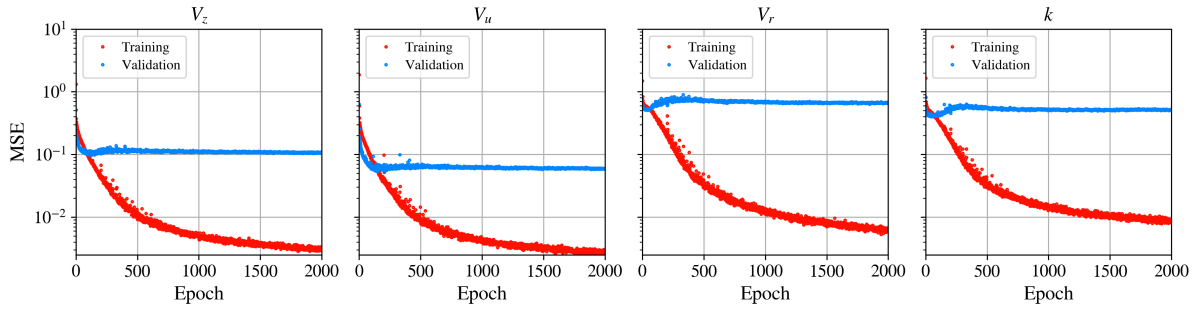

Figure A.2: Evolution of the training and validation loss function for each inlet profile in the draft tube case.

Despite *overfitting* shown in Figs. A.1 and A.2, the results obtained by the ANN LES discussed in Chapters 6 and 7 show that the trained models are still able to predict proper inlet boundary conditions for the simulation. Indeed, limiting the analysis to the MSE evolution can be misleading and, in the case of the proposed Machine Learning strategy, we systematically checked if the results of the trained model.

Bibliography

[1] BP Statistical review of world enegry 2021. `https://www.bp.com/content/dam/bp/business-sites/en/global/corporate/pdfs/energy-economics/statistical-review/bp-stats-review-2021-full-report.pdf`. Accessed: 2021-06-30.

[2] Jean-Luc Aider and Alexandra Danet. Large-eddy simulation study of upstream boundary conditions influence upon a backward-facing step flow. *Comptes Rendus Mécanique*, 334(7):447–453, 2006.

[3] ANSYS. Solver theory guide. *Ansys CFX Release*, 19, 2018.

[4] S W Armfield, N-H Cho, and C A J Fletcher. Prediction of turbulence quantities for swirling flow in conical diffusers. *AIAA Journal*, 28(3):453–460, 1990.

[5] François Avellan. Flow investigation in a francis draft tube: the FLINDT project. In *Proceedings of the 20th IAHR Symposium, Charlotte, North Carolina, USA, August*, volume 1, pages 1–18. International Association For Hydraulic Research, 2000.

[6] Paul Batten, Uriel Goldberg, and Sukumar Chakravarthy. Interfacing statistical turbulence closures with large-eddy simulation. *AIAA Journal*, 42(3):485–492, 2004.

[7] Carl-Anthony Beaubien. *Simulations numériques de l'écoulement turbulent dans un aspirateur de turbine hydraulique*. PhD thesis, Université Laval, Quebec, Canada, 2013.

[8] P Bélanger-Vincent. Simulations avancées de l'écoulement turbulent dans les aspirateurs de turbines hydrauliques. Master's thesis, Université Laval, Quebec, Canada, 2010.

[9] Pierre Benard, Guillaume Balarac, Vincent Moureau, Cecile Dobrzynski, Ghislain Lartigue, and Yves D'Angelo. Mesh adaptation for large-eddy simulations in complex geometries. *International Journal for Numerical Methods in Fluids*, 2015.

[10] J Bergstra and Y Bengio. Random search for hyper-parameter optimization. *Journal of Machine Learning Research*, 13(2), 2012.

[11] Sofien Bouajila. *Analyse expérimentale et numérique des écoulements à charge partielle dans les turbines Francis-Étude des vortex inter-aubes.* PhD thesis, Université Grenoble Alpes (ComUE), 2018.

[12] O Bounous. Studies of the ERCOFTAC conical diffuser with OpenFOAM. *Department of Applied Mechanics Chalmers University of technology, Göteborg, Sweeden*, 2008.

[13] Joseph Boussinesq. *Essai sur la théorie des eaux courantes.* Impr. nationale, 1877.

[14] Olivier Brugière. *Fiabilité et évaluation des incertitudes pour la simulation numérique de la turbulence: application aux machines hydrauliques.* PhD thesis, Université Grenoble Alpes, 2015.

[15] DE Carl. *A practical guide to splines*. Springer, 2001.

[16] Michel Cervantes and Fredrik Engström. Eddy viscosity turbulence models and steady draft tube simulations. In *IAHR/ERCOFTAC workshop on draft tube flow: 08/12/2005-09/12/2005*, pages 37–44. Luleå tekniska universitet, 2005.

[17] Michel Cervantes, Fredrik Engström, and Håkan Gustavsson. *Turbine-99 III: Proceedings of the third IAHR/ERCOFTAC workshop on draft tube flow*. Luleå tekniska universitet, 2005.

[18] Michel J Cervantes and T Fredrik Engstroöm. Factorial design applied to CFD. *Journal of Fluids Engineering*, 126(5):791–798, 2004.

[19] P D Clausen, S G Koh, and D H Wood. Measurements of a swirling turbulent boundary layer developing in a conical diffuser. *Experimental Thermal and Fluid Science*, 6(1):39 – 48, 1993.

[20] DA Clevert, T Unterthiner, and S Hochreiter. Fast and accurate deep network learning by exponential linear units (ELUs). *arXiv preprint arXiv:1511.07289*, 2015.

[21] Alessandro Corsini, Giovanni Delibra, Marco Giovannelli, and Stefania Traldi. Machine learnt synthetic turbulence for LES inflow conditions. In *ASME Turbo Expo 2020: Turbomachinery Technical Conference and Exposition*. American Society of Mechanical Engineers Digital Collection, 2020.

[22] Jiahuan Cui, V Nagabhushana Rao, and Paul G Tucker. Numerical investigation of secondary flows in a high-lift low pressure turbine. *International Journal of Heat and Fluid Flow*, 63:149–157, 2017.

[23] L Davidson and M Billson. Hybrid LES-RANS using synthesized turbulent fluctuations for forcing in the interface region. *International Journal of Heat and Fluid Flow*, 27(6):1028–1042, 2006.

[24] Lars Davidson. Hybrid LES-RANS: inlet boundary conditions for flows with recirculation. In *Advances in Hybrid RANS-LES Modelling*, pages 55–66. Springer, 2008.

[25] V De Henau, FA Payette, M Sabourin, C Deschênes, JM Gagnon, and P Gouin. Computational study of a low head draft tube and validation with experimental data. In *IOP Conference Series: Earth and Environmental Science*, volume 12, page 012084. IOP Publishing, 2010.

[26] Gizem Demirel, Erdem Acar, Kutay Celebioglu, and Selin Aradag. CFD-driven surrogate-based multi-objective shape optimization of an elbow type draft tube. *International Journal of Hydrogen Energy*, 42(28):17601–17610, 2017.

[27] Sh Derakhshan and A Mostafavi. Optimization of gamm francis turbine runner. *World Acad. Sci. Eng. Technol*, 59:717–723, 2011.

[28] C Deschênes, S Houde, V Aeschlimann, R Fraser, and GD Ciocan. Modern challenges for flow investigations in model hydraulic turbines on classical test rig. In *IOP Conference Series: Earth and Environmental Science*, volume 22, page 022013. IOP Publishing, 2014.

[29] Claire Deschênes, Gabriel Dan Ciocan, Vincent De Henau, Felix Flemming, Jinxing Huang, Marcel Koller, Fidel Arzola Naime, Maryse Page, Ruixia Qian, and Thi Vu. General overview of the AxialT Project: a partnership for low head turbine developments. In *IOP Conference Series: Earth and Environmental Science*, volume 12, page 012043. IOP Publishing, 2010.

[30] Nitin S Dhamankar, Gregory A Blaisdell, and Anastasios S Lyrintzis. Overview of turbulent inflow boundary conditions for large-eddy simulations. *AIAA Journal*, 56(4):1317–1334, 2018.

[31] L Di Mare, M Klein, WP Jones, and J Janicka. Synthetic turbulence inflow conditions for large-eddy simulation. *Physics of Fluids*, 18(2):025107, 2006.

[32] C. Dobrzynski and P. Frey. *Anisotropic Delaunay mesh adaptation for unsteady simulations*, pages 177–194. Springer Berlin Heidelberg, 2008.

[33] Francois Doussot. *Simulation numérique de l'écoulement de charge partielle dans les turbines Francis: analyse de la topologie et de la dynamique des vortex inter-aubes*. PhD thesis, Université Grenoble Alpes, 2019.

[34] T Dozat. Incorporating Nesterov momentum into Adam. 2016.

[35] John Duchi, Elad Hazan, and Yoram Singer. Adaptive subgradient methods for online learning and stochastic optimization. *Journal of Machine Learning Research*, 12(7), 2011.

[36] C Duprat. *Simulation numérique instationnaire des écoulements turbulents dans les diffuseurs des turbines hydrauliques en vue de l'amélioration des performances*. PhD thesis, Institut National Polytechnique de Grenoble (INPG), Grenoble, France, 2010.

[37] C Duprat, G Balarac, O Métais, P Congedo, and O Brugière. A wall-layer model for large-eddy simulations of turbulent flows with/out pressure gradient. *Physics of Fluids*, 23(1):015101, 2011.

[38] Pierre Duquesne, Yvan Maciel, and Claire Deschênes. Unsteady flow separation in a turbine diffuser. *Experiments in Fluids*, 56(8):1–15, 2015.

[39] Yu Egorov and F Menter. Development and application of sst-sas turbulence model in the desider project. In *Advances in Hybrid RANS-LES Modelling*, pages 261–270. Springer, 2008.

[40] Ralf Eisinger and Albert Ruprecht. Automatic shape optimization of hydro turbine components based on CFD. *TASK Q*, 6(1):101–111, 2002.

[41] T Elsken, J H Metzen, F Hutter, et al. Neural architecture search: a survey. *Journal of Machine Learning Research*, 20(55):1–21, 2019.

[42] Robert Fares, Xiaomin Chen, and Ramesh Agarwal. Shape optimization of an axisymmetric diffuser and a 3D hydro-turbine draft tube using a genetic algorithm. In *49th AIAA Aerospace Sciences Meeting including the New Horizons Forum and Aerospace Exposition*, page 1243, 2011.

[43] A Favrel, A Müller, C Landry, K Yamamoto, and F Avellan. Ldv survey of cavitation and resonance effect on the precessing vortex rope dynamics in the draft tube of francis turbines. *Experiments in Fluids*, 57(11):1–16, 2016.

[44] A Ferrante and SE Elghobashi. A robust method for generating inflow conditions for direct simulations of spatially-developing turbulent boundary layers. *Journal of Computational Physics*, 198(1):372–387, 2004.

[45] Joel H Ferziger and Milovan Perić. *Computational methods for fluid dynamics*, volume 3. Springer, 2002.

[46] Matthias Feurer and Frank Hutter. Hyperparameter optimization. In *Automated Machine Learning*, pages 3–33. Springer, Cham, 2019.

[47] B Fleischli, A Del Rio, E Casartelli, L Mangani, BF Mullins, C Devals, and M Melot. Application of a general discrete Adjoint Method for draft tube optimization. In *IOP Conference Series: Earth and Environmental Science*, volume 774, page 012012. IOP Publishing, 2021.

[48] Hosein Foroutan and Savas Yavuzkurt. Flow in the simplified draft tube of a francis turbine operating at partial load—part I: Simulation of the vortex rope. *Journal of Applied Mechanics*, 81(6), 2014.

[49] Kai Fukami, Yusuke Nabae, Ken Kawai, and Koji Fukagata. Synthetic turbulent inflow generator using machine learning. *Physical Review Fluids*, 4(6):064603, 2019.

[50] Jean-Mathieu Gagnon, Vincent Aeschlimann, Sébastien Houde, Felix Flemming, Stuart Coulson, and Claire Deschenes. Experimental investigation of draft tube inlet velocity field of a propeller turbine. *Journal of fluids engineering*, 134(10), 2012.

[51] S Galván, M Reggio, and F Guibault. Numerical optimization of the inlet velocity profile ingested by the conical draft tube of a hydraulic turbine. *Journal of Fluids Engineering*, 137(7), 2015.

[52] Sergio Galván, Carlos Rubio, Jesús Pacheco, Crisanto Mendoza, and Miguel Toledo. Optimization methodology assessment for the inlet velocity profile of a hydraulic turbine draft tube: part I — computer optimization techniques. *Journal of Global Optimization*, 55(1):53–72, 2013.

[53] Sergio Galván, Carlos Rubio, Jesús Pacheco, Gildardo Solorio, and Georgina Carbajal. Optimization methodology assessment for the inlet velocity profile of a hydraulic turbine draft tube: part II — performance evaluation of draft tube model. *Journal of Global Optimization*, 55(4):729–749, 2013.

[54] Manuel García-Villalba and Jochen Fröhlich. LES of a free annular swirling jet - Dependence of coherent structures on a pilot jet and the level of swirl. *International Journal of Heat and Fluid Flow*, 27(5):911–923, 2006.

[55] Rikard Gebart, Håkan Gustavsson, and Rolf Karlsson. Proceedings of Turbine-99: workshop on draft tube flow, 2000.

[56] A Gehrer, H Benigni, and M Köstenberger. Unsteady simulation of the flow through a horizontal-shaft bulb turbine. In *Proceedings of the 22nd IAHR Symposium on Hydraulic Maschines and Systems, Stockholm*, 2004.

[57] Massimo Germano. Turbulence: the filtering approach. *Journal of Fluid Mechanics*, 238:325–336, 1992.

[58] Massimo Germano, Ugo Piomelli, Parviz Moin, and William H Cabot. A dynamic subgrid-scale eddy viscosity model. *Physics of Fluids A: Fluid Dynamics*, 3(7):1760–1765, 1991.

[59] X Glorot, A Bordes, and Y Bengio. Deep sparse rectifier neural networks. In *Proceedings of the fourteenth international conference on artificial intelligence and statistics*, pages 315–323. JMLR Workshop and Conference Proceedings, 2011.

[60] I Goodfellow, Y Bengio, A Courville, and Y Bengio. *Deep learning*, volume 1. MIT press Cambridge, 2016.

[61] Maksimilian Fedorovich Gubin. *Draft tubes of hydro-electric stations*. Amerind Publishing Company for the US Bureau of Reclamation, 1973.

[62] V Guénette, S Houde, GD Ciocan, G Dumas, J Huang, and C Deschênes. Numerical prediction of a bulb turbine performance hill chart through RANS simulations. In *IOP Conference Series: Earth and Environmental Science*, volume 15, page 032007. IOP Publishing, 2012.

[63] W Gyllenram and H Nilsson. Very large eddy simulation of draft tube flow. In *Proc. 23rd IAHR Symp. on Hydraulic Machinery and Systems, Yokohama, Japan F*, volume 159, 2006.

[64] Lucian Hanimann, Luca Mangani, Ernesto Casartelli, Thomas Mokulys, and Sebastiano Mauri. Development of a novel mixing plane interface using a fully implicit averaging for stage analysis. *Journal of Turbomachinery*, 136(8), 2014.

[65] S Houde, A Carrier, JD Buron, and C Deschênes. Numerical analysis of a measured efficiency hysteresis on a bulb turbine model. In *IOP conference series: earth and environmental science*, volume 22, page 022009. IOP Publishing, 2014.

[66] R Iovanel, D Bucur, and Michel Cervantes. Study on the accuracy of rans modelling of the turbulent flow developed in a kaplan turbine operated at bep. part 1-velocity field. *Journal of Applied Fluid Mechanics*, 12(5):1449–1461, 2019.

[67] R Iovanel, Georgiana Dunca, and Michel Cervantes. Study on the accuracy of rans modelling of the turbulent flow developed in a kaplan turbine operated at bep. part 2-pressure fluctuations. *Journal of Applied Fluid Mechanics*, 12(5):1463–1473, 2019.

[68] N Jarrin, S Benhamadouche, D Laurence, and R Prosser. A synthetic-eddy-method for generating inflow conditions for large-eddy simulations. *International Journal of Heat and Fluid Flow*, 27(4):585–593, 2006.

[69] N Jarrin, R Prosser, J-C Uribe, S Benhamadouche, and D Laurence. Reconstruction of turbulent fluctuations for hybrid RANS/LES simulations using a synthetic-eddy method. *International Journal of Heat and Fluid Flow*, 30(3):435–442, 2009.

[70] Javier Jiménez, Sergio Hoyas, Mark P Simens, and Yoshinori Mizuno. Turbulent boundary layers and channels at moderate reynolds numbers. *Journal of Fluid Mechanics*, 657:335–360, 2010.

[71] WP Jones and Brian Edward Launder. The prediction of laminarization with a two-equation model of turbulence. *International Journal of Heat and Mass Transfer*, 15(2):301–314, 1972.

[72] PP Jonsson, BG Mulu, and MJ Cervantes. Experimental investigation of a Kaplan draft tube - Part II: Off-design conditions. *Applied Energy*, 94:71–83, 2012.

[73] D Jošt and A Škerlavaj. Efficiency prediction for a low head bulb turbine with SAS SST and zonal LES turbulence models. In *IOP Conference Series: Earth and Environmental Science*, volume 22, page 022007. IOP Publishing, 2014.

[74] M Kato. The modelling of turbulent flow around stationary and vibrating square cylinders. *Turbulent Shear Flow*, 1:10–4, 1993.

[75] H Kawajiri, Y Enomoto, and S Kurosawa. Design optimization method for francis turbine. In *IOP Conference Series: Earth and Environmental Science*, volume 22, page 012026. IOP Publishing, 2014.

[76] Anthony Keating, Ugo Piomelli, Elias Balaras, and Hans-Jakob Kaltenbach. A priori and a posteriori tests of inflow conditions for large-eddy simulation. *Physics of Fluids*, 16(12):4696–4712, 2004.

[77] Junhyuk Kim and Changhoon Lee. Deep unsupervised learning of turbulence for inflow generation at various Reynolds numbers. *Journal of Computational Physics*, 406:109216, 2020.

[78] Diederik P Kingma and Jimmy Ba. Adam: A method for stochastic optimization. *arXiv preprint arXiv:1412.6980*, 2014.

[79] M Klein, A Sadiki, and J Janicka. A digital filter based generation of inflow data for spatially developing direct numerical or large eddy simulations. *Journal of Computational Physics*, 186(2):652–665, 2003.

[80] R H Kraichnan. Diffusion by a random velocity field. *The Physics of Fluids*, 13(1):22–31, 1970.

[81] B E Launder and D B Spalding. The numerical computation of turbulent flows. *Computer Methods in Applied Mechanics and Engineering*, 3(2):269 – 289, 1974.

[82] Yann A LeCun, Léon Bottou, Genevieve B Orr, and Klaus-Robert Müller. Efficient backprop. In *Neural networks: Tricks of the trade*, pages 9–48. Springer, 2012.

[83] Jae Hwa Lee and Hyung Jin Sung. Direct numerical simulation of a turbulent boundary layer up to $re_\theta = 2500$. *International Journal of Heat and Fluid Flow*, 32(1):1–10, 2011.

[84] S Lemay, V Aeschlimann, R Fraser, GD Ciocan, and C Deschênes. Velocity field investigation inside a bulb turbine runner using endoscopic PIV measurements. *Experiments in Fluids*, 56(6):1–12, 2015.

[85] Marcel Lesieur. *Turbulence in fluids: Stochastic and numerical modelling*. Kluwer Academic Publishers, 1993.

[86] Marcel Lesieur, Olivier Métais, Pierre Comte, et al. *Large-eddy simulations of turbulence*. Cambridge university press, 2005.

[87] R Lestriez, D Calvo, and D Mendicino. Advanced optimization tools for hydro turbine runner design. In *IOP Conference Series: Earth and Environmental Science*, volume 774, page 012001. IOP Publishing, 2021.

[88] Douglas K Lilly. A proposed modification of the Germano subgrid-scale closure method. *Physics of Fluids A: Fluid Dynamics*, 4(3):633–635, 1992.

[89] C Liu, B Zoph, M Neumann, J Shlens, W Hua, L-J Li, L Fei-Fei, A Yuille, J Huang, and K Murphy. Progressive neural architecture search. In *Proceedings of the European conference on computer vision (ECCV)*, pages 19–34, 2018.

[90] Thomas S Lund, Xiaohua Wu, and Kyle D Squires. Generation of turbulent inflow data for spatially-developing boundary layer simulations. *Journal of Computational Physics*, 140(2):233–258, 1998.

[91] AE Lyutov, DV Chirkov, VA Skorospelov, PA Turuk, and SG Cherny. Coupled multipoint shape optimization of runner and draft tube of hydraulic turbines. *Journal of Fluids Engineering*, 137(11), 2015.

[92] Andrew L Maas, Awni Y Hannun, Andrew Y Ng, et al. Rectifier nonlinearities improve neural network acoustic models. In *Proc. icml*, volume 30, page 3. Citeseer, 2013.

[93] G. D. MacIsaac, S. A. Sjolander, and T. J. Praisner. Measurements of Losses and Reynolds Stresses in the Secondary Flow Downstream of a Low-Speed Linear Turbine Cascade. *Journal of Turbomachinery*, 134(6), 2012.

[94] Mathias Malandain, Nicolas Maheu, and Vincent Moureau. Optimization of the deflated conjugate gradient algorithm for the solving of elliptic equations on massively parallel machines. *Journal of Computational Physics*, 238:32–47, 2013.

[95] L Mangani, E Casartelli, L Hanimann, M Wild, and N Spyrou. Assessment of an implicit mixing plane approach for pump-turbine applications. In *IOP Conference Series: Earth and Environmental Science*, volume 22, page 022003. IOP Publishing, 2014.

[96] B D Marjavaara, T S Lundström, T Goel, Y Mack, and W Shyy. Hydraulic turbine diffuser shape optimization by multiple surrogate model approximations of Pareto fronts. *Journal of Fluids Engineering*, 129(9):1228–1240, 04 2007.

[97] Daniel Marjavaara, Ramji Kamakoti, Staffan Lundström, Siddharth Thakur, Jeffrey Wright, and Wei Shyy. Steady and unsteady cfd simulations of the turbine-99 draft tube using cfx-5 and stream. In *IAHR/ERCOFTAC workshop on draft tube flow: 08/12/2005-09/12/2005*, pages 83–99. Luleå tekniska universitet, 2005.

[98] S Mauri. *Numerical simulation and flow analysis of an elbow diffuser*. PhD thesis, École Polytechnique Fédérale de Lausanne (EPFL), Lausanne, Switzerland, 2002.

[99] AT McDonald, RW Fox, and RV Van Dewoestine. Effects of swirling inlet flow on pressure recovery in conical diffusers. *AIAA Journal*, 9(10):2014–2018, 1971.

[100] J McNabb, C Devals, SA Kyriacou, N Murry, and BF Mullins. CFD based draft tube hydraulic design optimization. In *IOP Conference Series: Earth and Environmental Science*, volume 22, page 012023. IOP Publishing, 2014.

[101] F R Menter. Two-equation eddy-viscosity turbulence models for engineering applications. *AIAA Journal*, 32(8):1598–1605, 1994.

[102] Florian R Menter. Improved two-equation k-omega turbulence models for aerodynamic flows. *NASA STI/Recon Technical Report N*, 93:22809, 1992.

[103] Florian R Menter. Best practice: scale-resolving simulations in ANSYS CFD. *ANSYS Germany GmbH*, 1, 2012.

[104] Florian R Menter, Martin Kuntz, and Robin Langtry. Ten years of industrial experience with the sst turbulence model. *Turbulence, heat and mass transfer*, 4(1):625–632, 2003.

[105] Fadl Moukalled, L Mangani, Marwan Darwish, et al. *The finite volume method in computational fluid dynamics*, volume 113. Springer, 2016.

[106] V Moureau, P Domingo, and L Vervisch. Design of a massively parallel CFD code for complex geometries. *Comptes Rendus Mécanique*, 339(2):141–148, 2011.

[107] BG Mulu, MJ Cervantes, Christophe Devals, TC Vu, and F Guibault. Simulation-based investigation of unsteady flow in near-hub region of a kaplan turbine with experimental comparison. *Engineering Applications of Computational Fluid Mechanics*, 9(1):139–156, 2015.

[108] BG Mulu, PP Jonsson, and MJ Cervantes. Experimental investigation of a Kaplan draft tube - Part I: Best efficiency point. *Applied Energy*, 93:695–706, 2012.

[109] V Nair and G E Hinton. Rectified linear units improve restricted Boltzmann machines. In *Icml*, 2010.

[110] Kazuyuki Nakamura and Sadao Kurosawa. Design optimization of a high specific speed francis turbine using multi-objective genetic algorithm. *International Journal of Fluid Machinery and Systems*, 2(2):102–109, 2009.

[111] Y.E. Nesterov. A method for solving the convex programming problem with convergence rate O(1/k2). pages 372–376. Soviet Mathematics, 1983.

[112] Christophe Nicolet, Amirreza Zobeiri, Pierre Maruzewski, and François Avellan. Experimental investigations on upper part load vortex rope pressure fluctuations in francis turbine draft tube. *International Journal of Fluid Machinery and Systems*, 4(1):179–190, 2011.

[113] J Nicolle, P Labbé, G Gauthier, and M Lussier. Impact of blade geometry differences for the CFD performance analysis of existing turbines. In *IOP Conference Series: Earth and Environmental Science*, volume 12, page 012028. IOP Publishing, 2010.

[114] F Nicoud, H Baya Toda, O Cabrit, S Bose, and J Lee. Using singular values to build a subgrid-scale model for large eddy simulations. *Physics of Fluids*, 23(8):085106, 2011.

[115] Franck Nicoud and Frédéric Ducros. Subgrid-scale stress modelling based on the square of the velocity gradient tensor. *Flow, turbulence and Combustion*, 62(3):183–200, 1999.

[116] Michael A Nielsen. *Neural networks and deep learning*, volume 25. Determination press San Francisco, CA, 2015.

[117] H Nilsson, M Page, M Beaudoin, B Gschaider, and H Jasak. The OpenFOAM turbomachinery working-group, and conclusions from the turbomachinery session of the third openfoam workshop. In *IAHR: 24th Symposium on Hydraulic Machinery and Systems, Foz do Iguassu, Brazil*, 2008.

[118] Håkan Nilsson. Evaluation of OpenFOAM for CFD of turbulent flow in water turbines. In *IAHR: 23rd Symposium on Hydraulic Machinery and Systems, Yokohama, Japan*, 2006.

[119] Håkan Nilsson and MJ Cervantes. Effects of inlet boundary conditions, on the computed flow in the Turbine-99 draft tube, using OpenFOAM and CFX. In *IOP Conference Series: Earth and Environmental Science*, volume 15, page 032002. IOP Publishing, 2012.

[120] Edwin Roman Ortiz, Jean Mathieu Gagnon, and Claire Deschênes. Numerical simulation in the runner of a propeller turbine-tip leakage flow and blade tip vortex. In *Annual General Meeting CFD Society of Canada and Lunch 18 May 2010*. Citeseer, 2010.

[121] Mathieu Pamiès, Pierre-Elie Weiss, Eric Garnier, Sébastien Deck, and Pierre Sagaut. Generation of synthetic turbulent inflow data for large eddy simulation of spatially evolving wall-bounded flows. *Physics of Fluids*, 21(4):045103, 2009.

[122] Simon Pasche, François Gallaire, and François Avellan. Origin of the synchronous pressure fluctuations in the draft tube of francis turbines operating at part load conditions. *Journal of Fluids and Structures*, 86:13–33, 2019.

[123] F-A Payette. Simulation de l'écoulement turbulent dans les aspirateurs de turbines hydrauliques: impact des paramètres de modélisation. Master's thesis, Université Laval, Quebec, Canada, 2008.

[124] Charles D Pierce and Parviz Moin. Method for generating equilibrium swirling inflow conditions. *AIAA Journal*, 36(7):1325–1327, 1998.

[125] R Poletto, T Craft, and A Revell. A new divergence free synthetic eddy method for the reproduction of inlet flow conditions for LES. *Flow, Turbulence and Combustion*, 91(3):519–539, 2013.

[126] Stephen B Pope. *Turbulent flows*. Cambridge University Press, 2001.

[127] L Puente, Marcelo Reggio, François Guibault, et al. Automatic shape optimization of a hydraulic turbine draft tube. In *International Conference, CFD2003, Vancouver, BC*, volume 28, 2003.

[128] Ning Qian. On the momentum term in gradient descent learning algorithms. *Neural Networks*, 12(1):145–151, 1999.

[129] Prajit Ramachandran, Barret Zoph, and Quoc V Le. Searching for activation functions. *arXiv preprint arXiv:1710.05941*, 2017.

[130] W Rodi, JC Bonnin, and T Buchal. ERCOFTAC workshop on data bases and testing of calculation methods for turbulent flows. In *Part of the Proceedings of the 4th ERCOFTAC/IAHR Workshop on Refined Flow Modelling*. University of Karsruhe, 1995.

[131] Frank Rosenblatt. Principles of neurodynamics: Perceptrons and the theory of brain mechanisms. Technical report, Cornell Aeronautical Lab Inc Buffalo NY, 1961.

[132] Sebastian Ruder. An overview of gradient descent optimization algorithms. *arXiv preprint arXiv:1609.04747*, 2016.

[133] David E Rumelhart, Geoffrey E Hinton, and Ronald J Williams. Learning internal representations by error propagation. Technical report, California University, San Diego La Jolla, Institute for Cognitive Science, 1985.

[134] Albert Ruprecht, Thomas Helmrich, Thomas Aschenbrenner, and Thomas Scherer. Simulation of vortex rope in a turbine draft tube. In *Proceedings of the 21st IAHR Symposium on Hydraulic Machinery and Systems*, volume 1, pages 259–266. EPFL/STI/LMH, Lausanne, Switzerland, 2002.

[135] Pierre Sagaut. *Large eddy simulation for incompressible flows: an introduction*. Springer Science & Business Media, 2006.

[136] JU Schlüter, H Pitsch, and P Moin. Large-eddy simulation inflow conditions for coupling with Reynolds-averaged flow solvers. *AIAA Journal*, 42(3):478–484, 2004.

[137] Joseph Smagorinsky. General circulation experiments with the primitive equations: I. The basic experiment. *Monthly Weather Review*, 91(3):99–164, 1963.

[138] A Smirnov, S Shi, and I Celik. Random flow generation technique for large eddy simulations and particle-dynamics modeling. *Journal of Fluids Engineering*, 123(2):359–371, 2001.

[139] P E Smirnov and F R Menter. Sensitization of the SST turbulence model to rotation and curvature by applying the Spalart-Shur correction term. *Journal of Turbomachinery*, 131(4), 2009.

[140] I Sobol and Y L Levitan. The production of points uniformly distributed in a multidimensional cube. *Preprint IPM Akad. Nauk SSSR*, 40(3):30, 1976.

[141] Gabriel Sottas and Inge L Ryhming. *3D-Computation of incompressible internal flows: Proceedings of the GAMM Workshop held at EPFL, 13–15 september 1989, Lausanne, Switzerland*, volume 39. Springer Science & Business Media, 2012.

[142] PR Spalart and M Shur. On the sensitization of turbulence models to rotation and curvature. *Aerospace Science and Technology*, 1(5):297–302, 1997.

[143] A Spille-Kohoff and Hans-J Kaltenbach. Generation of turbulent inflow data with a prescribed shear-stress profile. Technical report, TECHNISCHE UNIV BERLIN (GERMANY) HERMANN-FOTTINGER INST FUR STROMUNGSMECHANIK, 2001.

[144] N Srivastava, G Hinton, A Krizhevsky, I Sutskever, and R Salakhutdinov. Dropout: a simple way to prevent neural networks from overfitting. *The journal of machine learning research*, 15(1):1929–1958, 2014.

[145] IEC Standard et al. Hydraulic turbines, storage pumps and pump-turbines - model acceptance tests. 1999.

[146] Richard JAM Stevens, Jason Graham, and Charles Meneveau. A concurrent precursor inflow method for large eddy simulations and applications to finite length wind farms. *Renewable Energy*, 68:46–50, 2014.

[147] Romeo Susan-Resiga, Gabriel Dan Ciocan, Ioan Anton, and François Avellan. Analysis of the swirling flow downstream a francis turbine runner. *Journal of Fluids Engineering*, 128(1):177–189, 2006.

[148] G R Tabor and MH Baba-Ahmadi. Inlet conditions for large eddy simulation: a review. *Computers & Fluids*, 39(4):553–567, 2010.

[149] A Taheri. *Detached Eddy simulation of unsteady turbulent flows in the draft tube of a bulb turbine*. PhD thesis, Université Laval, Quebec, Canada, 2015.

[150] Sylvain Tridon. *Etude expérimentale des instabilités tourbillonnaires dans les diffuseurs de turbomachines hydrauliques*. PhD thesis, PhD thesis, Institut National Polytechnique de Grenoble, 2010.

[151] Stijn Vantieghem. Numerical simulations of quasi-static magnetohydrodynamics using an unstructured finite volume solver: development and applications. *Université Libre de Bruxelles*, 2011.

[152] Pedro Véras. Estudo numérico da extensão na saída do tubo de sucção de uma turbina hidráulica do tipo bulbo. Master's thesis, Universide de Brasília, 2018.

[153] Aakash Vijay Patil. Development of Deep Learning Methods for inflow turbulence generation. *arXiv e-prints*, pages arXiv–1910, 2019.

[154] TC Vu, C Devals, Y Zhang, B Nennemann, and F Guibault. Steady and unsteady flow computation in an elbow dr aft tube with experimental validation. In *IOP Conference Series: Earth and Environmental Science*, volume 12, page 012045. IOP Publishing, 2010.

[155] TC Vu, M Gauthier, B Nennemann, H Wallimann, and C Deschênes. CFD analysis of a bulb turbine and validation with measurements from the BulbT project. In *IOP Conference Series: Earth and Environmental Science*, volume 22, page 022008. IOP Publishing, 2014.

[156] Thi Vu, Marcel Koller, Maxime Gauthier, and Claire Deschênes. Flow simulation and efficiency hill chart prediction for a propeller turbine. *International Journal of Fluid Machinery and Systems*, 4(2):243–254, 2011.

[157] J Vuillemard, V Aeschlimann, R Fraser, S Lemay, and C Deschênes. Experimental investigation of the draft tube inlet flow of a bulb turbine. In *IOP Conference Series: Earth and Environmental Science*, volume 22, page 032010. IOP Publishing, 2014.

[158] David Wilcox. A half century historical review of the k-omega model. In *29th Aerospace Sciences Meeting*, page 615, 1991.

[159] S Wilhelm, G Balarac, O Metais, and C Ségoufin. Analysis of head losses in a turbine draft tube by means of 3D unsteady simulations. *Flow, Turbulence and Combustion*, 97(4):1255–1280, 2016.

[160] Sylvia Wilhelm. *Étude des pertes de charge dans un aspirateur de turbine bulbe par simulations numériques instationnaires*. PhD thesis, Institut National Polytechnique de Grenoble (INPG), Grenoble, France, 2017.

[161] Xiaohua Wu. Inflow turbulence generation methods. *Annual Review of Fluid Mechanics*, 49:23–49, 2017.

[162] Matthew D Zeiler. Adadelta: an adaptive learning rate method. *arXiv preprint arXiv:1212.5701*, 2012.

Published in Physics of Fluids

Reconstruction of numerical inlet boundary conditions using machine learning: application to the swirling flow inside a conical diffuser

Pedro Véras,[1, a)] Guillaume Balarac,[1, 2] Olivier Métais,[1] Didier Georges,[3] Antoine Bombenger,[4] and Claire Ségoufin[4]

[1)] *Université Grenoble Alpes, CNRS, Grenoble-INP, LEGI, 38000 Grenoble, France*

[2)] *Institut Universitaire de France (IUF), 75000 Paris, France*

[3)] *Université Grenoble Alpes, CNRS, Grenoble-INP, GIPSA-lab, 38000 Grenoble, France*

[4)] *GE Renewable Energy, 82 Avenue Léon Blum, 38100 Grenoble, France*

(Dated: 16 July 2021)

A new approach to determine proper mean and fluctuating inlet boundary conditions is proposed. It is based on data driven techniques, i.e. machine learning approach, and its goal is to use any known information about the downstream flow to reconstruct the unknown or incomplete inlet boundary conditions for a numerical simulation. The *European Research Community On Flow, Turbulence And Combustion* (ERCOFTAC) test case of the swirling flow inside a conical diffuser is investigated. Despite its relatively simple geometry, it constitutes a very challenging test case for numerical simulations due to incomplete experimental data and to the delicate balance between core flow recirculation and boundary layer separation. Simulations are performed using both Reynolds Averaged Navier-Stokes (RANS) and Large-Eddy Simulations (LES) turbulence methods. The mean velocity and turbulence kinetic energy profiles obtained with the machine learning approach in RANS are found to be in very good agreement with the experimental measurements and the numerical predictions are greatly improved as compared to the previous results using basic inlet boundary conditions. They are indeed comparable to the best previous RANS using empirical *ad hoc* inlet conditions to accurately simulate the downstream flow. In LES, in addition to the mean velocity profiles, the machine learning approach also allows to properly reconstruct the fluctuating part of the turbulent field. In particular, the methodology allows to circumvent the lack of turbulent correlations associated with classical inlet synthetic turbulence.

I. INTRODUCTION

It is well known that inlet boundary conditions can have a major impact on the results and accuracy of a numerical simulation. Despite many advancements over the past few decades regarding the computational methods, it is still a challenge to specify proper inlet boundary conditions in the case of spatially developing turbulent flows (e.g., jets, mixing layers, wall-bounded flows etc.). For Reynolds Averaged Navier-Stokes (RANS) simulations, inlet boundary conditions are easier to prescribe and normally consist in Reynolds average mean quantities, turbulent length scale(s) and Reynolds stresses. However, in the case of more advanced Direct Numerical Simulations (DNS) and Large-Eddy Simulations (LES), imposing only time-averaged quantities at the inlet of a simulation means that the deterministic information about the inflow is definitely lost and that the final numerical solution is possibly compromised. However, since high resolution (spatially and temporally) flow information at the inlet plane of a simulation is rarely available, realistically determining the fluctuating quantities at this location is a major challenge for LES. Nevertheless, multiple solutions for this problem have been proposed along the years and can normally be classified in three groups[1–5]: synthetic turbulence, precursor simulations and recycling methods.

Synthetic turbulence is usually the most economical method to create the fluctuating inflow field for LES and the main idea behind this method is to superimpose artificially generated fluctuations to the mean inlet velocity field. The easiest way to achieve that is to generate and superimpose a random noise (such as white-noise) with an amplitude determined by the turbulent intensity level, however, since these random fluctuations completely lack spatial and temporal correlations, they are instantly destroyed by the Navier-Stokes solver[6]. For this reason, more advanced synthetic turbulence methods must include some way of reconstructing these correlations and therefore preventing them from quickly vanishing. One of the earliest approaches was proposed by Lee *et al.*[7], who applied an inverse discrete Fourier transform to generate synthetic fluctuations with a specified power spectrum and random phase. Later, based on the work of Kraichnan[8] and starting with an isotropic turbulent velocity field generated using random Fourier modes, Smirnov *et al.*[9] proposed the Random Flow Generation (RFG) method, which applied some scaling and orthogonal transformations to generate anisotropic and divergence-free synthetic fluctuations, with prescribed length and time scales, and a required energy spectrum. Batten *et al.*[10] simplified this method to introduce a Cholesky-decomposition-based scaling to specify a Reynolds stress tensor for the fluctuations and Davidson[11,12] introduced nonzero temporal correlation to the fluctuations generated at consecutive time-steps by applying an asymmetric time filter. In a different approach, Klein *et al.*[13] and later di Mare *et al.*[14] used digital linear nonrecursive filters to establish a Gaussian two-point correlation function in random fluctuations, which featured the required multidimensional space-time correlations and could conform to a prescribed Reynolds stress tensor. Jarrin *et al.*[15,16], on the other hand, proposed a Synthetic Eddy Method (SEM) based on the superposition of coherent structures with random signs and positions which

[a)] Electronic mail: pedro.veras@univ-grenoble-alpes.fr

are constantly convected through the inlet plane. A specific shape function is assigned to each eddy in this methodology to define its spatial and temporal characteristics, and turbulence anisotropy can be enforced via a Cholesky-decomposition of the Reynolds stress tensor. Some modifications to the shape functions have been proposed to improve SEM performance in wall-bounded flows[17] and to render its generated synthetic fluctuations divergence-free[18]. Finally, Druault *et al.*[19] used Proper-Orthogonal Decomposition (POD) analysis of experimental hot-wire rake measurements to generate a synthetic turbulent inflow.

Despite their relatively low computational cost, the synthetic methods still depend on flow information that is often hard to obtain, especially in complex flow configurations (e.g., Reynolds stresses components to determine turbulence anisotropy) and, more importantly, systematically produce a transition region close to their injection plane where the synthetic turbulent inflow is still developing, mostly because the fluctuations are not *completely* turbulent in nature. The problem is that, if the injection plane is close to the area of interest of the flow (i.e., the region we want to analyze), the decay of these unrealistic fluctuations can affect the mean velocity field via the production term. In this context, precursor simulations are much better in producing realistic fluctuating inflow conditions, as they give enough time and space for these fluctuations to develop and rely on actual turbulent data extracted from a fully-developed region of the flow. These simulations are performed in a separate numerical domain, which represents only a fraction of the main domain, and are often launched before the main simulation, requiring thus a significative amount of storage for the generated inflow data. Beside the obviously higher computational cost compared to synthetic methods, the fact a precursor simulation is performed in a separate computational domain means that no feedback information from the main domain is possible, which limits the application of this method to very simple flow configurations, notably those where the considered geometry yields fully-developed mean flow in the streamwise direction, such as channel flows[20,21] or pipe flows[22–24].

Finally, a way to overcome this limitation of precursor simulations, specially for the case of spatially-developing boundary layers, consists in integrating the separate numerical domain into the main domain and recycling the information extracted in a downstream station as inflow conditions for the simulations. In this case, there is no more need for performing or storing the results of a separate precursor simulation. One problem though with this method is that, in the case of spatially-developing boundary layers, the mean flow is not parallel and the information extracted at the downstream station needs to be rescaled before being used at the inlet. Lund *et al.*[25] proposed such a rescaling technique that used different similarity laws for the inner and outer regions of the boundary layer. While this technique produced turbulent boundary layer flows with the expected physical features, it can still lead to some transitional region near the inlet[26,27] and (similar to synthetic methods) and it suffered from inherent flaws[17], such as the need for the inlet plane to have some kind of synthetic fluctuations added at the beginning of the simulation (which can interfere with the final results) and spurious coupling in the computed solution if the extraction station is not far enough from the inlet. Moreover, although some techniques using forcing terms have been developed to improve the control over the rescaling over the inlet plane[28], these recycling method are still restricted to very simple flow configurations.

The present paper focuses on a way to properly generate turbulent inlet conditions for the swirling flow inside a conical diffuser. This flow has been extensively studied by Clausen *et al.*[29] in their laboratory experiment and constitutes one of the test cases of the *European Research Community On Flow, Turbulence And Combustion* (ERCOFTAC) database. As shown by Duprat[30], this test case constitutes a good example of a flow configuration where most of the previously described inlet generation techniques are not adequate. In this flow (explained in more details in section II), a constant air flow is forced into a long rotating cylinder (including a honeycomb screen) which generates a swirling flow at the inlet of a simple long conical diffuser. The particularity of this flow is that the swirl is finely adjusted both to prevent the spatially developing boundary layer to separate from the diffuser walls and to avoid core flow recirculation. The boundary layer inside the diffuser is indeed subjected to an adverse pressure gradient while the flow swirl has a positive effect in stabilizing it[31]. This test case has been the subject of many numerical investigations since, despite its geometrical simplicity, it exhibits some of the main characteristics of the complex turbulent flow within hydraulic turbine draft tubes (turbulent, unsteady, swirling, divergent etc.)[32].

Duprat[30] performed one of the few LES studies of the ERCOFTAC conical diffuser. He was interested particularly on the influence of turbulent inlet conditions in LES, and investigated the three previously described methods. For instance, starting with a numerical domain containing the conical diffuser and the upstream swirl generator, Duprat[30] recycled the flow information extracted at a downstream station back to the inlet of the domain and, at the same time, a forcing term ensured the correct flow rate and swirl number downstream. The problem was that both the flow rate and the swirl number are evaluated as velocity integral and different profiles can lead to correct values. A shorter upstream domain starting at the first measurement station was used for the investigation of the last two methods. Using both a white noise and the results of a precursor pipe flow simulation to obtain the inflow fluctuations, Duprat[30] improved the results compared to the recycling method but the mean velocity profiles still did not compare very well with the experiments.

One may think that RANS computations of this test case are easier to perform since, in principle, only mean quantities have to be prescribed at the inlet. However, due to some technical difficulties, the radial velocity component was not measured by Clausen *et al.*[29]. Therefore, early RANS simulations by Armfield *et al.*[33] and Mauri[34], using the k-ε turbulence model[35] along with wall functions, set this velocity component equal to zero at the first measurement station (inlet of the numerical domain) but the results were not correct as the turbulence model delayed flow separation. In their contribution to the original ERCOFTAC Workshop that numerically inves-

tigated this flow, Vu and Shyy[36] showed that the radial velocity should not be zero at the first measurement station due to its proximity to the divergent section of the diffuser. They used an upstream extension in order to recover this component but the obtained velocity profiles downstream in the diffuser were still not satisfactory as compared to the experimental data. In the context of a OpenFOAM Workshop[37], Bounous[38] conducted an extensive investigation of the swirling flow inside the conical diffuser using both k-ε and k-ω SST[39] turbulence models. Bounous[38] confirmed the high sensitivity of the results to the proper prescription of the inlet radial velocity profile. He thus simulated the upstream cylinder and adjusted the mean inlet profiles to obtain improved results. The best results in RANS for this flow configuration, though, were obtained by Payette[40] using the k-ω SST turbulence model. He also simulated the flow in the upstream cylinder, but this time only to recover the radial velocity profile at the first measurement station. He then imposed this profile along with the experimental axial and circumferential velocity profiles at the inlet of a second numerical domain starting at the first measurement station.

Both Bounous[38] and Payette[40] furthermore found their results to be very sensitive to the turbulent inlet conditions. To obtain their best results, the former used the turbulent inlet conditions proposed in Gyllenram *et al.*[41] while the latter reconstructed the turbulent kinetic energy profile from the incomplete experimental data and used the expression proposed by Armfield *et al.*[33] to obtain the turbulent kinetic energy dissipation rate ε. Payette[40] results will be used in the present article as a reference case to test our own computations.

It is important to note that the best tuned inlet conditions for RANS do not necessarily yield good results when more advanced unsteady techniques are employed. Indeed, Bélanger-Vincent[42] and Taheri[43] tried to reproduce Bounous[38] and Payette[40] results using hybrid turbulence methods, particularly Detached Eddy Simulations (DES) and Delayed Detached Eddy Simulations (DDES). The results obtained by both authors were extremely sensitive to the turbulent inlet conditions, which are very different from RANS due to the different nature of the turbulence model and unsatisfactory compared with the experimental data. Moreover, as pointed out by Duprat[30] and Taheri[43], an approach like the one proposed by Payette[40] is not applicable to more complex flow configurations, such as hydraulic turbines draft tubes, as the guide-vanes and runner blades are positioned just upstream the diffuser and generate a highly inhomogeneous and turbulent inflow for the draft tube.

Based on these discussions, it is clear that whenever the inlet boundary conditions for a numerical simulation are unknown or only partially known, simplistic assumptions for reconstructing the missing information are often insufficient to yield satisfactory results, except for very simple flow configurations. Moreover, while more elaborate approaches can sometimes improve the numerical results, they cannot be generalized to any turbulence model and flow configuration. Therefore, the real challenge consists in defining a method capable of determining the appropriate mean and fluctuating fields that should be imposed at the inlet of a numerical domain and that is applicable to multiple turbulence models and, more importantly, to multiple flow configurations.

In this paper, a new approach to determine proper mean and fluctuating inlet boundary conditions for a numerical simulation based on data driven techniques, such as machine learning, is proposed and applied to the case of the swirling flow inside a conical diffuser using both RANS and LES turbulence methods. Its goal is to use any known information about the downstream flow along with a previously generated database to reconstruct unknown or incomplete inlet boundary conditions for the simulation, so the downstream flow field is correctly recovered. In the case of LES, an artificial upstream extension used in conjunction with this approach can also give the space and time required for synthetic fluctuations to develop before reaching the important portion of the numerical domain. Despite the high computational cost associated with the generation of an appropriate database to train an Artificial Neural Network (ANN), the application of data-driven techniques in the field of CFD is growing, and recent applications have investigated its use for the generation of turbulent inlet conditions in DNS and LES, but all in the case of simple channel flows[44–46]. In the context of RANS simulations of the ERCOFTAC conical diffuser and hydraulic turbines draft tubes, optimization methods based on data-driven techniques have also been used, but normally as a way to improve their hydraulic performances[47–52].

The paper is organized as follows. It starts with a detailed explanation of our test case (Section II) corresponding to the swirling flow inside a conical diffuser experimentally investigated by Clausen *et al.*[29]. After discussing the choice of turbulence models and the numerical tools used to perform our simulations (Section III), we present our reference results based on standard approaches to define both the numerical domain and inlet boundary conditions (Section IV). Section V discusses the three main steps of the proposed Machine Learning strategy. Finally, a thorough application of this strategy to the test case is presented in Section VI and the results are compared to the reference simulations.

II. FLOW CONFIGURATION

The test case chosen for the current study is part of the classic ERCOFTAC database (Case 60) and consists in the swirling flow inside a conical diffuser experimentally studied by Clausen *et al.*[29]. Figure 1 shows a scheme of the diffuser, which is 510 mm long, has an inlet diameter $D_0 = 260$ mm and a 20° opening angle. A constant air flow, with kinematic viscosity $\nu = 1.5 \times 10^{-5}$ m^2/s, was forced through the diffuser and discharged into to the atmosphere at a constant flow rate $Q = 0.616$ m^3/s, which corresponds to an average axial velocity at the inlet $U_b = 11.6$ m/s and a Reynolds number $Re \approx 2 \times 10^5$.

A 400 mm long rotating cylinder (including a honeycomb screen) positioned 100 mm upstream the diffuser inlet generated flow swirl. The corresponding swirl number, S_w, defined as the ratio between the axial flux of angular momentum and the axial flux of axial momentum multiplied by the radius, is

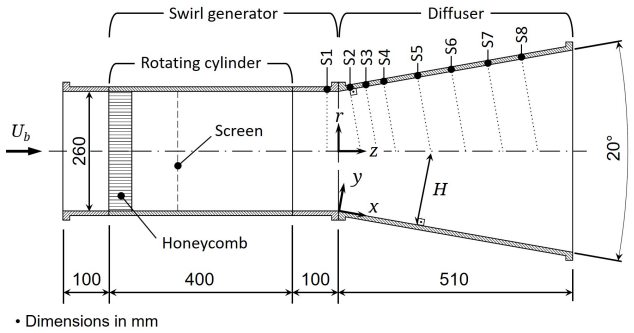

FIG. 1: Scheme of the diffuser studied by Clausen *et al.*[29].

given by Eq. (1) and was taken equal to 0.295. It was adjusted so the flow remains attached to the diffuser walls and, at the same time, no recirculation was created in its core.

$$S_w = \frac{\int_0^R |U_\theta| U_z dr}{\int_0^R U_z^2 dr} \tag{1}$$

As shown in Fig. 1, there are two coordinate system used in the conical diffuser. Inside the upstream swirl generator, U_z is the mean axial velocity of the flow, U_r is the mean radial velocity and U_θ is the mean circumferential velocity. However, inside the cone, Clausen *et al.*[29] measured the velocity profiles using a local coordinate system with an axis parallel (x) and another normal (y) to the walls. In this coordinate system, U_x is the mean velocity component parallel to the walls (streamwise) and U_y is the mean velocity component perpendicular to the walls (normal). The mean circumferential velocity component is the same in both coordinate systems. It should be noticed, though, that U_x and U_z are equivalent at the first measurement station, S1, as well as U_y and U_r.

Mean velocity profiles were measured using hot-wires at the eight traverses perpendicular to the walls (stations S1 to S8 shown in Fig. 1). The positioning of these traverses was accurate to 0.01 mm and the estimated error in the mean velocities was approximately 2%. Both mean streamwise (U_x and U_z) and circumferential (U_θ) velocity components were measured in the experiments, but, due to some technical difficulties, the mean velocity normal to the walls U_y as well as the mean radial velocity U_r components were not measured by Clausen *et al.*[29]. The six components of Reynolds stresses were also measured at the same eight traverses, but they were limited to the region very close to the walls and their accuracy was estimated in 10%. Nevertheless, it is possible to determine the turbulence kinetic energy, k, from these measurements using Eq. 2:

$$k = \frac{1}{2}\left(u_r'^2 + u_\theta'^2 + u_z'^2\right) \tag{2}$$

Despite its simplicity, simulating this flow is challenging due to its delicate balance between core flow recirculation and boundary layer separation. Moreover, inflow conditions at the diffuser inlet are not completely defined since the radial velocity component, U_r, was not measured and turbulence measurements are quite limited.

Finally, in addition to the mean velocity and turbulence profiles, the evolution of static pressure is key in the analysis of any flow passing through diffuser, as its main purpose is to efficiently convert the dynamic pressure into static pressure. In this regard, Clausen *et al.*[29] also measured the static pressure at the walls in the form of a coefficient of pressure, given by:

$$C_p = \frac{P_{\text{wall}} - P_{\text{atm}}}{0.5\rho U_b^2} \tag{3}$$

where P_{wall} is the pressure at the walls, P_{atm} is the atmospheric pressure and ρ is the density of the air.

III. TURBULENCE MODELLING

A. Steady RANS simulations

Early numerical studies of the flow inside the ERCOFTAC conical diffuser performed steady RANS simulations used two-equations linear eddy-viscosity turbulence models[33,34,36]. Only mean properties (in the sense of Reynolds decomposition) of the flow are resolved in this approach and the effects of turbulence are modelled by an eddy viscosity ν_t, which is evaluated by two extra transport equations. Their low computational cost and relative numerical robustness is an advantage when it comes to the application of data-driven techniques, which is the reason they are also used in this present work. The commercial flow solver ANSYS CFX is used to perform these calculations and the k-ω SST turbulence model[39] is chosen since it has been shown to be one of the most suitable for this particular flow[40]. Two corrections are applied to the production term in the k and ω transport equations: one to limit its value at stagnation points[53] and another to render it sensitive to the effect of streamline curvature and system rotation[54]. Regarding the numeric of the solution, the *high resolution scheme*[55] of ANSYS CFX is used for the spatial discretization of the advection term. In this scheme, a blend factor limits its order between a first order upwind scheme and a second order central scheme while keeping the solution bounded. Finally, a first order spatial discretization scheme is used for the two extra transport equations for k and ω.

B. Large-Eddy Simulations (LES)

The problem with steady RANS using two-equation linear eddy-viscosity models is that they are inherently unable to capture flow unsteadiness[56] and to correctly predict turbulent production in the case of a draft tube despite the aforementioned corrections[57]. More advanced turbulence models, such as LES, can overcome these problems and obtain a better description of this type of flow[32]. Therefore, we also investigate the ERCOFTAC conical diffuser using LES. In this approach,

instead of modelling all turbulent scales of the flow, most of them are resolved and only those smaller than a certain filter width (normally the grid spacing) are modelled[58]. LES computations are performed with YALES2 incompressible fractional-step solver[59] using finite-volume formulation and precise 4th order space centred and time numerical schemes. Sub-grid scales (SGS) effects on the flow are modelled by the Dynamic Smagorinsky turbulence model[60] and time steps are evaluated so CFL number is smaller than 0.9 in the whole numerical domain. In all LES cases, an initial simulation is run to stabilize the flow field within the diffuser and only then a second simulation is run to accumulate the statistics used in the final analysis of the flow during the equivalent of ten complete flow passages throughout the domain.

IV. BASIC INLET BOUNDARY CONDITIONS

The simplest approach to simulate the swirling flow inside the conical diffuser follows the proposition given for the original ERCOFTAC Workshop[36]. The swirl generator upstream the diffuser is not simulated and the upstream numerical domain is thus shortened. Available experimental data at the first upstream station are utilized as inlet conditions for the computations. As a result, many numerical works used this approach in their reference simulations of the test case[30,34,37,38,40,43].

A. Numerical domain

The numerical domains for these reference simulations are shown in Fig. 2. In the case of steady RANS simulations, the statistical flow axisymmetry is utilized to restrict to 2D computations. Conversely, in LES, the full 3D geometry of the diffuser has to be considered. In both cases, the computational domain consists in the conical diffuser and a very short cylindrical extension upstream of the diffuser. The inlet of this domain thus corresponds to the first measurement station, S1. The outlet is positioned at the end of a 500 mm long straight extension downstream the diffuser exit, which helps with the convergence and stability of the numerical solution without interfering with the flow inside the cone[40]. Different levels of refinement for a block structured hexahedral mesh are tested in RANS to guarantee that results are independent of the spatial discretization. The final mesh has approximately 6×10^3 elements and $y^+ \approx 1$. In the case of LES, an automatic two-criteria based mesh adaptation[61] is used in the spatial discretization study of the domain and the final mesh is composed by 3.3×10^6 tetrahedral elements. It also contains 4 layers of prismatic elements of aspect ratio equal to 4 at the walls to reduce the maximum y^+ to approximately 20 and to keep the simulation at a reasonable computational cost.

B. Boundary conditions

As the inlet of the numerical domain corresponds to the first measurement station, S1, the experimental mean velocity and

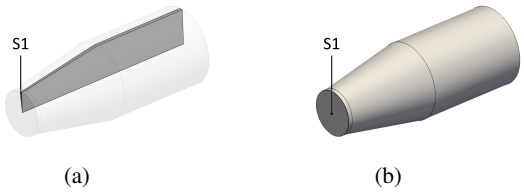

(a) (b)

FIG. 2: Numerical domains used in reference simulations. (a) RANS; (b) LES.

turbulence kinetic energy profiles measured at this location are imposed as inlet boundary conditions. These profiles are shown in Fig. 3 as a function of the normalized distance to the walls, y/H_i, where y is the normal distance to the walls, H_i is the maximum distance between the walls and the centreline of the diffuser at the i^{th} section, and $y/H_i = 1$ correspond to the axis of the conical diffuser. Their distribution over the inlet plane is considered as axisymmetric. Mean axial and circumferential velocity profiles are interpolated from experimental data. We emphasize that, since the radial velocity component was not measured in the original experiments[29], U_r is set equal to zero at the inlet.

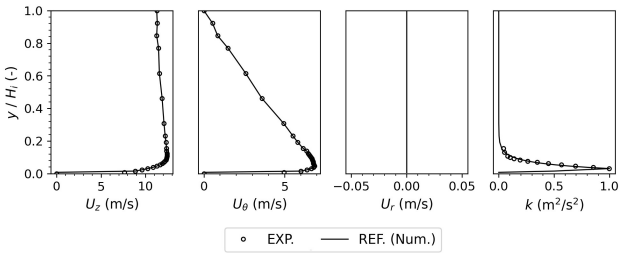

FIG. 3: Mean velocity and turbulence kinetic energy profiles measured by Clausen *et al.*[29] at station S1 and imposed as inlet conditions for the reference simulations.

Turbulent inlet boundary conditions are required in the case of RANS simulations using the k-ω SST and the profiles of turbulence kinetic energy, k, obtained from the Reynolds stresses measurements are used in this regard. As these measurements are limited to the region close to the walls ($y/H_i \approx 0.03$ and 0.15), k is assumed to vary linearly between $k = 0$ at the walls and its value at the first experimental point (at $y/H_i \approx 0.03$). Moreover, an exponential regression curve[40] given by Eq. 4 is used to complete the profile. Finally, an equation[33] for the dissipation rate, ε, given by Eq. 5, is used to close the system of equations.

$$k = e^{29.2(r/H_i)-28.3} \tag{4}$$

$$\varepsilon = \frac{C_\mu^{3/4} k^{3/2}}{0.01 D_0} \tag{5}$$

where $C_\mu = 0.09$ is the classical constant of the k-ε and k-ω models and D_0 is the diameter of the diffuser inlet.

In the case of LES, we want to avoid the use of *ad hoc* methods specific to the swirling diffuser flow to generate the inlet turbulent conditions. We therefore choose the two simplest conditions: no inlet turbulence or an homogeneous isotropic synthetic turbulent field at the inlet plane. One may indeed be tempted to impose rudimentary inlet turbulent conditions since the swirling flow inside a straight or diverging duct is known to be more easily unstable due to centrifugal instability and to adverse pressure gradient effects.

In YALES2, the scheme to generate and inject isotropic synthetic fluctuations is shown in Fig. 4. Initially, a divergence-free spatial and temporal correlated homogeneous isotropic turbulence (HIT) field of specified length scale l_e and velocity scale u' is generated, following the RFG method[9], in cubes of edge length equal to $4l_e$. Then, multiples copies of this HIT field are positioned side by side until the entire surface of the injection plane is covered by the synthetic fluctuations. Next, these fluctuations are scaled by an specified normalized turbulence kinetic energy profile, $k/k_{\max}$, and finally advected (injected) into the domain at a specified speed $\overline{U}$.

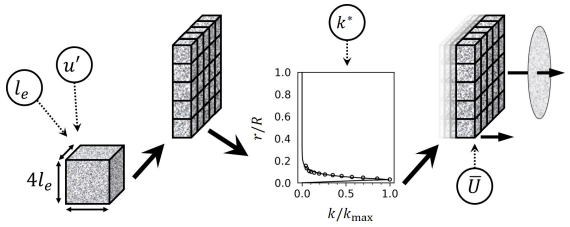

FIG. 4: Scheme of the synthetic HIT field generation and injection in YALES2.

Regarding the LES of the swirling flow inside the conical diffuser, the normalized turbulence kinetic energy profile follows the same construction proposed for the RANS simulations, i.e., linear k variation between the walls and $y/H_i \approx 0.03$, and Eq. (4) for the rest of the inlet. The injection speed, $\overline{U}$, is assumed to be equal to the average axial velocity at the inlet, $U_b = 11.6$ m/s. The synthetic turbulence length scale, l_e, is considered as being equal to 10% of the inlet diameter, D_0, or 26 mm, which correspond to a classical characteristic turbulent length scale for pipe flows or channel flows. The velocity scale, u', is approximately to 0.82 m/s, or 7% of the average axial velocity, U_b, and is estimated from Eq. (6):

$$u' = \sqrt{\frac{3}{2} k_{\max}} \tag{6}$$

Finally, an average static pressure equal to 0 is applied to the outlet of the numerical domains and no-slip conditions are imposed at the walls. In the case of RANS simulations using the k-ω SST turbulence model, the automatic wall treatment[55] present in ANSYS CFX is used. This model can automatically switch from a logarithmic wall-function to a low-Re near wall formulation if the mesh is sufficiently refined. In the case of LES, an appropriate wall-model designed for dealing with boundary layer flows subjected to adverse pressure gradients[62] is used. The main characteristics of the three reference simulations of the flow inside the conical diffuser are resumed in Tab. I.

C. Results

Comparisons between the mean streamwise velocity profiles obtained by the reference RANS and LES numerical simulations and the experimental measurements of the flow at the various downstream measurement stations are shown in Fig. 5. Both turbulence models yield very similar results and agree quite well with the experimental data until station S4. At station S5, the k-ω SST turbulence slightly underestimates U_x near the walls and, as a consequence, overestimates this velocity component towards the center of the flow ($y/H_i = 1$). This behaviour is amplified between S6 and S8 and results in boundary layer separation between stations S5 and S6 as testified by negative U_x values in the wall vicinity. As previously stated, this unphysical separation is symptomatic of RANS computations using the k-ω SST turbulence model and with zero inlet radial velocity[40]. Conversely, LES results do not show any signs of separation and the near wall behaviour of the diffuser is well captured in both cases, i.e. with or without inlet turbulence. Nevertheless, the mean streamwise velocity values at the center of the flow are still overestimated between S5 and S8. This is due to the poor prediction of the streamwise velocity peak, which is both underestimated and further away from the walls compared to experimental data. We can remark that the injection of synthetic turbulence fluctuations seems to had little effect on the mean streamwise velocity profiles

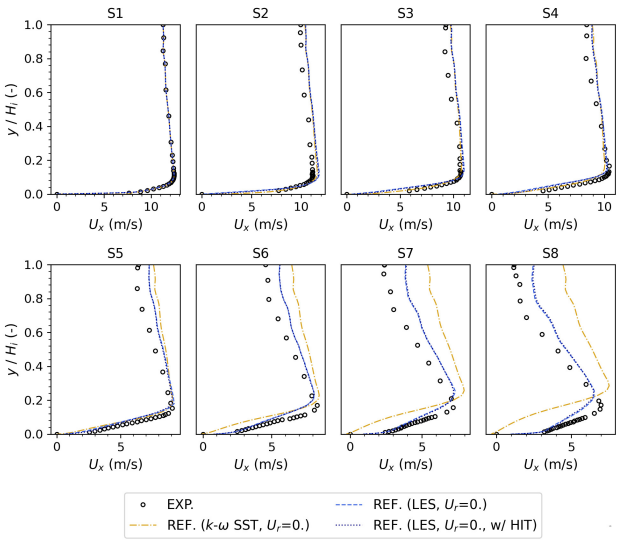

FIG. 5: Comparisons of mean streamwise velocity profiles for the reference simulations using RANS and LES.

Figure 6 shows the comparisons between numerical and experimental mean circumferential velocity profiles. LES pre-

TABLE I: Characteristics of the reference RANS and LES computations of the swirling flow inside the conical diffuser.

Case	Turbulence method	Numerical domain	Inlet conditions
Ref. RANS	RANS k-ω SST	Fig. 2a	U_z and U_θ from experiments, $U_r = 0$ k from Eq. (4) and ε from Eq. (5)
Ref. LES	LES	Fig. 2b	U_z and U_θ from experiments, $U_r = 0$ No turbulence injection
Ref. LES w/ HIT	LES	Fig. 2b	U_z and U_θ from experiments, $U_r = 0$ u' from Eq. (6) and $l_e = 0.1D_0$

dictions are very good compared to experiments, despite the discrepancies previously noted for U_x. Similarly to the U_x component, inlet turbulence injection has almost no effects on U_θ profile. RANS results are very similar to LES until station S4. After that, the boundary layer separation also affects the mean circumferential velocity profiles. Starting at S6, the near wall peak of U_θ moves away from the walls and this velocity component is greatly overestimated towards the center of the flow.

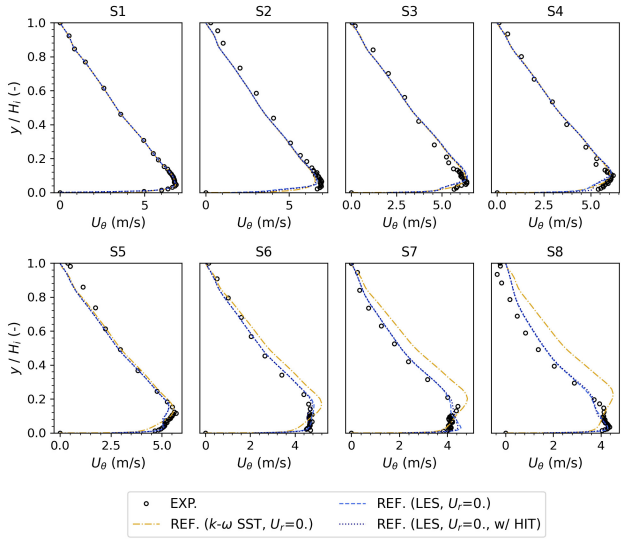

FIG. 6: Comparisons of mean circumferential velocity profiles for the reference simulations using RANS and LES.

The turbulence kinetic energy profiles for these reference simulations are shown in Fig. 7. For the RANS simulation, due to the imposed turbulent inlet boundary conditions, the results agree very well with the experiments until station S4. The peak value of k is slightly underestimated at station S5 and it is at the correct level at station S6. However, as a results of the flow separation, this peak is overestimated and is at a higher y/H_i position compared to the experiments at stations S7 and S8. In the LES case, as expected, k at the inlet of the numerical domain (station S1) is equal to zero in the case without turbulence. With imposed synthetic fluctuations, the k profile matches the experimental data in S1. Further downstream, the turbulence kinetic energy quickly increases due to the instability associated with the swirl and by the increased shear at the wall. Furthermore, with a simple HIT injection, the synthetic fluctuations are not completely realistic and are damped as one moves downstream. As a result, both LES cases with or without inlet turbulence exhibit very similar k distributions of k at station S2 and further downstream. Their values are largely overestimated with respect to the experimental measurements at stations S3, S4, and S5 and slowly decrease to finally reach the correct level at stations S7 and S8. On may also notice that, although the location of the turbulence kinetic energy maximum is well predicted, the near wall energy peak is wider in LES than in the experiments.

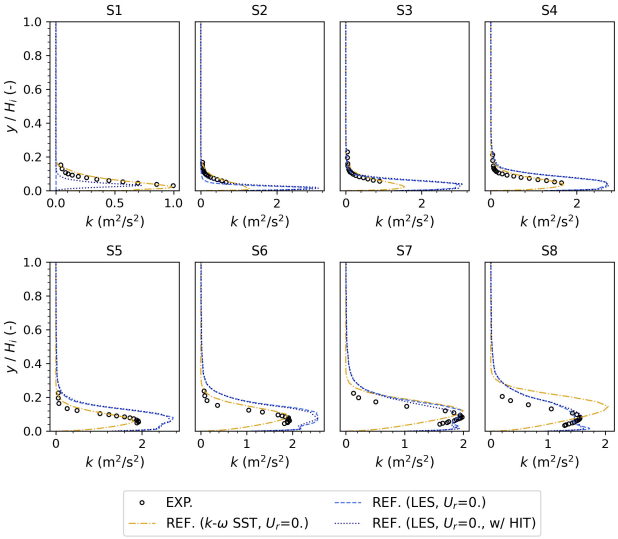

FIG. 7: Comparisons of turbulence kinetic energy profiles for the reference simulations using RANS and LES.

It is important to emphasize that the inlet turbulence measured in the experiment is anisotropic. Indeed, both $\langle u'_r u'_\theta \rangle$ and $\langle u'_r u'_z \rangle$ components exhibit negative values near the wall due to the radial variations of the circumferential and of the axial mean velocity respectively. In the case of the LES with turbulence injection at the inlet, we have checked that these

correlations are zero at station S1 due to the isotropic nature of the synthetic fluctuations. We will show in the next sections that this lack of correlation is responsible for the overestimation of the turbulent kinetic energy maximum (see Fig. 26).

V. OPTIMAL INLET BOUNDARY CONDITIONS BASED ON MACHINE LEARNING

A. Motivation

The previous simulations demonstrate that basic inlet conditions are not capable of providing satisfactory results even for the simple case of the swirling flow in a conical diffuser. As pointed out in the introduction, previous numerical studies showed that the main problem comes from the inadequacy of the inlet boundary conditions and, in particular, the ignorance of U_r velocity component which is assumed to be zero. For LES, a key issue is also to be able to generate proper inlet turbulent fluctuations with the right intensity, the right characteristic length scale and the right anisotropy characteristics.

In the present approach, we want to determine the optimal conditions at the inlet of the numerical domain (e.g. station S1) allowing to recover a downstream flow in good correspondence with experimental measurements. For this purpose, any known experimental information about the downstream flow along with a previously generated numerical database are utilized to construct the inlet boundary conditions.

B. Machine Learning strategy

Machine learning algorithms can and have been used to solve a variety of problems, such as classification problems, regression, transcription, translation etc.[63]. As previously stated, the goal of the proposed machine learning strategy is to use any known downstream flow experimental data (e.g., mean velocity and turbulence profiles) to determine the optimal upstream inlet boundary conditions. For this purpose, we shall train an Artificial Neural Network (ANN) to solve a non-linear regression problem, where the learning algorithm is asked to output a function $f : \mathbb{R}^m \rightarrow \mathbb{R}^n$. A schematic view of the complete strategy is shown in Fig. 8 and it can be divided into three main steps:

1. *Creating the database:* the first step consists in running multiple simulations to create a database which will be used to train our ANN. All numerical parameters (computational domain, boundary conditions, turbulence model etc.) are identical to those from the case we want to optimize, except for a different set of inlet boundary conditions. For instance, in the case of RANS simulations of the conical diffuser, different U_x, U_θ, U_r and k profiles would be used in each simulation. In LES, the parameters required to define the synthetic fluctuations would also vary. As a result, any differences on the downstream flow field behaviour in the simulations exclusively derive from the inlet boundary conditions.

2. *Training the ANN:* once the database is created, the second step consists in training the ANN, i.e. creating a non-linear regression model that will correlate ANN inputs with outputs. In our case, the inputs are the downstream flow results obtained from the database (e.g., mean velocity profiles, turbulence kinetic energy profiles etc.) while outputs consist in the inlet boundary conditions applied to each simulation of the database. In the case of the swirling flow inside the conical diffuser, despite having the access to flow measurements at eight stations, we will show in Section VI that we can successfully train an ANN with far less inputs. However, the amount of data required to train the ANN is case dependent and the ERCOFTAC conical diffuser represents a simple flow configuration.

3. *Predicting optimal inlet BCs:* finally, once the ANN is trained and the model is created, the last step consists in informing to the ANN the actual downstream flow results we want our numerical simulations to match (e.g., the experimental measurements) and, in return, it will output the corresponding optimal inlet boundary conditions for the simulation.

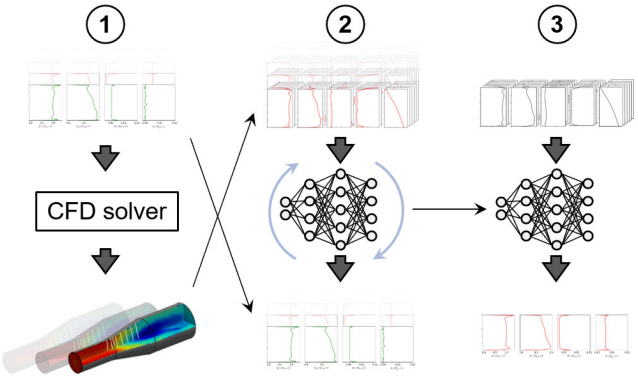

FIG. 8: Scheme of the proposed Machine Learning strategy to determine optimal inlet boundary conditions for a numerical simulation.

It should be noticed, however, that the proposed approach has some limitations, especially in terms of what can be used as inputs and outputs for the ANN. For instance, if we want our optimized numerical simulation to reproduce the experimental results at the same eight measurement stations inside the ERCOFTAC conical diffuser, we could *not* use the mean radial velocity component as an input because its measurements are not available from the experiments. Its outputs, however, are not limited by the experimental data, but by the parameters we varied during our database simulations. Therefore, we can *not* optimize a quantity that was not varied when creating the database. Otherwise, the proposed approach is relatively flexible and can be easily applied to different types of problems.

VI. APPLICATION TO THE ERCOFTAC CONICAL DIFFUSER CASE

A. Step 1: Numerical setup and database generation

The first step in the proposed Machine Learning strategy consists in creating a database containing the results of multiple simulations of the configuration we want the inlet conditions to be optimized for. Prior to launch any of these simulations, it is necessary to define the numerical domain that is going to be used. In RANS, the reference domain (see Fig. 2a) starting at station S1 can be employed since only mean quantities need to be prescribed and it is therefore not compulsory to have an artificial inlet domain allowing the fluctuations correlations to build up. As it will be shown below, an upstream extension may however permit to improve the prediction of missing quantities like the U_r component. Conversely, in LES, the addition of an upstream extension greatly improved the results.

The choice of the upstream extension length then needs to be settled. A first choice would be to take a length equal to the swirl generator upstream the conical diffuser (i.e. 500 *mm* long) as several previous authors[30,38,40–43]. However, it is also essential for the success of the proposed Machine Learning strategy that the downstream flow behaviour be dependent on the boundary conditions at the inlet extension. In the case of the swirling flow inside the conical diffuser, a real concern is that, if the upstream extension is too long, the turbulence generated at the walls due to flow shear becomes the dominant effect on the downstream flow behaviour. Therefore, using the two numerical domains shown in Fig. 9, with an upstream extension length of 500 *mm* and 250 *mm*, a parametric study was conducted in LES to evaluate the sensitivity of the downstream turbulence kinetic energy to the upstream synthetic turbulence parameters, specifically the length scale l_e and the velocity scale u'. The former is varied between $2\% \leq l_e \leq 40\%$ of the extension diameter, D_0, and the later is varied between $1.5\% \leq u' \leq 15\%$ of the average axial velocity at the inlet, U_b. The results for the evolution of turbulence kinetic energy profile between the inlet of the upstream extension, IN, and the first measurement station S1 are shown in Fig. 10.

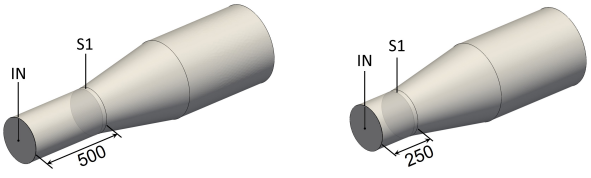

(a) (b)

FIG. 9: Numerical domains with upstream extension used in LES. (a) 500 mm long extension; (b) 250 mm long extension.

Looking at the results for the 500 mm long upstream extension, Fig. 10a, it is clear that the values of k near the walls, i.e. $y/H_i \leq 0.1$, and at station S1 do not depend on the imposed inlet boundary conditions. In fact, the lines defining the minimum and maximum values of k overlap at the walls around station -200 and numerical results at S1 are always overestimated with respect to experiments. In the case of the shorter domain, with a 250 mm long upstream extension, Fig. 10b, results for turbulence kinetic energy at station S1 are still dependent on the upstream inlet boundary conditions and, more importantly, experimental values are within the solution space of the parametric study. For this reason, the proposed Machine Learning strategy is applied to this shorter numerical domain in LES. In the case of RANS, although this upstream extension is not necessary, the proposed Machine Learning strategy is also applied to a simplified axisymmetric version of this shorter domain, shown in Fig. 11.

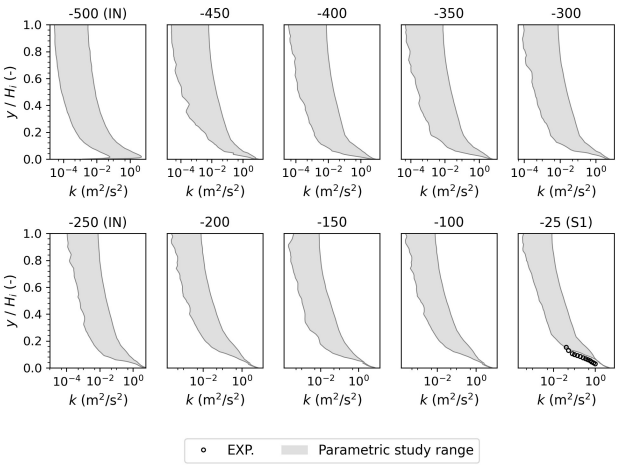

(a)

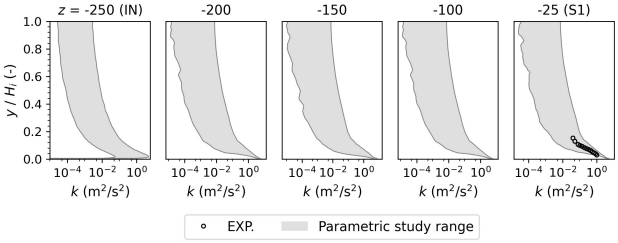

(b)

FIG. 10: Evolution of turbulence kinetic energy profiles inside the upstream extension during parametric studies in LES. (a) 500 mm long extension; (b) 250 mm long extension.

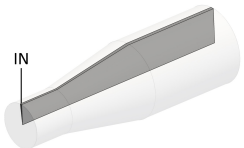

FIG. 11: Simplified numerical domain with 250 mm long upstream extension used in RANS.

Another important aspect of the first step of the proposed

Machine Learning strategy is to define the sets of inlet boundary conditions that will be used in each simulation of the database. In the case of RANS, these conditions are defined by four different profiles, the three mean velocity components (U_x, U_θ and U_r) and the turbulence kinetic energy profile k. The dissipation rate, ε, is not optimized and is still defined by Eq. 5. In the case of LES, the two synthetic turbulence parameters varied in the previous parametric study are also required to completely define the inlet boundary conditions for the simulation. In any case, each inlet profile in the database is automatically generated by a Python script and defined by a B-spline[64], which is a generalization of Bézier curves and a simple method to create complex smooth curves based on a set parameters, particularly: a knots vector, the B-spline degree and a set of coefficients. The knots vector determines the radial position of each point in the final inlet profile(s), which, in our case, corresponds to a simple geometric distribution from $y/H_i = 0.01$ to $y/H_i = 1.0$. The B-spline degree is determined empirically and varies depending on the inlet profile (i.e. U_z, U_θ, U_r and k). For instance, it is equal to 2 in the case of U_z and either 2, 3 or 4 in the case of k. The set of coefficients determines the shape of the final profile and so, to *efficiently* cover a wide range of inlet conditions, these coefficients are distributed according to a Sobol quasirandom sequence[65]. However, given that some of generated profiles are not physically correct, a final step in the process of generating the set of inlet boundary conditions consists in *filtering out* those profiles that do not follow some simple rules, e.g.: a positive mean axial velocity gradient at the walls, zero U_θ values at the center line, positive k profiles etc. In total, approximately 1700 different sets of inlet boundary conditions have been generated and Fig. 12 shows their distributions and average values compared to the experimental data at S1.

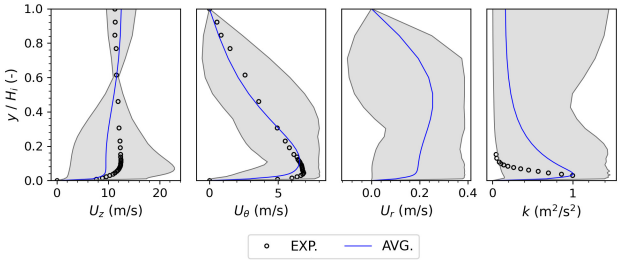

FIG. 12: Distribution of the mean velocity and turbulence kinetic energy profiles generated for the proposed Machine Learning strategy.

With both numerical domain and sets of inlet boundary conditions well defined, the simulations to create the database for the proposed Machine Learning strategy could be launched. In RANS, two databases containing the results of 800 simulations each were created: one for the reference domain (without upstream extension) and another for the simplified extended domain (with 250 mm long extension). In LES, a single database for the case with a short upstream extension (see Fig. 10b) was created, but it is smaller and contains 450 simulations in total. In both cases, post-processing is done at the end of each simulation and all flow field information measured at the eight stations inside the diffuser are stored along with the set of inlet boundary conditions that generated them.

B. Step 2: ANN architecture and training

Once the database created, the second step in the proposed Machine Learning strategy consists in determining the nonlinear model that will correlate the downstream flow field behaviour and upstream inlet boundary conditions. This is achieved by training an Artificial Neural Network (ANN) specifically designed to *learn* these correlations in a supervised manner, i.e., by looking at examples of both inputs and outputs in the flow[63]. First of all, it is necessary to define the data structure of these inputs and outputs for the ANN. In the case of swirling flow inside the conical diffuser, inputs consists in the mean axial and circumferential velocity profiles, as well as turbulence kinetic energy profiles, measured at the stations inside the diffuser. To handle the differences in numerical and experimental data format (i.e. array length), a simple linear interpolation is performed. However, since preprocessing these profiles can improve the training and performance of the ANN, each of these profiles is *scaled* by dividing its absolute value by their respective area averaged value at each section, i.e.:

$$\phi^* = \frac{\phi}{\frac{1}{A_{\text{sec}}} \iint_{A_{\text{sec}}} \phi \, dA} \tag{7}$$

where ϕ^* is the scaled variable (e.g., U_x^*, U_θ^* and k^*) and A_{sec} is the cross-section area. While this scaling regards each profile separately, a second pre-processing called *normalization* is also applied to the ensemble of the inputs vectors[63], $\mathbf{X}$, so:

$$\mathbf{X}' = \frac{\mathbf{X} - \mu}{\sigma} \tag{8}$$

where μ and σ are vectors containing, respectively, the mean and the standard deviation of each variable.

Outputs, on the other hand, consists in the sets of inlet boundary conditions imposed at each simulation of the database. In the case of RANS, this would be the four inlet profiles (U_x, U_θ, U_r and k) and, in LES, we add the two parameters required to define the synthetic turbulence field at the inlet (l_e and u'). Each profile is composed by 50 points unevenly distributed along the inlet radius. For instance, points density is higher closer to the walls where velocity and turbulence kinetic energy profiles gradients are more important. Finally, like the inputs, these profiles are also normalized before training.

After defining both inputs and outputs data structure, the last step before training is to determine the architecture of the ANN, i.e., how the different layers will connect and what are the *hyperparameters* used (e.g., the number of layers and its sizes, the activation functions, optimizer, learning rate etc.). Determining these different parameters is an optimization process by itself[66–69] and in the context of this paper all of them

have been determined manually. The final architecture of the ANN used in the optimization of the inlet boundary conditions for the three conical diffuser configurations considered is shown in Fig. 13.

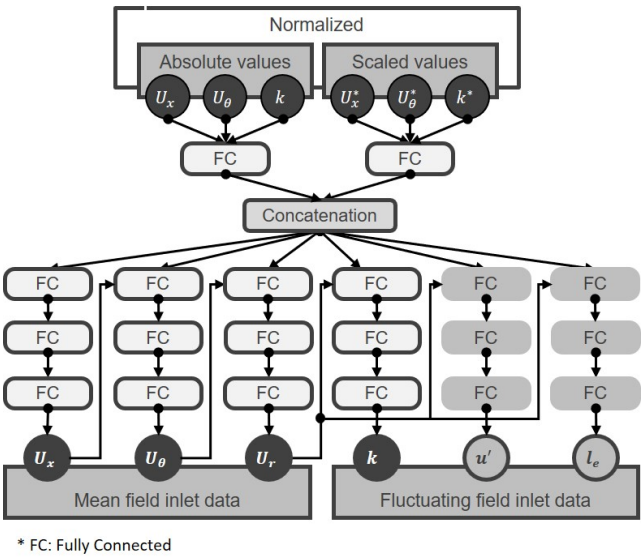

FIG. 13: Scheme of the ANN architecture used to obtain optimized inlet boundary conditions for the conical diffuser case.

The ANN consists in four or six Multi-Layer Perceptron (MLP), one for each output, designed to learn in a supervised manner and composed mostly by fully-connected layers, FC. In this type of layer, every unit in one layer is connected to every unit in the other layer, therefore its name fully-connected. A concatenation layer is also used to concatenate the inputs coming from both absolute and scaled inputs. Exponential Linear Units[70] (ELU) are used as activation functions because, differently from simpler and more commonly used ReLU[71,72], they can handle negative outputs. At the end of each fully-connected layer, a dropout rate of 50% is applied to reduce overfitting and improve the model's performance[73]. Due to the nature of the problem (i.e., a non-linear regression), the loss function is equal to the Mean-Squared Error (MSE) between the training (true) set, $\mathbf{Y^{true}}$, and predictions, $\mathbf{Y^{pred}}$,

$$\mathrm{MSE} = \frac{1}{N}\sum_{i}^{N}\left(\mathbf{Y^{true}} - \mathbf{Y^{pred}}\right)_i^2 \tag{9}$$

Finally, the machine learning algorithm is implemented in Python 3.7 using Tensorflow 2.1 and training is conducted for 5000 epochs using NAdam as optimizer[74]. In all three configurations investigated (two RANS and one LES), 400 cases from their respective databases are used for training and 10% it (i.e., 40 cases) is used as validation for the model. The results from all stations are used as inputs for the ANN, except for station S2. At this location, experimental mean streamwise velocity profile seems underestimated with respect to the rest of the diffuser, which could potentially affect the ANN model prediction. Moreover, since station S1 corresponds to the inlet of the numerical domain without upstream extension, it is also not used in this particular case.

C. Step 3: Predicted inlet boundary conditions and results

After finishing the training, the final step in the proposed Machine Learning strategy consists in feeding the experimental data of the ERCOFTAC conical diffuser back into the trained ANN model and, as a result, it provides the optimized inlet boundary conditions for the numerical simulation. As explained in Step 1, the proposed strategy has been applied to three different configurations of the conical diffuser, which are resumed in Tab. II.

1. RANS with and without upstream extension

We start with the numerical domain with upstream extension (see Fig. 11) simulated in RANS using the k-ω SST turbulence model. Although the upstream extension is not as essential in RANS as it is in LES, this case represents some of the previous attempts to recover the missing U_r profile at station S1 of the conical diffuser case[38,40–43] in RANS. Fig. 14 shows the inlet (IN station) boundary conditions predicted by the Machine Learning strategy.

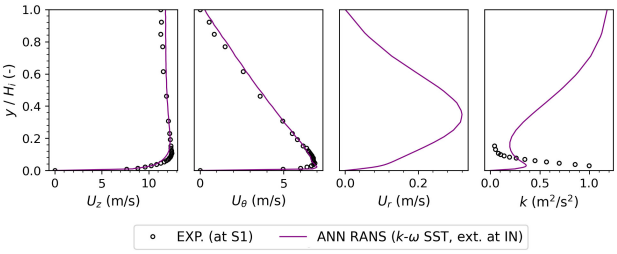

FIG. 14: Inlet boundary conditions predicted by the Machine Learning strategy at station IN for the ANN-RANS simulation of the case with upstream extension.

In this figure, the three mean velocity profiles are similar to the experimental measurements at station S1, although the axial velocity profile is flatter in the center region of the flow. Turbulence kinetic energy values, on the other hand, are significantly lower at the walls but larger in the center. These adjustments are important to recover the correct velocity and turbulence kinetic energy distributions at station S1 and further downstream. Previous attempts to adjust the inlet boundary conditions for the extended conical diffuser configuration indeed failed because they underestimated U_z and U_θ at the wall[38,42,43] at station S1. In the case of mean axial velocity profiles, there are two opposite effects acting inside the upstream extension: (i) the flow shear at the walls, which reduces U_z at the walls and, therefore, increases its values at the center; and (ii) the flow swirl, which forces the flow towards

TABLE II: Characteristics of the ANN RANS and ANN LES computations of the swirling flow inside the conical diffuser.

Case	Turbulence method	Numerical domain	Inlet conditions
ANN-RANS not extended	RANS k-ω SST	Fig. 2(a)	U_z, U_θ, U_r and k from ANN ε from Eq. (5)
ANN-RANS extended	RANS k-ω SST	Fig. 11	U_z, U_θ, U_r and k from ANN ε from Eq. (5)
ANN-LES	LES	Fig. 9(b)	U_z, U_θ, U_r, k, u' and l_e from ANN

the walls, increasing thus U_z values at this region and reducing it at the center. The proposed Machine Learning strategy has thus the ability to correctly account for both effects to match the experimental data at station S1 and inside the conical diffuser.

To demonstrate the importance of the upstream extension, an ANN-RANS simulation without upstream extension is although performed. In that case, the inlet station is the S1 station (see Fig. 2a) instead of the IN station and the simulation is directly initiated with the mean velocity and k profiles predicted by the Machine Learning strategy. Fig. 15 shows the various profiles at S1 station for the two ANN-RANS cases, i.e. with and without upstream extension. The numerical profiles are compared with the experimental data when available. To demonstrate the added value of the ANN strategy, ANN results are also compared with the reference RANS case of Section IV.

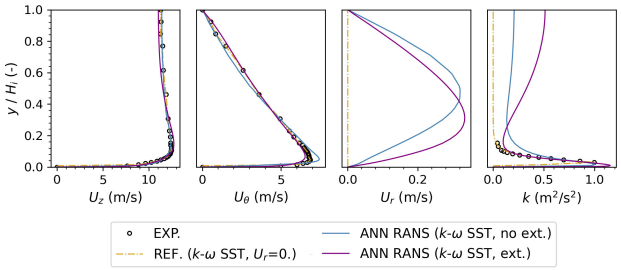

FIG. 15: Comparison of experimental and numerical mean velocity and turbulence profiles at station S1 using the RANS and the Machine Learning strategy.

Overall, the predicted profiles agree very well with the experiments. In the case without upstream extension, the predicted U_z values are very similar to the experimental measurements at S1 in the case without upstream extension whereas the mean circumferential velocity profile, U_θ, is overestimated near the wall ($y/H_i \approx 0$) and slightly underestimated between $0.5 \leq y/H_i \leq 0.8$. The turbulence kinetic energy profile, k, is also very similar to experiments close to the walls, but is overestimated towards the center of the flow. Conversely in the case with upstream extension, U_θ agrees well with the experimental data but the maximum value of U_z near the walls is slightly overestimated and is located at a slightly higher position ($y/H_i \approx 0.2$ instead of 0.1). Compared to the case without upstream extension, the peak of turbulence kinetic energy profile is now closer to the walls and at a higher value, however, this profile is still overestimated towards the center of the flow. Notice though that there is no experimental data available between $y/H_i \approx 0.15$ and 1.0 to inform the ANN about the expected values of k in this region. Moreover, as compared to previous attempts to impose turbulent inlet boundary conditions based only on integral quantities[34,40] (e.g., turbulence intensity and characteristic length scale), the profile of k predicted by the proposed ML strategy leads to a much better agreement with the experimental measurements at station S1. The real contribution though of the proposed strategy is to obtain a more adequate mean radial velocity inlet profile at S1. Even if it is much smaller than the other two velocity components, both predicted radial velocity profiles are positive and therefore forces the flow towards the walls, helping it to stay attached throughout the diffuser. Moreover, as pointed out by Payette[40], to impose a r varying profile of U_r at the inlet is equivalent to specify the rate of longitudinal variation of the axial velocity, U_z, at the inlet. This can be understood by looking at the continuity equation in cylindrical coordinates, Eq. 10:

$$\frac{\partial U_z}{\partial z} + \frac{1}{r}\frac{\partial U_\theta}{\partial \theta} + \frac{1}{r}\frac{\partial r U_r}{\partial r} = 0 \tag{10}$$

Since the flow is axisymmetric, $\partial/\partial\theta = 0$. Therefore, imposing a profile of U_r implies that $\frac{1}{r}\frac{\partial r U_r}{\partial r} \neq 0$ and sets an axial evolution for U_z due to the term $\frac{\partial U_z}{\partial z}$. However, the distribution of this radial velocity profile is also important, as it will, for instance, define the regions where the axial flow is accelerated and/or slowed down. This is illustrated by Fig. 16 which compares the inlet radial velocity profile at station S1 obtained by the proposed Machine Learning strategy and by the separate simulation of the swirl generator upstream the conical diffuser performed in Payette[40]. All profiles predict an accelerated axial flow close to the walls and slowed down towards the center due to the change in the sign of $\frac{1}{r}\frac{\partial r U_r}{\partial r}$, but the position of the peak is better captured in the case with upstream extension, which is explained by the effect of the circumferential velocity profile imposed at station IN.

Looking at the flow behaviour inside the conical diffuser, Fig. 17 shows the results of mean streamwise velocity pro-

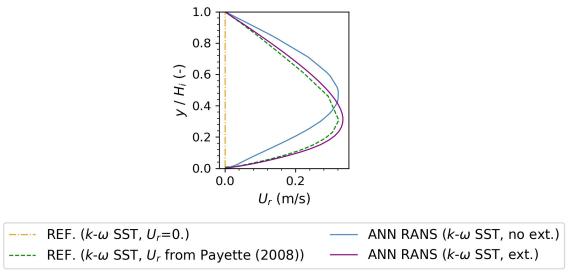

FIG. 16: Mean radial velocity profiles at station S1 predicted by the proposed Machine Learning strategy and the separate swirl generator simulation in Payette[40].

files obtained with the ANN-RANS approach in comparison with the basic RANS case of Section IV and the *ad hoc* solution proposed in Payette[40]. The impact of the ML strategy on the flow behaviour downstream is noticeable. For instance, as a result of the more appropriate radial velocity profile imposed at station S1, the boundary layer is much better predicted compared to the basic simulations and the flow remains attached to the walls throughout the diffuser. In the case with upstream extension, though, the slightly overestimated and higher U_x peak at station S1 leads to a small difference in the prediction of the streamwise velocity peak compared to the case without upstream extension. The position and magnitude of this velocity peak agree very well with the experimental data, except for the last two stations, where it is overestimated. ANN-RANS profiles also agree very well with the best solution obtained in Payette[40] using RANS and k-ω SST turbulence model, although he managed to better capture the small variations in the center of the flow.

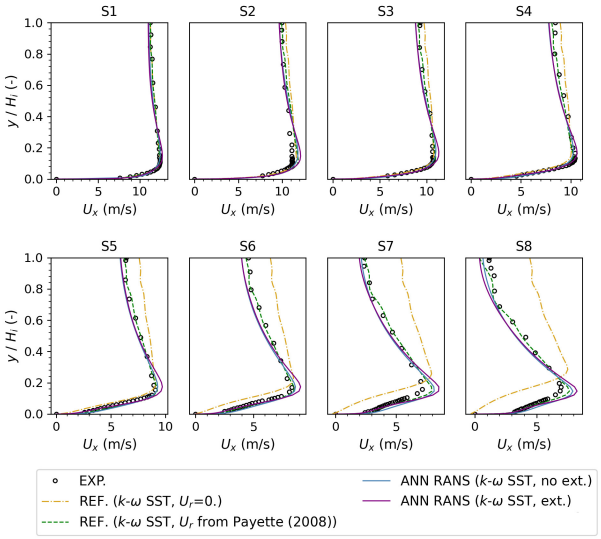

FIG. 17: Comparisons of experimental and numerical mean streamwise velocity profiles inside the diffuser using RANS and the proposed strategy.

Figure 18 shows the results for mean circumferential velocity profiles. Overall, the results agree very well with the experimental data and the best solution obtained in Payette[40], and are much improved compared to the basic RANS simulations discussed in Section IV. In spite of U_θ values near the walls at station S1 being overestimated in the case without upstream extension and underestimated in the case with upstream extension, the numerical results obtained with the Machine Learning strategy agree well with the experimental data in this region along the diffuser. However, the slight underestimation between $0.5 \leq y/H_i \leq 0.8$ at the inlet of the domain without upstream extension (S1 station) causes the circumferential velocity profile to be underestimated in the center region of the flow compared to the other cases.

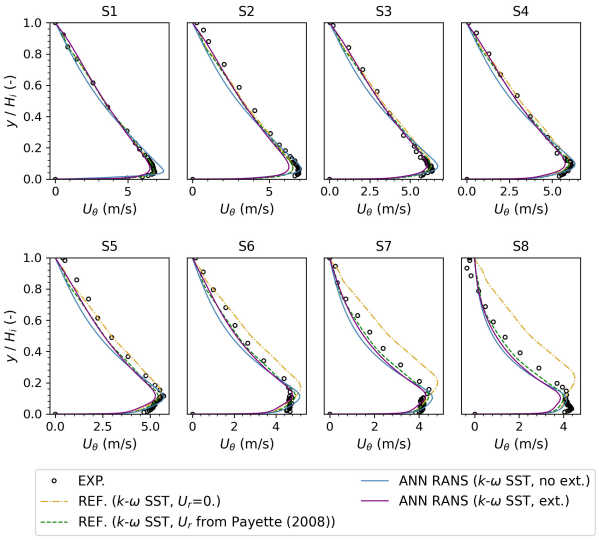

FIG. 18: Comparisons of experimental and numerical mean circumferential velocity profiles inside the diffuser using RANS and the proposed strategy.

The results for turbulence kinetic energy profiles are shown in Fig. 19. In the case without upstream extension, k values are overestimated between $y/H_i = 0.1$ and 0.2 at station S1, but they slowly decrease and a very good agreement is found at S4. However, while the experimental measurements predict a constant peak value of $k \approx 2$ m^2/s^2 between S5 and S7 followed by a very slow displacement of this peak towards the duct center and a strong decrease at S8, the numerical results keep reducing until the end of the diffuser and are quite underestimated at the last four stations. This is consistent though with previous studies that investigated this flow using two-equation linear eddy viscosity models[33,34,38,40].

Conversely to the *ad hoc* solution proposed in Payette[40] and many other methods discussed in the introduction to determine proper inlet boundary conditions for the case of the swirling flow inside the conical diffuser and any other flow configuration, one key aspect of the proposed Machine Learning strategy is that it relies only on the known downstream experimental information to automatically construct the optimized inlet conditions. While the results at seven out of

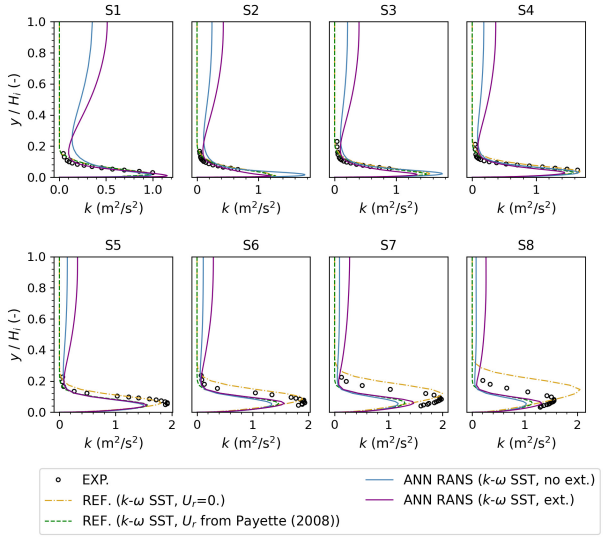

FIG. 19: Comparisons of experimental and numerical turbulence kinetic energy profiles inside the diffuser using RANS and the Machine Learning strategy.

the eight measurement stations have been used in the previous discussions, we also investigated the Machine Learning strategy performance using a limited number of stations to train the ANN model. Figure 20 compares the streamwise velocity profiles of the previous ANN RANS case with upstream extension against an identical configuration but only trained with the two stations S1 *and* S8.

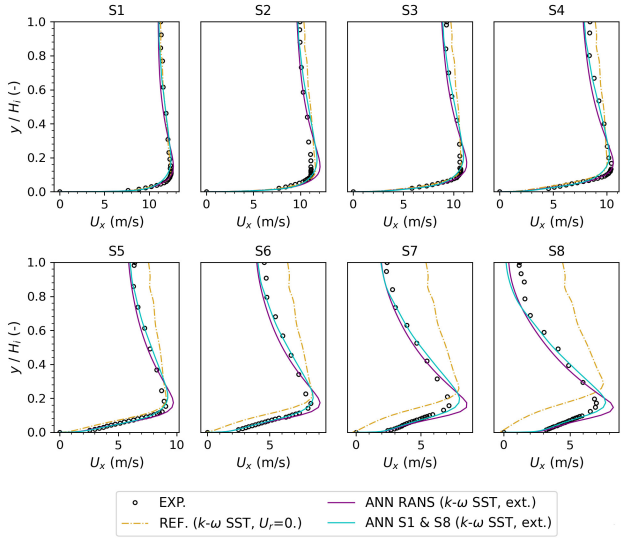

FIG. 20: Comparisons of experimental and numerical mean streamwise velocity profiles inside the diffuser using RANS and different amount of stations for the ANN.

The results obtained with the two approaches with a different number of stations are still close and both exhibit a good agreement with the experimental data. It is important to remark that the relative simplicity of the present diffuser (constant opening angle, free flow outlet) renders the use of a limited amount of experimental data to trained the ANN particularly favourable. This may not be the case for more complex geometries, but is nevertheless promising since it demonstrates the potential of the proposed Machine Learning strategy to be applied to cases with very limited experimental information.

2. *LES with upstream extension*

The next configuration to which the Machine Learning strategy has been applied consists in the numerical domain with upstream extension shown in Fig. 9b using LES. The goal is then to construct proper flow characteristics (mean and fluctuating) in the inlet section IN in order to match as closely as possible the available experimental information in the S1 section as well as in the following sections.

As compared to RANS, the LES approach requires a considerably higher computational cost to generate a proper LES database for the Machine Learning strategy. Therefore, one be tempted to use the inlet profiles predicted by the ANN-RANS procedure to initiate the LES simulation. First, this does not solve the problem of defining the correct l_e and u' for the inlet (IN section) synthetic turbulence. Second, the inlet profiles issued from the ANN procedure take into account all the model errors and numerical errors which are distinct in the RANS and in the LES cases. This is clearly demonstrated on Fig. 21 which displays the mean axial velocity profiles given by the ANN-RANS (with extension) described in Section VI. These are compared with the LES profiles issued from a LES with the ANN-RANS inlet mean profiles shown on Fig. 14 imposed at the IN section. For the synthetic turbulence length and velocity scales, l_e and u', we choose generally used values[40], i.e. $10\%U_b$ and $10\%D_0$, respectively. Fig. 21 clearly shows that the LES results thus obtained exhibit a degraded quality as compared to the ANN-RANS ones specially downstream of S4 station. Therefore, it is essential that the simulations in the database reflect as much as possible the numerical case we want to optimize.

After training the ANN with a LES database consisting of 400 cases and feeding the experimental data back to the trained model, the predicted inlet boundary conditions of the IN section are shown in Fig. 22. The profiles are compared to the equivalent RANS configuration discussed in the previous section (see Fig. 11). The various inlet profiles predicted by the ANN-LES et ANN-RANS approaches are noticeably different, specially their near wall behaviour. This clearly shows that the ANN procedure includes both the numerical errors and the modelling errors to construct the inlet profiles adapted to a specific simulation, i.e. RANS or LES. The injected synthetic fluctuations are still isotropic and generated according to the scheme presented in Fig. 4 using the turbulence kinetic energy profile to set its radial distribution. Due to the additional parameters required to define the upstream synthetic turbulence, the ANN strategy also determined the optimal u'

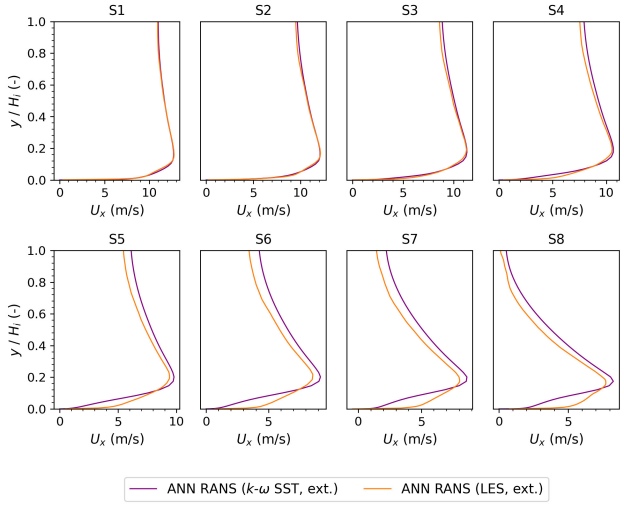

FIG. 21: Comparisons of experimental and numerical mean streamwise velocity profiles inside the diffuser using the inlet boundary conditions predicted by the proposed strategy with a RANS database in LES and the proposed strategy.

and l_e at the IN section. It is found $u' = 0.551$ m/s, or $\approx 5\%$ of U_b, and $l_e = 0.042$ m, or $\approx 16\%$ of D_0.

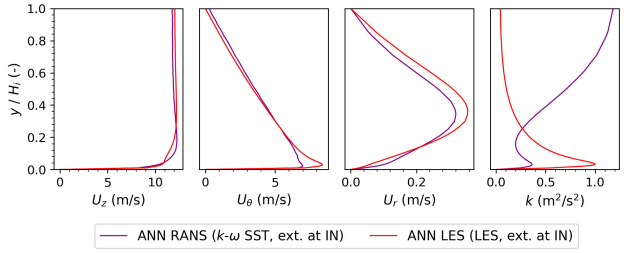

FIG. 22: Inlet boundary conditions predicted by the proposed Machine Learning strategy at station IN using LES and the proposed strategy.

Compared to the previous ANN-RANS case with upstream extension, the predicted optimal mean velocity profiles in LES are slightly different. For instance, after a rapid increase at the walls, U_z varies almost linearly before reaching its maximum value at around $y/H_i = 0.2$. Moreover, while optimal k values predicted in RANS are large at the center compared to its values at the walls, the normalized turbulence kinetic energy predicted in LES presents a single peak at the wall. More importantly though is the impact of these adjustments right upstream the conical diffuser, at station S1. As shown in Fig. 23, the mean axial velocity agrees very well with the experimental measurements at this location and the same can be said for the mean circumferential velocity, U_θ. The radial velocity profile is once again similar to what has been found previously in RANS and in Payette[40], and the turbulence kinetic energy profile is at the correct level near the walls.

The downstream evolution of the mean streamwise velocity

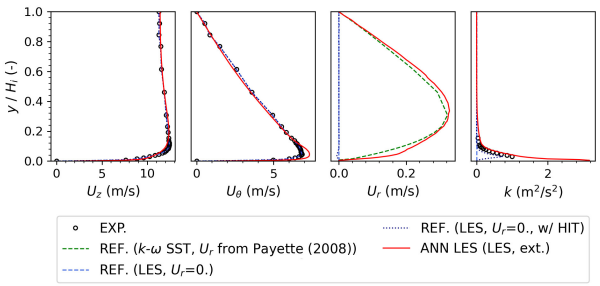

FIG. 23: Comparison of experimental and numerical velocity and turbulence profiles at station S1 using the LES and the proposed strategy.

shown on Fig. 24 demonstrates that the ANN-LES approach yields much better results than the basic LES approach described in Section IV without extension, zero radial velocity and zero turbulence at the inlet. We have also checked that the results are significantly improved as compared with the previous works attempting to adjust the upstream inlet boundary conditions in LES[30]. The streamwise velocity is slightly overpredicted at the walls, but its peak position and magnitude are very close to the experimental measurements. While previous ANN-RANS simulations overestimated the value of the mean streamwise velocity peak at the last two measurement stations (S7 and S8, see Fig. 17), LES results agree very well with the experiments. Moreover, the correct levels of mean streamwise velocity at the center of the flow is also obtained along the diffuser, except for stations S7 and S8, where they are slightly overpredicted.

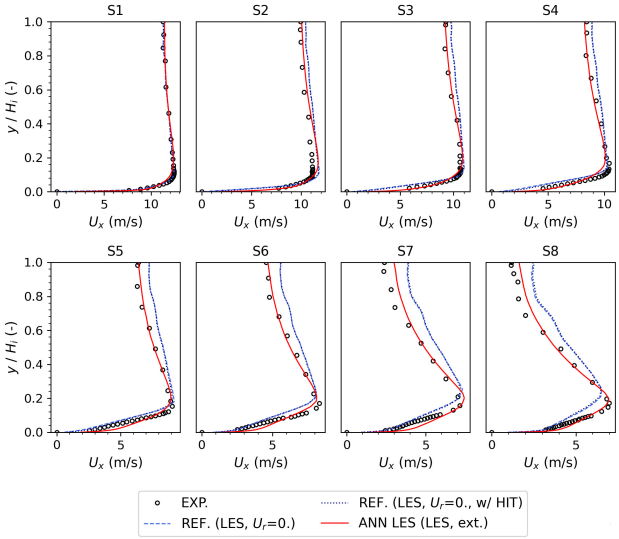

FIG. 24: Comparisons of experimental and numerical mean streamwise velocity profiles inside the diffuser using LES and the proposed strategy.

Figure 25 shows the results for mean circumferential velocity profiles inside the conical diffuser. Once again, the numer-

ical results agree very well with the experimental data in spite of the slight overestimated values of U_θ near the walls at station S1. Between stations S2 and S4, the correct level of mean circumferential velocity is found right to the walls.

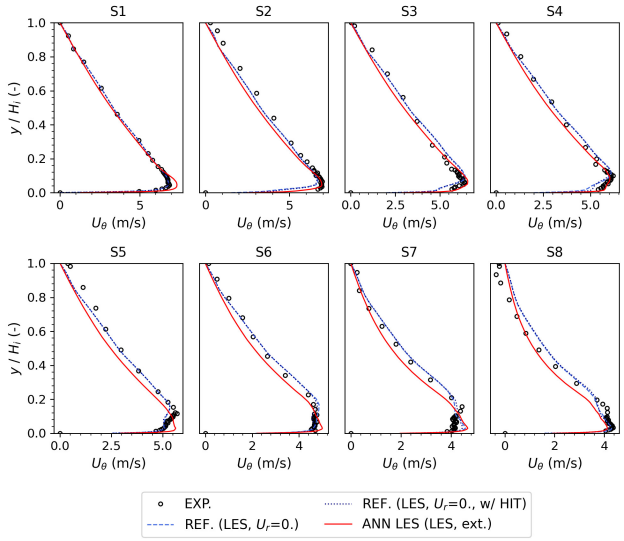

FIG. 25: Comparisons of experimental and numerical mean circumferential velocity profiles inside the diffuser using LES and the proposed strategy.

Turbulence kinetic energy profiles are shown in Fig. 26. The turbulent characteristics determined by the ANN procedure at the inlet of numerical domain (station IN) allow to obtain turbulence levels and distribution very similar to experimental measurements, with a strong peak near the wall and almost no turbulence towards the center of the flow. However, contrary to the two basic reference cases, k is overestimated at S2 and S3 but is closer to the experimental values at S4 and S5. Between S6 and S8, although the numerical results of the predicted extended case agree quite well with experimental measurements close to $y/H_i = 0.2$, their maximum values near the wall are underpredicted. It should be noticed that, compared to previously discussed RANS simulations, y^+ values in LES are significantly higher and the appropriate wall-model used in these simulations[62] is not particularly built to properly predict the RMS velocity components in the vicinity of the wall, which could explain the strong peak of k near the walls. However, as the Machine Learning strategy required a large number of simulations to be applied, the computational cost was a limiting factor. We are presently investigating the possibility to train the ANN with a reduced database involving a smaller number of LES simulations but with an improved wall resolution.

The main reason to add an upstream extension though is to give the incoming synthetic fluctuations enough space and time for them to develop into more realistic turbulence before reaching the conical diffuser. Figure 27 show the evolution of $\langle u'_r u'_\theta \rangle$ and $\langle u'_r u'_z \rangle$ correlations at station S1 of the conical diffuser. As expected, in the case without upstream extension, since the injected synthetic turbulence field is isotropic, cor-

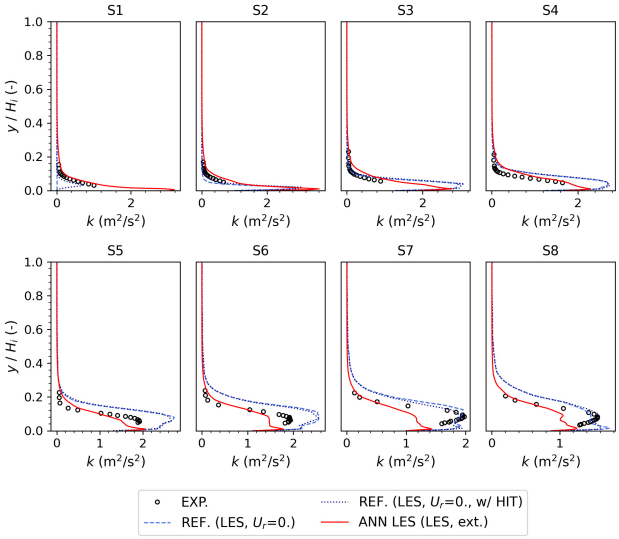

FIG. 26: Comparisons of experimental and numerical turbulence kinetic energy profiles inside the diffuser using LES and the proposed strategy.

relations are zero at the inlet of the domain (station S1). Conversely, in the ANN-LES case with upstream extension, these correlations are allowed to build up and a very good agreement with the experimental values of $\langle u'_r u'_\theta \rangle$ is recovered at station S1. Numerical results for $\langle u'_r u'_z \rangle$ exhibit the same trend as the corresponding experimental profile but with a larger absolute value of the near wall peak.

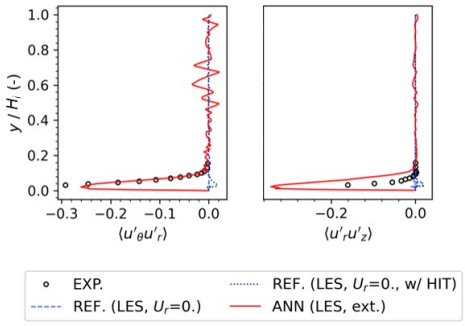

FIG. 27: Comparisons of experimental and numerical Reynolds stresses profiles at station S1 using LES and the proposed strategy.

Another way of visualizing the differences for the inlet turbulent fluctuations between the three different LES (the two basics and the ANN) consists in investigating the turbulent structures inside the conical diffuser. Figure 28 shows these structures using iso-surfaces of Q-criterion[58] coloured by the vorticity magnitude. In the reference case, if synthetic fluctuations are added in the section S1 (see Fig. 28a), turbulent structures can be seen from the beginning of the numerical domain, but they still need to develop into more realistic turbulence downstream in the diffuser. In the case of ANN-LES

(see Fig. 28b), the synthetic turbulence injected at the inlet (section IN) of the upstream extension is more realistic when it arrives at the section S1. Well defined coherent structures can thus be observed at the beginning of the domain and consist of vortices aligned with the mean flow direction due to centrifugal instabilities at the upstream extension.

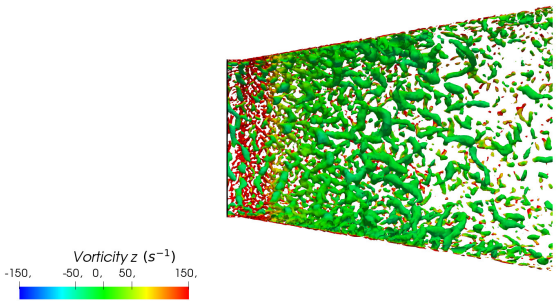

(a)

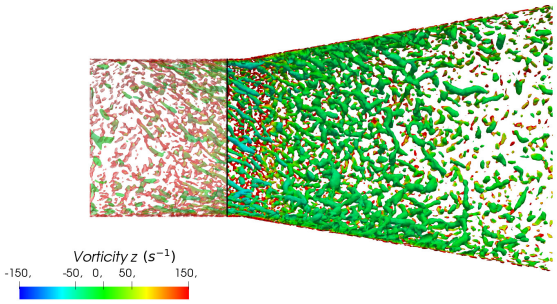

(b)

FIG. 28: Turbulent structures inside the conical diffuser visualized by iso-surfaces of $Q = 25000\ \mathrm{s}^{-2}$ and coloured by their vorticity in the z-axis direction. (a) LES w/o upstream extension and w/ synthetic fluctuations; (b) LES w/ upstream extension and w/ synthetic fluctuations.

Finally, Fig. 29 shows the evolution of the coefficient of pressure C_p along the walls of the conical diffuser. Notice that the static pressure at station S8 is used as reference instead of the atmospheric pressure in Eq. (3). As the static pressure on the walls is greatly affected by the near wall velocity distribution, numerical results obtained with the Machine Learning strategy are clearly improved compared to the basic simulations. As discussed by Payette[40], this constitutes an important result since the Cp is closely related to the hydraulic performance of the diffuser (i.e. how efficiently it converts the dynamic pressure into static pressure).

VII. CONCLUSION

A new approach to determine proper mean and fluctuating inlet boundary conditions for a numerical simulation is proposed and discussed. It is based on machine learning and its goal is to use *any* known downstream data about the

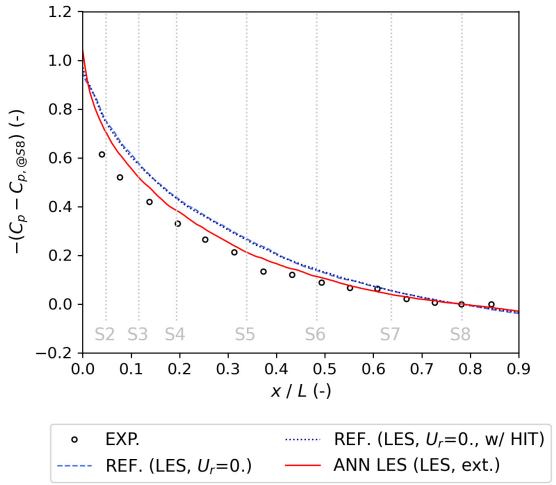

FIG. 29: Comparisons of experimental and numerical C_p evolution using LES and the proposed strategy.

flow to determine the optimal upstream inlet boundary conditions. The proposed approach is applied to the test case of the swirling flow inside a conical diffuser using both RANS k-ω SST and LES turbulence models. Despite its geometric simplicity, the delicate balance between core flow recirculation and boundary layer separation renders numerical simulations of this case very sensitive to inlet conditions and constitutes a real challenge.

Previous works as well as our simulations showed that the main difficulty in RANS consists in determining the radial velocity distribution at the inlet of the diffuser, which is not known from experiments. In LES, the difficulty is even higher since it is compulsory to generate and inject proper synthetic fluctuations into the numerical domain. One of the solutions consists in the addition of an artificial extension upstream of the original numerical domain to give these fluctuations the space and time required to develop before reaching the diffuser. However, the inlet conditions need to be empirically adjusted and, as previous simplistic methods fail to match the downstream flow behaviour, a more sophisticated approach is here developed based on machine learning.

The machine learning approach is applied to three different configurations and the results are considerably improved with respect to the reference case with simplistic inlet conditions. In RANS, the optimized inlet conditions keep the boundary layer attached to the walls throughout the diffuser and allow to recover the correct level of streamwise velocity at the center of the flow. Moreover, circumferential velocity profiles and turbulence kinetic energy evolution are also better predicted. In LES, the proposed machine learning strategy is able to significantly improve the prediction of the streamwise velocity peak and its distribution in the diffuser core. Moreover, the circumferential velocity and turbulence kinetic energy profiles exhibit a very good agreement with the experiments. The impact of the upstream extension on the turbulent structures at the inlet of the diffuser is also noticeable. The correct turbu-

lent correlations are thus created upstream and a more realistic turbulence flow field is recovered downstream. Finally, the prediction of the pressure coefficient evolution at the wall is greatly improved by the application of the proposed strategy, which has an important impact on the analysis of the hydraulic performance of the diffuser.

The numerical results obtained with the proposed Machine Learning strategy could be further improved by adding more simulations into the database used to than the ANN model. However, since the computational cost would be directly affected by the additional numerical simulations, a ongoing investigation consists in enhancing the performance of the model by increasing the comprehensiveness of a reduced database. Nevertheless, despite its relatively high computational cost, one advantage of the proposed machine learning strategy is that it can be generalized to different flow configurations and types of problems. For many industrial applications, the proper prescription of the inlet flow characteristics is often impossible to obtain without expensive extra computations. Although the present study is here devoted to a simple flow geometry, it is currently applied to the reconstruction of mean and fluctuating turbulent fields in complex geometries of industrial interest using adequately chosen downstream measurements.

ACKNOWLEDGEMENTS

The authors would like to thank the *Hydro'Like* industrial chair for funding this research and the *Grand Equipement National de Calcul Intensif* (GENCI), Grant2A00611, for providing the computing resources.

DATA AVAILABILITY

The data that support the findings of this study are available from the corresponding author upon reasonable request.

[1]A. Keating, U. Piomelli, E. Balaras, and H.-J. Kaltenbach, "A priori and a posteriori tests of inflow conditions for large-eddy simulation," Physics of Fluids **16**, 4696–4712 (2004).

[2]P. Sagaut, *Large eddy simulation for incompressible flows: an introduction* (Springer Science & Business Media, 2006).

[3]G. R. Tabor and M. Baba-Ahmadi, "Inlet conditions for large eddy simulation: a review," Computers & Fluids **39**, 553–567 (2010).

[4]X. Wu, "Inflow turbulence generation methods," Annual Review of Fluid Mechanics **49**, 23–49 (2017).

[5]N. S. Dhamankar, G. A. Blaisdell, and A. S. Lyrintzis, "Overview of turbulent inflow boundary conditions for large-eddy simulations," AIAA Journal **56**, 1317–1334 (2018).

[6]J.-L. Aider and A. Danet, "Large-eddy simulation study of upstream boundary conditions influence upon a backward-facing step flow," Comptes Rendus Mécanique **334**, 447–453 (2006).

[7]S. Lee, S. K. Lele, and P. Moin, "Simulation of spatially evolving turbulence and the applicability of Taylor's hypothesis in compressible flow," Physics of Fluids A: Fluid Dynamics **4**, 1521–1530 (1992).

[8]R. H. Kraichnan, "Diffusion by a random velocity field," The Physics of Fluids **13**, 22–31 (1970).

[9]A. Smirnov, S. Shi, and I. Celik, "Random flow generation technique for large eddy simulations and particle-dynamics modeling," Journal of Fluids Engineering **123**, 359–371 (2001).

[10]P. Batten, U. Goldberg, and S. Chakravarthy, "Interfacing statistical turbulence closures with large-eddy simulation," AIAA Journal **42**, 485–492 (2004).

[11]L. Davidson and M. Billson, "Hybrid LES-RANS using synthesized turbulent fluctuations for forcing in the interface region," International Journal of Heat and Fluid Flow **27**, 1028–1042 (2006).

[12]L. Davidson, "Hybrid LES-RANS: inlet boundary conditions for flows with recirculation," in *Advances in Hybrid RANS-LES Modelling* (Springer, 2008) pp. 55–66.

[13]M. Klein, A. Sadiki, and J. Janicka, "A digital filter based generation of inflow data for spatially developing direct numerical or large eddy simulations," Journal of Computational Physics **186**, 652–665 (2003).

[14]L. Di Mare, M. Klein, W. Jones, and J. Janicka, "Synthetic turbulence inflow conditions for large-eddy simulation," Physics of Fluids **18**, 025107 (2006).

[15]N. Jarrin, S. Benhamadouche, D. Laurence, and R. Prosser, "A synthetic-eddy-method for generating inflow conditions for large-eddy simulations," International Journal of Heat and Fluid Flow **27**, 585–593 (2006).

[16]N. Jarrin, R. Prosser, J.-C. Uribe, S. Benhamadouche, and D. Laurence, "Reconstruction of turbulent fluctuations for hybrid RANS/LES simulations using a synthetic-eddy method," International Journal of Heat and Fluid Flow **30**, 435–442 (2009).

[17]M. Pamiès, P.-E. Weiss, E. Garnier, S. Deck, and P. Sagaut, "Generation of synthetic turbulent inflow data for large eddy simulation of spatially evolving wall-bounded flows," Physics of Fluids **21**, 045103 (2009).

[18]R. Poletto, T. Craft, and A. Revell, "A new divergence free synthetic eddy method for the reproduction of inlet flow conditions for LES," Flow, Turbulence and Combustion **91**, 519–539 (2013).

[19]P. Druault, S. Lardeau, J.-P. Bonnet, F. Coiffet, J. Delville, E. Lamballais, J.-F. Largeau, and L. Perret, "Generation of three-dimensional turbulent inlet conditions for large-eddy simulation," AIAA Journal **42**, 447–456 (2004).

[20]A. Ferrante and S. Elghobashi, "A robust method for generating inflow conditions for direct simulations of spatially-developing turbulent boundary layers," Journal of Computational Physics **198**, 372–387 (2004).

[21]R. J. Stevens, J. Graham, and C. Meneveau, "A concurrent precursor inflow method for large eddy simulations and applications to finite length wind farms," Renewable Energy **68**, 46–50 (2014).

[22]C. D. Pierce and P. Moin, "Method for generating equilibrium swirling inflow conditions," AIAA Journal **36**, 1325–1327 (1998).

[23]J. Schlüter, H. Pitsch, and P. Moin, "Large-eddy simulation inflow conditions for coupling with Reynolds-averaged flow solvers," AIAA Journal **42**, 478–484 (2004).

[24]M. García-Villalba and J. Fröhlich, "LES of a free annular swirling jet - Dependence of coherent structures on a pilot jet and the level of swirl," International Journal of Heat and Fluid Flow **27**, 911–923 (2006).

[25]T. S. Lund, X. Wu, and K. D. Squires, "Generation of turbulent inflow data for spatially-developing boundary layer simulations," Journal of Computational Physics **140**, 233–258 (1998).

[26]J. Jiménez, S. Hoyas, M. P. Simens, and Y. Mizuno, "Turbulent boundary layers and channels at moderate reynolds numbers," Journal of Fluid Mechanics **657**, 335–360 (2010).

[27]J. H. Lee and H. J. Sung, "Direct numerical simulation of a turbulent boundary layer up to $re_\theta = 2500$," International Journal of Heat and Fluid Flow **32**, 1–10 (2011).

[28]A. Spille-Kohoff and H.-J. Kaltenbach, "Generation of turbulent inflow data with a prescribed shear-stress profile," Tech. Rep. (TECHNISCHE UNIV BERLIN (GERMANY) HERMANN-FOTTINGER INST FUR STROMUNGSMECHANIK, 2001).

[29]P. D. Clausen, S. G. Koh, and D. H. Wood, "Measurements of a swirling turbulent boundary layer developing in a conical diffuser," Experimental Thermal and Fluid Science **6**, 39 – 48 (1993).

[30]C. Duprat, *Simulation numérique instationnaire des écoulements turbulents dans les diffuseurs des turbines hydrauliques en vue de l'amélioration des performances*, Ph.D. thesis, Institut National Polytechnique de Grenoble (INPG), Grenoble, France (2010).

[31]A. McDonald, R. Fox, and R. Van Dewoestine, "Effects of swirling inlet flow on pressure recovery in conical diffusers," AIAA Journal **9**, 2014–2018 (1971).

[32]S. Wilhelm, G. Balarac, O. Metais, and C. Ségoufin, "Analysis of head losses in a turbine draft tube by means of 3D unsteady simulations," Flow,

Turbulence and Combustion **97**, 1255–1280 (2016).
[33]S. W. Armfield, N.-H. Cho, and C. A. J. Fletcher, "Prediction of turbulence quantities for swirling flow in conical diffusers," AIAA Journal **28**, 453–460 (1990).
[34]S. Mauri, *Numerical simulation and flow analysis of an elbow diffuser*, Ph.D. thesis, École Polytechnique Fédérale de Lausanne (EPFL), Lausanne, Switzerland (2002).
[35]B. E. Launder and D. B. Spalding, "The numerical computation of turbulent flows," Computer Methods in Applied Mechanics and Engineering **3**, 269 – 289 (1974).
[36]W. Rodi, J. Bonnin, and T. Buchal, "ERCOFTAC workshop on data bases and testing of calculation methods for turbulent flows," in *Part of the Proceedings of the 4th ERCOFTAC/IAHR Workshop on Refined Flow Modelling* (University of Karsruhe, 1995).
[37]H. Nilsson, M. Page, M. Beaudoin, B. Gschaider, and H. Jasak, "The OpenFOAM turbomachinery working-group, and conclusions from the turbomachinery session of the third openfoam workshop," in *IAHR: 24th Symposium on Hydraulic Machinery and Systems, Foz do Iguassu, Brazil* (2008).
[38]O. Bounous, "Studies of the ERCOFTAC conical diffuser with OpenFOAM," Department of Applied Mechanics Chalmers University of technology, Göteborg, Sweeden (2008).
[39]F. R. Menter, "Two-equation eddy-viscosity turbulence models for engineering applications," AIAA Journal **32**, 1598–1605 (1994).
[40]F.-A. Payette, *Simulation de l'écoulement turbulent dans les aspirateurs de turbines hydrauliques: impact des paramètres de modélisation*, Master's thesis, Université Laval, Quebec, Canada (2008).
[41]W. Gyllenram and H. Nilsson, "Very large eddy simulation of draft tube flow," in *Proc. 23rd IAHR Symp. on Hydraulic Machinery and Systems, Yokohama, Japan F*, Vol. 159 (2006).
[42]P. Bélanger-Vincent, *Simulations avancées de l'écoulement turbulent dans les aspirateurs de turbines hydrauliques*, Master's thesis, Université Laval, Quebec, Canada (2010).
[43]A. Taheri, *Detached Eddy simulation of unsteady turbulent flows in the draft tube of a bulb turbine*, Ph.D. thesis, Université Laval, Quebec, Canada (2015).
[44]K. Fukami, Y. Nabae, K. Kawai, and K. Fukagata, "Synthetic turbulent inflow generator using machine learning," Physical Review Fluids **4**, 064603 (2019).
[45]A. Corsini, G. Delibra, M. Giovannelli, and S. Traldi, "Machine learnt synthetic turbulence for LES inflow conditions," in *ASME Turbo Expo 2020: Turbomachinery Technical Conference and Exposition* (American Society of Mechanical Engineers Digital Collection, 2020).
[46]J. Kim and C. Lee, "Deep unsupervised learning of turbulence for inflow generation at various Reynolds numbers," Journal of Computational Physics **406**, 109216 (2020).
[47]R. Eisinger and A. Ruprecht, "Automatic shape optimization of hydro turbine components based on CFD," TASK Q **6**, 101–111 (2002).
[48]B. D. Marjavaara and T. S. Lundström, "Redesign of a sharp heel draft tube by a validated CFD-optimization," International Journal for Numerical Methods in Fluids **50**, 911–924 (2006).
[49]B. D. Marjavaara, T. S. Lundström, T. Goel, Y. Mack, and W. Shyy, "Hydraulic turbine diffuser shape optimization by multiple surrogate model approximations of Pareto fronts," Journal of Fluids Engineering **129**, 1228–1240 (2007).
[50]J. McNabb, C. Devals, S. Kyriacou, N. Murry, and B. Mullins, "CFD based draft tube hydraulic design optimization," in *IOP Conference Series: Earth and Environmental Science*, Vol. 22 (IOP Publishing, 2014) p. 012023.
[51]S. Galván, M. Reggio, and F. Guibault, "Optimization of the inlet velocity profile in a conical diffuser," in *Fluids Engineering Division Summer Meeting*, Vol. 44755 (American Society of Mechanical Engineers, 2012) pp. 125–134.
[52]S. Galván, M. Reggio, and F. Guibault, "Numerical optimization of the inlet velocity profile ingested by the conical draft tube of a hydraulic turbine," Journal of Fluids Engineering **137** (2015).
[53]M. Kato, "The modelling of turbulent flow around stationary and vibrating square cylinders," Turbulent Shear Flow **1**, 10–4 (1993).
[54]P. E. Smirnov and F. R. Menter, "Sensitization of the SST turbulence model to rotation and curvature by applying the Spalart-Shur correction term," Journal of Turbomachinery **131** (2009).
[55]ANSYS, "Solver theory guide," Ansys CFX Release **19** (2018).
[56]A. Gehrer, H. Benigni, and M. Köstenberger, "Unsteady simulation of the flow through a horizontal-shaft bulb turbine," in *Proceedings of the 22nd IAHR Symposium on Hydraulic Maschines and Systems, Stockholm* (2004).
[57]D. Jošt and A. Škerlavaj, "Efficiency prediction for a low head bulb turbine with SAS SST and zonal LES turbulence models," in *IOP Conference Series: Earth and Environmental Science*, Vol. 22 (IOP Publishing, 2014) p. 022007.
[58]M. Lesieur, O. Métais, P. Comte, *et al.*, *Large-eddy simulations of turbulence* (Cambridge university press, 2005).
[59]V. Moureau, P. Domingo, and L. Vervisch, "Design of a massively parallel CFD code for complex geometries," Comptes Rendus Mécanique **339**, 141–148 (2011).
[60]M. Germano, U. Piomelli, P. Moin, and W. H. Cabot, "A dynamic subgrid-scale eddy viscosity model," Physics of Fluids A: Fluid Dynamics **3**, 1760–1765 (1991).
[61]P. Benard, G. Balarac, V. Moureau, C. Dobrzynski, G. Lartigue, and Y. D'Angelo, "Mesh adaptation for large-eddy simulations in complex geometries," International Journal for Numerical Methods in Fluids (2015).
[62]C. Duprat, G. Balarac, O. Métais, P. Congedo, and O. Brugière, "A wall-layer model for large-eddy simulations of turbulent flows with/out pressure gradient," Physics of Fluids **23**, 015101 (2011).
[63]I. Goodfellow, Y. Bengio, A. Courville, and Y. Bengio, *Deep learning*, Vol. 1 (MIT press Cambridge, 2016).
[64]D. Carl, *A practical guide to splines* (Springer, 2001).
[65]I. Sobol and Y. L. Levitan, "The production of points uniformly distributed in a multidimensional cube," Preprint IPM Akad. Nauk SSSR **40**, 30 (1976).
[66]J. Bergstra and Y. Bengio, "Random search for hyper-parameter optimization." Journal of Machine Learning Research **13** (2012).
[67]C. Liu, B. Zoph, M. Neumann, J. Shlens, W. Hua, L.-J. Li, L. Fei-Fei, A. Yuille, J. Huang, and K. Murphy, "Progressive neural architecture search," in *Proceedings of the European conference on computer vision (ECCV)* (2018) pp. 19–34.
[68]M. Feurer and F. Hutter, "Hyperparameter optimization," in *Automated Machine Learning* (Springer, Cham, 2019) pp. 3–33.
[69]T. Elsken, J. H. Metzen, F. Hutter, *et al.*, "Neural architecture search: a survey." Journal of Machine Learning Research **20**, 1–21 (2019).
[70]D. Clevert, T. Unterthiner, and S. Hochreiter, "Fast and accurate deep network learning by exponential linear units (ELUs)," arXiv preprint arXiv:1511.07289 (2015).
[71]V. Nair and G. E. Hinton, "Rectified linear units improve restricted Boltzmann machines," in *Icml* (2010).
[72]X. Glorot, A. Bordes, and Y. Bengio, "Deep sparse rectifier neural networks," in *Proceedings of the fourteenth international conference on artificial intelligence and statistics* (JMLR Workshop and Conference Proceedings, 2011) pp. 315–323.
[73]N. Srivastava, G. Hinton, A. Krizhevsky, I. Sutskever, and R. Salakhutdinov, "Dropout: a simple way to prevent neural networks from overfitting," The journal of machine learning research **15**, 1929–1958 (2014).
[74]T. Dozat, "Incorporating Nesterov momentum into Adam," (2016).

SIGILLUM UNIVERSITATIS GRATIANOPOLITANÆ
VERI TAS LIBE RABIT
1339